UNIVERSIDADE
BEIRA INTERIOR

Propulsive Enhancement and Dynamic Stall Mitigation in Flapping Airfoils

Emanuel António Rodrigues Camacho

Tese para obtenção do Grau de Doutor em
Engenharia Aeronáutica
(3º ciclo de estudos)

Orientador: Prof. Doutor André Resende Rodrigues da Silva
Coorientador: Prof. Doutor Flávio Donizetti Marques

novembro de 2024

UNIVERSIDADE
BEIRA INTERIOR

Propulsive Enhancement and Dynamic Stall Mitigation in Flapping Airfoils

Emanuel António Rodrigues Camacho

Tese para obtenção do Grau de Doutor em
Engenharia Aeronáutica
(3º ciclo de estudos)

Orientador: Prof. Doutor André Resende Rodrigues da Silva
Coorientador: Prof. Doutor Flávio Donizetti Marques

Júri:
Prof. Doutor Joaquim Mateus Paulo Serra
Prof. Doutor Joaquim Rafael Rost Ávila Martins
Prof. Doutor William Roberto Wolf
Prof. Doutor Leandro Barbosa Magalhães
Prof. Doutor Jorge Manuel Martins Barata
Prof. Doutor João Manuel Melo de Sousa
Prof. Doutora Maíra Martins da Silva
Prof. Doutor André Resende Rodrigues da Silva

8 de novembro de 2024

Declaração de Integridade

Eu, Emanuel António Rodrigues Camacho, que abaixo assino, estudante com o número de inscrição D2719 de Engenharia Aeronáutica da Faculdade de Engenharia, declaro ter desenvolvido o presente trabalho e elaborado o presente texto em total consonância com o **Código de Integridades da Universidade da Beira Interior**.

Mais concretamente afirmo não ter incorrido em qualquer das variedades de Fraude Académica, e que aqui declaro conhecer, que em particular atendi à exigida referenciação de frases, extratos, imagens e outras formas de trabalho intelectual, e assumindo assim na íntegra as responsabilidades da autoria.

Universidade da Beira Interior, Covilhã, 19 de novembro de 2024

Emanuel António Rodrigues Camacho

Assinado por: **Emanuel António Rodrigues Camacho**
Num. de Identificação: 14740765
Data: 2024.11.19 17:50:12 +0000

Acknowledgments

"Appreciation is a wonderful thing: It makes what is excellent in others belong to us as well."

Voltaire

I see life as a mix of events governed by one or more differential equations that are, at least for now, unknown to Mankind. The beauty of these equations is that they have an infinite number of solutions and to find your solution, meaning to understand how our life evolves over space and time, we need to set what are known as initial or boundary conditions. Some of the starting conditions can be very harsh leading to very difficult life experiences while some are easier, but at the end of the day, we are all just integrating our differential equation with some step size to discover what the next day will bring. The step size is another interesting parameter that can be discussed philosophically in the context of our lives, but let us not enter such a black hole. One can look at these boundary conditions as being the environment and people that surround us. They do not govern us *per se* but have a great influence on our life path and help us achieve great things. So it is now time to properly mention the boundary conditions that made this path such an enjoyable and rich journey. Here are the credits if this thesis was a film:

Professor André Resende Rodrigues Silva

Professor Flávio Donizetti Marques

Professor Jorge Manuel Martins Barata

Mechanical Engineering Department of EESC-USP

LABDIN (EESC-USP) Research Group

AEROG (LAETA) Research Group

Rui Paulo

Fernando Neves

Leandro Carlos Pedrassolli

Jair Diego Antonietti

Sérgio Donizeti Ferreira

José Francisco de Moraes

Professor Leopoldo P. R. de Oliveira

Professor Maíra Martins da Silva

César Santos

Diana Rodrigues

Rúben Meireles

David Izquierdo

Friends

Family

People who taught me what to not do or be in life

Emanuel Camacho

Funding

The present work was performed under the scope of the Aeronautics and Astronautics Research Center (AEROG) of the Laboratório Associado em Energia, Transportes e Aeronáutica (LAETA) activities, supported by the Fundação para a Ciência e Tecnologia (FCT) through the grant 2020.04648.BD and projects UID / EMS / 50022 / 2019, UIDB / 50022 / 2020, UIDP / 50022 / 2020 and LA / P / 0079 / 2020. The work was also supported by the grant co-sponsored by Santander-UBI BID / FE / 2019.

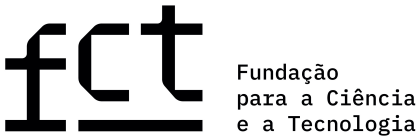

Resumo

O estudo de perfis alares oscilantes é a peça central para a biomimetização do voo, explorar novos sistemas de extração energética e para melhorar o projeto de pás de rotores. Tipicamente, estes sistemas são caracterizados por efeitos aerodinâmicos altamente não lineares, que na maioria dos casos, ainda necessita de uma profunda investigação no que diz respeito à aerodinâmica e aos parâmetros que governam estes sistemas.

Esta investigação debruça-se em alguns destes temas, escrutinando-os em duas frentes: a melhoria propulsiva e a mitigação da perda dinâmica de perfis alares oscilantes. Após uma longa revisão de estudos anteriores, o presente projeto propõe um novo perfil alar, designado por NACA0012-IK30, que introduz o conceito de curvatura dinâmica. Este conceito bioinspirado é aplicado ao conhecido perfil NACA0012, produzindo uma geometria inovadora que divide o referido perfil em duas partes, onde existe a possibilidade de defletir o bordo de ataque de forma independente do resto do perfil alar. Este novo sistema passou por um conjunto de análises paramétricas e ótimas através de várias metodologias experimentais e numéricas, que se dividem em duas partes: estudos num número de Reynolds mais baixo, onde as capacidades propulsivas são estudadas, e num número de Reynolds mais elevado, onde a mitigação da perda dinâmica é explorada.

Na parte inferior do espectro do número de Reynolds, os resultados demonstram que a ativação do bordo de ataque oferecida pelo mecanismo IK30, demonstrou a habilidade de aumentar consideravelmente a potência propulsiva e eficiência. Ao comparar a geometria proposta com o movimento de oscilação tradicionalmente estudado na literatura, tornou-se óbvio que o mecanismo proposto pode oferecer tração máxima com uma eficiência propulsiva quase ótima, algo que é totalmente inconcebível em movimentos oscilantes tradicionais. Os resultados obtidos na gama superior do número de Reynolds, onde o sistema proposto foi utilizado como recurso de mitigação da perda dinâmica, mostram a eficácia do mecanismo quando sujeito a diferentes movimentos de translação e rotação. Ao usar corretamente o sistema IK30, a perda dinâmica experienciada em condições permanentes e transientes conseguiu ser mitigada ou até mesmo erradicada, o que proporcionou reduções consideráveis na resistência aerodinâmica e aumentos notáveis na sustentação produzida.

Embora o presente estudo tenha mostrado resultados interessantes, o sistema proposto, em conjunto com o conceito amplo de curvatura dinâmica, deverá ser estudado profundamente. Ao juntar novas tecnologias, como por exemplo, a deformação contínua da curvatura acoplada a novas cinemáticas, poderemos explorar novos caminhos que estenderão o nosso conhecimento e aproveitamento da aerodinâmica de perfis alares oscilantes.

Palavras-chave

Perfis Alares Oscilantes; Bordo de Ataque Móvel; Otimização; Aumento Propulsivo; Mitigação de Perda Dinâmica

Resumo Alargado

Os perfis oscilantes estão presentes em vários tópicos relacionados com a aérea aeronáutica, desde a miniaturização de sistemas para um voo baseado na biomimetização, no projeto de mecanismos para extração energética através de superfícies oscilantes e no desenvolvimento de pás aplicadas ao voo que recorre a asas rotativas. Ao ser um tema tão abrangente, existem portanto várias veias de estudo onde são realizadas inúmeras investigações com um objetivo central: o de compreender como a geometria e a cinemática destas superfícies oscilantes influenciam o desempenho aerodinâmico das mesmas.

Um dos assuntos que se levanta quando analisamos o presente estado de arte de perfis oscilantes, debruça-se sobre quais os caminhos que propiciarão um aumento do desempenho propulsivo, quando os perfis são usados como propulsores, ou uma melhoria no comportamento aerodinâmico quando usados como mitigadores da perda dinâmica. Sabendo que a resposta reside na geometria e cinemática, uma atenção redobrada deverá ser redirecionada para o desenvolvimento de novas morfologias acopladas de novos movimentos. Este é o centro da tese, que debruçou-se sobre várias possibilidades geométricas, teve em conta os possíveis regimes operacionais e considerou diversos constrangimentos, culminando numa proposta que materializou-se através de um novo perfil alar: o NACA0012-IK30. Tal como o nome indica, esta nova geometria baseia-se numa modificação denominada IK30 do tradicional perfil NACA0012, onde este é dividido em duas partes que se movem de forma independente. Este movimento independente entre o bordo de ataque e o restante perfil alar, leva a que surja uma curvatura efetiva do perfil que pode ser ajustada dinamicamente, mimetizando um pouco do que é visto nas superfícies utilizadas no mundo natural. No presente trabalho, a geometria proposta é testada em dois regimes operacionais distintos, sendo estes o de propulsão e o de mitigação de perda dinâmica.

O estudo do perfil enquanto propulsor, ocorre num número de Reynolds mais baixo, onde a oscilação do perfil tem a capacidade de induzir um excesso de momento linear na esteira. Esta fase de estudo foi conseguida através de uma montagem experimental, onde foram feitos testes de visualização de escoamento através de fumo, e de uma metodologia numérica que recorre à dinâmica de fluidos computacional, onde a média de Reynolds das equações de Navier-Stokes é utilizada. Além das análises paramétricas, é criada uma metodologia de otimização acoplada à formulação numérica, onde é feita a busca de tração ou eficiência propulsiva máxima. Com base nas metodologias implementadas, foi possível verificar que a deflexão do bordo de ataque ao longo do tempo possui uma elevada influência, principalmente na dimensão do vórtice de perda dinâmica, podendo mesmo eliminá-lo em algumas condições. Relativamente às capacidades propulsivas, a adição da componente rotacional ao bordo de ataque, fez com que a potência propulsiva tenha aumentado de forma considerável, acompanhada com uma melhoria notória na eficiência propulsiva. Relativamente à potência requerida do movimento, esta mantém-se, para várias condições consideradas, quase independente da amplitude rotacional do bordo de ataque. Quando sujeito à otimização, o

mecanismo IK30 demonstrou ser um sistema altamente capaz, quando comparado ao que é tipicamente observado na literatura. Um resultado central nesta fase do estudo centra-se na capacidade que o mecanismo proposto tem em obter tração ótima com eficiência perto da máxima, algo que é inconcebível por oscilações convencionais onde um destes parâmetros é sacrificado pelo aumento do outro.

No âmbito da mitigação de perda dinâmica, onde o número de Reynolds sobe uma ordem de magnitude relativamente a quando o perfil é usado como propulsor, é estabelecida uma montagem experimental desenvolvida para a medição das cargas aerodinâmicas. À metodologia experimental, é também conectado um inovador algoritmo de otimização em tempo real, onde a minimização da resistência aerodinâmica ou a maximização da sustentação é desejável. É também implementada uma extensão da metodologia numérica mencionada anteriormente para um breve estudo da influência da deflexão do bordo de ataque na distribuição de pressão da superfície alar. Os resultados são claros no que diz respeito às melhorias aerodinâmicas, obtidas em ambos os casos estáticos e dinâmicos, demonstrando que a deflexão do bordo de ataque relativamente ao resto da estrutura, reduz ou, em certas condições, elimina por completo a presença da perda aerodinâmica. Isto leva à inevitável redução da resistência aerodinâmica e aumento da sustentação, que normalmente vem acompanhado com um aumento do momento de arfagem. Importante mencionar que em condições onde a perda aerodinâmica era inexistente ou negligenciável, o mecanismo IK30 demonstrou ser capaz de reduzir a intensidade do momento, sem sacrificar as forças aerodinâmicas, algo desejável quando o objetivo será a redução global dos esforços aplicados. Estes efeitos foram verificados especialmente em condições oscilantes de translação e rotação, onde o mecanismo proposto mostrou a capacidade enquanto mitigador da perda dinâmica. Foi também vista a necessidade de explorar ainda mais a cinemática e o cuidado a ter com esta, de modo a não degradar o desempenho aerodinâmico além de todas as adversidades impostas pela perda dinâmica.

A presente tese deverá funcionar não como um fim, mas como um início de uma longa e profunda exploração de novas geometrias e cinemáticas. Sendo estas as duas variáveis que governam este problema, é necessário continuar a construir sobre o conceito de curvatura dinâmica, e acoplá-la a novas cinemáticas. Isto levará ao surgimento de novas possibilidades, onde poderá ser feito um ajuste mais flexível do escoamento em torno do perfil, olhando para este como um conjunto de partes interagindo entre si, e não como um todo, rígido e imutável.

Abstract

The study of oscillating airfoils is the centerpiece for the biomimetization of flight, exploring newer energy-extracting devices, and improving rotor blade design. Typically, these are affected by highly nonlinear aerodynamic effects, which in most cases, still require substantial research regarding the aerodynamics and parameters that govern these systems.

The present investigation looks into some of these topics by scrutinizing two primary fronts: the propulsive enhancement and the dynamic stall mitigation of flapping airfoils. After a comprehensive review of past investigations, the current work proposes a newer airfoil, the NACA0012-IK30 airfoil, that introduces the concept of dynamic curvature. This bioinspired concept is applied to the conventional NACA0012, producing an innovative geometry by dividing the airfoil into two parts, where we can deflect the leading edge independently from the rest of the airfoil. This newer design went through parametrical and optimal analysis by employing a diverse set of experimental and numerical methodologies, divided into two domains: lower Reynolds number, where the propulsive capabilities are studied, and higher Reynolds number, where dynamic stall mitigation is explored.

At the lower spectrum of the Reynolds number, results show that the activation of the leading edge offered by the IK30 mechanism demonstrated the ability to improve considerably the propulsive power and efficiency. When comparing the proposed geometry with standard flapping, it is clear that the suggested design can provide optimal thrust with near-optimal propulsive efficiency, something unachievable in traditional flapping. Results obtained at the higher range of the Reynolds number, where the IK30 mechanism functions with dynamic stall mitigation purposes, show the adequacy of the proposed geometry under different plunging and pitching conditions. When correctly deflecting the leading edge, the aerodynamic stall experienced both in static and dynamic conditions can be mitigated or even eradicated, leading to significant drag reductions and modest lift enhancements.

While the present study yielded encouraging results, the IK30 mechanism and the broad concept of dynamic curvature need to be the focus of further research. Using newer technologies, for instance, continuous camber morphing, coupled with ingenious kinematics, will allow us to explore newer pathways to extend our knowledge and exploit the aerodynamics of unsteady airfoils.

Keywords

Flapping Airfoils; Movable Leading Edge; Optimization; Propulsive Enhancement; Dynamic Stall Mitigation

Contents

List of Figures

List of Tables

Chapter 1

Introduction

> *"I think the biggest innovations of the 21st century will be at the intersection of biology and technology. A new era is beginning."*
>
> *Steve Jobs*

In this introductory chapter, we will first look at the motivation for the work, where we discuss the overall potential and applications of oscillating airfoils. Then, based on this unexplored potential and the current state of the art, the objectives of the thesis are presented together with subtasks needed to push the topic of unsteady airfoils even further.

1.1 Motivation

Humans have been observing the processes of nature and using them as their source of inspiration to develop new systems. Biomimicry has undoubtedly pushed the aeronautical industry standards to higher levels and with newer concepts, such as morphing, aviation will become more sustainable, with much cleaner and greener operations.

The Biomimicry Institute from the United States of America, whose mission is to help solve humanity's biggest challenges through the adoption of biomimicry, defines the concept of biomimetics as an approach to innovation that seeks sustainable solutions to human challenges, by emulating nature's time-tested patterns and strategies [1]. Nature is powered by mechanisms that typically offer well-adapted solutions to animals subjected to any given environment, being often called by naturalists and biologists the natural selection process.

The father of the theory of evolution, Charles Darwin, explains in his 1859 masterpiece, *On the Origin of Species by Means of Natural Selection* [2], this effective process that has governed species evolution for millions of years, saying that

> "Can it, then, be thought improbable, seeing that variations useful to man have undoubtedly occurred, that other variations useful in some way to each being in the great and complex battle of life, should occur in the course of many successive generations? If such do occur, can we doubt (remembering that many more individuals are born than can possibly survive) that individuals having any advantage, however slight, over others, would have the best chance of surviving and of procreating their kind? On the other hand, we may feel sure that any varia-

> tion in the least degree injurious would be rigidly destroyed. This preservation of favourable individual differences and variations, and the destruction of those which are injurious, I have called Natural Selection, or the Survival of the Fittest."

However, from an engineering standpoint, in Darwin's explanation, there is no reference to whether the natural solutions are the most efficient, meaning that the energy input for a given system would be converted to the type of energy we desire, in simpler words, the good use of time and energy in a way that does not waste any. Nevertheless, an important concept is introduced by Darwin: effectiveness. Understood as the ability to be successful and produce the intended results, effectiveness is an interesting concept that suggests that with nature, we can obtain adequate solutions, or at least a starting point for several design problems.

A practical application, whose inspiration came from nature, was the introduction of refined wing tips that offered useful operational advantages for airlines operating long-range flights. Inspiration for the design came from birds observed to curl their wing tip feathers upward when requiring a high lift. A well-designed winglet, as the case of the A350 XWB family wing tip illustrated in Figure 1.1, rises vertically and is swept back such that it significantly reduces the size of the wingtip vortex, thus reducing induced drag.

Figure 1.1: A350 XWB family wing tip.

Recently, aircraft manufacturers have been looking forward to improving the way we fly, making use of the new propulsive systems that can drag the aeronautical industry towards a more sustainable environment. Martin Aston, a Senior Manager at Airbus [3] says that

> "One of the priorities for the entire industry is how to make aviation more sustainable – making flying cleaner, greener, and quieter than ever before. We know from our work on the A350 XWB family passenger jet that through biomimicry, nature has some of the best lessons we can learn about design."

The new Airbus conceptual aircraft, the Bird of Prey (Figure 1.2), is then the culmination of a mix of concepts extracted from nature that could offer the morphing capabilities that aeronautical engineering is eager for and, although it is not an actual aircraft, it could very well represent a solution for the short-range class. This proposed design considers a hybrid-electric, turbo-propeller system, an elegant wing-to-fuselage joint based on the geometry of faster birds, and revolutionary wing and tail structures. This design would exploit the

wingtips similar to individual feathers to actively control the aircraft and massively increase the operational efficiency [3]. The flight mechanics of insects and birds under several airflow fluctuations may also help to develop new systems to be applied in auto flight computers' response.

Ideas of developing newer surface finishings are also in the front line of engineering projects. This is the case of textured surfaces that mimic the sharkskin structures that challenge the predefined idea that an aircraft should have every surface as smooth as possible. Suitable for long-range aircraft, this new concept can offer a good solution that together with other futuristic solutions, represents a renewed engineering [4].

Figure 1.2: Bird of Prey - Airbus conceptual aircraft [3].

Another project fueled by biomimicry is the Airbus' AlbatrossOne [5] that focuses on the importance of wing tips and the effects happening on these extremities, opening new ways to transform aircraft wing design.

The concept based on a semi-aeroelastic hinge has the potential to reduce drag and wing weight by diminishing turbulence and gust effects allowed by the freely flapping wing tips. The inspiration comes from the albatross marine bird that can lock or unlock their wing structures at the shoulder when turbulence occurs or active flight control is required [6]. Jean-Brice Dumont [5] explains that

> "When there is a wind gust or turbulence, the wing of a conventional aircraft transmits huge loads to the fuselage, so the base of the wing must be heavily strengthened, adding weight to the aircraft. Allowing the wing-tips to react and flex to gusts reduces the loads and allows us to make lighter and longer wings – the longer the wing, the less drag it creates up to an optimum, so there are potentially more fuel efficiencies to exploit."

But Airbus is moving further with the concept of biomimicry by introducing another demonstrator project based on what we have been seeing in Nature for hundreds of years: V formation in birds' flight. This new project called fello'fly will explore the technical and commercial

Figure 1.3: AlbatrossOne - Airbus project [5].

viability of two aircraft flying together for long-haul flights, which will help the environmental performance of commercial aircraft and move towards an improved and more sustainable aviation industry. This concept could provide a significant reduction in emissions, which could hit the targets defined by the International Civil Aviation Organisation (ICAO) and the Committee on Aviation Environmental Protection (CAEP) [7].

From a practical standpoint, this project encourages engineers to explore innovative ways to exploit the energy content that an aircraft wake has, just like birds. For a long time, these animals have been using the V shape to fly together, but only recently have scientists understood the real potential that this flying configuration has, especially on long-haul flights [8].

Hence, it is possible to extract the kinetic energy by positioning a follower aircraft in the air upwash of one of the lead aircraft's wakes, as illustrated in Figure 1.4. With this, the upwash created upstream will contribute to lift production and decreased engine thrust and, therefore, fuel consumption that could be reduced by more than 5 %.

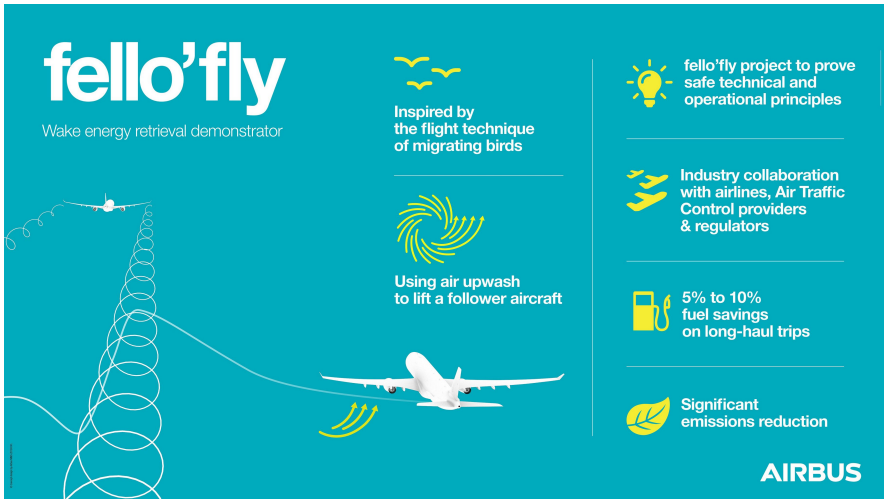

Figure 1.4: fello'fly - Airbus project [7].

Oscillating hydrofoils and airfoils have been used by animals as their locomotive system. The structures themselves are indeed intriguing but the most interesting question is without a

doubt how these animals have been using these foils and how this system can provide such high effectiveness and maneuverability.

Insect flight, associated with lower length scales and velocities, is based on the favorable vortex interactions between the leading and trailing edge vortices, which are achieved by large geometric deformations and corrugations. The tandem wing configuration offers an additional advantage regarding vertical takeoff and hovering flight, where the downstream wings can retrieve some wake energy from the front ones.

On the other hand, bird flight presents different characteristics where feathering controls prevents flow separation at large incidences, and the variable wing geometry in flight allows alternating flapping flight modes with gliding phases. Flight efficiency can also be enhanced by using non-uniform air such as wind gusts.

The study of unsteady airfoils has the potential to boost new technologies for numerous engineering applications such as MAV (Micro Air Vehicle) flight, rotor dynamics, aircraft response in gusty weather, and improved design of energy extraction devices. Moreover, their superior propulsive efficiency at low Reynolds number environments, makes flapping wings desirable for futuristic applications such as planetary exploration [9]. At higher Reynolds number environments, for instance, helicopter flight, their study leads to improving blade design and mitigating the adverse effects of dynamic stall that compromise maneuverability and structural soundness.

Also in naval engineering, unsteady hydrofoils are a great propulsive system replacement for conventional propellers. This was confirmed by the MS Triade ship, a pioneer project (O-foil) (Figure 1.5), developed by the Netherlands Maritime Research Institute, where the flapping foil was a serious competitor for the conventional ship propeller, offering an appreciable increase in propulsive efficiency with an achievable $50\,\%$ reduction in fuel consumption. The same institute is also dedicated to improving the naval industry by implementing the concepts of the sailfish shape, frictionless shark skin, and flexible moving tails [10].

1.2 Objectives

The applications of unsteady airfoils are numerous, permeating into several research fields and industries. The present work builds upon the motivation by bringing a bioinspired solution to two distinct fields: propulsive enhancement of flapping airfoils and dynamic stall mitigation.

Regardless of these two fields, the core objective of the thesis is to

1. Propose a bioinspired airfoil that uses the concept of a deflectable leading edge, presenting enough operational flexibility to improve both the propulsive characteristics of unsteady airfoils and mitigate the adverse effects of stall.

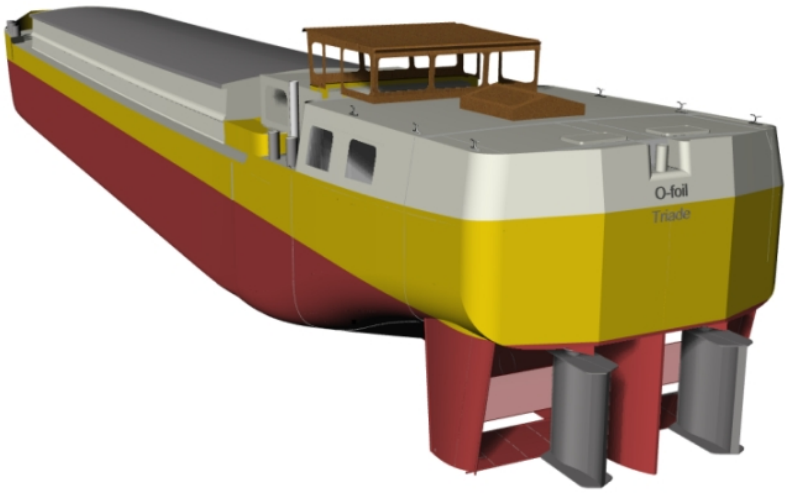

Figure 1.5: O-Foil concept by Marin [10].

Yet, achieving this objective relies on additional goals and tasks, which depend on how the airfoil is used. Regarding the propulsive enhancement of flapping airfoils, the work focuses on

2. Understanding the influence of a movable leading edge on the flow field surrounding a flapping airfoil at a lower Reynolds number by
    - designing and building an experimental rig that allows for smoke visualization,
    - and setting up an image processing framework for flow visualization.
3. Verifying the influence of a dynamic actuation of the leading edge on the propulsive characteristics of a flapping airfoil by
    - implementing a numerical methodology capable of providing the aerodynamic and propulsive coefficients,
    - and comparing them with classical potential flow theory.
4. Finding optimal operation leading-edge kinematics for maximum thrust generation and propulsive efficiency by
    - numerically coupling the proposed airfoil with a gradient-based algorithm.

Concerning the dynamic stall mitigation, the work looks into

5. Characterizing the steady operation of the proposed geometry at a higher Reynolds number by
    - designing and building an experimental rig capable of measuring all aerodynamic

coefficients,

- conducting tufts visualization, combined with video processing, to observe the onset of stall,

- and CFD simulations for a complete understanding of the influence of the leading edge position on the pressure distribution.

6. Optimizing the wing's drag and lift coefficients by

   - incorporating a real-time optimization algorithm into the control system to find steady optimal values for various configurations.

7. Studying the proposed geometry under several dynamic conditions by

   - considering a time-varying activation of the leading edge on plunging conditions with a mean angle of attack,

   - checking the influence of a pitching leading edge when the back part is fixed,

   - and checking the influence of curvature in pitching by deflecting the leading edge relative to the rest of the airfoil.

1.3 Thesis Outline

Following this introductory chapter is the literature review, where a wide selection of papers regarding unsteady airfoils are presented. A background section is also provided for the familiarization of flapping airfoils nomenclature and parameters, which are used to investigate their performance.

The four subsequent chapters concern the various methodologies implemented for the analysis of the proposed airfoil: the experimental methodology, where all information is provided for the flow visualization and force measurements tests; the numerical methodology that explains the numerical algorithms used for CFD simulations; the unsteady panel method chapter, in which the mathematical formulation of the panel method used is shown and the optimization chapter, where the optimization algorithms implemented are explained in detail.

These chapters are then followed by the results chapters, where special focus is given to the propulsive enhancement and dynamic stall mitigation. The document ends with the conclusions chapter, where an overview of the work is provided together with future work suggestions.

Chapter 2

Literature Review

"Wisdom is not a product of schooling but of the lifelong attempt to acquire it."

Albert Einstein

In this chapter, a broad review is made regarding the current state of the art of unsteady airfoil aerodynamics. Several topics are discussed, including bi- and tridimensional effects, the influence of structural flexibility, and flow control techniques. Furthermore, governing parameters and aerodynamic and propulsive indicators used to evaluate the unsteady airfoil phenomena are explained.

2.1 Background

The study of oscillating airfoils, either plunging, pitching, or flapping, started due to a substantial demand concerning the understanding of the aerodynamics surrounding flutter and gust-response effects [11]. Also of interest was opening new ways to study the negative impact of dynamic stall on helicopter rotors and propeller blades performance and how one could reduce it or even eliminate it [12].

Although the studies of flapping airfoils started at the beginning of the twentieth century, it is only at the beginning of the 21st that the topic has seen considerable growth, with more than 20 papers published every year in the past years, mainly from the US and China with a proportion of $40.2\,\%$ and $16.5\,\%$, respectively [13].

At such an early phase of studying oscillating airfoils, little effort was made regarding drag or thrust forces since the analysis performed at the time typically required only the determination of the lifting forces generated by the moving airfoil. However, in 1924, the flapping airfoil had already been identified as a possible substitute for the conventional propeller by Birnbaum [14, 15].

The first explanation of the flapping mechanism was given by Knoller [16] and Betz [17] who noticed that a flapping airfoil had an effective angle of attack that created an oscillatory aerodynamic force normal to the relative velocity. However, this explanation, based only on the airfoil kinematics, did not account for the wake effects.

In 1935, von Kármán and Burgers [18] clarify the thrust generation mechanism based on

the vortex shedding of the airfoil. They modeled the wake of the flow past bluff bodies at low-Reynolds numbers by an infinite row of alternating vortices, commonly known as the von Kármán vortex street, which is associated with the production of drag, as illustrated in Figure 2.1, considering an airfoil.

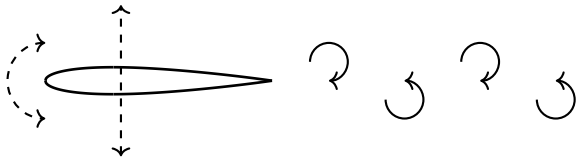

Figure 2.1: Drag-producing wake.

On the other hand, a flapping airfoil with the right combination of kinematics parameters may produce a wake where vortices induce a velocity or a momentum surplus in the wake compared to the upstream flow. This creates a jet-like flow that generates a propulsive force explained by Newton's third law of motion [18]. Hence, this type of wake results in thrust production, as shown in Figure 2.2.

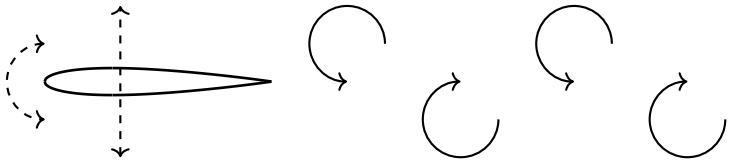

Figure 2.2: Thrust-producing wake.

These earlier studies opened new ways to explore the flapping airfoil problem. Since then, the studies mainly fall under two classifications: zoological and simplified configurations [19]. The zoological studies observe insects, birds, and animals and how they adjust their surfaces to environmental conditions. The simplified studies concern research based on flow aerodynamics, where the prediction of aerodynamic forces and propulsive efficiency are obtained using 2D or 3D simulations and experiments.

These studies consider the flapping airfoil as the combination of surging, plunging, and pitching, with these being the three degrees of freedom in a two-dimensional space, as shown in Figure 2.3.

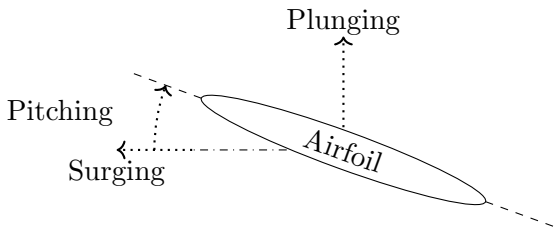

Figure 2.3: Two dimensional flapping scheme.

However, the majority of studies on flapping airfoils neglect the surging component, emphasizing pure plunging, pure pitching, or a combination of both. The main objective is to investigate the influence of kinematic parameters, such as reduced frequency and nondimensional

amplitude, on the aerodynamic and propulsive forces of the airfoil. By conducting experimental and numerical simulations, one can find combinations of the governing parameters that can enhance or degrade the airfoil performance.

2.2 Governing Parameters and Performance Indicators

Firstly, let us define the airfoil position and orientation. Based on an inertial frame of reference, an airfoil executing an unsteady motion, including rotation and translation, can be described by its three degrees of freedom, being these

$$x, y, \theta, \tag{2.1}$$

where x is the horizontal component, y is the vertical component, and θ is its orientation, commonly known as the pitch angle. All three degrees of freedom are illustrated in Figure 2.4.

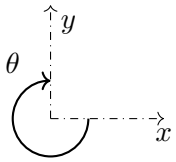

Figure 2.4: Axis system (Positive directions indicated).

However, for the sake of this analysis, the pitch angle equals the angle of attack, α (angle between the chord line and the direction of the approaching flow), as we assume that the flow velocity has an x component only.

Considering now the time derivative of x, y and α we have

$$\dot{x}, \dot{y}, \dot{\alpha}, \tag{2.2}$$

which are the surging, plunging, and pitching velocities, respectively.

Due to the existing relative motion between the airfoil and the approaching flow, in addition to the angle of attack, it is possible to define an effective angle of attack as

$$\alpha_{\text{eff}} = \alpha + \arctan\left(\frac{-\dot{y}}{U_\infty + \dot{x}}\right), \tag{2.3}$$

where U_∞ is the flow velocity.

The aerodynamic and propulsive characteristics of an oscillating airfoil are commonly expressed as a function of a group of dimensionless parameters that govern the problem. One of these parameters is the Reynolds number, which indicates whether the inertial or viscosity

effects are preponderant. It is defined as

$$Re = \frac{\rho U_\infty c}{\mu}, \tag{2.4}$$

where ρ is the density, U_∞ is the flow velocity, c is the airfoil chord, and μ is the dynamic viscosity.

In the specific subject of flapping airfoils, the Reynolds number parameter is crucial to identify the range of length and velocity scales where the oscillating airfoil shows different aerodynamic and propulsive behaviors. For instance, we see this in nature where the flapping strategies used by birds (higher Reynolds numbers) are very different from those used by insects (ultra-low Reynolds numbers), in which massive leading-edge separation is present.

Another essential parameter is the reduced frequency defined by Birnbaum in 1924 [14]. It is a measure of the unsteadiness of the flow field and is a crucial similarity parameter [20]. It is expressed as

$$k = \frac{2\pi f c}{U_\infty}, \tag{2.5}$$

where f is the motion frequency. This parameter is also viewed as the ratio between the airfoil speed and the wind speed, being used predominantly in unsteady aerodynamic and aeroelastic problems.

Similar to the motion frequency, the motion amplitude is presented in its dimensionless form by dividing it by the aerodynamic chord. It is called the nondimensional amplitude and is expressed by

$$h = \frac{A}{c}, \tag{2.6}$$

where A is the motion amplitude.

If we combine these two last parameters by multiplying them, we obtain the nondimensional amplitude, kh, defined as

$$kh = \frac{2\pi f c}{U_\infty}\frac{A}{c} = \frac{2\pi f A}{U_\infty}. \tag{2.7}$$

As this problem presents oscillating flow mechanisms, an obvious parameter to be considered is the Strouhal number. It represents the ratio between inertial forces due to the local and convective acceleration, indicating whether unsteady or convective terms are predominant. It is defined as

$$St = \frac{fW}{U_\infty}, \tag{2.8}$$

where W is the wake height.

Instinctively, at high Strouhal numbers, oscillations will dominate the flow field, while at low Strouhal numbers, the oscillations are transported by the surrounding fluid.

The combination of the aforementioned governing parameters will produce different results concerning force production and required power. Hence, aerodynamic and propulsive coefficients are defined to methodically evaluate the influence of the governing parameters, working as performance indicators.

Concerning propulsive parameters, the propulsive power is obtained by multiplying the thrust, T, by the flow velocity, as seen in equation (2.9).

$$P_{\mathrm{P}} = TU_{\infty}. \tag{2.9}$$

Concerning the required power, it is defined as

$$P_{\mathrm{R}} = -D\dot{x} - L\dot{y} - M\dot{\alpha}, \tag{2.10}$$

where D and L are the drag and lift forces, respectively, and M is the pitching moment. Important to note that the term required power in equation (2.10) only provides the aerodynamic required power, meaning the power needed to counteract the aerodynamic forces while oscillating the airfoil. Equation (2.10) shows this power as the sum of the required power of surging, plunging, and pitching.

The propulsive power can be expressed in its dimensionless form by dividing equation (2.9) by $\frac{1}{2}\rho U_{\infty}^{3}S$, obtaining

$$\frac{P_{\mathrm{P}}}{\frac{1}{2}\rho U_{\infty}^{3}S} = \frac{TU_{\infty}}{\frac{1}{2}\rho U_{\infty}^{3}S}, \tag{2.11}$$

which can be simplified to

$$C_{P_P} = C_t, \tag{2.12}$$

where C_{P_P} is the propulsive power coefficient and C_t is the thrust coefficient.

Likewise, the required power defined in equation (2.10) is divided by $\frac{1}{2}\rho U_{\infty}^{3}S$,

$$\frac{P_{\mathrm{R}}}{\frac{1}{2}\rho U_{\infty}^{3}S} = \frac{-D\dot{x} - L\dot{y} - M\dot{\alpha}}{\frac{1}{2}\rho U_{\infty}^{3}S}, \tag{2.13}$$

which is reduced to

$$C_{P_R} = -C_d \frac{\dot{x}}{U_\infty} - C_l \frac{\dot{y}}{U_\infty} - C_m \frac{\dot{\alpha} c}{U_\infty}, \tag{2.14}$$

where C_{P_R} is the required power coefficient, and C_d, C_l, and C_m are the drag, lift, and pitching moment coefficients, respectively. The required power must not be confused with its traditional definition of the required power to keep steady level flight. Here, the required power coefficient is the power required to maintain or sustain the prescribed kinematics.

There is also interest in knowing the mean propulsive and required power values over n periods T, which are crucial parameters for the operation and energy consumption in a time-varying system. These are calculated by

$$\overline{C_{P_P}} = \frac{1}{nT} \int_t^{t+nT} C_t \, \mathrm{dt}, \tag{2.15}$$

and

$$\overline{C_{P_R}} = \frac{1}{nT} \int_t^{t+nT} -C_d \frac{\dot{x}}{U_\infty} - C_l \frac{\dot{y}}{U_\infty} - C_m \frac{\dot{\alpha} c}{U_\infty} \, \mathrm{dt}, \tag{2.16}$$

respectively.

The propulsive efficiency is then obtained by dividing the mean propulsive power coefficient by the mean required power coefficient, as in equation (2.17).

$$\eta = \frac{\overline{C_{P_P}}}{\overline{C_{P_R}}} \tag{2.17}$$

2.3 State of the Art

In this section, we offer a comprehensive review which is divided into the main topics that researchers focus on while studying oscillating airfoils. This review goes from the most fundamental concepts of flapping airfoils such as the influence of kinematics and vortex dynamics to more complex and current topics such as energy extraction, structural parameters, three-dimensional effects, and dynamic stall.

2.3.1 Kinematics

One significant section of flapping airfoils is kinematics, where the existing relationship between kinematic parameters and the resulting performance is studied. Early observations made by Katzmayr [21] had shown that soaring flight seemed to be feasible when an airfoil or wing could draw energy from the surrounding air. Such observation occurs, for instance, in the presence of gusty weather where periodic changes in the angle of attack could offer a considerable reduction in drag with a negligible influence on lift production.

One of the first mathematical theories regarding unsteady airfoils was made by Theodorsen [22], which predicts the unsteady aerodynamics of pitching and plunging airfoils. In 1936, Garrick [23] makes use of the previously proposed formulas and the method drafted by von Kármán and Burgers [18] to study the propulsion capabilities of a movable wing with three degrees of freedom. Considering small oscillation amplitudes and a perfect fluid, results show that there is always a propelling force in the reduced frequency range, with a propulsive efficiency of $100\,\%$ when flapping is infinitely slow, and $50\,\%$ when the reduced frequency tends to infinity. Furthermore, the thrust produced by the airfoil was approximately proportional to the square of kh, whereas pitching airfoils do so only with frequencies above a critical value and as a function of the pivot location. However, the use of inviscid methods is not unreasonable when considering a satisfactorily large Reynolds number and a reduced angle of attack as suggested by Platzer et al. [24].

The beginning of numerical studies regarding oscillating airfoils started by performing analyses that are ideal for calculating the flow field over an airfoil in an inviscid incompressible medium [25, 26]. However, over time, improvements in computational resources caused an inevitable migration from these simplified methods to newer CFD techniques that offered an improved and closer representation of reality.

After the development of classical theories, several were the works that followed. Freymuth [27] studied experimentally both pure plunging and pitching motions and identified thrust-producing wakes at low angles of attack, small plunging amplitudes, and high reduced frequencies. At such regimes, he identified that the airfoil could avoid, to some extent, severe flow separation from the leading edge, and even suggested that this may be the signature of propulsive bird flight.

When it comes to the plunging motion, Tuncer and Platzer [28] used a Navier-Stokes solver to estimate the thrust and propulsive efficiency of a NACA0012. At $Re = 3 \times 10^6$, the maximum propulsive efficiency reached values close to $75\,\%$ but with considerably low thrust coefficients. They also studied the flapping/stationary airfoil combination in tandem configuration, concluding that placing a stationary airfoil downstream of a plunging airfoil has a beneficial impact on propulsive efficiency.

Jones et al. [29] used laser-Doppler velocimetry to measure the mean jet profile in the wake of a plunging airfoil and saw that thrust increases with both frequency and amplitude. They then compared the experimental data with the unsteady panel method developed by Teng [30]. Results show that inviscid phenomena govern the thrust wake structures. They also showed that at Strouhal numbers higher than 1, asymmetrical and deflected wakes tend to occur, as illustrated in Figure 2.5, which could offer the advantage of producing both thrust and lift.

The flow around oscillating airfoils was further studied by Anderson et al. [31] who used DPIV (Digital Particle Image Velocimetry) at a Reynolds number of 1.1×10^2 and measured

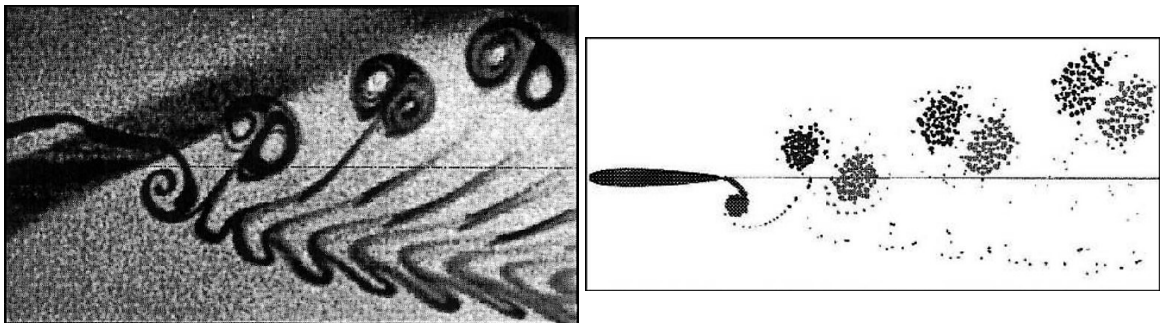

Figure 2.5: Asymmetrical wake regime [29].

force and required power at a Reynolds number of 4.0×10^4. Highly focused on obtaining the highest propulsive efficiency, authors found out that four requirements should be met, being these: a Strouhal number between 0.25 and 0.40, large nondimensional amplitudes (≈ 1), a maximum angle of attack somewhere between $15°$ and $25°$, and a phase angle between plunging and pitching of about $75°$ (considering that the pivot point is at one-third chord length from the leading edge). With these conditions, Anderson et al. reached in their study a maximum measured propulsive efficiency of $87\,\%$.

Lai and Platzer [32] studied experimentally the plunging airfoil and found that the nondimensional plunge velocity (kh) is a crucial parameter to study the region located downstream of a plunging airfoil, especially the mean jet profile. They offered useful correlations concerning the maximum jet velocity in the wake as a function of the distance to the airfoil. They also verified that the maximum velocity can be described as a function of kh and concluded that U_{max} decreased with the distance x/c to the trailing edge as

$$\frac{\mathrm{d}U_{max}}{\mathrm{d}(kh)} \approx \left(\frac{x}{c}\right)^{-0.5}, \tag{2.18}$$

thus indicating a two-dimensional turbulent jet behavior.

Thrust production was also studied by Tuncer and Platzer [12] who concluded that when the flow remains attached during the period of the oscillatory cycle, thrust production becomes way more efficient. Avoiding flow separation is easily achieved when combining pitching and plunging since lower effective angles of attack are experienced. Moreover, when a leading-edge vortex was present, the efficiency was considerably affected, even though high thrust was still attainable.

As seen before by Anderson et al. [31], the Strouhal number can be a reliable indicator of good propulsive performance, at least in controlled studies. A comprehensive study made by Taylor et al. [33] who studied several species of birds, bats, and insects in the cruising flight condition shows that propulsive efficiency peaks within the interval $0.2 < St < 0.4$. Although lower and higher values are detected for some species, the intriguing part is that regardless of scale, the vast majority of animals fall on the same interval, as shown in Figure 2.6.

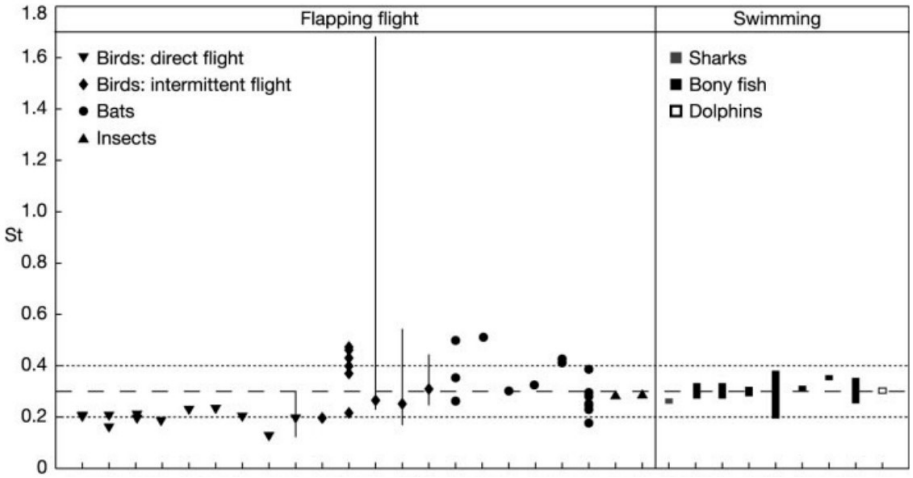

Figure 2.6: Strouhal number in the various species studied by Taylor et al. Adapted from [33].

When it comes to the Strouhal number, only on some specific moments, as in takeoffs, landings, and quick maneuvers, the Strouhal number can take values higher than one. Otherwise, it falls under the optimal range observed in nature, somewhere between 0.2 and 0.4. Regarding the plunging amplitude, it normally does not exceed the aerodynamic chord length, while the pitching amplitude is usually within 0 and $45°$. In all cases, the mean angle of attack is kept at a low value, and the phase angle between plunging and pitching is set to $90°$, although other values have been considered [31, 34].

The same problem was investigated by Young and Lai [35] who by observing the wake structures and thrust calculations at constant kh, concluded that this parameter was not controlling the flow, but rather the combination of k and h. At a Reynolds number of 2.0×10^4, the airfoil surface pressure distribution obtained by the authors, presented in Figure 2.7, made them conclude that leading-edge effects have a direct influence on force generation, while trailing-edge only played a primary role on the wake structures.

In 2006, Yang et al. [36] investigated the effects of unstalled pitching and plunging airfoils by limiting the maximum effective angle of attack. When searching for an optimal reduced frequency and phase angle between plunging and pitching, the authors found the highest propulsive efficiency of $90\,\%$ and a maximum thrust coefficient of 0.86. However, these two values occur at opposite sides of the reduced frequency range since good efficiency values are obtained at lower reduced frequencies, while higher thrust occurs at higher reduced frequencies.

Heathcote et al. [37] concluded that the trust coefficient has almost no dependence on the Reynolds number, and Lua et al. [38] saw that the drag coefficient is not related to this parameter. These conclusions are made for a Reynolds number less than 1.0×10^4 and may not be valid for values outside this range. Studies show that if the Reynolds number is calculated based on the flapping airfoil thickness, the thrust coefficient will be affected by it [39]. On the other hand, Visbal [40] and Liang et al. [41] while studying a flapping foil conclude that

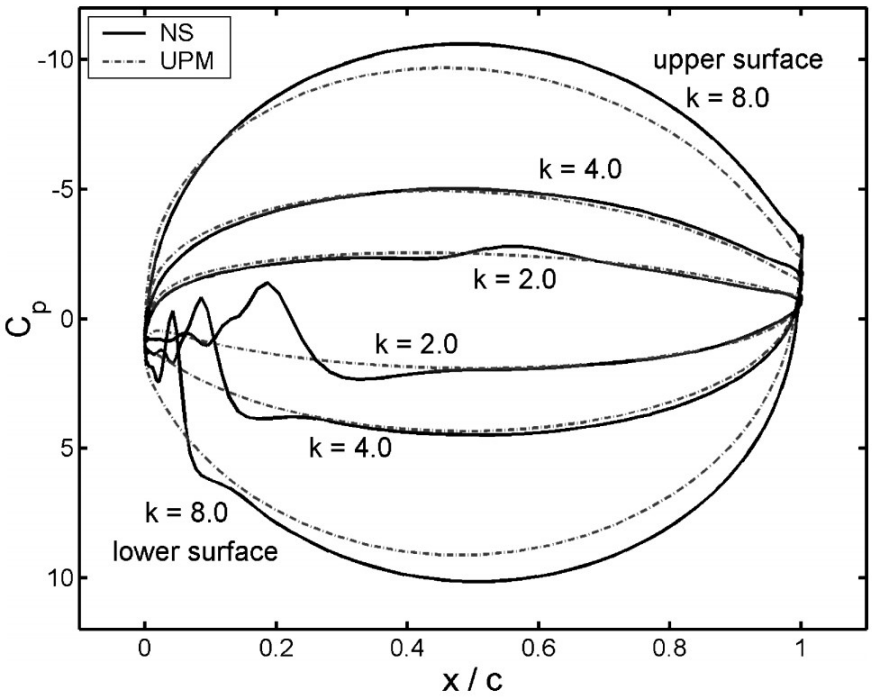

Figure 2.7: C_P distribution at $Re = 2.0 \times 10^4$ and $kh = 0.3$ at the top of the stroke [35].

while increasing the Reynolds number, the drag coefficient reduces.

Ashraf et al. [42] studied the possibility of replacing conventional propulsive systems with flapping airfoils, by investigating whether flapping wings could offer advantages for HALE (High-Altitude Long-Endurance) aircraft. They concluded that the plunging airfoil would not be a feasible solution as a very small efficiency was achieved. Meanwhile, when combining pitching and plunging, lift and thrust production were favored as well as propulsive efficiency which made them recommend flapping-wing propellers as an attractive and practical solution to be considered as a propulsive system.

Ashraf et al. [43] studied flapping-wing aerodynamics with nondimensional amplitudes up to 48, achieving enormous thrust coefficients but really small propulsive efficiencies. By studying a wide range of values, authors tried to answer what combinations of k and h favor thrust generation and propulsive performance, and how some phenomena such as leading-edge separation affect optimal efficiency. Based on the results, Ashraf et al. [43] recommend that turbulence and 3D effects, as well as different types of motion other than sinusoidal motion, should be studied to achieve the base of knowledge required for the development of MAVs.

Newer kinematics were considered by Lu et al. [44], who investigated the influence of asymmetric sinusoidal motion on pitching airfoil aerodynamics, transforming a standard sinu-

soidal wave into an asymmetric function along the motion period, given by

$$\begin{cases} \alpha(t) = A_\alpha \sin\left(\dfrac{2\pi}{2\zeta T}t + \dfrac{\pi}{2}\right) & \text{if } 0 \leqslant t < \zeta T \\ \alpha(t) = A_\alpha \sin\left(\dfrac{2\pi}{2(1-\zeta)T}(T-t) + \dfrac{\pi}{2}\right) & \text{if } \zeta T \leqslant t \leqslant T \end{cases}. \tag{2.19}$$

The asymmetry parameter, ζ, revealed that there is an enormous influence on the aerodynamic performance, in particular on the lift coefficient, that increases by the emergence of a mean effective angle of attack. As expected, the wake configuration is altered, exhibiting too an asymmetric behavior.

Pitching airfoil propulsion with a nonsinusoidal motion was investigated by Lu et al. [45] using

$$\begin{cases} \alpha(t) = \dfrac{A_\alpha \arcsin\left(-K\sin(2\pi f t)\right)}{\arcsin\left(-K\right)} & \text{if } -1 \leqslant K < 0 \\ \alpha(t) = A_\alpha \sin(2\pi f t) & \text{if } K = 0 \\ \alpha(t) = \dfrac{A_\alpha \tanh\left(K\sin(2\pi f t)\right)}{\tanh K} & \text{if } K > 0 \end{cases}, \tag{2.20}$$

where K is a parameter used to control the squareness of the periodic curve. Furthermore, the influence of camber was studied by considering several NACA 4-digit series airfoils. Results indicate that increasing the pitching amplitude is linked to an increase in thrust production until a critical value. The same is not verified when it comes to the propulsive efficiency, which at a constant reduced frequency, typically reduces with the pitching amplitude.

Regarding nonsinusoidal effects, the conducted simulations confirmed that considering new types of motion can improve thrust production, together with the increase in power demand. Nevertheless, the use of nonsinusoidal waves contributes to some improvements when it comes to propulsive efficiency but with some complexities, as seen in Figure 2.8.

When the pitching amplitude was $2.5°$, the squarer waveform presented improved results regarding propulsive efficiency, but such effect did not occur when A_α increased to $7.5°$. Overall, higher propulsive efficiencies occurred when the motion was close to a triangular waveform. This deep connection between geometry and prescribed kinematics reveals that special attention should be given to when and how newer motion types other than the traditional sinusoidal function can be used and exploited.

Das et al. [46] using a high-resolution viscous vortex particle method found out that the time-averaged power coefficient follows the power-law scaling $\overline{C_P} \sim St^3$, showing almost no dependency to the Reynolds number. On the other hand, the time-averaged thrust coefficient increased both with the Reynolds and Strouhal numbers. A highly detailed wake map was also obtained where three different wake patterns associated with a pitching airfoil were explored, here shown in Figure 2.9. Based on this map, the authors say that the

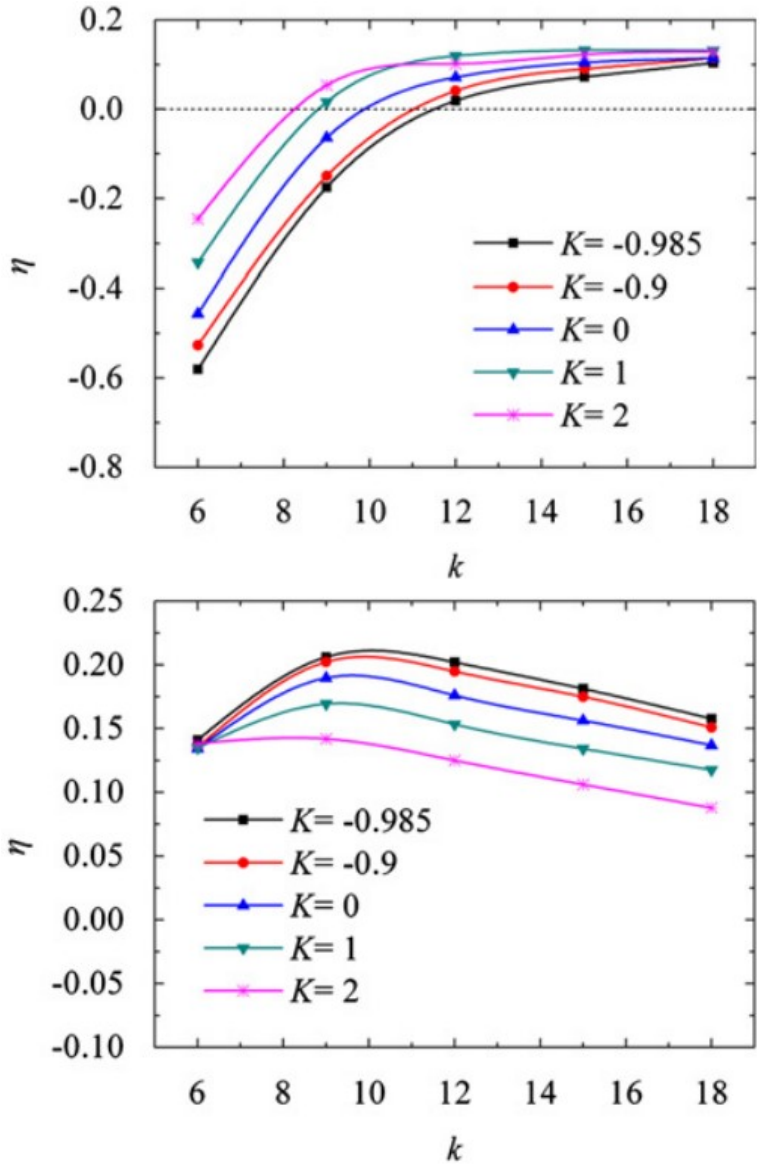

Figure 2.8: η as a function of k and K for $A_\alpha = 2.5°$ (above) and $A_\alpha = 7.5°$ (below) [45].

Strouhal number at which the transition occurs is strongly dependent on the Reynolds number ($St \sim Re^{-0.37}$), as well as the power coefficient ($\overline{C_P} \sim Re^{-1.12}$).

While the vast majority of research focuses on studying the problem parametrically at different airspeeds, frequencies, and amplitudes, Luo et al. [47] investigated how one could transition between two specific flight conditions by using a multi-objective optimization algorithm. They verified that increasing the plunging amplitude or frequency enhances the output lift force. However, the thrust generation process is not that simple since thrust does not necessarily increase when the amplitude increases. An important conclusion was that decreasing frequency in the adjustment phase is recommendable to achieve a higher lift force with lower input power.

The effects of continuously increasing the pitching and plunging amplitudes were studied nu-

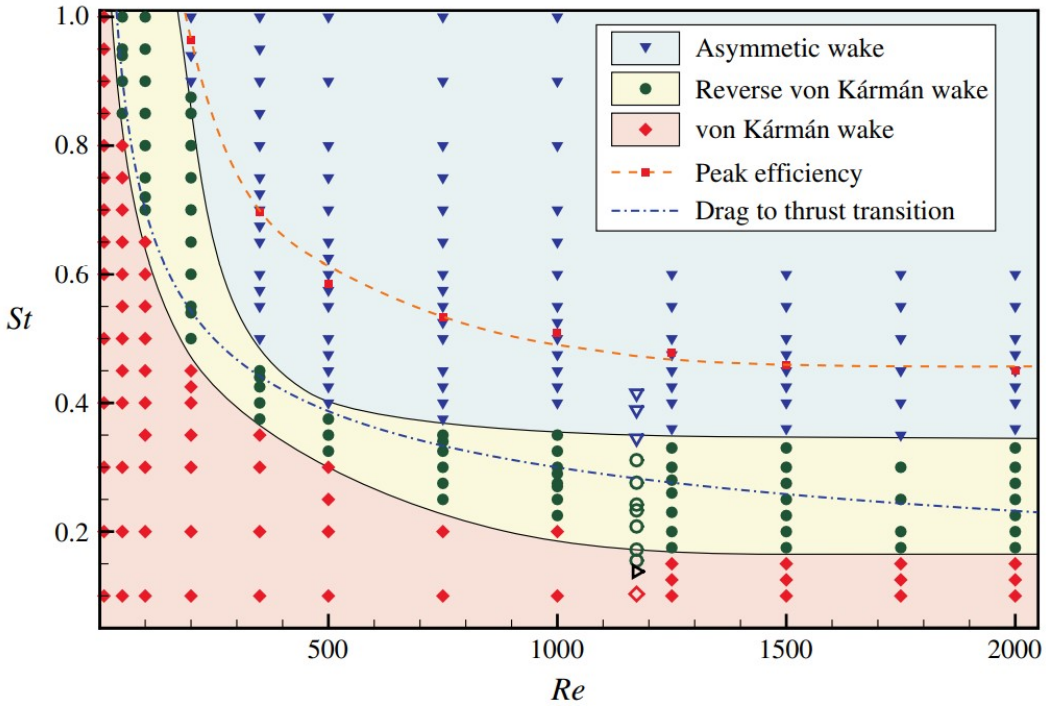

Figure 2.9: Wake patterns as a function of St and Re [46].

merically by Hu et al. [48], who saw an enormous influence on aerodynamic performance, especially concerning lift production. On the other hand, although lift is enhanced, the increase in pitching amplitude may lead to the production of drag forces.

Lin et al. [49] studied both plunging and pitching separately as the combined option on a self-propulsive airfoil. When comparing plunging and pitching separately, the first is typically the case where higher thrust and propulsive efficiency occur. However, combining plunging and pitching greatly favors propulsive efficiency. The Reynolds number also presented a challenge regarding self-propulsion since at a value less than 8.0×10^2, the performance is degraded. The authors also studied the influence of the pivot location on the propulsive efficiency, concluding that it is maximized close to the airfoil center of mass ($x/c = 0.4$), accompanied by a minimum in power consumption.

Senturk and Smits [50] studied the propulsive performance of pitching airfoils and found that the Reynolds number, as well as the Strouhal number, have an enormous influence on the thrust coefficient. Moreover, $\overline{C_t}$ for a given Strouhal number, appears to approach a constant value with the increasing of Reynolds number, as seen in Figure 2.10. At higher Reynolds numbers, the propulsive efficiency seems to be highly affected by the offset drag. The maximum thrust production decreases with the airfoil thickness when keeping the Strouhal number constant. The proposed model offers the possibility to obtain the maximum achievable efficiency manually and allows a better understanding of the involvement of the Reynolds number in the aerodynamic and propulsive coefficients.

Wang et al. [51] used a NACA0012 to study the response of an airfoil freely undergoing two-

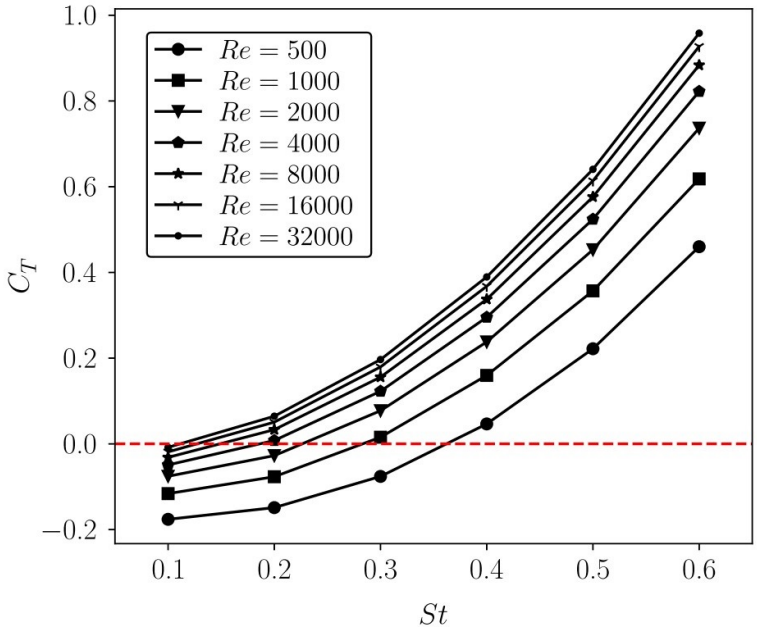

Figure 2.10: Time averaged thrust coefficient for $\alpha_0 = 8°$ [50].

degrees-of-freedom motions of plunging and pitching. By changing the reduced velocity and the pivot location authors found eight regimes in the pivot-reduced velocity space, four of which presented synchronized responses and the other four exhibited chaotic behavior.

The pivot location, typically given as a function of chord percentage, is also a deciding factor that influences the aerodynamic performance, being a parameter that impacts the pressure distribution on the airfoil surface. Research has demonstrated that a pivot point located between $25\,\%$ and $50\,\%$ (values close to the airfoil maximum thickness) offers an improvement of the performance parameters [52, 53].

Most studies assume the sinusoidal motion as the governing motion equation to represent the flapping foil problem. However, deeper examination must be made regarding non-sinusoidal or even aperiodic motions that may unleash new aerodynamic phenomena that are still to be discovered [54, 55].

There are three main modes at which an airfoil or wing can oscillate, being full-active motion, where kinematics are prescribed, the semi-activated systems, where pitching is imposed and the plunging is induced (or vice versa), and the full-passive systems, where there is self-sustained pitching and/or plunging motion.

Boudreau et al. [56, 57] show that a semi-passive flapping foil can deliver as much performance as a regular oscillatory foil with prescribed plunging and pitching, which was also verified by Tsarsitalidis and Politis [58] and Bockmann and Steen [59] who, analyzing semi-activated systems, realized that this configuration not only can enhance thrust production but also the power extraction capability of a harvesting device.

2.3.2 Vortex Dynamics

Vortex dynamics under the scope of flapping airfoils are an insightful matter to be discussed since observing the behavior of vortices and their features, such as their position and size, can offer a proper qualitative evaluation of the aerodynamics and propulsive characteristics of airfoils under unsteady conditions.

Koochesfahani [11] explored the pitching airfoil with different waveforms by introducing some level of asymmetry, ζ, to a sinusoidal wave, as illustrated in Figure 2.11.

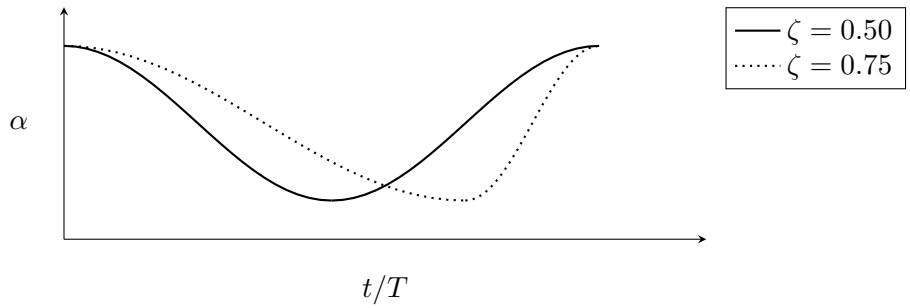

Figure 2.11: Waveforms considered by Koochesfahani [11].

He concluded that the wake created by an oscillating airfoil can greatly change with the motion amplitude, frequency, and waveform shape. The level of asymmetry used in the study creates a variety of vortex-vortex interactions that produce interesting patterns, which the author recommends studying in terms of stability and interactions.

Ohmi et al. [60] studied the vortices produced by a pitching airfoil at incidences above the static stall angle. They identified that the reduced frequency has a crucial role in the flow field configuration, especially when combined with large amplitudes, which creates a cyclic superposition of leading-edge vortices.

Lewin and Hariri [61] also studied numerically the plunging motion and found both periodic and aperiodic solutions, with the latter being found when the airfoil is at high kh with high reduced frequencies. At a Reynolds number of 5.0×10^2, these authors analyzed the interaction between the leading and trailing edge vortices, concluding that when an LEV (leading edge vortex) is entrained in the nascent TEV (trailing edge vortex), the latter loses its strength. Also, when the LEV remains attached over the full stroke, there is a significant gain in propulsive efficiency. Vortex recapture can also be exploited when the surging motion is added, which provides helpful enhancements to thrust generation [62].

This was seen by Kurtulus et al. [19], who studied the hover flight condition at a Reynolds number of 1.0×10^3 both experimentally and numerically. The instantaneous pressure coefficient distribution showed the importance of recapturing low-pressure zones shed during the past periods to enhance aerodynamic force.

Young and Lai [63] conclude that at low Strouhal numbers, the viscous forces are the reason

why an evident reduction concerning propulsive efficiency occurs. The reduced frequency seems to control the leading-edge shedding effects, which limited the leading-edge vortex formation time and its transport along the airfoil surface. The authors acknowledged that the Strouhal number should not be used individually to characterize the flow mechanisms, as the reduced frequency and nondimensional amplitude play distinct roles.

In the same year, Young and Lai [64] studied the vortex lock-in phenomenon where an anomalous vortex shedding mode occurs. This shedding mode is characterized by the interaction between the natural bluff-body shedding frequency and the plunging frequency. This phenomenon is somewhat similar to the vortex lock-in observed in vibrating cylinders, although flow separation occurs differently due to geometric reasons. The authors observed that when increasing the plunging frequency beyond the natural shedding frequency, the vortex lock-in starts to occur at low plunge amplitudes.

Lua et al. [65] studied the interaction between the leading edge and trailing edge vortices and affirmed that this interaction is a crucial phenomenon that dictates the wake configuration together with the advance ratio, reduced frequency, and nondimensional amplitude.

Ol et al. [66] in a unified experimental and numerical study, investigated the pitching motion on an SD7003 airfoil considering newer kinematics which are sporadically used (triangular and trapezoidal waves). The airfoil, when subjected to the trapezoidal motion, showed a double-vortex structure which the authors associated with the angle of attack plateau of the trapezoidal wave. Such an effect was not observed when the triangular wave was used, showing many similarities with the sinusoidal kinematics, as you can see in Figure 2.12.

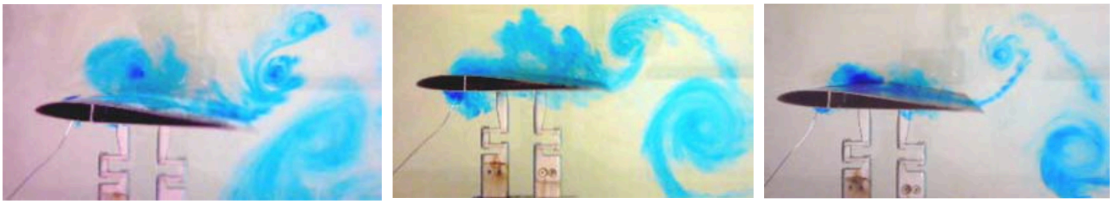

Figure 2.12: Wake structures under different kinematics (trapezoidal, sinusoidal, and triangular from left to right) [66].

Recently, the AEROG-LAETA laboratory has also been looking at the wakes generated by unsteady airfoils, creating a considerable dataset of experimental and numerical results. In this dataset, several studies were made regarding the influence that the motion frequency and amplitude have on the wake configuration [67] but also on the propulsive performance [68]. Throughout time, studies were also extended to observe the influence that kinematics has on the downstream distribution of vortices, for instance, Rodrigues et al. [69] who considered different waveforms and the influence that an asymmetric periodic motion could have. Other works, such as from Gonçalves et al. [70], were more focused on the geometry, more specifically, the trailing edge shape.

Lua et al. [38] tried to correlate these wake structure configurations with force measure-

ments. Results support that fluid inertia and LEV have a great influence on the aerodynamic forces, especially when the airfoil is subjected to changes in the angular amplitude. This is the case where the authors found an optimal lift coefficient for $A_\alpha = 45°$, which creates a stronger jet when compared to $30°$ or $60°$. Concerning drag, and regardless of the Reynolds number, an increase in the angular amplitude will propitiate a thrust reduction.

Yu et al. [39] saw that, together with airfoil thickness, the different kinematics also affect the LEV evolution and LEV-TEV interaction. The tested conditions indicate that when employing the appropriate kinematics, the LEV-associated low-pressure zone can be adjusted in a manner to improve thrust production.

One area where the presence of vortices is important is when the flapping airfoil experiences ground effect. The performance of flapping airfoils in forward flight while close to the ground was studied by Li et al. [71], as well as the hovering conditions. Overall, the ground proximity affects the vortex convection, which influences lift production. Regarding forward flight, the interaction between the ground causes the vortices to acquire an oblate spheroid geometry that leads to changes in the aerodynamic forces.

Andersen et al. [72] presented a combined numerical and experimental study of a symmetric airfoil exploring pure pitching and plunging. The authors also compared these two types of kinematics. The wake maps for the two modes revealed that both are qualitatively similar, where the main differences are the drag-to-thrust transition and the changes in the wake configuration. For the heaving case, at low frequencies and high amplitudes exhibited a drag-thrust transition in which two pairs of vortices are shed per period, different from the typical transition with horizontally aligned inverted von Kármán vortices.

Yu et al. [73] studied the effect of a mean shear flow, illustrated in Figure 2.13, on the aerodynamic performance. They discovered for the pitching cases that the mean shear flow couples with the vortex structures in the wake and changes its orientation. Furthermore, the mean shear flow can even promote the transition from a symmetrical to an asymmetrical arrangement. In the plunging case, the mean shear flow plays an important role in the LEV-TEV interaction, which also induces aperiodic vortex shedding when a large leading edge separation is present. An interesting conclusion is that when considering the same amount of lift, the flapping airfoils subjected to a negative mean shear flow generated a higher thrust, which may be beneficial when operating in atmospheric flows.

Moriche et al. [74] performed a numerical and experimental study using DNS and PIV, concluding that LEV detachment and TEV formation highly depend on 3D and turbulent effects, as well as changes in the Reynolds number. Some differences were found when comparing the numerical and experimental data in the wake which the authors relate to the nonexistent 3D vortex stretching and tilting. The numerical results obtained by 2D DNS showed to be an efficient tool for calculating the aerodynamic forces, even when 3D effects are already present.

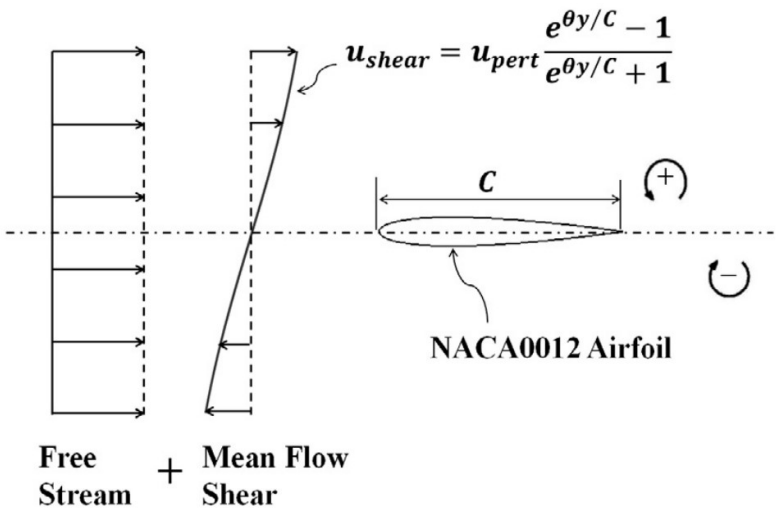

Figure 2.13: Mean shear flow formulation used in [73].

At relatively high amplitude, the boundary layer tends to separate and roll into a concentrated leading-edge vortex. Gao et al. [75] studied this mechanism as a possible high-lift production and saw that the passing-over LEV also acts as a thrust enhancement mechanism. The formation of a passing-over LEV occurred when crossing a critical line in the $A - St$ domain and its presence, especially at higher frequencies, seems to induce a chaotic behavior. The proposed correlation by the authors can give great insights regarding this mechanism, which is crucial for the extra suction that possibilities natural flight at such low Reynolds numbers.

Rahman and Tafti [76] studied the role of vortex–vortex interactions in thrust production for a plunging flat plate and found that the thrust coefficient did not increase monotonically with kh, reaching a maximum at approximately $kh = 1$. Authors also saw that leading-edge vortices are the flow structures responsible for thrust production whereas trailing-edge vortices may induce drag. Flow control methods that could prevent TEV formation were suggested as a drag reduction mechanism that can monotonically increase thrust with kh.

In a very complete and comprehensive review, Gursul and Cleaver [77] affirm that inviscid predictions should not be considered good enough to study the mean thrust. Hence, viscous computations must be carried out (even with the laminar flow assumption) to obtain better predictions. Data published has shown that mean thrust heavily depends on the Strouhal number. However, when this number stays constant, LEV formation is seen at larger amplitudes which is unfavorable to thrust production.

When the flow remains attached, TEVs are the mechanisms responsible for thrust generation. Such a condition leads to Gursul and Cleaver [77] saying that in these conditions, the Strouhal number should be calculated based on the peak-to-peak amplitudes of the trailing edge. However, when flow separation appears, calculating the Strouhal number using the airfoil chord length becomes dominant as it represents the effect of LEV while convecting on the airfoil surface.

At first, one could expect that flow separation at the leading edge followed by LEV formation could be strongly dependent on the maximum effective angle of attack. However, no such thing is observed, as two conditions with the same maximum effective angle of attack can present very different results. Instead, flow separation depends more on the motion amplitude.

Ohmi et al. [60] while studying the wake behind an oscillating foil with a Reynolds number between 1.5×10^3 and 1.0×10^4, detected that this dimensionless parameter, considering the studied range, does not influence the periodic vortex formation seen downstream. However, the leading and trailing edge vortices, as their structure, are sensitive to the Reynolds number. Lang et al. [78] studying the flapping motion understood that the LEV would only form at a lower Reynolds number and that at higher values, the flow would be more attached over the airfoil surface.

In the flapping foil problem, as mentioned before, symmetry-breaking phenomena may occur at relatively high frequencies or amplitudes (high Strouhal numbers). These asymmetries create a row of vortices with a deflection angle that Liang et al. [41] identified to be a function of the operating Reynolds number, observing that increasing this parameter would also increase the deflection angle.

The reduced frequency is identified by Wu et al. [13] as the parameter that has the most control on flow development, whose can predict the transition between the various wake configurations [79–81]. The study of Panah and Buchholz [82] shows four possibilities regarding the wake patterns. These four configurations can be: the LEV merges with the TEV (both with the same sign), the LEV interacts with a stronger opposite signed TEV, the LEV reaches the trailing edge one period after the TEV generation process, and the LEV stays at the airfoil surface for more than three periods.

The prescribed amplitude, when compared to the reduced frequency, holds the same influence and tendencies on the aerodynamic coefficients and wake phenomena. However, the effects induced by the reduced frequency and nondimensional amplitude may differ since the first mainly affects the temporal features of the wake, while the latter changes the spatial distribution of the wake structures.

A phenomenon that is strongly affected by the amplitude is the leading-edge vortex formation, as studied by Panah and Buckholz [83], in which results reveal unequivocally that higher amplitudes strengthen the LEV vorticity.

2.3.3 Geometric Parameters

Although kinematics play a crucial role in unsteady airfoils, geometric parameters such as airfoil thickness and camber, have a meaningful effect on the aerodynamics and propulsive characteristics of flapping airfoils. Several foils have been used for these analyses, and even

some have been proposed to enhance certain qualities [84] but, in the vast majority of cases, the NACA four-digit series airfoils are the chosen ones.

Lee et al. [84] explored the flapping mechanism by geometrically modifying the studied airfoil. They decided to merge airfoils from the 4-digit NACA airfoil series considering a thicker and thinner airfoil as shown in Figure 2.14. Results indicated that when using a thicker airfoil on the leading edge and a thinner airfoil on the trailing edge, flow separation was prevented, and a stronger pressure difference at the trailing edge was induced, thus improving thrust production and maintaining reasonable propulsive efficiency.

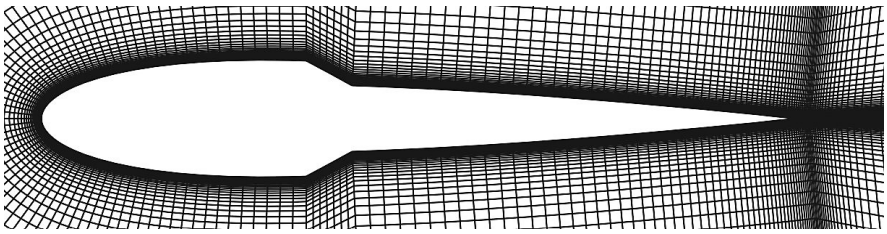

Figure 2.14: Combined airfoil shapes proposed by Lee et al. [84].

The importance of leading-edge geometry was also explored by Benton and Visbal [85]. Using LES (Large Eddy Simulation), four airfoils were tested regarding the role of the laminar separation bubble on the onset of dynamic stall. Results indicate that the leading-edge radius and its droop have a direct impact on the onset of dynamic stall. For instance, by modifying the leading edge, the dynamic stall of the NACA23012 airfoil started at the trailing edge and only then moved towards the leading-edge region, when turbulent separation emerged.

The influence of airfoil thickness on aerodynamic performance was studied by Yu et al. [39] who conducted high-fidelity simulations of some NACA 4-digit airfoils. Results demonstrate that the airfoil thickness plays an important role in the propulsive performance, especially in the thrust production, which becomes higher on thinner airfoils.

Platzer et al. [24] explored flapping wings and their ability to produce thrust and lift, the hovering flight condition, and the tandem wings and biplane configurations. Based on their review, the experimental and numerical studies are typically focused almost exclusively on NACA airfoils which can be restrictive. Other geometries should be considered, focusing on the leading edge, which has an important role regarding flow separation. These newer configurations must be subjected to distinct kinematics, as non-sinusoidal velocity waves that coupled with optimization algorithms can find optimal conditions [86].

The study of non-symmetrical airfoil was conducted by Tay and Lim [87] in an extensive parametric investigation where 4-digit NACA airfoils, the S1020 airfoil, and an airfoil bioinspired on a swift bird were used, illustrated in Figure 2.15. Simulations showed that thrust production depended heavily on motion parameters, rather than the shape of the airfoil while lift production was primarily dominated by the airfoil geometry. On the other hand, propulsive efficiency was a combination of both. The most suitable airfoil for efficiency and thrust

production is the NACA0012 airfoil and for lift production, the birdy airfoil presented more favorable results. However, the S1020 airfoil was the most suitable airfoil for most applications since it can provide relatively good propulsive efficiency and at the same time generate high thrust and lift forces.

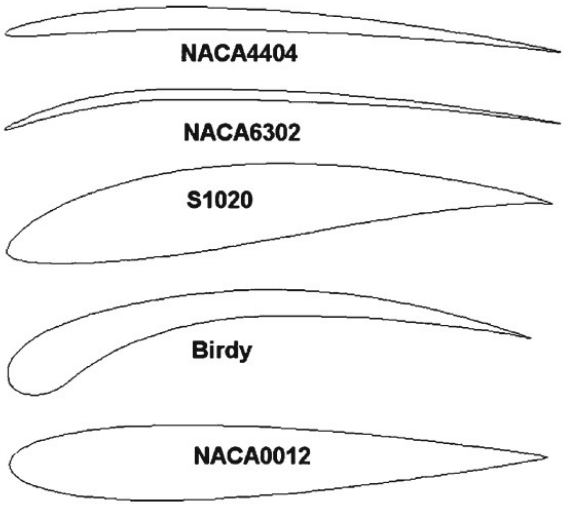

Figure 2.15: Airfoils considered by [87].

Geometric changes can also be accomplished by considering in-line tandem flapping foils, which were studied by Muscutt et al. [88] who performed, at a Reynolds number of 7.0×10^3. They conducted an extensive parametric study that allowed them to find the effects of the interaction (spacing and phasing) between foils. Numerical simulations indicate that the downstream foil can have its thrust doubled compared to the value of a single foil, occurring when the downstream foil oscillates between the vortices shed by the upstream foil.

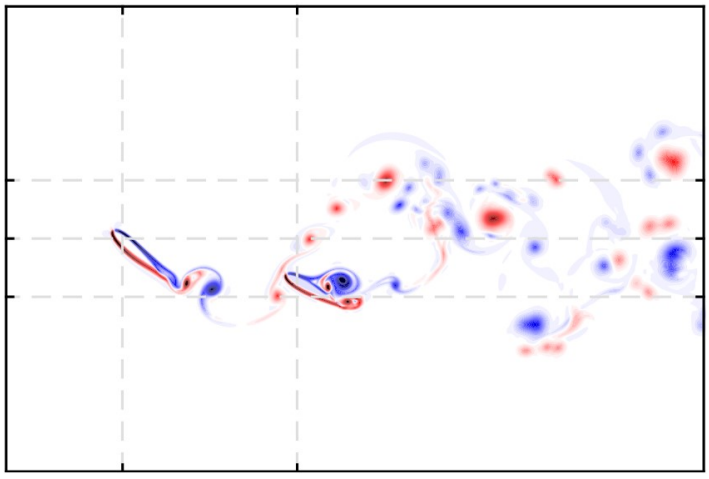

Figure 2.16: High performance case [88].

2.3.4 Structural Parameters

The inherent flexibility of natural wings and the way animals use them lead us to think that this attribute can offer great suggestions for the improvement of the aerodynamic and propulsive capabilities of unsteady airfoils or wings [24].

Concerning the influence of the Reynolds number on the required power coefficient of a flexible flapping airfoil, Miao and Ho [89] conclude that it is fairly independent for values between 1.0×10^2 and 1.0×10^4 and that the same tendency is verified for the force generation, which shows a weak reliance on the Reynolds number. When it comes to the influence of chordwise flexibility, it can affect negatively thrust production. On the other hand, with an adequate flexure amplitude, the propulsive efficiency may be optimized with a phase angle of $90°$. Furthermore, for a given Reynolds number, the authors saw a corresponding reduced frequency that maximized the propulsive efficiency.

Heathcote and Gursul [90] also studied the effects of flexible airfoils in the chordwise direction and observed an increase in both thrust and propulsive efficiency with some degree of flexibility. The flow field shows stronger trailing-edge vortices along with strong time-averaged flow fields that resemble a jet-like flow. At the same time, weaker leading-edge vortices contribute to improved propulsive efficiency. At lower Reynolds numbers, the chordwise-flexible airfoils demonstrated to offer a huge leap in performance when using purely plunging airfoils, as shown in Figure 2.17.

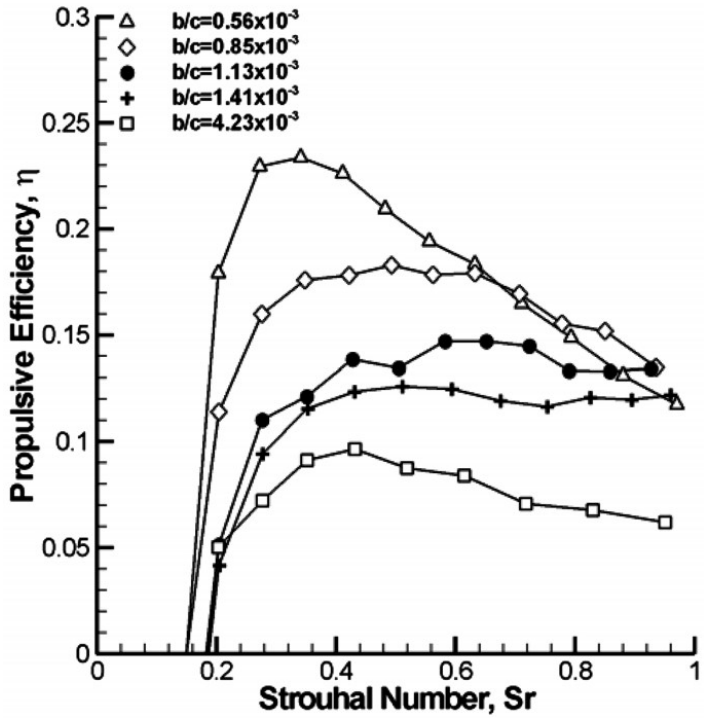

Figure 2.17: Effect of flexibility on the propulsive efficiency at $Re = 9.0 \times 10^3$ Heatcote and Gursul [90].

Spanwise flexibility was studied by Heathcote et al. [37] using a wing that oscillated in heave at one end. Some degree of flexibility is highly recommended since an increase of $50\,\%$ in thrust production, as observed in Figure 2.18, was achieved together with a small reduction of required power. However, highly flexible wings degrade performance due to a phase lag that leads to the root and tip moving in opposite directions. Interestingly, the degree of flexibility that offered the best results overlapped the same range observed in nature.

Flexibility was also studied by Zhang et al. [91] who merged the unsteady potential method

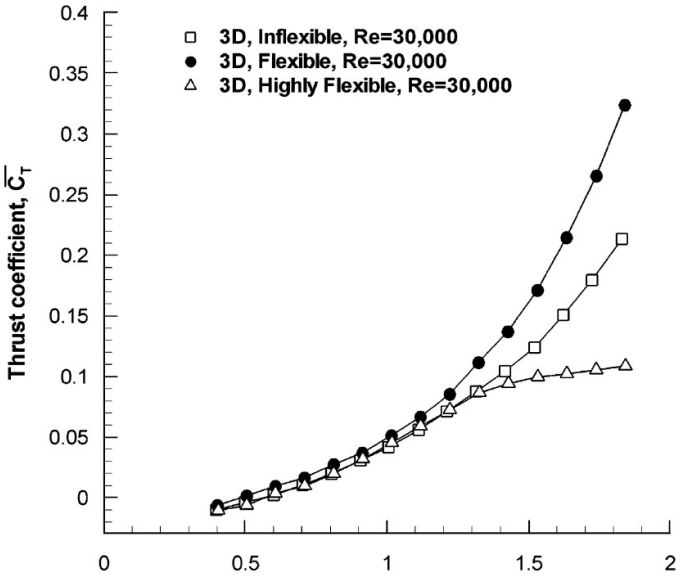

Figure 2.18: Effect of spanwise flexibility on thrust coefficient [37].

proposed by Teng [30] with a structure solver. Their geometry is composed of a rigid airfoil with a thin flexible plate connected at the trailing edge, the latter parametrically studied with different Young's modulus. Besides, simulations show the strong influence of this attached thin plate on drag production and especially on propulsive efficiency, which is seen in Figure 2.19.

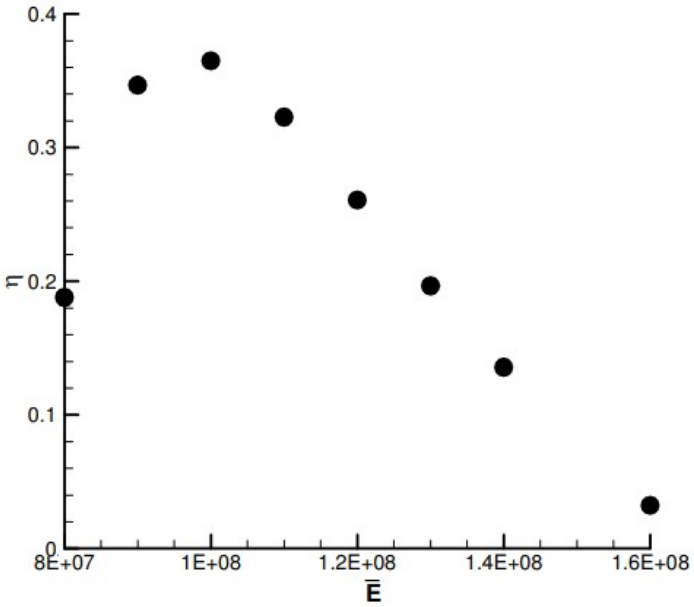

Figure 2.19: Propulsive efficiency as a function of nondimensional Young's modulus [91].

These results open new ways to answer the question of how flexibility should be implemented in an oscillating airfoil or wing, and what is the exact optimal degree of flexibility that improves the aerodynamic or propulsive performance.

In terms of engineering, reproducing biologically inspired air and underwater vehicles that

achieve an efficient operation is still an enormous challenge. However, several researchers, such as Akkala et al. [92], dedicated their studies to the effects of flexibility on aerodynamic performance by using PIV and time-resolved force measurements. They concluded that at low frequencies, the flexible airfoil behavior is very similar to a rigid airfoil but when the frequency was increased, the flexible airfoils started to show their advantages, by producing a larger thrust coefficient with low power coefficients which resulted in an outstanding increase of the propulsive efficiency.

Zhou et al. [93] studied the commonly known idea that when introducing flexibility into flapping wings there is typically a considerable increase in its aerodynamic performance. The authors considered three main configurations: a rigid airfoil, one where the airfoil was partially flexible with a rigid leading edge, and a fully flexible airfoil. Results indicated that flexibility helped to reduce drag generation and the maximum lift production, compared to the rigid configuration, is almost three times higher due to trailing edge deformation enhancing the resultant force. Results also show that a rigid airfoil undergoing plunging and pitching motion can be used as a way to estimate the aerodynamic characteristics of a purely plunging and flexible airfoil.

Another parameter that must be considered is flexibility which allows a time-varying airfoil shape over the flapping cycle, a crucial characteristic of natural structures. The advantages are seen by Dewey et al. [94] who caught the potential of structural flexibility to increase the propulsive efficiency. It also has the potential to affect the leading-edge and trailing-edge vortice configuration, which directly changes the performance parameters. Flexibility is still a unique property that accounts for approximately 15 % of the research topics, which may be an indicator of its complexity [13]. The influence of the reduced frequency on the thrust coefficient was also studied, which typically rises while increasing the reduced frequency. However, Dewey et al. [94] point out that the thrust coefficient may not have a monotonical behavior since for flexible pitching plates, the thrust coefficient decreases after reaching a certain value.

2.3.5 3D Effects

When three-dimensionality is the norm, simplifying problems to a bi-dimensional model or representation will inevitably impact the performance indicators we use to study unsteady wings [86]. Extrapolating the aerodynamic and propulsive performance of wings from the study of unsteady airfoils has been witnessed to undervalue some results since spanwise and wingtip effects, which are significant in low-aspect-ratio structures, are neglected.

Jones et al. [95] studied the influence of the aspect ratio and reduced frequency at the higher end of the range experienced by flapping vehicles, seen in Figure 2.20. As expected, the mean thrust production is negatively affected when the aspect ratio decreases. This collaborative study suggests that more testing should be performed, especially at higher frequencies where flow separation is a dominant feature.

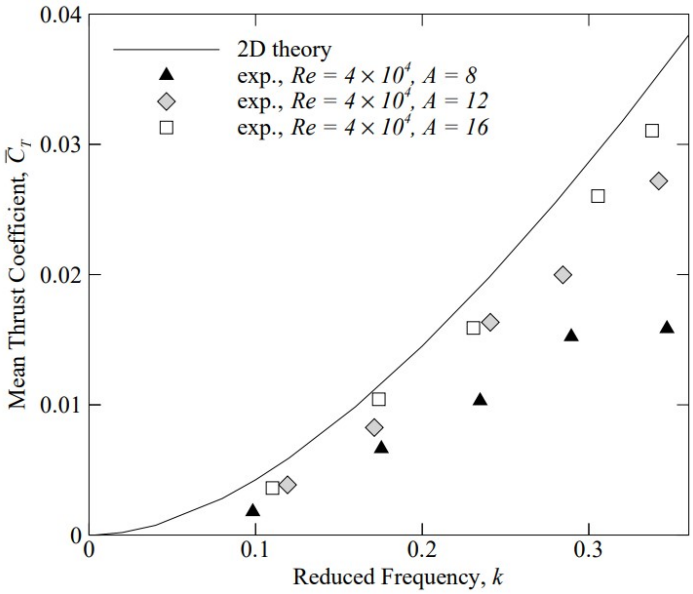

Figure 2.20: $\overline{C_t}$ as a function of k and aspect ratio A [95].

Performing 3D computations, Shyy and Liu [96] explored the role of leading-edge vortices as a lift enhancement mechanism. Such an effect could be questionable since a dynamic-stall vortex typically breaks away and convects as the wing moves. Furthermore, the authors observed that the influence of wing rotation on the leading-edge vortex is more apparent when the Reynolds number is lower.

Platzer et al. [24] indicates that three-dimensional effects should also be studied, especially the effects of spanwise flow and vortices. The influence of the aspect ratio is another crucial parameter that highly affects the aerodynamic and propulsive performance, mainly on the natural wings.

Visbal et al. [97] conducted numerical and experimental studies concerning 3D unsteady separation at large plunging amplitudes and low Reynolds numbers of a low aspect ratio wing. Results expose the complexity of dynamic stall where the first phase corresponds to the appearance of a leading-edge vortex that presents a strong transverse flow toward the wing centerline. The next stage is the detachment of the vortex from the wingtips, evolving into an arch-type structure that afterward connects its extremities, forming a ring-like structure that is after shed. The authors also verified that these three main phases were detected in all of the Reynolds numbers tested when the reduced frequency presented a relatively high value.

Nonetheless, most studies assume bidimensionality, which undeniably simplifies the problem while still representing the major characteristics of the flapping wing [98]. Nevertheless, The structures observed in nature are not high aspect ratio surfaces, which makes them susceptible to induced drag and the emergence of spanwise flow. However, the problem's three-dimensionality is not easy to tackle due to the large number of variables, making it hard to find optimal operating conditions [24].

Three-dimensionality is an inherent feature of nature, and when it comes to the analysis of flapping wings, it certainly plays a crucial role. A two-dimensional analysis can provide some insights regarding the observed 3D phenomena, but flow features such as tip vortices influence the overall vorticity distribution generated by the wing motion [34, 99].

An interesting observation regarding the aspect ratio is that the low aspect ratio and good flexibility of natural swimmers can allow two modes of propulsion (high thrust or high efficiency), which can be selected by the interaction between the vortices shed by the body and the control surfaces [13], similar to fish-like swimming [100].

2.3.6 Energy Extraction

Flying animals transfer energy from the wings to the fluid, effectively creating thrust and lift. However, the study of oscillating airfoils has undergone a drastic shift when researchers identified the potential of flapping airfoils to extract energy from the flow field [101].

Studies on energy harvesting efficiency over oscillating airfoils revealed that a harvester could achieve maximum efficiency of about $30\,\%$ on a sinusoidal motion for $Re = 1.0 \times 10^3$, and $40\,\%$ to $50\,\%$ on the non-sinusoidal cases. These studies became common where there is a constant search for newer kinematics that can enhance the power extraction efficiency of flapping wing devices Wang et al. [102]. Other efficiency-enhancing mechanisms might include corrugations at the foil surface, its structural flexibility, and multiple foil configuration [103] such as the parallel foil configuration numerically investigated by Wang et al. [104].

When introducing structural flexibility, as studied by Zhu et al. [105], the airfoil shows a superior capability regarding energy extraction compared to the rigid case, also verified by Jeanmonod and Olivier [106]. They firmly stated that a foil with constant structural properties in the chordwise direction is far from an optimal solution, demonstrating that a flexible plate can extract double the power of a rigid structure.

Regarding energy extraction, it is unanimous that increasing the aspect ratio improves energy extraction efficiency [107, 108]. The same is said about the Reynolds number, which favors the energy extraction process [109]. Nevertheless, newer configurations must be explored, for instance, tandem airfoils that have shown promising performance enhancement in energy extraction systems [86].

Another way to improve extraction efficiency can also be achieved by creating an effective camber that produces a lift enhancement that is associated with the output power. This concept was studied by Bouzaher et al. [110], who added a Gurney flap at the trailing edge that when synchronized with the flapping motion at a $Re = 1.1 \times 10^3$ creates this virtual camber that improved the output power. The lift production can be further improved by controlling the development of the leading-edge vortex that, when attached to the airfoil surface, contributes to the improvement of lift generation which brings once again, an increase in the

energy harvesting magnitude [101]. The same concept may be applied for thrust enhancement where camber morphing also reveals the potential to maximize the ratio of thrust to lift of flapping airfoils in several flight conditions [111].

Regarding the type of motion, Boudis et al. [112] conclude that the sinusoidal waveform appears to favor the maximum propulsive efficiency even though non-sinusoidal trajectories can offer undeniable improvements, offering an increase of up to $110\,\%$ in terms of thrust production. At a Reynolds number of 5.0×10^3, Dash et al. [113] also studied the influence of the airfoil motion concluding that, when at high frequencies, the thrust performance can be recovered when tweaking the effective angle of attack profile to a different type of wave, such as the square waveform. Others, such as Müller-Vahl et al. [114], consider new degrees of freedom where, for instance, simultaneous changes in pitch and surge are studied in the context of horizontal axis and vertical axis wind turbine blades.

Concerning energy extraction, the nondimensional amplitude does not show a universal law [13] but, a general rule is suggested by Jones and Platzer [25]. The authors suggest that the effective angle of attack induced by the plunging motion should be kept below the angle of attack that achieves a power extraction state.

2.3.7 Dynamic Stall

Another central topic in unsteady aerodynamics is dynamic stall, which gathers so much attention mainly because it is a synonym for performance degradation in helicopter rotor blades and similar systems, such as vertical wind turbines [115].

Dynamic stall is characterized as a vorticity eruption from the airfoil where typically a leading-edge vortex (LEV) is formed and is later convected on the surface, producing undesirable oscillations in aerodynamic loads [116]. It can also present a different configuration, for instance, when a trailing-edge stall starts developing from a relatively gradual progression from the trailing edge toward the leading edge, as seen by McCroskey et al. [117]. These authors also found that, in most cases, the onset of a dynamic stall occurs with the breakdown of the turbulent boundary layer instead of the bursting of a laminar separation bubble.

When looking at oscillating structures, the effects of dynamic stall can quickly couple with structural dynamics, contributing to accelerated fatigue which when not considered seriously can lead to structural failure [118]. Dynamic stall is also part of natural flight and swimming and plays an important role when it comes to the design of innovative energy harvesters [102].

Oscillating structures subjected to the dynamic stall regime are highly dependent on several geometric and kinematic parameters such as the angle of attack and pitch rate. For instance, Francis and Keesee [119] saw that when the airfoil undergoes rapid and large-amplitude pitching motions at a constant rate, the airfoil can offer close to three times the lift com-

pared to quasi-steady values, as shown in Figure 2.21. This is justified by the presence of a high energy separation vortex located at the leading edge, which dominates force generation, as corroborated by Favier et al. [120] who studied a combined translation/pitch motion of a NACA0012 airfoil.

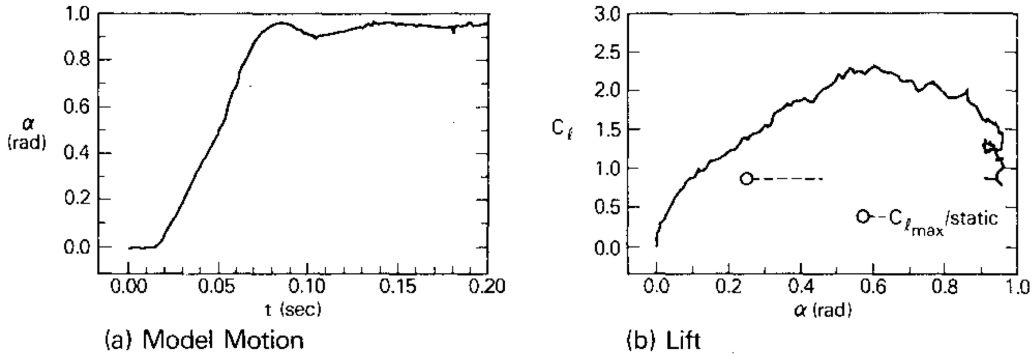

Figure 2.21: Lift coefficient as a function of α during a ramp-up motion [119].

This leading-edge vortex was also noticed by Lorber and Carta [121] as a central mechanism of the unsteady aerodynamic response during and after stall. They looked at the aircraft poststall maneuvers and helicopter high-speed forward flight regimes, concluding that this vortex strengthens with a higher pitch rate and loses its intensity with the Mach number and the proximity to the steady-state stall angle. However, as noted by Visbal [122], at the upper range of the Mach number, the dynamic stall process is more affected by the boundary layer and shock interaction rather than by the formation of a leading-edge vortex.

The dynamics of this vortex have been studied both experimentally and numerically by Wernert et al. [123] when testing a pitching airfoil. They present four distinct phases that generally characterize the dynamic stall phenomena: attached flow, leading-edge vortex formation followed by post-stall vortex shedding, and finally, the reattachment. As seen by Mulleners and Raffael [124], the onset of dynamic stall is intensified by increasing unsteadiness. Results show that when flow separation starts before reaching the critical angle of attack, the flow field presents features of a deep stall. On the other hand, a less intense dynamic stall is experienced when the airfoil inverts its oscillation direction right before reaching the angle of attack that initiates the stall.

The onset phase was also analyzed by Geissler and Haselmeyer [125], who looked at specific stall triggers, for instance, transitional flow influence, compressibility effects, and the presence of boundary-layer tripping devices. Others, for instance, Kiefer et al. [126], analyzed the characteristics of dynamic stall, seeing that a power law governs the evolution of the phenomenon, where a small excess of the static stall angle leads to a prolonged stall delay. Understanding these fundamental concepts is crucial to avoid or mitigate the adverse effects of dynamics stall.

However, dynamic stall should not be looked at as something exclusively detrimental. As

we saw in the previous sections, and looking beyond common aeronautical applications, the dynamic stall is a key part of natural flight, where it may be a byproduct of thrust generation. Isogai et al. [127] looked into this topic by studying the effects of dynamic stall on the propulsive characteristics of a flapping airfoil, concluding that a less intense LEV formation is required for good efficiency. In the natural world, birds and insects present distinctive ways to fly, with the first preferring slower oscillating cycles while the latter flap their wings energetically, creating strong whirls and eddies that surround them and act as lift boosters [128]. Hence, the dynamic stall occurrence must be analyzed carefully based on the regime and environment to conclude if its effects are undesirable.

2.3.8 Flow Control

In aerodynamics, flow control is a common way to manipulate the flow field to produce the desired outcome regarding some unwanted flow behavior. In unsteady airfoils, flow control processes consist of actively or passively changing the flapping conditions, such as frequency and amplitude, or modifying the airfoils geometrically by adding some additional devices.

Tuncer and Kaya [129] used a gradient-based algorithm to optimize a flapping airfoil regarding its thrust production and propulsive efficiency. By employing this method, higher thrust production was achieved at large plunging amplitudes, with high effective angles of attack. However, optimal propulsive efficiency is only seen in the lower range of plunge amplitudes.

Wang and Wu [130] tried to mitigate the dynamic stall of a pitching NACA0012 airfoil by using a sinusoidal function that activates a synthetic jet. Five different jet locations were tested, between $30\,\%$ and $70\,\%$ of the aerodynamic chord, as well as different phase angles between the motion and jet activation. When placing the suction zone closer to the leading edge, better results were obtained, together with a well-tuned phase angle that affects the aerodynamic performance. The use of the synthetic jet showed a L/D ratio improvement that reached values up to $96\,\%$.

Similarly, Visbal and Garmann [131] used a very-high frequency, low-amplitude, and zero-net mass flow blowing/suction slot placed on the upper side close to the leading edge. They observed that these oscillations have the potential to inhibit the leading edge separation bubble and thus, the formation of large dynamic stall vortices. The same concept was also used to control the dynamic stall in a finite swept wing [132].

With the growing interest in creating micro aerial vehicles, comes the appeal of improving its thrust efficiency and flight performance. Similar to fixed wings, flapping airfoils can take advantage of leading-edge and trailing-edge devices that mimic the alula structure present in birds' wings. Bao et al. [133] investigated numerically such structure, by using two airfoils laid out as depicted in Figure 2.22.

By studying different angles of attack of the alula and its distance to the main airfoil, the au-

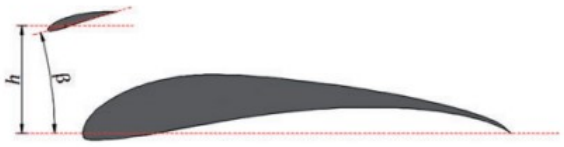

Figure 2.22: Configuration proposed by Bao et al. [133].

thors concluded that the alula deployment at pre-stall may not be desirable. However, when at post-stall conditions, the alula delayed flow separation, and enlarged the low-pressure zone on the upper surface which significantly improved lift. However, a 2D analysis cannot predict the alula tip vortex and twist, which may lead to results being very different from a future 3D case. Similarly, Ullah et al. [134] added slats to vertical axis wind turbine rotor blades at low wind speed conditions. The dynamic stall effects were reduced by optimally investigating the slats' deflection as a function of the wind speed.

As aforesaid, dynamic stall as a highly unsteady phenomenon can degrade the aerodynamic performance by drastically reducing lift and increasing drag, which also affects the control authority of aerodynamic surfaces. Hence, the importance of implementing mechanisms that can delay or mitigate dynamic stall, for instance, bioinspired devices, which can act like high lift systems, and can improve considerably the aerodynamic characteristics [51, 135].

Active flow control techniques, such as rotating cylinders at the leading edge, as the one illustrated in Figure 2.23, have been used to prevent dynamic stall, which is an effective way to prevent flow separation [136].

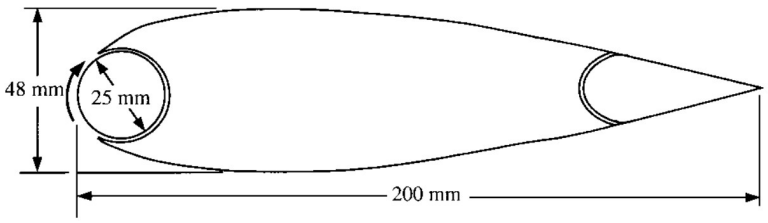

Figure 2.23: Configuration used by Al et al. [136].

Others may use plasma actuators such as Kumar and Wang [137], who used such a system to mitigate dynamic stall at different reduced frequencies. Results show that lift and drag can be improved and reduced, respectively, meaning that combining flapping airfoils with plasma actuation can promote MAV maneuverability. Other concepts, like dynamic roughness achieved with surface perturbations as considered by Huebsch et al. [138], are also interesting approaches to achieve an attached flow over the entire leading edge.

Although flow separation in airfoils can occur in multiple ways, the most common way is when it appears at or close to the leading edge. So it is common to modify the leading-edge geometric characteristics as Bai et al. [139] demonstrated. These authors showed that by

having an active elastic leading-edge deformation, a NACA0015 could improve its energy extraction efficiency, at the lower reduced frequency range, up to a value around $25\,\%$ when compared to the unmodified airfoil. Another technique used by Niu et al. [140] is a variable droop leading edge where one can locally change the angle of attack near the leading edge. Results indicate that drag is reduced, lift is kept at a higher level and the nose-down tendency after stall is very much reduced.

Morphing technologies are also an adequate solution to mitigate stall occurrence, showing the capability of delaying the stall angle coupled with an increase in lift production [141]. Additionally, the natural world can also provide good solutions when trying the reduce the adverse effects of dynamic stall, as Liu et al. [142], who saw that wingtip slots reduce the adverse pressure gradient, improving the wing's performance. Moreover, when further modifying the wing, for instance, adding dihedral, the wing can have its gliding capabilities improved considerably. Using bioinspired tubercles at the leading edge is also a common practice, as used by Sreejith and Sathyabhama [143] who saw some improvements in lift production. Furthermore, leading-edge tubercles were also considered for conventional propellers by Asghar et al. [144] who saw improvements in propeller efficiency.

The leading-edge role was further studied by Xing et al. [145], who considered an inflatable leading edge as a path to reduce dynamic stall phenomena. This inflatable membrane directly affects the radius of curvature, which also changes the pressure distribution. By changing the streamwise adverse pressure gradient, the dynamic stall vortex is eliminated. With this, although the maximum lift decreased, the pitching moment and drag were reduced, which are both a big plus for rotor dynamics.

Sahin et al. [146] carried out calculations concerning the dynamic stall occurrence. They proposed a dynamically deformed leading edge (DDLE) applied to the NACA0012 airfoil, and by changing the leading edge thickness and radius at higher angles of attack, they found that lift, drag, and pitching-moment hysteresis were improved. When testing the same configuration at $Ma = 0.4$, the authors say that the DDLE shape experiences a shock-induced stall, something not desirable.

Remarkable aerodynamic devices on the leading-edge region appear naturally in nature, as the alula. This structure located between the hand-wing and arm-wing of birds can delay stall, when the wing is used at high angles of attack, resembling the leading-edge slat in aircraft [147].

Similarly, Geissler and van der Wall [148] recognize that flow separation limits flapping-wing efficiency and proposed a time-dependent deflectable leading-edge that minimizes the leading-edge vortex size, illustrated in Figure 2.24.

At $Ma = 0.3$, $Re = 10^6$, and $k = 0.5$, while using the deformable leading edge with a droop amplitude of only 10°, they saw that some cases saw the propulsive efficiency roughly doubled

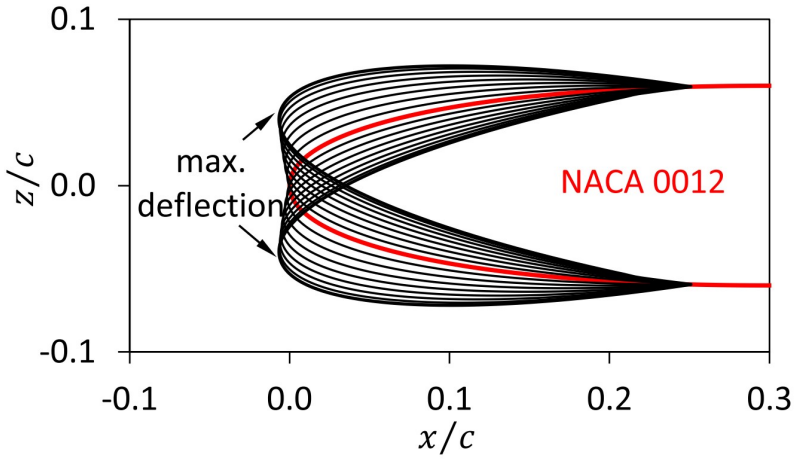

Figure 2.24: Configuration used by Geissler and van der Wall [148].

compared to the rigid airfoil. Mainly focused on the higher Reynolds number spectrum, they affirm that studies must be conducted in the low-Reynolds number region, where birds and insects operate.

2.3.9 Real-Time Optimization

This section is specially assembled to provide an overview of real-time optimization, as the present thesis will build upon previous methodologies to achieve maximum aerodynamic performance. Real-time optimization (RTO) consists of a family of techniques that use online measurements to improve a system's behavior subjected to a set of constraints [149]. The system dynamics are typically evaluated by defining an objective function that depends on some inputs. With real-time data, these inputs are swiftly adapted under varying conditions, with the typical goal being maximizing efficiency and responsiveness in dynamic systems.

These concepts can easily be adjusted to countless applications and industries. For instance, real-time optimization can play an important role in improving the operation of systems used in offshore oil rigs [150], optimally recovering and using the surplus heat generated by various manufacturing and processing plants [151] and enhancing the way a resource is used, for example, when a group of subsystems may consume or supply a common resource [152]. In the particular case of the aerospace industry, we see a swift reframing of aerospace engineering to a data-driven environment coupled with machine learning [153]. Connected to RTO methodologies, inevitable benefits regarding fuel efficiency, safety, and quick adaptation to flight conditions will emerge. RTO has been used in several studies with the intent of improving aircraft performance. Precup et al. [154] used a scaled wing model for low-speed wind tunnel tests to study camber and twist shaping concepts. Later, Nguyen et al. [155] conducted a wind tunnel investigation using an identical model to minimize drag through real-time adaptive adjustments. Using a highly flexible wing configuration, the authors achieved a drag reduction close to 10 %. Also with drag reduction in mind, Reist et al. [156] used existing control surfaces to optimize the performance of a business jet. Their results show that by transferring lift to the fuselage, reductions can be achieved in induced, wave, and trim drag.

Similarly, Forte et al. [157] used the aspect ratio 13.5 Common Research Model (CRM) with a distributed mini-plain flap system to conduct a real-time drag optimization and maneuver loading alleviation study. Results have shown that at Mach 0.85, this distributed flap system can reduce the drag by $6\,\%$. Additionally, real-time optimization can reduce the wing root bending moment by approximately $13\,\%$ when looking at maneuver loading alleviation.

A different application, yet crucial in aircraft operations is the optimization of wing geometry while considering some constraints, for instance, ice accretion as Li et al. [158] studied, observing that lift could increase $16.5\,\%$ on a iced airfoil while preserving the cruise aerodynamic performance.

An additional area of study that can hugely benefit from coupling it with RTO is aerodynamic stall. As the airfoil increases its angle of attack, flow instabilities at the upper side of the airfoil start appearing due to the adverse pressure gradient. When the airfoil reaches its critical angle of attack, the flow becomes separated, leading to a decrease in lift and a drastic increase in drag, making this phenomenon unwelcome. One common way to mitigate these unwanted effects is to employ some flow control, typically by modifying the airfoil geometry [159, 160]. Important to mention that other interesting approaches are also used as mentioned before, for instance, the actuation of synthetic jets on the suction side of the airfoil [161, 162], the non-intrusive use of plasmas that can mitigate stall effects [163–165] or even tubercled wings inspired from large aquatic mammals [166, 167]. This last concept has been coupled with optimization algorithms to improve UAV design and flight performance [168] with optimal geometries increasing the stall angle as well as the lift when compared to a smooth wing [169].

Focusing on all the possible geometry modifications, one of the most common ways is to direct the attention to the leading-edge geometry. Slats are a much-known example of a device that effectively mitigates stall at high angles of attack. Also, the actuation of the leading edge can provide noise reduction when wings are used as high-lift devices [170]. However, their deployment at lower angles of attack quickly degrades the aerodynamic performance [171]. Others recur to bioinspired solutions, for instance, Gopinathan and Rose [172], who developed a wing with leading-edge tubercles to delay the stall phenomenon. The same concept was used by Zhang et al. [173] to improve wind turbine blade aerodynamics. The leading-edge protuberances proved to be a convincing passive flow control that improved the aerodynamic efficiency up to $11\,\%$ in the post-stall region. Indeed, Miklosovic et al. [174] showed that with these leading-edge structures, as the ones shown in Figure 2.25, the wing would experience softer stall characteristics by maintaining the flow attached.

Other bioinspired concepts, such as imitating a bird's cover feathers placed close to the leading edge, have also shown the potential to enhance lift when the airfoil exceeds its critical angle of attack [135]. However, the usage of these high-lift devices may affect the aerodynamic performance at lower angles of attack. This problem can be tackled with a continuous morphing strategy, as implemented by Colletti and Ansell [175], who used a genetic algorithm

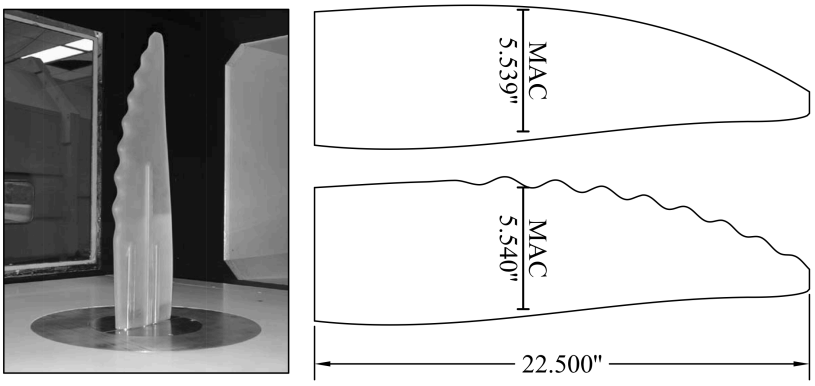

Figure 2.25: Configuration used by Miklosovic et al [174].

to design a morphed leading edge for high-lift applications. The authors also add that morphing is used to maximize the presence of laminar flow in cruise flight by removing surface discontinuities. Similarly, Kintscher et al. [176] and Monner et al. [177] developed morphing leading-edge devices that act as a step-less droop nose device, demonstrating why many works indicate camber morphing as a viable solution to future aerodynamic surfaces [178].

Anderson et al. [179] also studied the leading-edge drooping mechanism and analyzed both drooped and undrooped wings after the critical angle of attack, with the drooped leading edge being more effective at the stall region. A similar study by Chandrasekhara et al. [180] demonstrates how a deflected leading edge can control the dynamic stall. Results have shown that the negative peak pitching moment can be reduced considerably together with a $75\,\%$ reduction in drag. Other authors push the geometrical modifications even further by coupling the movable leading edge with a Coanda-type flap. This was studied by Burnazzi and Radespiel [181] who saw a prominent growth in the critical angle of attack while providing extremely high lift coefficients.

Although offering valuable aerodynamic improvements to these systems, there is a lack of optimal studies. While there are some optimization studies concerning airfoil morphology, these are typically kept in the computational realm and are not conducted in a real-time manner. Finding an experimental work that pursues the optimal use of a wing is rare, as well as searching for an experimental rig coupled with an algorithm that runs in real-time, which is even rarer.

Having completed the general overview of the basics from various aspects of unsteady airfoils, we now move on to one of the central chapters of the thesis, where a newer generation of the commonly known NACA0012 airfoil is presented. This unique version will offer a substitute way to study oscillating airfoils while at the same time improving the propulsive performance of flapping airfoils and mitigating the adverse effects of dynamic stall.

Chapter 3

NACA0012-IK30 Airfoil

> *"The real voyage of discovery consists not in seeking new landscapes, but in having new eyes."*
>
> *Marcel Proust*

Central to this thesis is the development of some type of mechanism that can improve the aerodynamic and propulsive characteristics of unsteady airfoils. In this short chapter, we bring the concept of dynamic curvature to life, while trying to move away from the conventional rigid airfoils that move with traditional kinematics. The result is the proposal of an innovative geometry: the NACA0012-IK30 airfoil.

3.1 Airfoil Development

The performance of unsteady airfoils relies on two variables: geometry and kinematics. Since the beginning up until now, these two variables, while widely studied, have been somewhat constricted to a narrow set of conditions, that are still rather conservative. While looking at unsteady airfoil research, the vast majority of studies still use traditional airfoils without a deep exploration of newer kinematics.

Hence, there is a need to move towards a newer generation of aerodynamic devices that can elevate even further the performance of unsteady airfoils. The present work builds upon this necessity, by bringing an important concept from the various ways of natural locomotion: dynamic curvature. With dynamic curvature, traditional airfoils gain new degrees of freedom moving closer to the time-varying morphology of natural structures. This is the basic concept for the proposed geometry: the NACA0012-IK30 airfoil.

The NACA0012-IK30 has been designed with thrust enhancement, power reduction, and dynamic stall mitigation in mind. This is accomplished by dividing the commonly used NACA0012 airfoil into two parts: the front part, which will be recurrently called the leading edge or the β part, and the back part, also referred to as the ψ part. These two parts can have different kinematics, which adds flexibility to the manipulation of several aerodynamic parameters, for instance, the effective angle of attack.

Between these two parts, an arc centered at $30\,\%$ of the chord, with an inner and outer radius of $t/2$ and $t/2 + 0.001\,\text{m}$ is extracted from the airfoil, where t is the thickness of the airfoil.

For clarity, Figure 3.1 illustrates where the cut was made. Based on the dimensions indicated before, this means that there is a 1 mm spacing between the leading edge and the main part, representing 0.5 % of the chord length. The 1 mm spacing between the two parts was selected to guarantee a $30°$ deflection between the β and ψ parts without any collision.

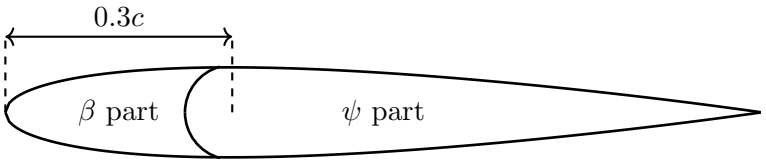

Figure 3.1: NACA0012-IK30 Airfoil.

With this geometry, by rotating the leading edge or main parts individually, one can easily apply the dynamic curvature concept without much difficulty. In the early design phase, several other configurations were considered, including geometries using camber morphing. While these are technologies that must be encouraged, for the present study it would create at least three major layers of complexity needed for an adequate investigation: material selection, structural design, and fatigue analysis. To initiate the studies of the proposed airfoil, while focusing exclusively on the aerodynamic effects, the present configuration was selected. However, it is highly recommended that a second generation of the NACA0012-IK30 airfoil explores advanced morphing capabilities.

3.2 NACA0012-IK30 Terminology

Concerning the current NACA0012-IK30 design, it is important to strictly define the governing parameters that allow for its methodical study. Figure 3.2 shows all parameters used to control the airfoil's state.

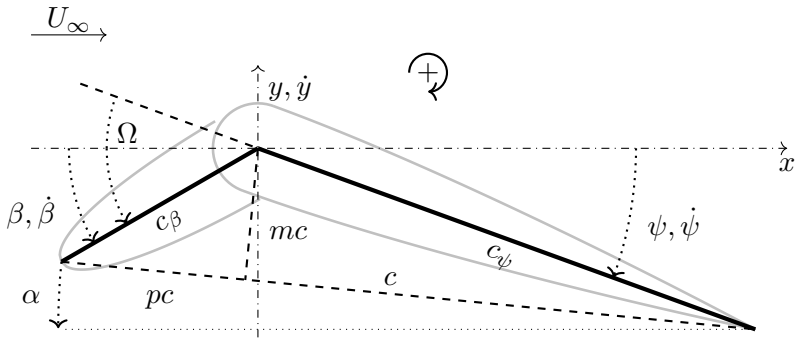

Figure 3.2: NACA0012-IK30 airfoil terminology.

Applying the concept of dynamic curvature implies that the airfoil will be used in a time-varying manner. Consequently, parameters that would be otherwise constant, become functions of time, for instance, the airfoil chord length. Using the conventional definition which states that the airfoil chord length is the dimension between the leading and trailing edges, c

is defined as

$$c = \sqrt{(c_\beta \cos\beta + c_2 \cos\psi)^2 + (c_\beta \sin\beta + c_\psi \sin\psi)^2}, \tag{3.1}$$

where c_β, c_ψ are the chords of the β and ψ parts, and β, ψ are the angles of attack of the front and back parts, respectively. As seen before, the NACA0012-IK30 has the pivot at 30 % of the airfoil's chord, which coincides with the maximum airfoil thickness of the NACA0012. This means that $c_\beta = 0.3c$ and $c_\psi = 0.7c$, when the airfoil is not deflected.

The maximum curvature is calculated similarly to traditional airfoils, by determining the distance normal to the chord line ending at the pivot point. Maximum curvature is expressed by m and defined as

$$m = \frac{c_\beta}{c} \sin(\alpha - \beta) = \frac{c_\psi}{c} \sin(\psi - \alpha), \tag{3.2}$$

and the position of maximum curvature along the chord line, p, is expressed as

$$p = \frac{c_\beta}{c} \cos(\alpha - \beta). \tag{3.3}$$

Now that the airfoil is divided into two parts, the angle of attack becomes a function of β and ψ. As in traditional airfoils, it is defined as the angle between the chord line and the incoming flow, given by

$$\alpha = \arctan\left(\frac{c_\beta \sin\beta + c_\psi \sin\psi}{c_\beta \cos\beta + c_\psi \cos\psi}\right). \tag{3.4}$$

As this is a geometry designed to be used in oscillating airfoils, apart from the angle of attack, we should consider the effective angle of attack, calculated as

$$\alpha_{\text{eff}} = \arctan\left(-\frac{\dot{y}}{U_\infty}\right) + \alpha, \tag{3.5}$$

where the first term of the right-hand side is the induced effective angle of attack by the plunging motion. One could also take into consideration the effective angles of attack of the individual parts, given by

$$\beta_{\text{eff}} = \arctan\left(-\frac{\dot{y}}{U_\infty}\right) + \beta, \tag{3.6}$$

and

$$\psi_{\text{eff}} = \arctan\left(-\frac{\dot{y}}{U_\infty}\right) + \psi, \tag{3.7}$$

for the leading edge and back parts, respectively. These parameters could be very useful to control and analyze local effects, instead of α_{eff}, which only reveals integral effects. Figure

3.3 illustrates these angles together with the effective flow velocity, U_{eff}.

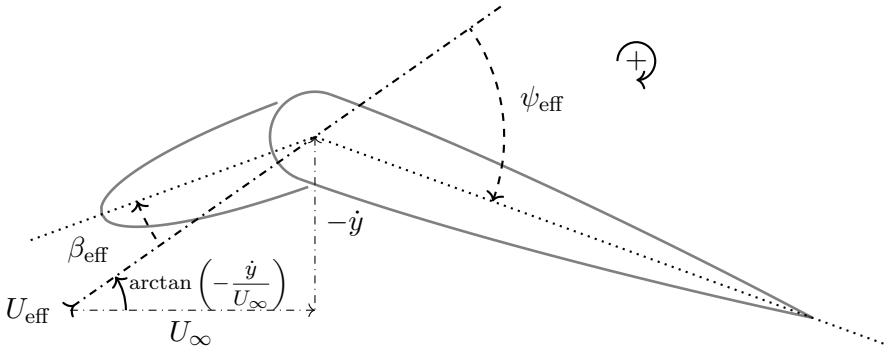

Figure 3.3: The effective angles of attack of the β and ψ parts.

After exploring the geometry and kinematics of the proposed airfoil, we now move to the parameters used to characterize both the airfoil operation and flow regimes. The first parameter is the Reynolds number, defined as

$$Re = \frac{\rho U_\infty c}{\mu}, \tag{3.8}$$

where ρ is the fluid density, U_∞ is the flow velocity, c is the chord, and μ is the dynamic viscosity. This parameter provides the ratio between inertial and viscous forces, indicating which of these is dominant. Throughout the study we will be using this classical definition, however, we need to raise the question if the airfoil motion does not contribute to the inertial loads of the flow field, especially in the region surrounding the airfoil. As a suggestion for future research, one could consider an updated definition of the Reynolds number, for instance

$$Re = \frac{\rho\sqrt{U_\infty^2 + V^2}\sqrt{L^2 + c^2}}{\mu}, \tag{3.9}$$

where V and L are, respectively, the reference velocity and length of the oscillatory motion. This would include not only the inertial effects of the flow velocity, U_∞, but also consider the contribution of the airfoil motion. Still, one should be very careful when considering updating the Reynolds number definition.

An additional parameter used to study the NACA0012-IK30 airfoil is the reduced frequency defined as

$$k = \frac{2\pi f c}{U_\infty}, \tag{3.10}$$

where f is the motion frequency, providing an overall idea of how fast the airfoil vibrates relative to the approaching flow. Together with the nondimensional amplitude given by

$$h = \frac{A}{c}, \tag{3.11}$$

in which A is the plunging amplitude, one can quickly obtain the nondimensional velocity

defined as

$$kh = \frac{2\pi f A}{U_\infty}. \tag{3.12}$$

This is an important parameter that provides the ratio between the airfoil's velocity and the flow velocity, which as seen in equation (3.5), strongly affects the effective angle of attack. This equation is valid for the specific case where the sinusoidal motion is prescribed, as the maximum velocity in absolute value is given by $2\pi f A$. For different kinematics, $\max \dot{y}$ may be used in the numerator.

Concerning the pitching motion, a similar parameter can be used, defined as

$$kA_\alpha = \frac{2\pi f c}{U_\infty} A_\alpha, \tag{3.13}$$

with A_α representing a pitching amplitude, which could also be A_β or A_ψ. We call this parameter the nondimensional angular velocity.

All these previous parameters control the kinematics of the airfoil, working as inputs to the study. Let us now analyze how the airfoil performance is evaluated by presenting the aerodynamic and propulsive indicators.

The three main aerodynamic indicators are the drag, lift, and moment coefficients given by

$$C_D = \frac{D}{\frac{1}{2}\rho U_\infty^2 S}, \tag{3.14}$$

$$C_L = \frac{L}{\frac{1}{2}\rho U_\infty^2 S}, \tag{3.15}$$

and

$$C_M = \frac{M}{\frac{1}{2}\rho U_\infty^2 S c}, \tag{3.16}$$

respectively, where S is the wing area that in a 2D analysis becomes just c. On a side note, the moment coefficients obtained throughout the study are measured at the pivot point (30 % of c). These three parameters are central to the whole investigation of the airfoil, especially in the stall mitigation, where we have the primordial objectives of reducing drag and increasing lift.

Concerning the propulsive enhancement capabilities of the airfoil, we will be focusing on

three different parameters. The first is the propulsive power coefficient given by

$$C_{P_P} = C_t^{\beta} + C_t^{\psi}, \tag{3.17}$$

where C_t is the thrust coefficient, defined as the symmetric value of drag. As seen in equation (3.17), thrust is subdivided into two parts, which as seen in the results, will be useful to understand the relative importance between the β and ψ parts.

An equally important parameter is the required power coefficient calculated as

$$C_{P_R} = -(C_l^{\beta} + C_l^{\psi})\frac{\dot{y}}{U_\infty} - C_m^{\beta}\frac{\dot{\beta}c}{U_\infty} - C_m^{\psi}\frac{\dot{\psi}c}{U_\infty}, \tag{3.18}$$

where $\dot{y}$ is the plunging velocity, $\dot{\beta}$ is the angular velocity of the leading edge, and $\dot{\psi}$ is the angular velocity of the main part. As in the previous coefficient, the required power is segmented into different terms to allow direct access to the improvements given by each part. Important to remember that this is the required power needed to overcome the aerodynamic forces applied during oscillations, which does not include any inertial effects. For the complete mathematical deduction of these propulsive coefficients, please revisit section 2.2.

Finally, to understand if thrust is efficiently achieved, we use the propulsive efficiency defined as

$$\eta = \frac{\overline{C_{P_P}}}{\overline{C_{P_R}}} = \frac{\overline{C_t^{\beta} + C_t^{\psi}}}{-(C_l^{\beta} + C_l^{\psi})\frac{\dot{y}}{U_\infty} - C_m^{\beta}\frac{\dot{\beta}c}{U_\infty} - C_m^{\psi}\frac{\dot{\psi}c}{U_\infty}}, \tag{3.19}$$

where we divide the cycle-averaged propulsive power, $\overline{C_{P_P}}$, by the mean required power, $\overline{C_{P_P}}$, needed to sustain the airfoil oscillation.

Now that the terminology of the proposed geometry and its performance indicators have been presented, we shall move to the following chapters, where the airfoil will be adjusted to the different numerical and experimental methodologies.

Chapter 4

Experimental Methodology

> *"The proper method for inquiring after the properties of things is to deduce them from experiments."*
>
> *Isaac Newton*

In this chapter, the experimental methodologies used to test the IK30 mechanism are presented. It includes the design of the experimental rigs, flow visualization technique, force measurements, kinematics, and the propagation of uncertainties.

4.1 Flow Visualization - Rig Design and Methodology

This first section concerns the experimental equipment and methodology implemented to observe the flow field surrounding the NACA0012-IK30. Tests are conducted at the facilities of the Aeronautics and Astronautics Research Center (AEROG) anemometry laboratory of the University of Beira Interior (UBI), located in Covilhã, Portugal.

4.1.1 Wind Tunnel

For the flow visualization, the wind tunnel used is the one designed and built by the AEROG laboratory. It is an open circuit, open section, and blower wind tunnel, illustrated in Figure 4.1.

Figure 4.1: Wind Tunnel for flow visualization experiments.

The wind tunnel has a 15 kW fan capable of providing a maximum volumetric flow rate of $3000\,\mathrm{m^3\,h^{-1}}$ passing through an air hose that is connected to the diffuser, being the latter connected to a settling chamber. At the settling chamber, the turbulence level of the flow is

reduced by using flow straighteners with a honeycomb design that lessens the lateral velocity fluctuations and turbulence screens that improve flow quality. Then, a contraction accelerates the flow with a contraction ratio of 6:1. The flow velocity is controlled either by the motor frequency and/or a guillotine located upstream, visible on the left image of Figure 4.1.

An extension was added to the wind tunnel where a smoke dispenser system was added with a 0.3×0.2 m outlet section. It includes a smoke machine, tubes, and a smoke rake to conduct flow visualization tests. Preliminary tests have shown that smoke insertion would create agglomerates of smoke, which degrades the flow quality. To counteract these flow structures created by the smoke rake, a honeycomb straightening section is positioned after smoke insertion to improve flow quality with no change in the turbulent intensity measured at the wind tunnel's exit.

4.1.2 Laser Doppler Anemometry (LDA)

The flow velocity at the wind tunnel's exit is measured with Laser Dopper Anemometry (LDA). This optical technique allows a non-intrusive and direct measurement, requiring tracer particles in the flow. This method has the particular advantages of not needing calibration, its directional sensitivity, and high spatial and temporal resolution.

The basic configuration of an LDA, shown in Figure 4.2, consists of a continuous wave laser, transmitting optics, receiving optics, a signal conditioner, and a signal processor. A Bragg cell is often a part of the transmitting optics that acts as a beam splitter. The output of this cell is two beams with two different frequencies. These two beams in a probe are focused and intersected in the probe volume.

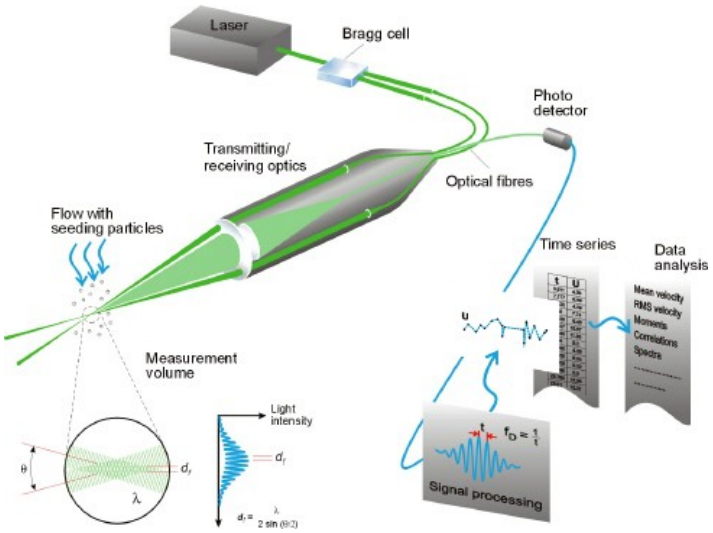

Figure 4.2: LDA principle [182].

This probe volume with a size in the order of millimeters has parallel planes of high light intensity called fringes, which come from the interference of the two laser beams. Particles passing through this probe volume scatter light proportionally to the local light intensity, being later received by a lens and focused on a photo-detector.

Signal processing consists of converting these fluctuations of light intensity into velocity based on a frequency analysis using the Fast Fourier Transform algorithm and fringe spacing. Moreover, with a frequency-shifted LDA system, we can determine flow direction. In the case of two-component measurements, the working principle stays the same, with the only distinction being the addition of two extra beams in the optics in a plane perpendicular to the first beams.

The methodology followed in the present study closely follows the one implemented by Vieira [183] where the flow velocity is measured with a two-component Laser-Doppler velocimetry (Dantec Flowlite 2D). The horizontal and vertical mean and turbulent velocities are determined by a two-velocity channel Dantec BSA F60 processor and the transmitting and collecting optics are mounted on a three-dimensional traversing unit that allows the accurate positioning of the control volume within 0.1 mm.

The BSA properties were changed in the BSA flow software so higher data rate and validation were achieved. With the smoke level used to visualize the flow field, validation was high (higher than 95 %) and the data rate was satisfactory, measuring ten thousand samples in less than 60 s.

4.1.3 Flow Properties

The air properties at which tests are conducted are measured by a weather station that indicates the temperature and ambient pressure. The two values are used to estimate dynamic viscosity and density.

The dynamic viscosity is calculated using Sutherland's law, as stated in equation (4.1)

$$\mu = \mu_0 \left(\frac{T}{T_0} \right)^{3/2} \frac{T_0 + S}{T + S}, \tag{4.1}$$

where $\mu_0 = 1.716 \times 10^{-5}$ Pa s, $T_0 = 273.15$ K and $S = 110.4$ K.

Using ambient pressure and temperature, the air density is calculated using the ideal gas law, expressed as

$$\rho = \frac{P}{RT}, \tag{4.2}$$

with $R = 287.058\,\mathrm{J\,kg^{-1}\,K^{-1}}$.

4.1.4 Smoke Dispenser System

Measuring the flow velocity using LDA inherently requires particles present in the flow field. With that in mind, a smoke dispenser system is developed to release particles in the wind tunnel. Furthermore, this smoke dispenser system is also used for visualization purposes. In Figure 4.3 the system is illustrated as is its configuration.

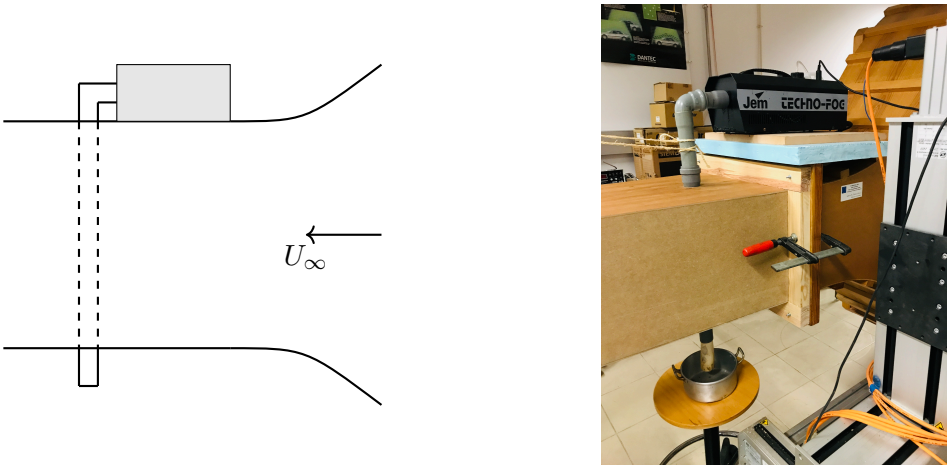

Figure 4.3: Smoke System.

The smoke machine was a TECHNO-FOG Jem machine which is a thermal smoke generating machine with Jem Regular DJ Fluid. This machine thermally vaporizes a water-glycerol mixture which condensates into small particles that can be used for LDA measurements, as other older work conducted in the AEROG anemometry lab indicates.

4.1.5 Image Acquisition System

Capturing images is a central part of the experimental methodology and for that, two cameras are used. One of the cameras is the FASTCAM Mini UX50, a high-speed camera produced by Photron that provides a 1.3-megapixel image resolution with frame rates up to 2000fps. This camera is controlled by the Photron FASTCAM Viewer software (PFV4) and is mainly used for kinematics validation. The high-speed camera is illustrated in Figure 4.4.

Figure 4.4: FASTCAM50

The other camera is a GoPro HERO10, shown in Figure 4.5. This camera is used in a Lagrangian perspective, being attached to the wingtip that offers a wide view of what happens on the airfoil's upper surface.

Video recordings are shot at 2.7K (horizontal) resolution (2704x1520) and 240 frames per second. To enhance flow features videos are slightly processed on MATLAB. Image processing gathers some instructions like resizing, grayscale conversion, pixel value adjustment, and sharpening.

Figure 4.5: GoPro HERO10 camera.

4.1.6 Flow Visualization Setup

To summarize, the flow visualization setup has three main components: the smoke dispenser, illumination, and image acquisition systems, all represented in Figure 4.6. The smoke inserted in the smoke rake is released at the middle section of the wind tunnel, which then goes through a flow straightener that removes any vertical velocity components created during the smoke injection. The floodlight containing several rows of LEDs emits light that is scattered by the smoke particles. The light scattering process is then captured by the GoPro camera used to record each experimental run.

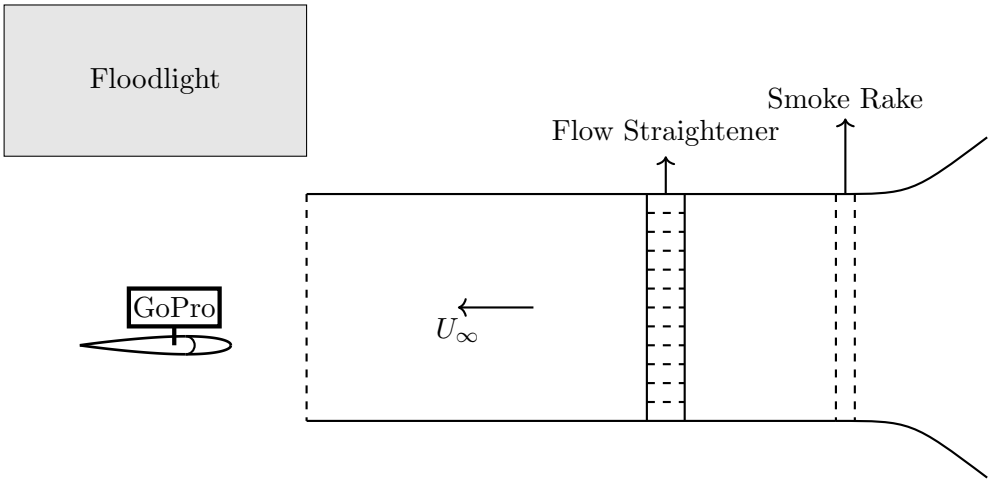

Figure 4.6: Flow visualization setup.

4.1.7 NACA0012-IK30 Wing

The wing design is created based on the NACA0012-IK30 airfoil and thoughtfully built for the flow visualization tests. It was designed in the CATIA V5 R20 software, according to the geometrical characteristics presented in Chapter 3. The result is presented in Figure 4.7.

The wing has a 20 cm chord and a span of 50 cm, placed at approximately 2 cm from the outlet section. The wingspan was selected to be larger than the outlet section so we would not record any wing tip effects. The wing has three main fixation points: two on the back part, where we fit two spars with circular sections, and one in the frontal part, where one spar with a square section that constrains the rotation of the leading edge is inserted.

Figure 4.7: Wing with the NACA0012-IK30 airfoil.

The manufacturing of the prototype is accomplished using additive manufacturing. The wing is produced using the Original Prusa i3 MK3S+ 3D printer with the PLA filament, both shown in Figure 4.8. For the wing spars, the material selected is aluminum.

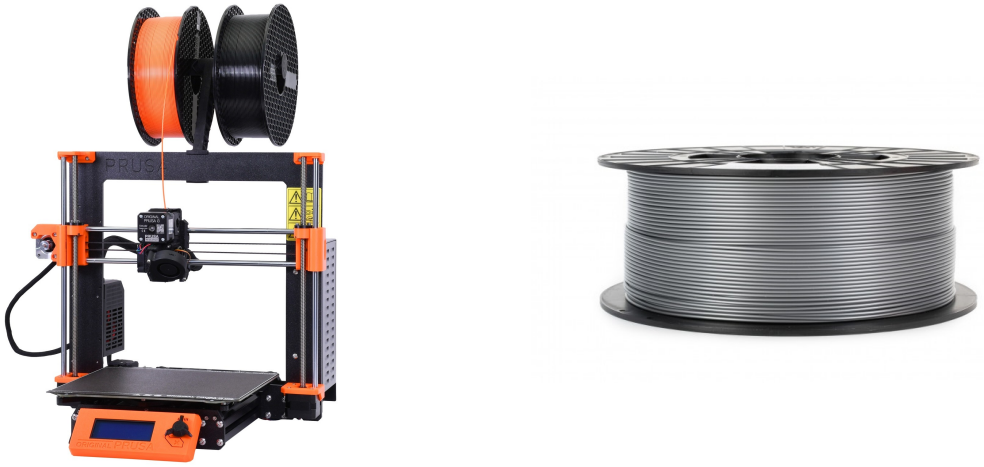

Figure 4.8: Prusa i3 MK3S+ 3D printer (left) and the PLA filament (right).

4.1.8 Support Structure

The wing is attached to a support structure as illustrated in Figure 4.9. The spars of the ψ part are connected to two components located at the extremities of the wing (red parts), which are both fixed in the U-shaped structure. This structure is connected to the plunging motor, which is itself secured by the base that is fixed to the ground.

The base of the structure is made of wood, which has metallic linkages to the plunging motor. The U-shaped structure is metallic too, while the components where the spars are connected, were also produced by 3D printing. Also illustrated in Figure 4.9, is the leading-edge pitching mechanism seen on the left side of the wing.

4.1.9 Leading-Edge Pitching Mechanism

A different perspective is shown in Figure 4.10 which shows where the main components of the rotational mechanism are.

The electric motor frame attaches to the support through the component colored in purple, which encloses the connection used to rotate the leading edge (orange part). This latter part has its pivot coincident with the frontal spar axis of the main airfoil part, which passes

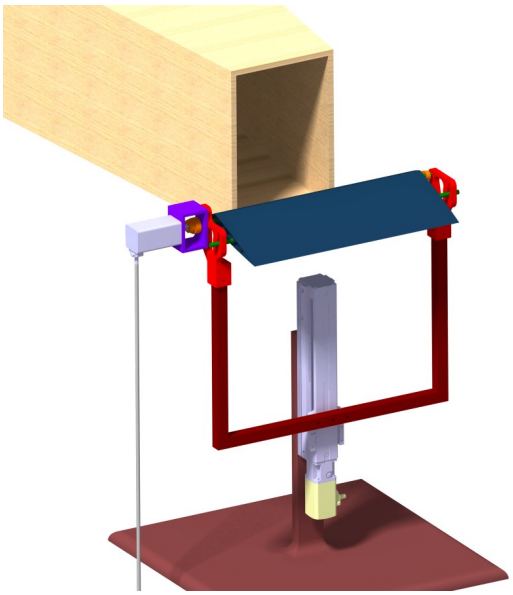

Figure 4.9: Support structure.

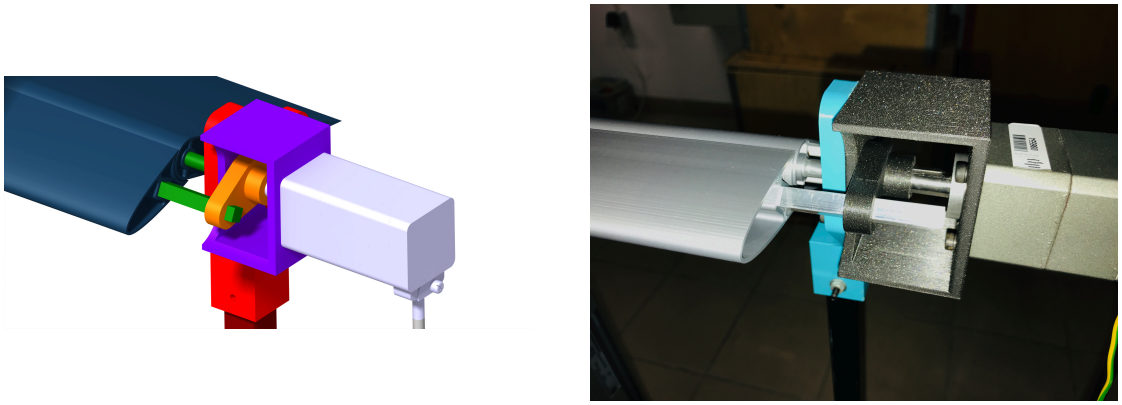

Figure 4.10: Leading-Edge Pitching Mechanism.

through the purple component. This ensures the concentricity of the leading edge rotation while reducing the possibility of collision between the airfoil parts.

4.1.10 Wing Motion Control

The wing kinematics are controlled using two stepper motors produced by Oriental Motor Co., Ltd. Plunging is performed with the EASM4XD020ARAC electric linear slide, which is a stepper motor coupled with a ball screw as the drive method. In Figure 4.11, the stepper motor (ARM46AC) and the linear slide are shown.

The linear actuator has a stroke of $0.2\,\mathrm{m}$ with a step size of $0.012\,\mathrm{mm}$ and a maximum operation speed of $0.8\,\mathrm{m\,s^{-1}}$. More information is described at [184].

For the pitching motion of the leading edge, the PKE543AC-PS50 stepper motor is used, as seen in Figure 4.12.

Figure 4.11: The stepper motor ARM46AC (left) and the linear slide EASM4XD020ARAC (right).

Figure 4.12: PKE543AC-PS50 stepper motor.

The step motor has a basic step angle of $0.0144°$ with a gear ratio of 50:1 which allows for fine adjustments. More information is detailed at [185].

The desired kinematics are prescribed by using the ARD-CD [186] and RKSD503-CD [187] controllers for plunging and pitching, respectively. These two controllers, shown in Figure 4.13, are connected to a laptop equipped with MEXE02 support software (v3.70) using the CC05IF-USB data setting software communication cable.

Figure 4.13: ARD-CD (left) and RKSD503-CD (right) controllers.

4.1.11 Kinematics

As is customary in the field of oscillating airfoils, the velocity profile follows a sinusoidal wave. In this section, the asymmetry level is also considered meaning that with this kinematics, it is possible to study the difference between the ascending and descending times. Mathematically, and considering only the plunging motion (pitching is similar), the position of the

airfoil as a function of time is expressed as

$$y = \begin{cases} A \sin\left(\dfrac{\pi}{\zeta T} t + \dfrac{\pi}{2}\right) & \text{if } 0 \leqslant t < \zeta T \\ A \sin\left(\dfrac{\pi}{(1-\zeta)T}(T-t) + \dfrac{\pi}{2}\right) & \text{if } \zeta T \leqslant t \leqslant T \end{cases}, \tag{4.3}$$

where ζ is the asymmetry level parameter and T is the period. A graphical representation is illustrated in Figure 4.14. The asymmetric motion is offered as a suggestion, as only symmetric kinematics were tested experimentally.

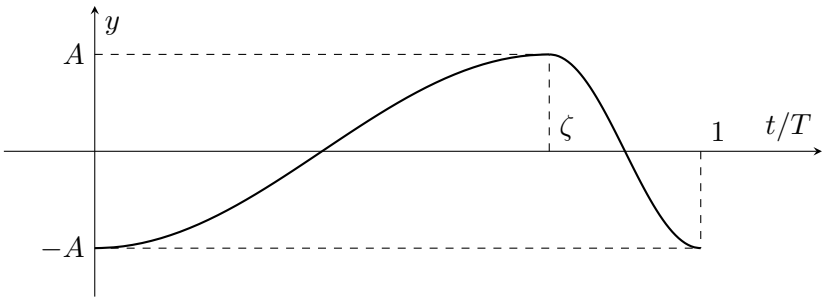

Figure 4.14: Sinusoidal position profile.

Unfortunately, the setup implemented to control the motors could only follow a trapezoidal velocity profile, meaning that to achieve the sinusoidal motion, an approximation needed to be made. This section is focused on creating a framework that approximates the desired sinusoidal motion with trapezoids. Figure 4.15 shows a generic trapezoidal velocity profile that considers the motion asymmetry, given by ζ, and the acceleration/deceleration times.

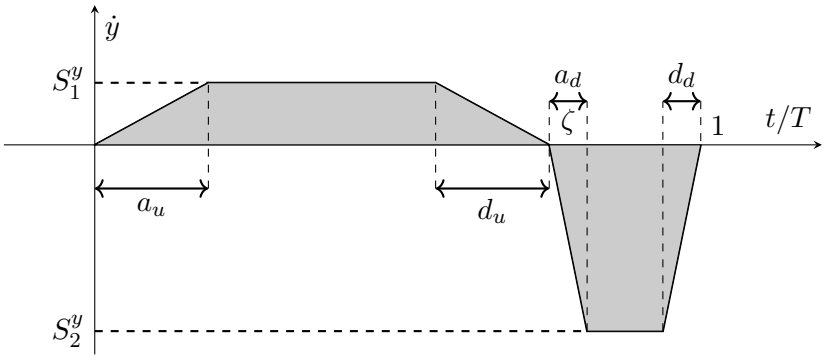

Figure 4.15: Trapezoidal velocity profile.

The acceleration/deceleration times illustrated are defined as

$$a_u = d_u = \xi \zeta T, \tag{4.4}$$

and

$$a_d = d_d = \xi (1-\zeta) T, \tag{4.5}$$

with ξ being called the acceleration parameter. Knowing that the areas of both trapezoids are

equal to the motion amplitude, A, then the velocities S_1^y and S_2^y are calculated as

$$S_1^y = \frac{2A}{\zeta(1-\xi)T}, \tag{4.6}$$

and

$$S_2^y = \frac{2A}{(1-\zeta)(1-\xi)T}. \tag{4.7}$$

Mathematically, the trapezoidal velocity profile is given by the piecewise function

$$\dot{y} = \begin{cases} \frac{S_1^y}{\zeta\xi T}\left(t - PT\right) & \text{if } t \in [t_a, t_b[\\ S_1^y & \text{if } t \in [t_b, t_c[\\ -\frac{S_1^y}{\zeta\xi T}\left(t - PT\right) + \frac{S_1^y}{\xi} & \text{if } t \in [t_c, t_d[\\ -\frac{S_2^y}{(1-\zeta)\xi T}\left(t - PT\right) + \frac{S_2^y\zeta}{(1-\zeta)\xi} & \text{if } t \in [t_d, t_e[\\ -S_2^y & \text{if } t \in [t_e, t_f[\\ \frac{S_2^y}{(1-\zeta)\xi T}\left(t - PT\right) - \frac{S_2^y}{(1-\zeta)\xi} & \text{if } t \in [t_f, t_g[\end{cases}, \tag{4.8}$$

with

$$P = \left\lfloor \frac{t}{T} \right\rfloor, \tag{4.9}$$

and

$$t_a = PT \tag{4.10}$$

$$t_b = t_a + \zeta\xi T \tag{4.11}$$

$$t_c = t_a + \zeta T - \zeta\xi T \tag{4.12}$$

$$t_d = t_a + \zeta T \tag{4.13}$$

$$t_e = t_a + \zeta T + (1-\zeta)\xi T \tag{4.14}$$

$$t_f = t_a + T - (1-\zeta)\xi T \tag{4.15}$$

$$t_g = t_a + T. \tag{4.16}$$

To obtain the position as a function of time, equation (4.8) is integrated, which results in equation (4.17).

$$y = \begin{cases} \frac{1}{2}\frac{S_1^y}{\zeta\xi T}t^2 & \text{if } t \in [t_a, t_b[\\ S_1^y t - \frac{1}{2}S_1^y \zeta\xi T & \text{if } t \in [t_b, t_c[\\ -\frac{1}{2}\frac{S_1^y}{\zeta\xi T}t^2 + \frac{S_1^y}{\xi}t + 2A - \frac{1}{2}\frac{S_1^y \zeta T}{\xi} & \text{if } t \in [t_c, t_d[\\ -\frac{1}{2}\frac{S_2^y}{(1-\zeta)\xi T}t^2 + \frac{S_2^y \zeta}{(1-\zeta)\xi}t + 2A - \frac{1}{2}\frac{S_2^y \zeta^2 T}{(1-\zeta)\xi} & \text{if } t \in [t_d, t_e[\\ -S_2^y t + 2A + S_2^y \zeta T + \frac{1}{2}S_2^y(1-\zeta)\xi T & \text{if } t \in [t_e, t_f[\\ \frac{1}{2}\frac{S_2^y}{(1-\zeta)\xi T}t^2 - \frac{S_2^y}{(1-\zeta)\xi}t + \frac{1}{2}\frac{S_2^y T}{(1-\zeta)\xi} & \text{if } t \in [t_f, t_g[\end{cases} \tag{4.17}$$

A graphical representation of the y position as a function of time is shown in Figure 4.16. Yet, this waveform still does not approximate the sinusoidal motion optimally.

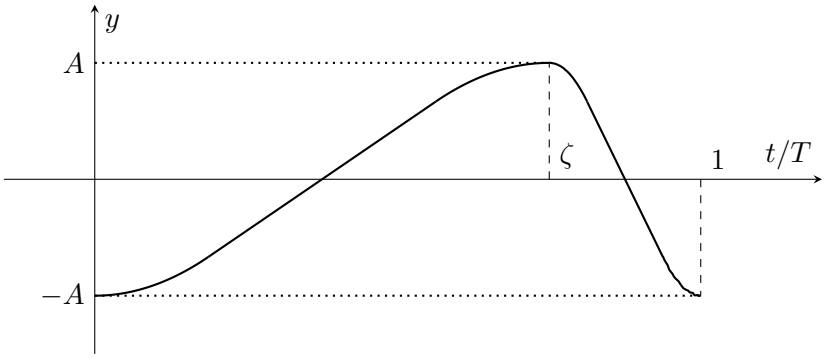

Figure 4.16: Position profile based on a trapezoidal velocity profile.

To find the best approximation of the sinusoidal profile, $S(t)$, by using the trapezoidal motion, $T(t)$, the least-squares method is used in which we minimize the sum of the squares of the residuals by searching for the optimal value of the ξ parameter, meaning that

$$\frac{\mathrm{d}}{\mathrm{d}\xi}\int_0^T [S(t) - T(t)]^2 \,\mathrm{d}t = 0. \tag{4.18}$$

To find the optimal ξ value, the above integral is discretized, as shown below.

$$\frac{\mathrm{d}}{\mathrm{d}\xi}\sum_{i=1}^{N} [S(t_i) - T(t_i)]^2 \,\mathrm{d}t = 0. \tag{4.19}$$

Equation (4.19) is solved iteratively, by changing N and ξ, from which we obtain that when

$$\xi \approx 0.33, \tag{4.20}$$

the trapezoidal wave offers an optimal approximation of the sinusoidal function. In Figure

4.17, both trapezoidal (with $\xi = 0.33$) and sinusoidal waveforms are shown for two cases, $\zeta = 0.5$ and 0.75.

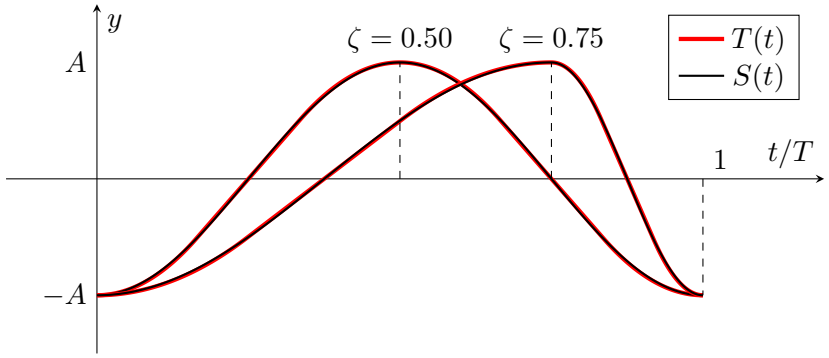

Figure 4.17: Comparison of trapezoidal and sinusoidal waveforms.

Although only plunging kinematics were presented here, the activation of the leading edge is similar but with a phase angle $\phi = 90°$, as commonly used in the literature. This means that the leading edge will be maximally deflected when the airfoil is at its maximum plunging velocity. As a resume, and to make it clear, equation (4.21) shows the kinematics that the airfoil is subjected to.

$$\text{IK30 kinematics} \rightarrow \begin{cases} y = A\sin(2\pi ft) \\ \beta = A_\beta \sin(2\pi ft + \pi/2) \\ \psi = 0° \end{cases} \tag{4.21}$$

4.1.12 Experimental Checklist

Before conducting the experimental study, a checklist was designed to guarantee the repeatability and reproducibility of the results. By following the instructions as presented, systematic errors, such as unwanted velocity variations over time, could be mitigated.

Flow visualization for the NACA0012-IK30 airfoil followed the next steps:

1. **Setting the flow velocity**

   (a) Set the Reynolds number.

   (b) Read ambient temperature and pressure (T and P).

   (c) Calculate fluid density, ρ, and dynamic viscosity, μ.

   (d) Calculate the desired velocity.

(e) Measure the flow velocity.

(f) Open/close the guillotine until the desired velocity is reached.

(g) Verify temperature, and pressure and measure flow velocity every 10 minutes. If needed, adjust the desired velocity and guillotine position accordingly to maintain the prescribed Reynolds number.

2. **Setting the kinematic parameters**

(a) Set the nondimensional amplitude, reduced frequency, and leading-edge pitching amplitude.

(b) Calculate the plunging amplitude based on the wing's chord.

(c) Calculate the motion frequency based on the flow velocity and the wing's chord.

(d) Set the leading-edge pitching amplitude.

3. **Programming the stepper motors**

(a) Insert the kinematic parameters, converted in steps and pulse commands, into the software used to control the stepper motors.

4. **Visualizing the flow field**

(a) Discharge smoke continually.

(b) Start recording using the GoPro camera.

(c) Initiate the oscillatory motion.

(d) Save recording for post-processing.

4.1.13 Propagation of Uncertainties

In this subsection, the expressions for the uncertainty of the several quantities are determined, according to what is explained by Taylor [188]. When considering a function F with arguments $x_1, x_2, ..., x_N$ and their respective uncertainties $\delta_1, \delta_2, ..., \delta_N$, the uncertainty in F is given by

$$\delta_F = \sqrt{\sum_{i=1}^{N} \left(\frac{\partial F}{\partial x_i} \delta x_i \right)^2}. \tag{4.22}$$

In this subsection, the equations needed to estimate the propagation of uncertainties are presented. These equations can only be used when values are measured. When prescribed, no uncertainty is assumed.

4.1.13.1 Density Uncertainty

The air density is estimated using the ideal gas law, expressed as

$$\rho = \frac{P}{RT}, \tag{4.23}$$

and its uncertainty depends on the uncertainty of both temperature and pressure, as shown in equation (4.24).

$$\delta\rho = \sqrt{\left(\frac{1}{RT}\delta P\right)^2 + \left(-\frac{P}{RT^2}\delta T\right)^2}. \tag{4.24}$$

Based on the equipment used to measure temperature and pressure, we have

$$\delta P = 1\,\text{hPa}, \tag{4.25}$$

and

$$\delta T = 0.1\,^\circ\text{C}, \tag{4.26}$$

as their respective uncertainties.

4.1.13.2 Dynamic Viscosity Uncertainty

The air dynamic viscosity is estimated using Sutherland's law, expressed as

$$\mu = \mu_0 \left(\frac{T}{T_0}\right)^{3/2} \frac{T_0 + S}{T + S}, \tag{4.27}$$

and its uncertainty comes from the uncertainty of the temperature measurement, as shown in equation (4.28).

$$\delta\mu = \sqrt{\left(\mu_0 \left[\sqrt{\frac{T}{T_0^3}}\left(\frac{T_0 + S}{T + S}\right) - \sqrt{\left(\frac{T}{T_0}\right)^3}\left(\frac{T_0 + S}{(T + S)^2}\right)\right]\delta T\right)^2}. \tag{4.28}$$

4.1.13.3 Flow Velocity Uncertainty

When using the LDA, uncertainty emerges due to calculating the average with a limited number of samples.

The mean velocity value is calculated as

$$\overline{u} = \frac{1}{N}\sum_{i=1}^{N} u_i, \tag{4.29}$$

with its uncertainty being calculated as

$$\delta\overline{u} = \sqrt{\sum_{i=1}^{N}\left(\frac{\partial\overline{u}}{\partial u_i}\delta u_i\right)^2}, \tag{4.30}$$

which is equivalent to

$$\delta\overline{u} = \sqrt{\sum_{i=1}^{N}\left(\frac{\delta u_i}{N}\right)^2}. \tag{4.31}$$

Even if each velocity measurement is accurate, which is typically the case of LDA, it surely is not a good estimate of the mean value. In terms of estimating the mean velocity, we can assume that the uncertainty in each velocity sample is two times the standard deviation, $\delta u_i = 2u_{\text{RMS}}$, meaning that we are $95\,\%$ confident that the true mean value is within this interval.

Thus, the uncertainty linked to the flow velocity is calculated as

$$\delta\overline{u} = \frac{2u_{\text{RMS}}}{\sqrt{N}}. \tag{4.32}$$

4.1.13.4 Reynolds Number Uncertainty

The Reynolds number is calculated based on the velocity, density, viscosity, and aerodynamic chord of the airfoil as

$$Re = \frac{\rho U_\infty c}{\mu} \tag{4.33}$$

and its uncertainty is determined as shown in equation (4.34).

$$\delta Re = \sqrt{\left(\frac{U_\infty c}{\mu}\delta\rho\right)^2 + \left(\frac{\rho c}{\mu}\delta U_\infty\right)^2 + \left(\frac{\rho U_\infty}{\mu}\delta c\right)^2 + \left(-\frac{\rho U_\infty c}{\mu^2}\delta\mu\right)^2} \tag{4.34}$$

The uncertainty of measuring the airfoil chord, δc, is $0.5\,$mm for the present work.

4.1.13.5 Reduced Frequency Uncertainty

The reduced frequency is determined using equation (4.35)

$$k = \frac{2\pi f c}{U_\infty} \tag{4.35}$$

and its uncertainty is calculated as

$$\delta k = \sqrt{\left(\frac{2\pi f}{U_\infty}\delta c\right)^2 + \left(-\frac{2\pi f c}{U^2}\delta U_\infty\right)^2} \tag{4.36}$$

4.1.13.6 Nondimensional Amplitude Uncertainty

The nondimensional amplitude is expressed as

$$h = \frac{A}{c} \tag{4.37}$$

has an uncertainty which is calculated as shown in equation (4.38).

$$\delta h = \sqrt{\left(-\frac{A}{c^2}\delta c\right)^2} \tag{4.38}$$

4.1.13.7 Nondimensional Velocity Uncertainty

The nondimensional velocity is defined by the kh product and its uncertainty is given equation (4.39).

$$\delta kh = \sqrt{(k\delta h)^2 + (h\delta k)^2} \tag{4.39}$$

4.1.13.8 Length Uncertainty (based on pixel conversion)

For the kinematics validation, dimensions in images are converted from pixels to meters using

$$a = C\text{px} \tag{4.40}$$

where C is a conversion factor determined by a known length reference. This means that with an uncertainty of one pixel, the dimensions have an uncertainty of C, as shown below.

$$\delta a = \sqrt{\left(C\delta_{\text{px}}\right)^2} = C \tag{4.41}$$

4.1.13.9 Leading-Edge Pitching Amplitude Uncertainty

As for the determination of the leading-edge pitching amplitude, two dimensions are used, the horizontal component, b, and the vertical component, a, of the distance from the pivot point to the leading edge. The pitching amplitude is determined as

$$A_\beta = \arctan\left(\frac{a}{b}\right) \tag{4.42}$$

with its uncertainty depending on the uncertainty of the two components, as shown in equation (4.43).

$$\delta A_\beta = \sqrt{\left(\frac{b}{a^2+b^2}\delta_a\right)^2 + \left(-\frac{a}{a^2+b^2}\delta_b\right)^2} \tag{4.43}$$

4.1.13.10 Nondimensional Angular Velocity Uncertainty

The nondimensional angular velocity is defined by the kA_β product and its uncertainty is given equation (4.44).

$$\delta kh = \sqrt{\left(k\delta A_\beta\right)^2 + \left(A_\beta \delta k\right)^2} \tag{4.44}$$

4.2 Force Measurements - Rig Design and Methodology

Force measurements were conducted at the Laboratory of Dynamics (LabDin), one of the laboratories of the Department of Mechanic Engineering at the São Carlos School of Engineering (EESC/USP), from the University of São Paulo (USP).

4.2.1 Wind Tunnel

For these experiments, one of the main components is the wind tunnel. The wind tunnel used is a subsonic blower composed of a diffuser, settling chamber, contraction, and turbulence screenings. It has a sirocco fan (Motovent SVDL-600 model) capable of providing a volumetric flow rate of $400\,\mathrm{m^3\,min^{-1}}$. With an exit of 0.5×0.5 m, it is capable of reaching approximately $27\,\mathrm{m\,s^{-1}}$. The wind tunnel is presented in Figure 4.18.

Regarding the equivalent airspeed (EAS), U_e, it is measured using a pitot tube placed at the exit section of the wind tunnel, which is connected to a VECTUS TIVA manometer. Then, the true airspeed (TAS) is calculated as

$$U_\infty = U_e\sqrt{\frac{\rho_0}{\rho}}, \tag{4.45}$$

where ρ_0 is the air density at sea level in the International Standard Atmosphere. The air density, ρ, is calculated using the ideal gas law, shown in equation (4.23). The temperature

Figure 4.18: Wind tunnel at LabDin (USP-EESC).

and pressure required to calculate the air density are measured using the MT-241A termo-higrometar and the VECpress 201 micromanometer, respectively. As before, the temperature is used to calculate the dynamic viscosity using Sutherland's law.

4.2.2 NACA0012-IK30 Wing

The overall design of the experimental rig is kept the same as in the flow visualization tests, including the manufacturing process. The main differences are that the wing is mounted vertically, has a larger wingspan of 60 cm, and that the axis of the motor used for the leading-edge pitching is not aligned with the pivot axis. This required the design of a new mechanism that could transmit the rotation from the motor axis to the leading edge while keeping the correct pivot point. The schematics of the mechanism are shown in Figure 4.19.

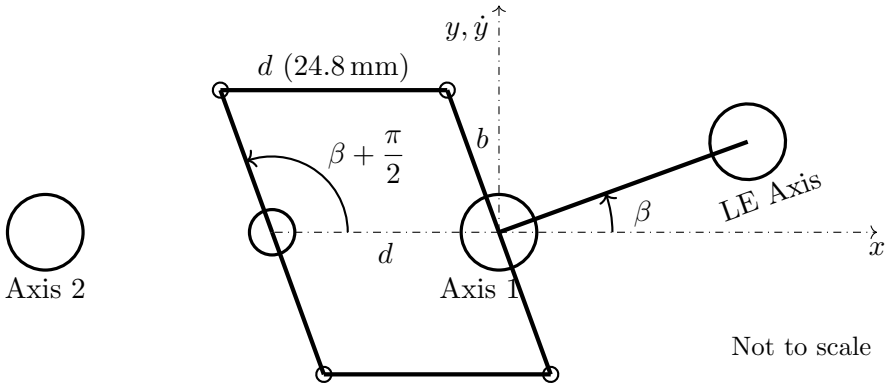

Figure 4.19: Leading-edge pitching mechanism schematics.

The final design developed in CATIAV5R20 and the final assembly are shown in Figure 4.20. As observed, the motor used for the pitching component of the leading edge is housed at a special hub mounted at the wing tip.

Figure 4.21 shows the final assembly of the experimental apparatus for the force measurement tests.

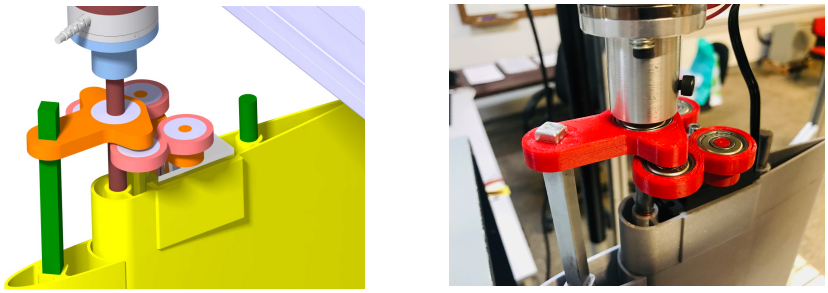

CAD **Final Assembly**

Figure 4.20: Final assembly of the leading-edge pitching mechanism.

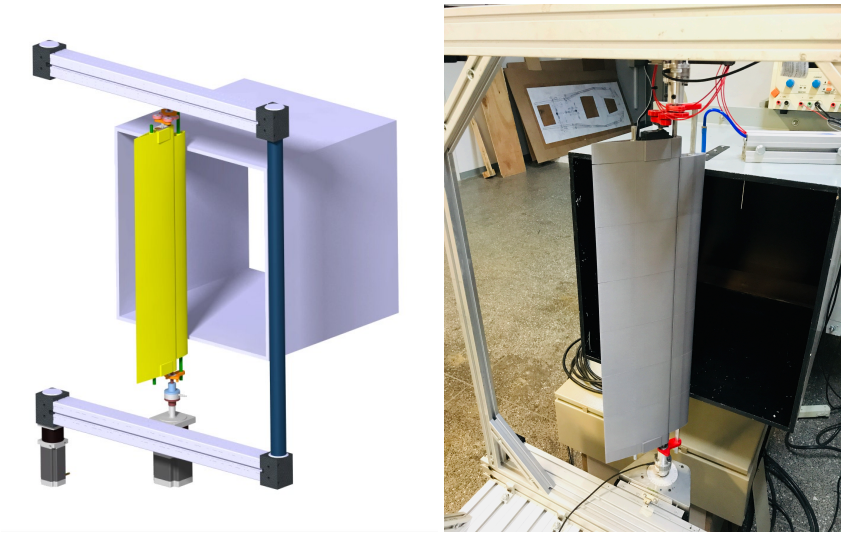

Figure 4.21: Experimental apparatus for force measurements.

4.2.3 Wing Motion Control

Regarding the wing movement, three motors were used: a stepper motor for plunging (KTC-HT23-402.8), another to control the angle of attack of the ψ part (KTC-KML093-F07), and a servo motor that handles the pitching of the leading-edge (SRT DL3017). Two STR8 drivers are used, one for each stepper. The stepper motors and driver are shown in Figure 4.22.

KTC-HT23-402.8 **KTC-KML093-F07** **STR8**

Figure 4.22: Stepper motors and driver.

The stepper motors have a step angle of $1.8°$ that matches the standard resolution of the driver, 200 PPR (Pulses per Revolution). The driver offers resolutions that can go up to 20000 PPR, meaning that it can effectively provide a step angle of $0.018°$. Besides, the step-

per motor responsible for plunging has a gear reduction of 1:4 and is connected to the linear guide SLDC-60, shown in Figure 4.23, that converts one revolution into $0.13\,\text{m}$. An additional linear guide of the same model is placed on the upper part and linked to the lower one through a common axis to prevent wing twisting.

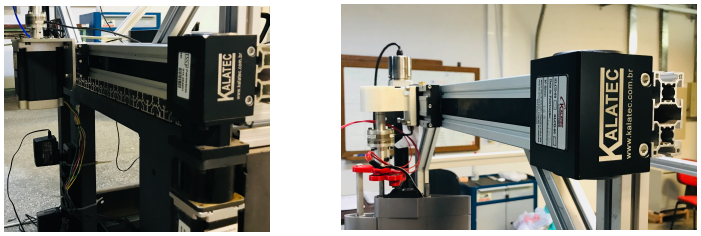

Lower Guide **Upper Guide**

Figure 4.23: Linear guides.

The servo motor used for the leading-edge pitching, shown in Figure 4.24, is a DC, digital type motor capable of executing a $60°$ turn from 0.17 to $0.15\,\text{s}$, depending on the operation voltage ($4.8 - 6.0\,\text{V}$).

Figure 4.24: SRT DL3017 servo motor.

The control of all motors used Simulink, a dSpace board (DS2101), and an Arduino Uno microcontroller board. At first, there was a plan to control all motors with the Arduino board. However, preliminary tests showed that the hardware did not have the computational power to generate the pulse frequencies needed for quicker oscillations of the stepper motors, leading to several task overruns.

Hence, the control of the stepper motors was migrated to a dSpace DS2101, while the Arduino board still handled the servo motion. The decision to keep the servo control on the Arduino board was motivated by the block already implemented in the MATLAB Support Package and the Simulink Support Package for Arduino Hardware that reliably controls the servo shaft angle.

Another challenge was that the dSpace and Arduino boards were not connected to the same computer, raising the question of synchronicity between the stepper and servo motors. The solution to this problem was accomplished by running the Simulink project autonomously on the dSpace board using an enabled subsystem that was turned ON/OFF with a signal provided by the Arduino. This signal is crucial for the motion synchronicity but also for the post-processing. The Simulink project implemented in the dSpace runs at $10\,\text{kHz}$, which allows smooth and fast stepper motions with guaranteed stepper-servo synchronization. Figure

4.25 shows the system architecture implemented for the wing motion.

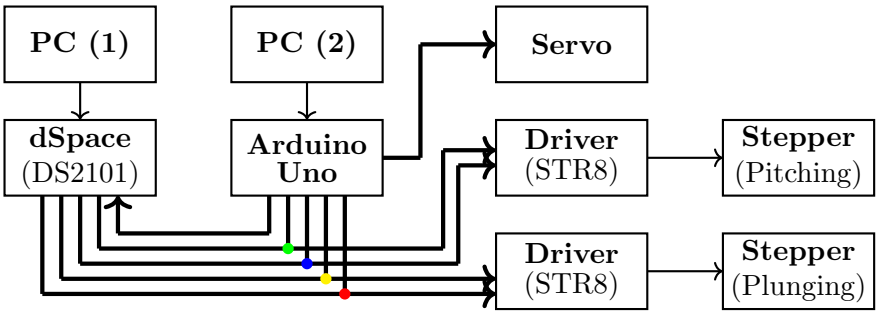

Figure 4.25: Architecture used for wing kinematics.

The two signals entering each driver are the pulse and direction instructions. The signal leaving the dSpace board and entering the Arduino board is used to start the servo motor motion. As one can see, the Arduino Uno can also provide instructions to the STR8 drivers. This is accomplished with an additional Simulink project that is only used when single adjustments (positioning operations) are required.

As in the previous section, wing kinematics tries to follow sinusoidal waveforms. However, the control methodology to achieve the desired kinematics is different from before, where only a trapezoidal motion was possible. For force measurements, the control of the steppers is made by providing the step and direction instructions directly to the STR8 drivers using a pulse-modulated signal (PWM) generated in Simulink. This signal converts the desired wave into a sequence of pulses that follows the desired motion, as shown in Figure 4.26.

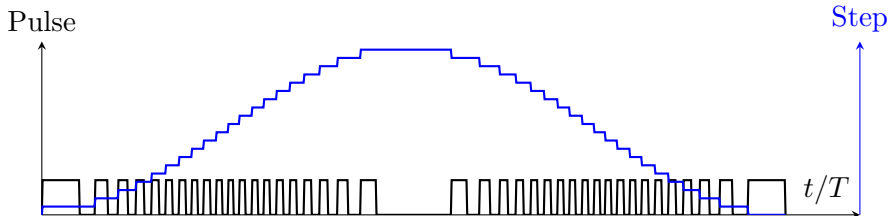

Figure 4.26: PWM strategy for stepper motor control.

The creation of this sequence of pulses is based on equation (4.46)

$$\vec{\omega} = \frac{\mathrm{d}\theta}{\mathrm{d}t} \approx \frac{\theta_{t+1} - \theta_t}{\Delta t} = \frac{1}{\Delta t}(\theta_{t+1} - \theta_t), \tag{4.46}$$

which can be rewritten in the form of a P-controller as

$$u(t) = K_p e(t), \tag{4.47}$$

where K_p is the proportional gain, u is the controller output and $e(t)$ is the controller error. For the present formulation, e is the difference between the current and desired stepper position, while u is the pulse rate required. Since the dSpace board is running at $10\,\mathrm{kHz}$, the controller gain, K_p, is set to the same value to guarantee that the desired kinematics are followed.

To assure a smooth transition between different and time-dependent pulse frequencies, the pulse rate given by u is fed through the function

$$P(t) = \sin\left(2\pi \int_0^t u(\tau)\,\mathrm{d}\tau\right), \tag{4.48}$$

that is later transformed into a square wave as

$$\begin{cases} \text{No pulse} & \text{if } P(t) \leq 0 \\ \text{Send pulse} & \text{if } P(t) > 0 \end{cases}. \tag{4.49}$$

When it comes to the step direction, it is simply selected based on the sign of u.

Returning to equation (4.46), the current stepper positions are computed using software encoders that count the steps and the direction they were taken. However, as these encoders are software-only, the real wing position may differ from the one computed in Simulink. This may happen due to several reasons, such as step skipping, and motor stalling due to the lack of available torque. To mitigate this limitation and guarantee the prescribed kinematics are accurate, physical encoders are implemented to monitor the wing motion, although these are used as verification only.

Regarding kinematics, it is important to mention the operational limits based on the hardware and software used. These are calculated and implemented into code to avoid the request of unattainable kinematics. As mentioned before, the dSpace boards were only able to run at $10\,\mathrm{kHz}$, which means that we were limited at a pulse rate of $5\,\mathrm{kHz}$ (Nyquist frequency). The other variable that affected kinematics was the step size of the motors, which were selected with two requirements in mind: provide relatively fast movements while maintaining motor vibrations in an acceptable range.

Hence, for the plunging mode, a basic angle of 1.8° is selected which when passing through the reduction gearbox and the linear guide, results in a step of $0.1625\,\mathrm{mm}$. This means that the maximum plunging velocity is

$$5000\,\mathrm{Hz} \times 0.000\,162\,5\,\mathrm{m} = 0.8125\,\mathrm{m\,s^{-1}}. \tag{4.50}$$

By bringing in the nondimensional velocity, kh, we see that, aerodynamically, the plunging conditions are limited to

$$kh = \frac{2\pi f c}{U_\infty}\frac{A}{c} = \frac{\max \dot{y}}{U} = \frac{0.8125}{U_\infty}. \tag{4.51}$$

When it comes to the pitching motion, a step angle of $0.028\,125^\circ$ was selected. This resulted in a maximum pitching velocity of

$$5000\,\mathrm{Hz} \times 0.028\,125^\circ = 140.625\,^\circ\,\mathrm{s^{-1}}, \tag{4.52}$$

which when written in a dimensionless form, kA_ψ, results in the aerodynamic limit

$$kA_\psi = \frac{2\pi f c}{U_\infty} A_\psi = \max \dot{A}_\psi \frac{c}{U_\infty} = \frac{140.625c}{U_\infty}. \tag{4.53}$$

It is crucial to mention that the above are software limits and do not take into account the available torque as a function of the pulse rate. As will be seen in Chapter 9, some conditions, in particular plunging conditions, the available torque exceeds the software limit.

4.2.4 Force Measurements

Regarding force measurements, they are conducted using two mini40 force and torque sensors, shown in Figure 4.27.

Figure 4.27: Force and torque sensor Mini40 (ATI Industrial Automation).

The sensors are produced by ATI Industrial Automation and come calibrated in advance by the manufacturer, with all calibration information loaded on the sensor. The ATI mini40 sensor properties are shown in Table 4.1. The uncertainty presented is the maximum amount of error for each axis expressed as a percentage of its full-scale load.

Table 4.1: ATI mini40 sensor characteristics.

Sensing Range					
F_x	F_y	F_z	M_x	M_y	M_z
40 N	40 N	120 N	2 N m	2 N m	2 N m
Resolution					
F_x	F_y	F_z	M_x	M_y	M_z
1/100 N	1/100 N	1/50 N	1/4000 N m	1/4000 N m	1/4000 N m
Measurement Uncertainty					
F_x	F_y	F_z	M_x	M_y	M_z
1.25 %	1.25 %	0.75 %	1.25 %	1.50 %	1.50 %

Each F/T sensor is connected to an Interface Power Supply (Model IFPS-1 by ATI) from which the transducer's six strain gauge outputs are amplified and conditioned so they can be connected directly to the inputs of standard data acquisition cards, which in the present work, is the dSpace DS2004 board. ATI software is provided for Simulink in which we can convert strain gauge data into force and torque data in the host computer in real-time. One aspect to be mentioned is the fact that, although the Simulink project was operating at 10 kHz to achieve the desired kinematics, force data was only measured at 1 kHz, which would otherwise be incredibly expensive computationally.

The sensors are connected to the main axis at the wing's extremities, with the sensor z-axis aligned with the pivot axis of the airfoil, as illustrated in Figure 4.28. Since sensors move with the back part, forces are measured at the ψ-part body axis, with F_a and F_n representing the forces in the chordwise and normal-to-chordwise direction, respectively.

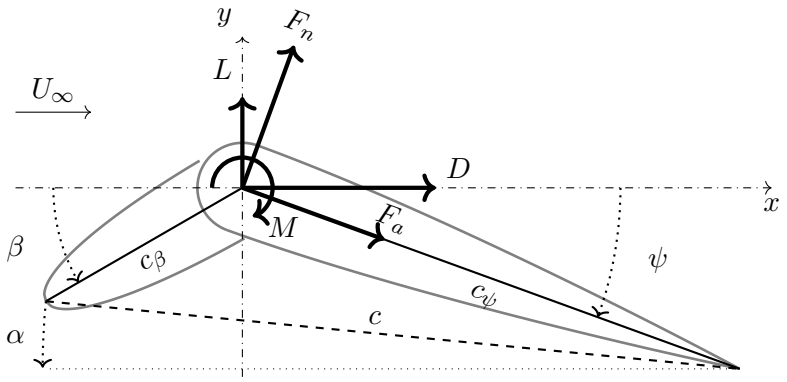

Figure 4.28: NACA0012-IK30 airfoil.

4.2.5 Post-Processing

After acquiring F/T data, all post-processing is made on MATLAB R2021a. The first stage consists of filtering data with a 8^{th}-order Butterworth with a given cutoff frequency. In the results section, the cutoff frequency and its selection are discussed. After signal filtering, force data is converted into drag and lift as

$$D = F_n \sin(\psi) + F_a \cos(\psi), \tag{4.54}$$

and

$$L = F_n \cos(\psi) - F_a \sin(\psi), \tag{4.55}$$

respectively. However, when calculating drag, lift, and moment by using sensor data one should not forget that these measurements include forces due to the assembly (bolt tightness and misaligned axis), inertial forces, and aerodynamic forces. Since drag, lift, and pitching moment are aerodynamic loads, there is a need to remove the assembly and inertial loads. This was accomplished by conducting each test condition with the wind tunnel turned ON and OFF and then, subtracting the first by the latter. With this methodology, we could calculate the aerodynamic loads without the necessity of zeroing the sensors or calculating inertial forces. Furthermore, we minimize other uncertainties that arise from, for instance, zeroing and sensitivity drifts.

Subtracting these two different data sets creates a challenge mainly because data is discrete. Instead of interpolating between data points and then conducting the subtraction, we went right to a spline approximation by using the smoothing spline algorithm implemented in the Filtering and Smoothing Data block of MATLAB. The smoothing spline algorithm uses a

parameter and tries to minimize

$$p\sum_i \left(y_i - s(x_i)\right)^2 + (1-p)\int \left(\frac{\mathrm{d}^2 s}{\mathrm{d}x^2}\right)^2 \mathrm{d}x, \tag{4.56}$$

where (x_i, y_i) are the data points and s is the smoothing spline function. The p parameter takes values between 0 and 1, which results in a least-squares straight-line fit or a cubic spline interpolant, respectively. If no value is assigned to p, MATLAB automatically prescribes a value near $1/(1 + h^3/6)$, where h is the average spacing of the data points. For the present study, p is set at 1, which provides an interpolant, offering a simple solution to manipulate F/T data. Data is further processed by looking into the uncertainties, as shown in section 4.2.7.

4.2.6 Kinematics

Departing from static cases, one of the central objectives of the present work is to investigate the NACA0012-IK30 wing under dynamic conditions, especially plunging and pitching modes. This section shows the methodology regarding the prescribed kinematics for the dynamic cases. Force measurements are carried out at much higher Reynolds numbers than the one used for flow visualization. This means that some parameters, for instance, reduced frequency and nondimensional velocity, are greatly modified. As will be shown in the results chapter, the usage of the NACA0012-IK30 airfoil at much higher Reynolds numbers requires different leading-edge kinematics, which is focused on the mitigation of dynamic stall instead of propulsive enhancement.

4.2.6.1 Plunging & Pitching Ramps

After testing several static conditions with different configurations, the wing is subjected to dynamic cases. In the first stage, to experiment and gather some knowledge about the rig, we use a double sigmoid function (Figure 4.29) to study ramp motion expressed as

$$y \text{ or } A_\psi = \frac{A \text{ or } A_\psi}{1 + e^{-s(t-t_0)}} + \frac{A \text{ or } A_\psi}{1 + e^{s(t-t_1)}} - A \text{ or } A_\psi. \tag{4.57}$$

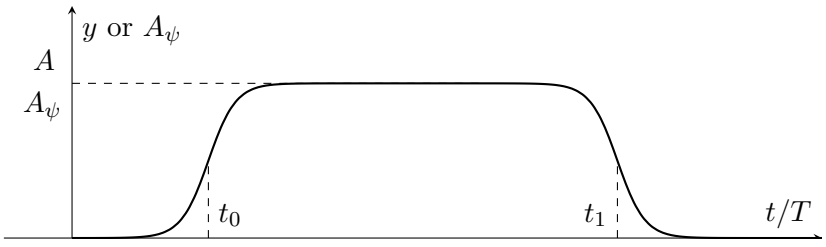

Figure 4.29: Ramps kinematics.

One important parameter in equation (4.57) is the curve steepness, s, which directly dictates the ramp's peak velocity. To control it, we prescribe slightly modified nondimensional veloc-

ities, kh or kA_ψ, defined as

$$kh = \frac{\dot{y}(t_0)}{U_\infty} \text{ or } kA_\psi = \frac{\dot{\psi}(t_0)c}{U_\infty}. \tag{4.58}$$

After selecting the nondimensional velocity, we solve

$$\dot{y} = khU_\infty \text{ or } \dot{\alpha} = kA_\psi U_\infty / c \tag{4.59}$$

iteratively to find the curve steepness, s, that verifies the prescribed condition.

4.2.6.2 Sinusoidal Plunging

The next phase of dynamic tests is comprised of sinusoidal plunging cases. Thus, the kinematics prescribed to the airfoil follow a sinusoidal wave with an imposed ψ. To ease into the prescribed kinematics without starting at maximum velocities, ramp-up, and down phases are added to the motion. This is accomplished by using

$$y(t) = A(t) \sin\left(2\pi \int_0^t f(\tau)\, \mathrm{d}\tau\right), \tag{4.60}$$

where A and f are changed linearly during the ramp-up and down stages, as illustrated in Figure 4.30.

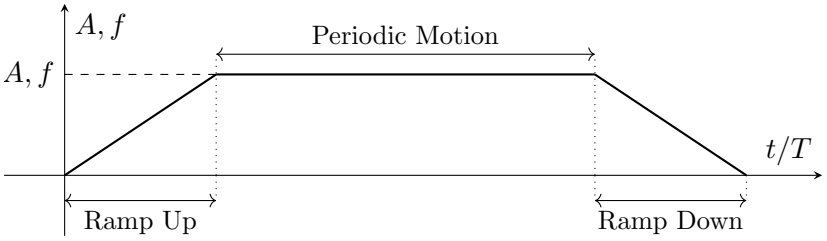

Figure 4.30: Ramp up and down phases of sinusoidal oscillation.

The plunging velocity, $\dot{y}$, is then determined by

$$\dot{y} = \dot{A} \sin\left(2\pi \int_0^t f(\tau)\, \mathrm{d}\tau\right) + 2\pi f(t) A(t) \cos\left(2\pi \int_0^t f(\tau)\, \mathrm{d}\tau\right), \tag{4.61}$$

which is later used for the calculation of the effective angle of attack, α_{eff}.

The same strategy is used for the leading-edge deflection, which follows

$$\beta = \overline{\beta} + A_\beta(t) \sin\left(2\pi \int_0^t f(\tau)\, \mathrm{d}\tau + \phi\right), \tag{4.62}$$

where ϕ is the phase angle between y and β, which throughout the whole study is set to $90°$. This angle is selected to achieve maximum leading edge deflection when the wing experiences maximum plunging velocity. Figure 4.31 shows the graphs of the prescribed motion for the plunging cases.

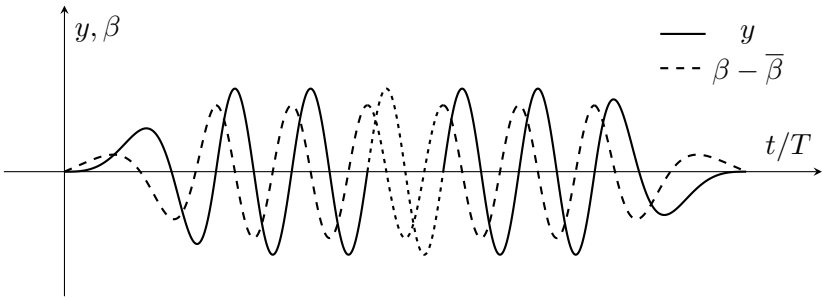

Figure 4.31: Plunging kinematics coupled with leading-edge deflection.

4.2.6.3 Sinusoidal Pitching

At last, after all plunging cases, the wing is tested under several sinusoidal pitching conditions. However, different from the plunging tests, the pitching cases consider two different configurations.

The first pitching layout consists of a fixed ψ with a variable leading-edge angle of attack, β. To accomplish this, the same equation (4.62) used for the plunging cases is applied, here plotted in Figure 4.32.

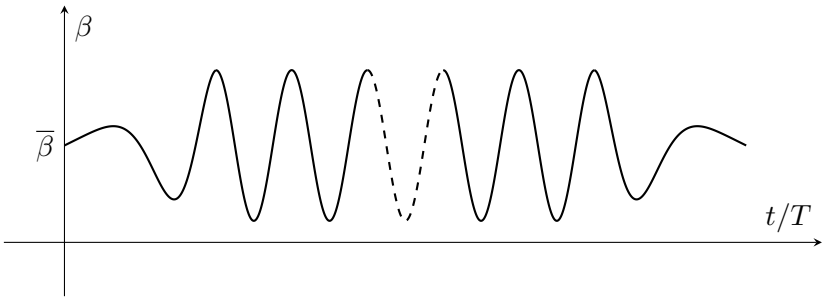

Figure 4.32: Pitching leading edge kinematics.

The second arrangement fixes a leading-edge deflection, Ω, and varies ψ as

$$\psi(t) = \overline{\psi} + A_{\psi}(t) \sin\left(2\pi \int_0^t f(\tau)\, \mathrm{d}\tau\right), \tag{4.63}$$

which follows the same strategy explained before. With this pitching mode, the leading edge angle of attack is simply given by

$$\beta = \psi + \Omega. \tag{4.64}$$

For a quicker understanding, Figure 4.33 illustrates the pitching motion prescribed.

Based on the kinematics prescribed, other important parameters to the wing motion are calculated and implemented during the post-processing stage. It is crucial to mention that the present study is conducted in a dimensionless manner, meaning that all the kinematics prescribed are determined as a function of the governing parameters of the problem, such as

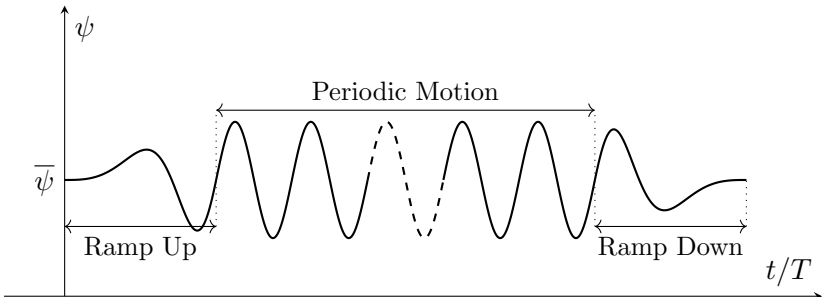

Figure 4.33: Pitching ψ kinematics.

the Reynolds number and nondimensional velocities. This will be made transparent in the results chapter.

4.2.7 Experimental Uncertainties

Also in the post-processing phase, it is relevant to consider the experimental uncertainties that affect measurements and examine how these propagate to other variables. The equations presented in the section can only be used when values are measured. When prescribed, no uncertainty is assumed. Uncertainties are estimated as in the previous section, following what is explained by Taylor [188].

Some of the limitations regarding the experimental facility are the difficulty in aligning the main axis of the wing with the F/T sensors, the possible low flow quality that is common in blower wind tunnels, and the inferior resolution of the servo motor when compared to the steppers used. This can produce slight misalignment in the angle of attack of the leading edge, resulting in small changes in the aerodynamic forces. Furthermore, the incoming flow can create an additional deformation that can slightly change the angle of attack of the leading edge.

The experiments concerning force measurements are conducted in a dimensionless manner, meaning that the governing parameters are prescribed, and only then, flow and kinematics variables are calculated. Considering a Reynolds number, the flow velocity is calculated as

$$Re = \frac{\rho U_\infty c}{\mu} \Rightarrow U_\infty = \frac{Re\mu}{\rho c}, \tag{4.65}$$

with air properties estimated using the ideal gas and Sutherland's laws. Air temperature and pressure are measured with uncertainties $\delta T = 0.1\,°\text{C}$ and $\delta P = 0.1\,\text{hPa}$, respectively.

Since the manometer used measures the equivalent airspeed (EAS), the true airspeed, U, is converted into the equivalent airspeed, U_e, as

$$U_e = U_\infty \sqrt{\frac{\rho}{\rho_0}}, \tag{4.66}$$

where ρ_0 is the air density at sea level in the International Standard Atmosphere (ISA).

Using a power regulator that controls the wind tunnel's fan velocity, we set the equivalent airspeed calculated by equation (4.66). However, oscillations in the flow velocity do happen at the manometer. Variations of up to $5\,\%$ of the desired velocity were deemed acceptable. This leads to an uncertainty in the equivalent airspeed of

$$\delta U_e = \underbrace{0.05 U_\infty}_{\text{Velocity tolerance}} + \underbrace{0.01}_{\text{TIVA Precision}} . \tag{4.67}$$

The equivalent airspeed is then converted to the true airspeed as

$$U_\infty = U_e \sqrt{\frac{\rho_0}{\rho}}, \tag{4.68}$$

which has an uncertainty

$$\delta U_\infty = \sqrt{\left(\sqrt{\frac{\rho_0}{\rho}}\delta U_e\right)^2 + \left(-U_e \frac{\sqrt{\rho_0}}{2\rho^{3/2}}\delta\rho\right)^2}. \tag{4.69}$$

Afterwards, the motion frequency is calculated based on a prescribed reduced frequency as

$$k = \frac{2\pi f c}{U_\infty} \Rightarrow f = \frac{k U_\infty}{2\pi c}, \tag{4.70}$$

with its uncertainty being defined as

$$\delta f = \sqrt{\left(-\frac{k U_\infty}{2\pi c^2}\delta c\right)^2 + \left(\frac{k}{2\pi c}\delta U_\infty\right)^2}. \tag{4.71}$$

The same is made for the plunging amplitude, calculated as

$$h = \frac{A}{c} \Rightarrow A = hc, \tag{4.72}$$

with an uncertainty of

$$\delta A = \sqrt{(h\delta c)^2}, \tag{4.73}$$

with $\delta c = 0.5\,\text{mm}$.

The angle of attack of the airfoil, defined as the angle between the chord line and the incoming flow, is defined as

$$\alpha = \arctan\left(\frac{c_\beta \sin\beta + c_\psi \sin\psi}{c_\beta \cos\beta + c_\psi \cos\psi}\right), \tag{4.74}$$

which has an uncertainty

$$\delta\alpha = \sqrt{\left(\frac{\partial\alpha}{\partial\beta}\delta\beta\right)^2 + \left(\frac{\partial\alpha}{\partial\psi}\delta\psi\right)^2}, \tag{4.75}$$

where $\delta\beta = 1°$ and $\delta\psi = 0.018°$ are the basic angles of the servo and stepper motors, respectively. As the stepper motor has a small basic step angle, we neglect its contribution to $\delta\alpha$. In equation (4.75), the derivatives are expressed as

$$\frac{\partial\alpha}{\partial\beta} = \frac{c_\beta \cos\beta\,(c_\beta\cos\beta + c_\psi\cos\psi) + c_\beta\sin\beta\,(c_\beta\sin\beta + c_\psi\sin\psi)}{(c_\beta\sin\beta + c_\psi\sin\psi)^2 + (c_\beta\cos\beta + c_\psi\cos\psi)^2}, \tag{4.76}$$

and

$$\frac{\partial\alpha}{\partial\psi} = \frac{c_\psi \cos\psi\,(c_\beta\cos\beta + c_\psi\cos\psi) + c_\psi\sin\psi\,(c_\beta\sin\beta + c_\psi\sin\psi)}{(c_\beta\sin\beta + c_\psi\sin\psi)^2 + (c_\beta\cos\beta + c_\psi\cos\psi)^2}. \tag{4.77}$$

In addition to these uncertainties, all motors present an error caused by the approximation of continuous functions (sinusoidal waveforms) by a series of steps. Although this is not a concern for the steppers, due to their high accuracy, the same cannot be regarded for the servo motor. With a precision of $1°$ it introduces an error in β expressed as

$$|\beta - \lfloor\beta\rceil|\,, \tag{4.78}$$

where the $\lfloor x\rceil$ notation represents the rounding to the closest integer. In Figure 4.34, the servo motion is shown together with the desired motion, error, and its uncertainty. The error affects other variables, by propagating itself, for instance, to the angle of attack.

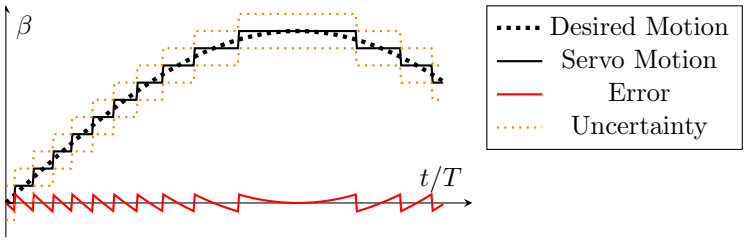

Figure 4.34: Servo motion.

In addition to the angle of attack, the effective angle of attack considers the plunging motion of the airfoil, being calculated as

$$\alpha_{\text{eff}} = \arctan\left(-\frac{\dot{y}}{U_\infty}\right) + \alpha, \tag{4.79}$$

with an uncertainty

$$\delta\alpha_{\text{eff}} = \sqrt{\left(-\sec^2\left(\frac{\dot{y}}{U_\infty}\right)\delta\dot{y}\right)^2 + \left(\frac{\dot{y}}{\dot{y}^2 + U_\infty^2}\delta U_\infty\right)^2 + (\delta\alpha)^2}. \tag{4.80}$$

Like the stepper motor that controls pitching, the plunging motor has a small step size which offers accurate positioning in the y axis. For that reason, we overlook the impact of δy.

It is worth mentioning that although having a relatively low precision, the servo motor has no major challenges. However, when it comes to the pitching mode, the significant difference between the stepper and servo resolutions creates a wobbling effect that renders their simultaneous use unacceptable.

Regarding F/T measurements, we use the data provided by the manufacturer in Table 4.1 to calculate force and moment uncertainties. In the specific case of the current experimental setup, the forces and moments are affected by an uncertainty of $0.5\,\mathrm{N}$ and $0.03\,\mathrm{N\,m}$, respectively.

Forces and moments are then used to calculate the aerodynamic coefficients. Force coefficients (C_D and C_L) are calculated as

$$C_F = \frac{F}{0.5\rho U_\infty^2 S}, \tag{4.81}$$

with an uncertainty

$$\delta C_F = \left\{ \left(\frac{1}{0.5\rho U_\infty^2 S} \delta F \right)^2 + \left(-\frac{F}{0.5\rho^2 U_\infty^2 S} \delta \rho \right)^2 + \right. \\ \left. + \left(-\frac{2F}{0.5\rho U_\infty^3 S} \delta U_\infty \right)^2 + \left(-\frac{F}{0.5\rho U_\infty^2 S^2} \delta S \right)^2 \right\}^{1/2}. \tag{4.82}$$

The moment coefficient calculated as

$$C_M = \frac{M}{0.5\rho U_\infty^2 S c}, \tag{4.83}$$

has an uncertainty given by

$$\delta C_M = \left\{ \left(\frac{1}{0.5\rho U_\infty^2 S c} \delta M \right)^2 + \left(-\frac{M}{0.5\rho^2 U_\infty^2 S c} \delta \rho \right)^2 + \right. \\ \left. + \left(-\frac{2M}{0.5\rho U_\infty^3 S c} \delta U_\infty \right)^2 + \left(-\frac{M}{0.5\rho U_\infty^2 S^2 c} \delta S \right)^2 + \left(-\frac{M}{0.5\rho U_\infty^2 S c^2} \delta c \right)^2 \right\}^{1/2}. \tag{4.84}$$

For each flapping condition, the wing executes ten periods (N_T). Data is then reduced to one period by averaging these ten oscillations as

$$\overline{C_{X_{t/kT}}} = \frac{1}{N_T} \sum_{k=1}^{N_T} C_{X_{t/kT}}, \tag{4.85}$$

where X can be D, L or M, and t/kT is the period fraction of the k oscillation. This averaging

process raises new uncertainties, being estimated as

$$\delta\overline{C_{X_{t/kT}}} = \frac{2\ (\text{RMS of } C_{X_{t/kT}})}{\sqrt{N_T}}. \tag{4.86}$$

4.3 Stall Visualization

To complement the F/T measurements and its analysis, we also provide flow visualization data by tufting the wing's upper surface. Recordings of the movement of the tufts are made with an iPhone 7, using the slow motion camera with 720p (1280×720 pixels) resolution at 240 frames per second. The experimental setup is presented in Figure 4.35 and is used exclusively for static conditions.

Figure 4.35: Experimental setup for flow visualization.

After recording the tufts' motion, videos are fed to a MATLAB code that creates an image illustrating what occurs on the wing surface. This code reads 480 consecutive frames (2 s) from each video and executes the following instructions:

- Convert each frame from RGB to grayscale for easier matrix manipulation.
- Resize each frame to half the size using bicubic interpolation, where the output pixel value is a weighted average of pixels in the nearest 4-by-4 neighborhood.
- Improve image quality using ***imadjust*** and ***imsharpen*** functions.
- Calculate the mean and standard deviation of the processed frames.
- Propose the final image by subtracting the mean by two times the standard deviation, capturing about 95 % of the tufts fluctuations.

This methodology produces an image where we can see the overall fluctuation of the strings, making it easy to identify flow separation, as will be shown in subsection 9.1.

Chapter 5

Numerical Methodology

> *"It is the mark of an instructed mind to rest satisfied with the degree of precision to which the nature of the subject admits and not to seek exactness when only an approximation of the truth is possible."*
>
> *Aristotle*

In this chapter, the numerical methodology regarding CFD simulations will be explained. Governing equations are presented as well as models adjacent to tackle the problem. The mesh generation is described in detail, together with the methods used to numerically solve the problem.

5.1 Governing Equations

It has been established that the equations governing fluid dynamics are the Navier-Stokes equations. These differential equations have several peculiarities, especially when turbulence (randomly moving three-dimensional fluid with high mixing capacity) appears. In the flow where turbulence is present, it is natural to occur eddies (in the most varied length, time, and velocity scales) that numerically offer challenges mainly in the level of computational resources needed to capture the smaller scales.

The resolution of the Navier-Stokes equations that solves all the flow scales is called Direct Numerical Simulation (DNS). It is computationally demanding, especially for high Reynolds numbers, so it becomes challenging with existing technology to study the majority of flows. It is therefore recurrent and sufficient, to resort to the Reynolds-Averaged Simulation (RAS) for most applications, where the focus is dedicated to the mean flow behavior and not its oscillations. The RAS approach is illustrated in Figure 5.1, where a flow property, Φ, is regarded as the sum of its mean, $\overline{\Phi}$, and the fluctuation component, Φ'.

However, that assumption creates a slightly different version of the Navier-Stokes equations. To sum up, the flow field is obtained by solving the continuity and momentum averaged equations simultaneously, which can be written in a Cartesian tensor form as

$$\frac{\partial \rho}{\partial t} + \frac{\partial (\rho u_i)}{\partial x_i} = 0, \tag{5.1}$$

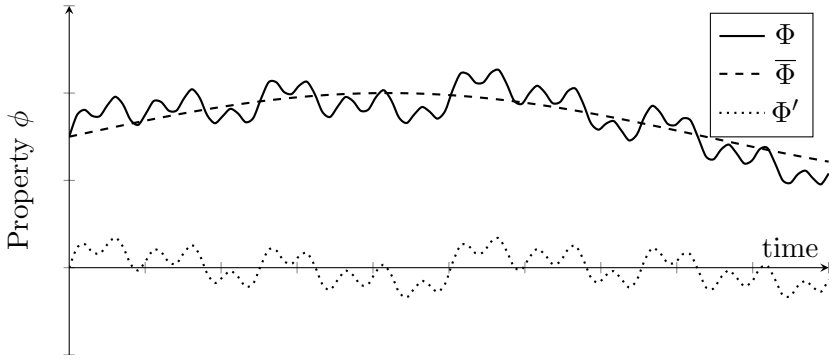

Figure 5.1: Statistical treatment of turbulence.

and

$$\frac{\partial(\rho u_i)}{\partial t} + \frac{\partial(\rho u_i u_j)}{\partial x_j} = -\frac{\partial p}{\partial x_i} + \frac{\partial}{\partial x_j}\left[\mu\left(\frac{\partial u_i}{\partial x_j} + \frac{\partial u_j}{\partial x_i} - \frac{2}{3}\delta_{ij}\frac{\partial u_l}{\partial x_l}\right)\right] + \frac{\partial(-\rho\overline{u_i' u_j'})}{\partial x_j}, \tag{5.2}$$

respectively. Equations are presented as defined in [189]. Some terms will not influence the results presented in this work, for instance, the density temporal derivative and compressibility terms. Furthermore, for notation simplicity, u_i denotes the mean velocity in the x_i direction while u_i' indicates the velocity fluctuation in the same component.

As aforementioned, the mean plus fluctuation premise changes the momentum equation by adding the last term of the right-hand side, called the Reynolds stress tensor. As no other equation is added to solve for the velocity fluctuations, this term is modeled. The modeling of $-\rho\overline{u_i' u_j'}$ recurs to the Boussinesq hypothesis, which relates the turbulent stresses and the mean flow to solve the system of equations, as shown in equation (5.3).

$$-\rho\overline{u_i' u_j'} = \mu_t\left(\frac{\partial u_i}{\partial x_j} + \frac{\partial u_j}{\partial x_i}\right) - \frac{2}{3}\left(\rho k + \mu_t\frac{\partial u_k}{\partial x_k}\right)\delta_{ij} \tag{5.3}$$

Although used to model the Reynolds stress, the Boussinesq hypothesis still contains variables that need to be determined, in this case, the turbulent viscosity, μ_t, and kinetic turbulence energy, k. The calculation of these parameters is the main objective of turbulence models (two-equation models) which offer two differential equations for the transport of the turbulent kinetic energy and its dissipation.

5.2 Turbulence Modelling

Turbulence is commonly solved through RAS (Reynolds Averaged Simulation), which is very reliable for a wide variety of problems while offering a relatively low computational cost. However, this approach does not offer any information regarding turbulent flow structures. For that, DNS (Direct Numerical Simulation) must be used, but its computational require-

ments make it unfeasible for the majority of cases. Another possibility is using LES (Large Eddy Simulation), which models the smallest length scales instead of solving them, making it less computationally expensive than DNS.

In the field of flapping foils, RAS is the most common approach, which focuses on solving the mean flow while modeling the velocity oscillations of the flow field. If we stick to the Boussinesq hypothesis, then determining the turbulent kinetic energy, k, and turbulent viscosity, μ_t, is the main focus of turbulence models.

Flapping foils have been analyzed using these turbulence models, of which the Baldwin-Lomax algebraic turbulence model, the single-equation Spalart-Allmaras model, and the two-equation $k-\omega$ SST model stand out. Their versatility under several problems such as energy extraction [190, 191] and novel kinematics [44, 45] show that these are reliable methods to study the flow field surrounding flapping foils. Other models are also used such as the Reynolds Stress Model (RSM), but typically add unnecessary complexity [13].

In the present work, the turbulence model selected is the Shear-Stress Transport (SST) $k-\omega$ model [192], which is accurate and reliable for a wider class of flows, such as boundary layers under adverse pressure gradients and separated flows. Furthermore, in the cases with lower Reynolds numbers, this model is coupled with the Intermittency Transition model to take into consideration laminar-turbulent transition.

The transport equations for k and ω in SST $k-\omega$ model are

$$\frac{\partial(\rho k)}{\partial t}+\frac{\partial(\rho k u_i)}{\partial x_i}=\frac{\partial}{\partial x_j}\left(\Gamma_k\frac{\partial k}{\partial x_j}\right)+\tilde{G}_k-Y_k+S_k, \tag{5.4}$$

and

$$\frac{\partial(\rho \omega)}{\partial t}+\frac{\partial(\rho \omega u_i)}{\partial x_i}=\frac{\partial}{\partial x_j}\left(\Gamma_\omega\frac{\partial \omega}{\partial x_j}\right)+G_\omega-Y_w+D_\omega+S_\omega, \tag{5.5}$$

where $\tilde{G}_k$ represents the generation of turbulence kinetic energy due to the mean velocity gradients and G_ω is the generation of ω. Γ_k and Γ_ω represent the effective diffusivity of k and ω, respectively. Y_k and Y_ω are the dissipation of k and ω due to turbulence and D_ω is the cross-diffusion term. Finally, the S_k and S_ω are the user-defined source terms.

The effective diffusivities for the SST $k-\omega$ model are defined as

$$\Gamma_k=\mu+\frac{\mu_t}{\sigma_k}, \tag{5.6}$$

and

$$\Gamma_\omega=\mu+\frac{\mu_t}{\sigma_\omega}, \tag{5.7}$$

where σ_k and σ_ω are the turbulent Prandtl numbers for k and ω, respectively. The two parameters are defined as

$$\sigma_k = \frac{1}{F_1/\sigma_{k,1} + (1 - F_1)/\sigma_{k,2}}, \tag{5.8}$$

and

$$\sigma_\omega = \frac{1}{F_1/\sigma_{\omega,1} + (1 - F_1)/\sigma_{\omega,2}}. \tag{5.9}$$

The turbulent viscosity, μ_t, is computed as

$$\mu_t = \frac{\rho k}{\omega} \frac{1}{\max\left[\frac{1}{\alpha^*}, \frac{SF_2}{a_1 \omega}\right]}, \tag{5.10}$$

where S is the strain rate magnitude. The coefficient α^* damps the turbulent viscosity, causing a low-Reynolds-number correction. It is given as

$$\alpha^* = \alpha^*_\infty \left(\frac{\alpha^*_0 + Re_t/R_k}{1 + Re_t/R_k}\right), \tag{5.11}$$

where

$$Re_t = \frac{\rho k}{\mu \omega}, \tag{5.12}$$

$$R_k = 6, \tag{5.13}$$

$$\alpha^*_0 = \frac{\beta_i}{3}, \tag{5.14}$$

and

$$\beta_i = 0.072. \tag{5.15}$$

The blending functions F_1 and F_2 are given by

$$F_1 = \tanh(\Phi_1^4), \tag{5.16}$$

and

$$F_2 = \tanh(\Phi_2^2), \tag{5.17}$$

where

$$\Phi_1 = \min\left[\max\left(\frac{\sqrt{k}}{0.09\omega y}, \frac{500\mu}{\rho y^2 \omega}\right), \frac{4\rho k}{\sigma_{\omega,2} D_\omega^+ y^2}\right], \tag{5.18}$$

$$\Phi_2 = \max\left[2\frac{\sqrt{k}}{0.09\omega y}, \frac{500\mu}{\rho y^2 \omega}\right], \tag{5.19}$$

and

$$D_\omega^+ = \max\left[2\rho\frac{1}{\sigma_{\omega,2}}\frac{1}{\omega}\frac{\partial k}{\partial x_j}\frac{\partial \omega}{\partial x_j}, 10^{-10}\right] \tag{5.20}$$

is the positive portion of the cross-diffusion term and y is the distance to the next surface.

The production of turbulence kinetic energy represented by $\tilde{G}_k$ is defined as

$$\tilde{G}_k = \min(G_k, 10\rho\beta^* k\omega), \tag{5.21}$$

where G_k is defined as in the Realizable $k-\varepsilon$ model.

The production of ω represented by G_ω is given by

$$G_\omega = \frac{\alpha}{\nu_t} G_k, \tag{5.22}$$

with

$$\alpha = \frac{\alpha_\infty}{\alpha^*}\left(\frac{\alpha_0^* + Re_t/R_\omega}{1 + Re_t/R_\omega}\right), \tag{5.23}$$

$$a_\infty = F_1 a_{\infty,1} + (1 - F_1) a_{\infty,2}, \tag{5.24}$$

$$a_{\infty,1} = \frac{\beta_{i,1}}{\beta_\infty^*} - \frac{\kappa^2}{\sigma_{\omega,1}\sqrt{\beta_\infty^*}}, \tag{5.25}$$

$$a_{\infty,2} = \frac{\beta_{i,2}}{\beta_\infty^*} - \frac{\kappa^2}{\sigma_{\omega,2}\sqrt{\beta_\infty^*}}, \tag{5.26}$$

where κ is 0.41.

The dissipation of turbulence kinetic energy, Y_k is defined as

$$Y_k = \rho\beta^* k\omega, \tag{5.27}$$

with

$$\beta^* = \beta_i^*[1 + \zeta^* F(M_t)], \tag{5.28}$$

$$\beta_i^* = \beta_\infty^* \left(\frac{4/15 + (Re_t/R_\beta)^4}{1 + (Re_t/R_\beta)^4} \right), \tag{5.29}$$

$$\zeta^* = 1.5, \tag{5.30}$$

$$R_\beta = 8, \tag{5.31}$$

and

$$\beta_\infty^* = 0.09, \tag{5.32}$$

where $F(M_t)$ is a compressibility function.

The dissipation of ω is defined as

$$Y_\omega = \rho\beta\omega^2, \tag{5.33}$$

where

$$\beta = \beta_i \left[1 - \frac{\beta_i^*}{\beta_i} \zeta^* F(M_t) \right], \tag{5.34}$$

and

$$\beta_i = F_1 \beta_{i,1} + (1 - F_1)\beta_{i,2}. \tag{5.35}$$

The SST $k-\omega$ model is based on both the standard $k-\omega$ model and the standard $k-\varepsilon$ model which leads to the introduction of a cross-diffusion term given by

$$D_\omega = 2(1 - F_1)\rho\sigma_{\omega,2} \frac{1}{\omega} \frac{\partial k}{\partial x_j} \frac{\partial \omega}{\partial x_j}. \tag{5.36}$$

The model constants are present in table 5.1.

As mentioned before, the cases with lower Reynolds numbers ($Re \leq 1 \times 10^5$) are simulated with the SST $k-\omega$ coupled with the Intermittency Transition model. This model is based on the $\gamma - Re_\theta$, though it is Gallilean invariant. This means that it can be used in surfaces moving relative to the coordinate system where the velocity field is computed. The main limitation is that it is unable to predict transition in free shear flows.

Table 5.1: Turbulence model constants for $k-\omega$ SST model.

$\sigma_{k,1}$	1.176
$\sigma_{\omega,1}$	2.0
$\sigma_{k,2}$	1.0
$\sigma_{\omega,2}$	1.168
a_1	0.31
$\beta_{i,1}$	0.075
$\beta_{i,2}$	0.0828

The transport equation for intermittency, γ, is

$$\frac{\partial(\rho\gamma)}{\partial t} + \frac{\partial(\rho U_j\gamma)}{\partial x_j} = P_\gamma - E_\gamma + \frac{\partial}{\partial x_j}\left[\left(\mu + \frac{\mu_t}{\sigma_\gamma}\right)\frac{\partial\gamma}{\partial x_j}\right], \tag{5.37}$$

where P_γ and E_γ are the transition and destruction sources, respectively. The transition source term is defined as

$$P_\gamma = F_{\text{length}}\rho S\gamma(1-\gamma)F_{\text{onset}}, \tag{5.38}$$

with $F_{\text{length}} = 100$. The destruction/relaminarization source is defined as

$$E_\gamma = c_{a2}\rho\Omega\gamma F_{\text{turb}}(c_{e2}\gamma - 1), \tag{5.39}$$

where Ω is the magnitude of the absolute vorticity rate, $c_{a2} = 0.06$, $c_{e2} = 50$ and $\Omega\gamma = 1.0$. The transition onset is controlled by the following functions

$$F_{\text{onset 1}} = \frac{Re_V}{2.2Re_{\theta c}}, \tag{5.40}$$

$$F_{\text{onset 2}} = \min(F_{\text{onset 1}}, 2.0), \tag{5.41}$$

$$F_{\text{onset 3}} = \max\left(1 - \left(\frac{R_T}{3.5}\right)^3, 0\right), \tag{5.42}$$

$$F_{\text{onset}} = \max(F_{\text{onset 2}} - F_{\text{onset 3}}, 0), \tag{5.43}$$

$$F_{\text{turb}} = \exp(-(R_T/2)^4), \tag{5.44}$$

$$R_T = \frac{\rho k}{\mu\omega}, \tag{5.45}$$

$$Re_V = \frac{\rho d_w^2 s}{\mu}, \tag{5.46}$$

and

$$Re_{\theta c} = f(Tu_L, \lambda_{\theta L}), \tag{5.47}$$

where d_w is the wall distance and $Re_{\theta c}$ is a correlation that triggers the transition model. It is defined as

$$Re_{\theta c}(Tu_L, \lambda_{\theta L}) = C_{TU1} + C_{TU2} \exp\left[-C_{TU3} Tu_L F_{PG}(\lambda_{\theta L})\right], \tag{5.48}$$

where Tu_L and $\lambda_{\theta L}$ are the freestream turbulent intensity and the pressure gradient parameters, respectively. These variables are calculated as

$$Tu_L = \min\left(100\frac{\sqrt{2k/3}}{\omega d_w}, 100\right), \tag{5.49}$$

and

$$\lambda_{\theta L} = -0.1111\frac{dV}{dy}\frac{d_w^2}{\nu} + 0.1875 \tag{5.50}$$

$$\lambda_{\theta L} = \min(\max(\lambda_{\theta L}, -10.0), 10.0). \tag{5.51}$$

The function F_{PG}, expressed as

$$F_{PG}(\lambda_\theta) = \begin{cases} \min(1 + C_{PG1}\lambda_\theta, C_{PG1}^{\lim}) & \text{if } \lambda_\theta \geq 0 \\ \min(1 + C_{PG2}\lambda_\theta + C_{PG3}\min(\lambda_\theta + 1.0, 0), C_{PG2}^{\lim}) & \text{if } \lambda_\theta < 0 \end{cases}, \tag{5.52}$$

is used to account for the influence of the pressure gradient on transition. The model constants are left at their default values.

The transition model is coupled with the SST $k-\omega$ by slightly modifying the production and destruction terms in the k equation in a similar way that the $\gamma - Re_\theta$ model does [189].

5.3 Law of the Wall & Wall Treatment

The law of the wall proposed by von Kármán, is one of the cornerstones of turbulence modeling, giving a straightforward yet very useful insight into how the mean velocity changes with the distance normal to a wall in a turbulent flow. On the same law, some regions of the flow closest to the wall are identified, which present different properties and phenomena. These are the viscous sublayer, the buffer sublayer, and the Log-Law region.

When using CFD to solve the turbulent flow close to the wall, two approaches may be considered: the Wall Function Approach or a Near-Wall Model Approach.

The first approach, instead of resolving the boundary layer, uses functions based on empirical conditions that bridge the inner region between the wall and the turbulence fully developed region, thus reducing significantly the mesh size. Although less computationally expensive, these relations are only valid under some conditions, and when the mesh and model requirements are correctly applied. A Near-Wall Model Approach, on the other hand, leads to a larger mesh number but typically performs better under certain conditions such as flow separation.

The characterization of the different layers of the turbulent boundary layer is mainly conducted by two dimensionless parameters, y^+ and u^+, which are defined as

$$y^+ = \frac{yu_\tau}{\nu}, \tag{5.53}$$

and

$$u^+ = \frac{u}{u_\tau}, \tag{5.54}$$

respectively. The friction velocity u_τ is calculated as

$$u_\tau = \sqrt{\frac{\tau_w}{\rho}}. \tag{5.55}$$

From experimental measurements, the lower layer of the turbulent boundary layer ($y^+ < 5$) was seen to behave as

$$u^+ = y^+, \tag{5.56}$$

while the upper layer ($30 < y^+ < 300$) follows the law expressed as

$$u^+ = \frac{1}{\kappa} \ln y^+ + C, \tag{5.57}$$

with κ and C being 0.41 and 5.0, respectively.

In Figure 5.2, a graph of the different layers of the turbulent boundary layer is presented.

When using the Wall Function Approach, the first mesh cell must be within the $30 < y^+ < 300$ range to guarantee the validity of results, while for a Near-Wall Model Approach, a $y^+ \approx 1$ is highly recommended (values up to 5 are acceptable), which means that the first cell must be within the viscous sublayer of the turbulent boundary layer. The $k-\omega$ SST turbulence model, used in this work uses a Near-Wall Model Approach which can give a superior performance concerning force calculation for flows where separation is expected.

Solving the transport equations for k and ω requires some type of treatment concerning boundary conditions, especially walls. The turbulent kinetic energy at the wall is, as in $k-\varepsilon$

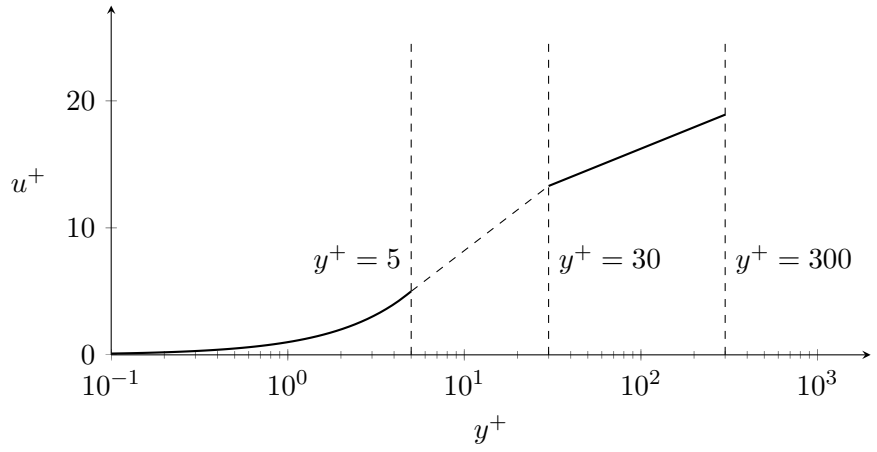

Figure 5.2: Law of the wall.

models where enhanced wall treatments are used, set to zero

$$k_w = 0. \tag{5.58}$$

Regarding the specific turbulence dissipation rate, its value at the wall is prescribed as

$$\omega_w = \frac{\rho(u_\tau)^2}{\mu}\omega^+. \tag{5.59}$$

The parameter ω^+ is calculated based on the region of the turbulent boundary layer where the wall cell is located. Solutions obtained analytically were given for the laminar sublayer

$$\omega^+ = \min\left(\omega_w^+, \frac{6}{\beta_i(y^+)^2}\right), \tag{5.60}$$

and the logarithmic region

$$\omega^+ = \frac{1}{\sqrt{\beta_\infty^*}}\frac{du^+}{dy^+}. \tag{5.61}$$

Based on this formulation, the wall treatment defined for the ω equation can effectively switch between the viscous sublayer formulation to the wall function, depending on the used mesh.

5.4 Computational Domain & Mesh Design

The numerical methodology starts by defining our problem and modeling it so it can be solved using computational fluid dynamics techniques. In the present work, we study the aerodynamic and propulsive phenomena surrounding a geometry derived from the NACA0012 airfoil. Using the mathematical expression of the NACA 4-digit series, the exact NACA0012

airfoil definition is given by

$$y = \pm 0.6 \left(0.2969\sqrt{x} - 0.1260x - 0.3516x^2 + 0.2843x^3 - 0.1015x^4\right). \tag{5.62}$$

However, the thickness at the trailing edge is not zero, which typically adds unnecessary mesh complexity. Commonly, a slightly modified expression is used to obtain a sharp leading edge [193]. This modified definition is expressed as

$$y = \pm 0.594689181(0.298222773\sqrt{x} - 0.127125232x - \\ - 0.357907906x^2 + 0.291984971x^3 - 0.105174606x^4). \tag{5.63}$$

5.4.1 Simulation with $Re \leq 1 \times 10^5$

For the simulations conducted at the lower Reynolds number, where the propulsive capabilities of the NACA0012-IK30 airfoil are explored, the computational domain consists of four parts: the NACA0012-IK30 airfoil (β and ψ parts), the inlet, the outlet, and the interior, all illustrated in Figure 5.3. At the inlet, the desired velocity is prescribed, together with the information needed for the turbulence model, for instance, the turbulence intensity, that is kept at $5\,\%$. The outlet is a pressure outlet, where it is assumed that no pressure gradients are present, while both airfoil parts act as walls, where the no-slip condition is applied. The inlet and outlet are placed at $20c$ from the IK30, where its placement does not influence the unsteady aerodynamics of the flapping airfoil.

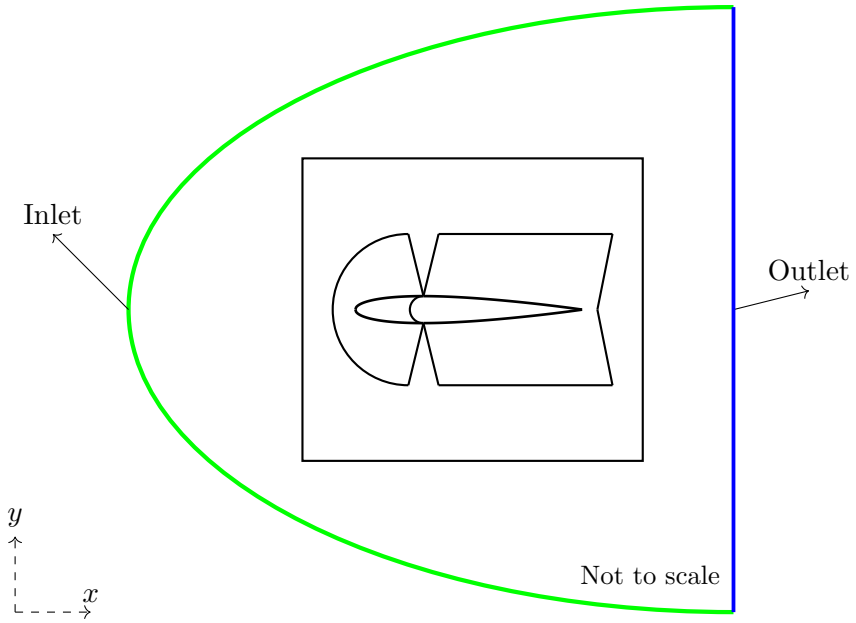

Figure 5.3: 2D computational domain.

Solving the NACA0012-IK30 numerically, presents several challenges regarding the design process of the mesh due to the relative motion between the front and back parts. Hence, studying oscillating airfoils requires some sort of mesh that can account for the airfoil motion.

Often a dynamic mesh is used where mesh elements deform as if they were interconnected by springs.

Moreover, to ensure mesh quality does not degrade after consecutive deformations, remeshing techniques are implemented which use some mesh indicators such as orthogonality to ensure that the mesh parameters stay within certain prescribed boundaries. This constant dynamic deformation and required reconstruction usually makes this approach error-prone and computationally expensive.

A good alternative is the use of an overset mesh in which multiple disconnected grids are created to discretize the computational domain. One of these grids is a background mesh while the others are called the component meshes. When changing the time step there is a comparison between the different grids to determine which points are out of the flow domain and to access the grid-to-grid connectivity.

The present work uses an overset mesh, where two component meshes and one background mesh are designed. The CAD file used for the experimental phase is also used to define the geometry being solved numerically. Thus, geometries are defined in CATIA V5R20 while the mesh is obtained using ANSYS Meshing. In Figure 5.4, the component meshes of both the frontal and back parts are shown.

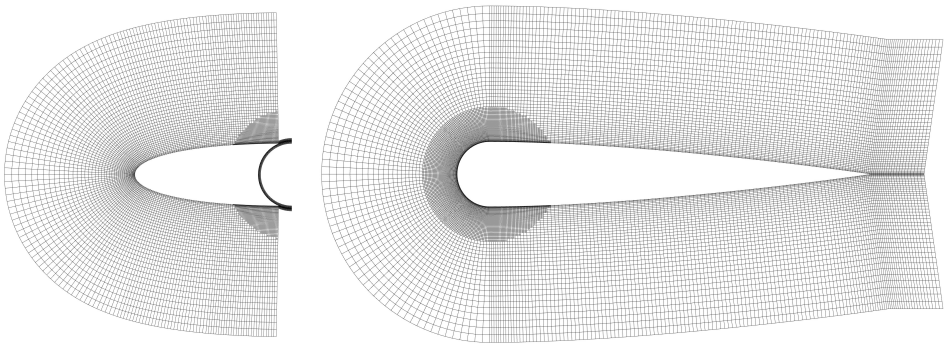

Figure 5.4: Components meshes of the β part (left) and psi part (right).

The background mesh is illustrated in Figure 5.5 which is comprised of an unstructured outer zone with triangular elements and an inner zone, where a structured mesh with rectangular elements is used.

5.4.2 Simulation with $Re > 1 \times 10^5$

For the computations carried out at a higher Reynolds number, the same approach was employed, although in a 3D geometry. This is because force experiments cannot be approximated aerodynamically with a 2D model.

Similar to the previous subsection, the computational domain has the NACA0012-IK30 wing (β and ψ parts) acting as walls, one pressure outlet, and for this computational model, two inlets: one velocity-prescribed inlet and a pressure inlet. Similar boundary conditions are

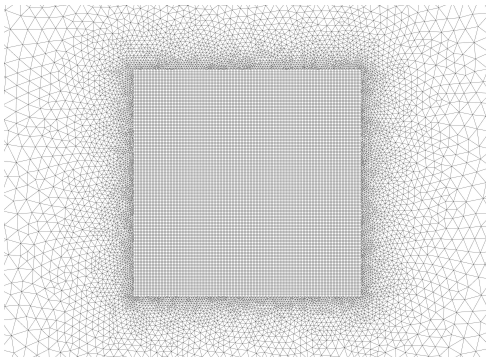

Figure 5.5: Background mesh.

applied in this computational domain, where the velocity is prescribed at the velocity inlet, considering the same standard turbulence intensity of $5\,\%$, being the same for the pressure inlet, where the inlet operation pressure is known but the flow velocity is not. The outlet is still a pressure outlet, where pressure gradients are assumed negligible while both β and ψ parts maintain the no-slip condition.

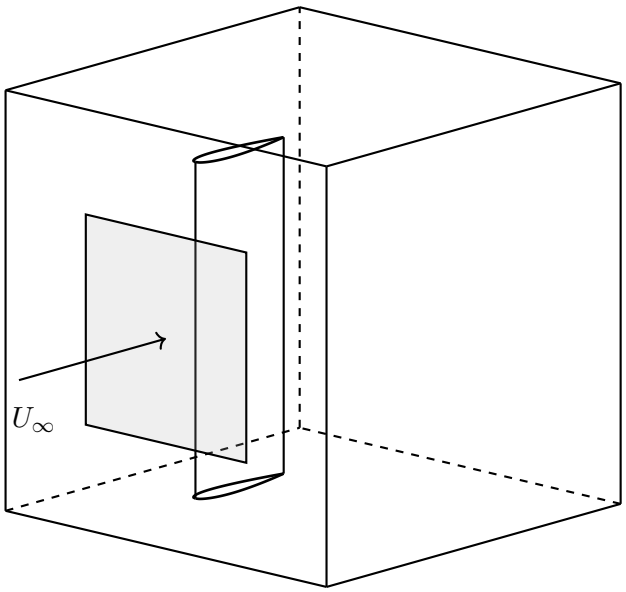

Figure 5.6: 3D computational domain.

In Figure 5.7, all meshes are presented, comprised of the background mesh, a refined zone mesh which is placed around the around for a better resolution of the area, and the meshes of the β and ψ parts.

5.5 Spatial Discretization

Solving partial differential equations numerically implies the necessity of discretization methods that convert continuous into discrete equations. The equations which govern the flow field are the continuity and Navier-Stokes equations, which are examples of a convection–diffusion equation.

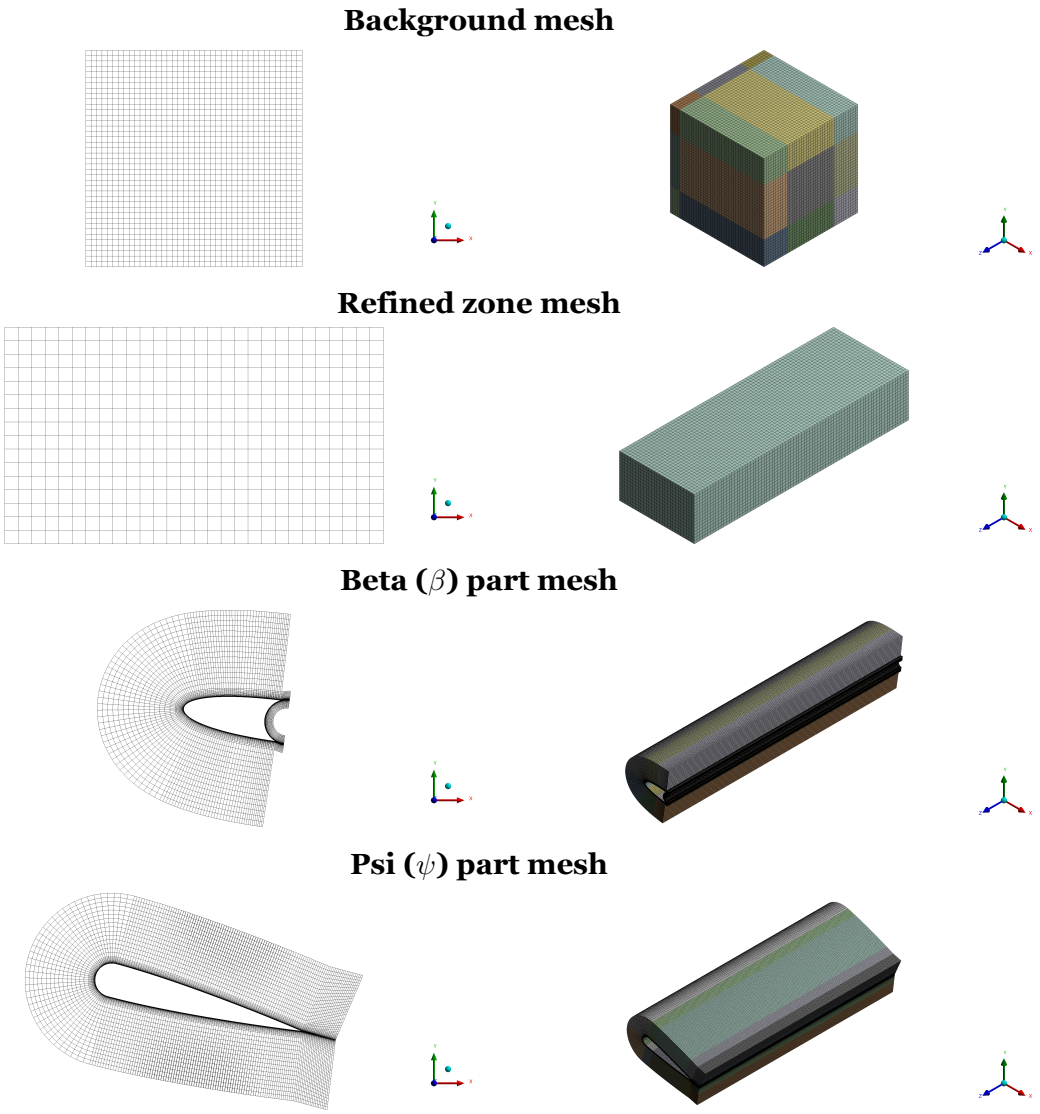

Figure 5.7: Background and component meshes used for simulations carried at $Re \geq 1 \times 10^5$.

The convection-diffusion equation that governs the transport of a property, ϕ, can be expressed as

$$\frac{\partial \rho\phi}{\partial t} + \nabla \cdot (\rho\phi\upsilon) = \nabla \cdot (\Gamma \nabla\phi) + S_\phi, \tag{5.64}$$

where ρ is the density, Γ is the diffusion coefficient, $\nabla \cdot (\rho\phi\upsilon)$ is the net rate of flow of ϕ out of fluid element, $\nabla \cdot (\Gamma\nabla\phi)$ is the rate of increase of ϕ due to diffusion , S_ϕ is the rate of increase of ϕ due to sources and $\frac{\partial \rho\phi}{\partial t}$ is the rate of increase of ϕ of fluid elements.

This equation can be discretized using several methods which stand out, the finite difference method (FDM), the finite element method (FEM) or the finite volume method (FVM). As in the vast majority of CFD software, ANSYS Fluent uses the FVM to solve the Navier-Stokes equations, where the equations are partitioned into small volumes containing each node point of the mesh.

Integrating equation (5.64) on time and space, we obtain

$$\int_t^{t+\Delta t} \iiint_V \frac{\partial \rho\phi}{\partial t} dV dt + \int_t^{t+\Delta t} \iiint_V \nabla \cdot (\rho\phi\upsilon)\, dV dt = \int_t^{t+\Delta t} \iiint_V \nabla \cdot (\Gamma \nabla\phi)\, dV dt + + \int_t^{t+\Delta t} \iiint_V S_\phi dV dt, \quad (5.65)$$

that can be simplified to

$$\int_t^{t+\Delta t} \iiint_V \frac{\partial \rho\phi}{\partial t} dV dt + \int_t^{t+\Delta t} \oiint_S (\rho\phi\upsilon) \cdot \vec{n}\, dS dt = \int_t^{t+\Delta t} \oiint_S (\Gamma \nabla\phi) \cdot \vec{n}\, dS dt + + \int_t^{t+\Delta t} \iiint_V S_\phi dV dt, \quad (5.66)$$

using the divergence theorem. The discretization of this equation on a given control volume results in

$$V \int_t^{t+\Delta t} \frac{\partial \rho\phi}{\partial t} dt + \sum_f^{N_{\text{faces}}} \rho_f \vec{v}_f \phi_f \cdot \vec{A}_f = \sum_f^{N_{\text{faces}}} \Gamma_\phi \nabla\phi_f \cdot \vec{A}_f + S_\phi V. \quad (5.67)$$

By definition, when resolving the discretized equations, values of scalars are available at the center of the cells but the convective term

$$\oiint_S (\rho\phi\upsilon) \cdot \vec{n}\, dS \approx \sum_f^{N_{\text{faces}}} \rho_f \vec{v}_f \phi_f \cdot \vec{A}_f, \quad (5.68)$$

requires special attention since the face values are needed to compute fluxes and with that, values must be interpolated from the center of the neighboring cells. Diffusion terms do not demand any face data interpolation, being central-differenced with guaranteed second-order accuracy. Hence, interpolation schemes for the convective terms must be considered.

In summary, spatial discretization is achieved with two different methods: the diffusion terms are central-differenced and are always second-order accurate while, for the present work, the convective terms are discretized using the second-order upwind. The latter method is more of an interpolation method to determine the values at the cells' faces. Values at the faces are then calculated as

$$\phi_f = \phi + \nabla\phi \cdot \vec{r}. \quad (5.69)$$

Since this is a second-order upwind scheme, the two upstream cells are used, as illustrated in Figure 5.8.

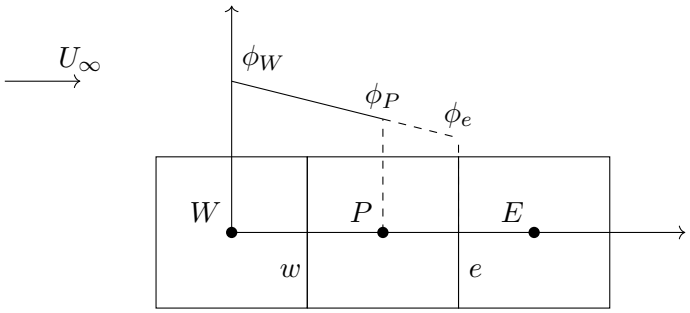

Figure 5.8: Second-Order Upwind Scheme determining ϕ_e.

5.6 Temporal Discretization

The Navier-Stokes equations when solved to obtain solutions of unsteady-state cases, need to be discretized not only spatially but also temporally. To initiate the numerical processes, one should know the time evolution of a generic variable, ϕ, typically given by

$$\frac{\partial \phi}{\partial t} = F(\phi). \tag{5.70}$$

To evaluate $F(\phi)$ at a future time step, explicit or implicit time integration methods can be used. Focusing on the latter, the function evaluation may be obtained by

$$\frac{\phi^{t+1} - \phi^t}{\Delta t} = F(\phi^{t+1}), \tag{5.71}$$

which can be rewritten as

$$\phi^{t+1} = \phi^t + \Delta t F(\phi^{t+1}). \tag{5.72}$$

While the explicit methods evaluate $F(\phi)$ recurring to information gathered on the previous time step, the implicit formulation uses the property ϕ at the current time step as the argument of F, which inevitably requires a recursive process to be implemented. The use of implicit time integration methods gives a huge advantage when compared to implicit methods since they are nearly unconditionally stable while executing much bigger time steps. However, stability should not be mistaken for accuracy, since in some problems, where specific time scales must be resolved, using larger time steps would naturally deliver less accurate results.

5.7 Pressure-Velocity Coupling

The Pressure-Velocity Coupling algorithms are based on an iterative search and interlace of velocity vector and pressure fields that combined must satisfy both the continuity and momentum equations. Various methods stand out: SIMPLE, SIMPLER, SIMPLEC, and PISO, which use the pressure-based segregated algorithm, and the Coupled algorithm, which uses

the pressure-based coupled solver.

In this work, the Coupled algorithm is selected due to its robustness and superior performance over segregated algorithms. This is particularly noticeable for transient flows, where poor mesh quality or large time steps are used. By solving the momentum and pressure-based continuity equations together, the coupled algorithm improves convergence speed, although being more computationally expensive due to its implicit formulation.

In simpler terms, the Coupled algorithm considers that the pressure gradient for component k is given by

$$\sum_f p_f A_k = -\sum_j a^{u_k p} p_j, \tag{5.73}$$

where $a^{u_k p}$ is the coefficient derived from the Gauss divergence theorem and the coefficients of the pressure interpolation scheme. For the present work, the second-order scheme is used as the interpolation scheme, which reconstructs the face pressure in the manner employed for the second-order accurate convection terms.

Taking this formulation and simplifying the governing equations mathematically, we can solve the momentum and pressure-based continuity together in a single overall system of equations from where the pressure and velocity corrections can be obtained [189].

5.8 Convergence and Convergence Rate

One major part of the numerical process is the convergence of the solution, which provides some guarantee that the solution is reliable. In the present work, the default convergence criterion in ANSYS FLUENT is used, where a scaled residual for a property ϕ is defined as

$$R^{\phi} = \frac{\sum_{\text{cells } P} \left| \sum_{\text{nb}} a_{\text{nb}} \phi_{\text{nb}} + b - a_P \phi_P \right|}{\sum_{\text{cells } P} |a_P \phi_P|}, \tag{5.74}$$

and must decrease below 10^{-3}. Likewise, the residual of the continuity equation, expressed by

$$R^{c} = \sum_{\text{cells } P} \left| \text{rate of mass creation in cell P} \right|, \tag{5.75}$$

is scaled by the largest absolute value of the residual in the first five iterations.

As it is not recommended to rely solely on residuals, to verify convergence, values of drag, lift, and moment coefficients are recorded. Thus, a converged solution is assumed, when all residuals are kept below 10^{-3}, and the aerodynamic coefficients do not change by more than 0.01.

Something that should be also taken into account is the rate of convergence, which can be excruciatingly long. One way to tune the convergence rate of the numerical solution is to modify the under-relaxation factors. As recommended by ANSYS FLUENT, one should consider first the default under-relaxation factors, but if residuals increase after the first five iterations or have an irregular behavior, the under-relaxation factors should be reduced.

5.9 Solution Initialization & Kinematics

The solution initialization concerns the initial flow field from which simulations start. In the present study, the standard initialization feature is used, where all flow field variables are equalized to their respective values at the inlet.

Furthermore, as we are conducting transient simulations, special attention is given to the kinematics, in particular to the first oscillation of the airfoil. Since the airfoil is positioned at the center of the domain, it would start moving with the maximum plunging velocity, which affects initial convergence and possibly delays the achievement of a periodic solution. For that reason, the first oscillation is altered so that the airfoil starts its oscillation cycles from rest. The same logic is applied to the pitching motion of the leading edge, as illustrated in Figure 5.9. After the initialization, the airfoil follows the same kinematics defined for the flow visualization study, shown in equation (4.21).

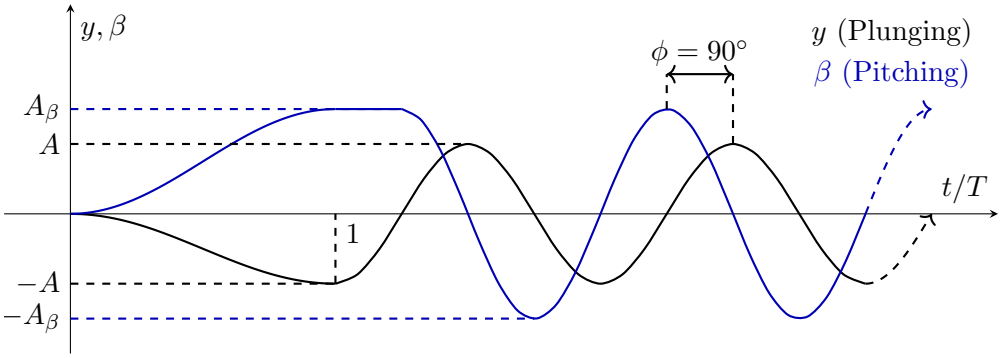

Figure 5.9: Solution initialization.

5.10 Results and Data Processing

During the preparation of the numerical setup, several variables are selected to be extracted and processed. These are the

- Drag coefficient of both parts
- Lift coefficient of both parts
- Moment coefficient (at the pivot) of both parts
- Viscous drag force of both parts

- Viscous lift force of both parts

With these variables and the prescribed kinematics, we calculate the:

- Drag coefficient

$$C_d = C_d^\beta + C_d^\psi \tag{5.76}$$

- Lift coefficient

$$C_l = C_l^\beta + C_l^\psi \tag{5.77}$$

- Moment coefficient (at the pivot point)

$$C_m = C_m^\beta + C_m^\psi \tag{5.78}$$

- Viscous drag coefficient

$$C_{d_f} = C_{d_f}^\beta + C_{d_f}^\psi = \frac{D_f^\beta + D_f^\psi}{\frac{1}{2}\rho U_\infty^2 S} \tag{5.79}$$

- Pressure drag coefficient

$$C_{d_p} = C_d - C_{d_f} \tag{5.80}$$

- Viscous lift coefficient

$$C_{l_f} = C_{l_f}^\beta + C_{l_f}^\psi = \frac{L_f^\beta + L_f^\psi}{\frac{1}{2}\rho U_\infty^2 S} \tag{5.81}$$

- Pressure lift coefficient

$$C_{l_p} = C_l - C_{l_f} \tag{5.82}$$

- Propulsive power coefficient

$$C_{P_P} = C_t = -C_d \tag{5.83}$$

- Required plunging power coefficient

$$C_{P_R^{\dot{y}}} = -\left(C_l^{\beta}\frac{\dot{y}}{U_\infty} + C_l^{\psi}\frac{\dot{y}}{U_\infty}\right) \tag{5.84}$$

- Required pitching power coefficient

$$C_{P_R^{\dot{\alpha}}} = -\left(C_m^{\beta}\frac{\dot{\beta}c}{U_\infty} + C_m^{\psi}\frac{\dot{\psi}c}{U_\infty}\right) \tag{5.85}$$

- Required power coefficient

$$C_{P_R} = C_{P_R^{\dot{y}}} + C_{P_R^{\dot{\alpha}}} \tag{5.86}$$

- Propulsive Efficiency

$$\eta = \frac{\overline{C_{P_P}}}{\overline{C_{P_R}}} \tag{5.87}$$

The mean values of the propulsive coefficients C_{P_P} and C_{P_R} must only be calculated when a periodic solution is achieved. Achieving the periodic solution for a certain flapping condition depends on the condition itself, as faster oscillating cases tend to need more periods to reach it. In the present work, we calculate

$$\frac{\overline{C_{P_P}}^{lT} - \overline{C_{P_P}}^{lT-1}}{\overline{C_{P_P}}^{lT-1}} \text{ and } \frac{\overline{C_{P_R}}^{lT} - \overline{C_{P_R}}^{lT-1}}{\overline{C_{P_R}}^{lT-1}} \tag{5.88}$$

where lT and $lT-1$ represent the mean coefficients calculated on the last and penultimate cycles, respectively. If the relative percentage difference between these two values is less than $1\,\%$ we assume that a periodic solution was reached.

Chapter 6

Unsteady Panel Method

> *"What is mathematics? It is only a systematic effort of solving puzzles posed by nature."*
>
> *Shakuntala Devi*

In this chapter, the extension of the Hess-Smith Panel Method (HSPM) to unsteady flows used by Teng [30] is presented. The objective of this chapter is to revive an old method used in the first numerical studies of oscillating airfoils, present its methodology, and provide the scientific community with an implementation of the method in a modern programming language.

6.1 Methodology Description

The extension of the Hess-Smith Panel Method proposed by Teng [30], as in the steady case formulation, assumes that the airfoil surface is discretized into several panels represented by a singularity distribution of source strength q_j at each panel ($j = 1, 2, ..., N$) and a vorticity τ over the airfoil surface, varying both in time. Hence, the subscript k is used to indicate the current time-step t_k ($k = 1, 2, ...$), at which the singularity distribution of source strength is $(q_j)_k$ and vorticity is τ_k.

In unsteady flows, according to Helmholtz and Kelvin's circulation theorems, the total circulation in the flow field must remain constant. That means that when there is a change in circulation Γ on the airfoil surface, there must be an equal and opposite change in the wake vorticity, which can be obtained as a vortex-shedding process at the trailing edge of the airfoil.

So, at each time step, to model such vortex shedding process, an additional panel with length, Δ_k, and inclination to the x-axis, Θ_k, is attached to the trailing edge with a uniform vorticity distribution, $(\tau_w)_k$, as shown in Figure 6.1.

With this extra panel at the trailing edge, to verify the Helmholtz and Kelvin theorems, equation (6.1) should be applied.

$$\Gamma_k + \Delta_k(\tau_w)_k = \Gamma_{k-1}, \tag{6.1}$$

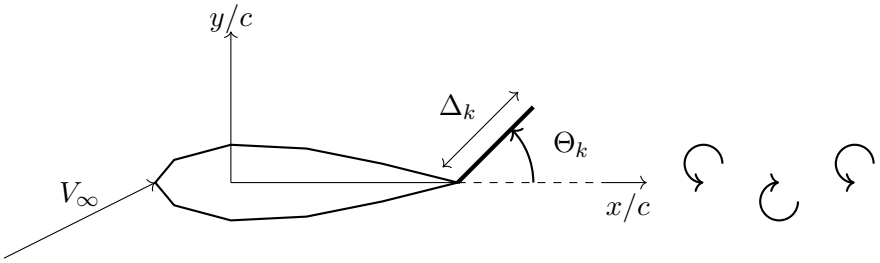

Figure 6.1: Unsteady potential flow formulation (Airfoil-Fixed Frame).

which may be written as

$$\Delta_k(\tau_w)_k = \Gamma_{k-1} - \Gamma_k = \ell(\tau_{k-1} - \tau_k), \tag{6.2}$$

where ℓ is the airfoil perimeter.

Regarding the length and orientation of the extra panel, the assumptions of Basu and Hancock [194] are used. These hypotheses state that

• The additional vorticity panel has the direction of the local resultant velocity at the panel midpoint.

$$\tan\Theta_k = \frac{(v_w)_k}{(u_w)_k}. \tag{6.3}$$

• The length of the additional panel depends on the velocity at the panel midpoint and the time step size used.

$$\Delta_k = (t_k - t_{k-1})\sqrt{(u_w)_k^2 + (v_w)_k^2}. \tag{6.4}$$

After finding the trailing edge panel characteristics, it is shed to the wake and convected as a concentrated free vortex by the flow field with circulation $\Delta_k(\tau_w)_k$.

6.1.1 Flow Tangency and Kutta Conditions

Additionally to the conservation of the flow field circulation, one should also impose the boundary condition where there is no permeability at the wall, where

$$[(V^n)_i]_k = 0 \qquad i = 1, 2, ..., N. \tag{6.5}$$

Moreover, there is the need to impose the Kutta condition, but unlike the steady case, the rate of change of potential at the trailing edge should now be included, which is linked to the

total circulation rate of change as

$$\left[(V^t)_1\right]_k^2 - \left[(V^t)_N\right]_k^2 = 2\left[\frac{\partial(\phi_N - \phi_1)}{\partial t}\right]_k = 2\left(\frac{\partial \Gamma}{\partial t}\right)_k, \tag{6.6}$$

where a backward finite difference is used to approximate the rate of change of total circulation as

$$\left[(V^t)_1\right]_k^2 - \left[(V^t)_N\right]_k^2 = 2\frac{\Gamma_k - \Gamma_{k-1}}{t_k - t_{k-1}} = 2\ell\frac{\tau_k - \tau_{k-1}}{t_k - t_{k-1}}. \tag{6.7}$$

6.1.2 Influence Coefficients

In this subsection, the influence coefficients are presented. These are matrices or column vectors that contain geometric data of the various elements that are being solved in the flow field. These coefficients are denoted as

$$\chi_{pq}^{c}, \tag{6.8}$$

where χ is the singularity type (source, vorticity, or vortex), c is the component of the induced velocity, and pq should be read as the induced velocity in p by the singularity q. Here, A, B, and C are the influence coefficients of the distributed source, vorticity, and core vortices, respectively.

6.1.2.1 Influence Coefficients A and B

The influence coefficients A and B are calculated as

$$A_{ij}^{n} = \begin{cases} \dfrac{1}{2\pi}\left[\sin(\theta_i - \theta_j)\ln\dfrac{r_{i,j+1}}{r_{i,j}} + \cos(\theta_i - \theta_j)\beta_{ij}\right] & i \neq j \\ \dfrac{1}{2} & i = j \end{cases}, \tag{6.9}$$

$$A_{ij}^{t} = \begin{cases} \dfrac{1}{2\pi}\left[\sin(\theta_i - \theta_j)\beta_{ij} - \cos(\theta_i - \theta_j)\ln\dfrac{r_{i,j+1}}{r_{i,j}}\right] & i \neq j \\ 0 & i = j \end{cases}, \tag{6.10}$$

and

$$B_{ij}^{n} = -A_{ij}^{t}, \tag{6.11}$$

$$B_{ij}^{t} = A_{ij}^{n}, \tag{6.12}$$

where

$$r_{i,j+1} = \sqrt{(x_{m_i} - x_{j+1})^2 + (y_{m_i} - y_{j+1})^2}, \tag{6.13}$$

$$r_{i,j} = \sqrt{(x_{m_i} - x_j)^2 + (y_{m_i} - y_j)^2}, \tag{6.14}$$

$$x_{m_i} = \frac{1}{2}(x_i + x_{i+1}) \qquad y_{m_i} = \frac{1}{2}(y_i + y_{i+1}), \tag{6.15}$$

$$\theta_i = \arctan\left(\frac{y_{i+1} - y_i}{x_{i+1} - x_i}\right) \qquad \theta_j = \arctan\left(\frac{y_{j+1} - y_j}{x_{j+1} - x_j}\right), \tag{6.16}$$

and

$$\beta_{ij} = \arctan\left(\frac{y_{m_i} - y_{j+1}}{x_{m_i} - x_{j+1}}\right) - \arctan\left(\frac{y_{m_i} - y_j}{x_{m_i} - x_j}\right). \tag{6.17}$$

The calculation of the A coefficients when the superscript is x and y are calculated using equations (6.10) and (6.9) with θ_i set to zero, respectively. Similarly, B coefficients when the superscript is x and y are calculated using equations (6.12) and (6.11) with θ_i set to zero, respectively. In all cases, the subscripts should be appropriately replaced whenever the trailing-edge panel or core vortices are being considered.

6.1.2.2 Influence Coefficients C

The influence coefficients C are calculated as

$$(C^n_{i,m})_k = -\frac{\cos\left[\theta_i - (\theta_{i,m})_k\right]}{2\pi(r_{i,m})_k}, \tag{6.18}$$

$$(C^t_{i,m})_k = -\frac{\sin\left[\theta_i - (\theta_{i,m})_k\right]}{2\pi(r_{i,m})_k}, \tag{6.19}$$

where

$$(r_{i,m})_k = \sqrt{(x_{m_i} - x_m)^2 + (y_{m_i} - y_m)^2}, \tag{6.20}$$

$$x_{m_i} = \frac{1}{2}(x_i + x_{i+1}) \qquad y_{m_i} = \frac{1}{2}(y_i + y_{i+1}), \tag{6.21}$$

$$\theta_i = \arctan\left(\frac{y_{i+1} - y_i}{x_{i+1} - x_i}\right), \tag{6.22}$$

and

$$(\theta_{i,m})_k = \arctan\left(\frac{y_{m_i} - y_m}{x_{m_i} - x_m}\right). \tag{6.23}$$

The calculation of the C coefficients when the superscript is x and y are calculated using equations (6.18) and (6.19) with θ_i set to zero, respectively.

6.2 Numerical Solution

The flow tangency condition in Equation (6.5) can be written in terms of the influence coefficients as

$$\begin{aligned}\sum_{j=1}^{N}(A_{ij}^n)_k(q_j)_k + \tau_k\sum_{j=1}^{N}(B_{ij}^n)_k + (\vec{V}_{\text{stream}}\cdot\vec{n}_i)_k + (\tau_w)_k(B_{i,n+1}^n)_k \\ + \sum_{m=1}^{k-1}(C_{i,m}^n)_k(\Gamma_{m-1} - \Gamma_m) = 0 \qquad i = 1,2,...,N\end{aligned}. \tag{6.24}$$

In equation (6.24), $\vec{V}_{\text{stream}}$, is the unsteady stream velocity that is observed on a coordinate system fixed on the airfoil (with its origin at the pivot point). It is calculated as

$$\vec{V}_{\text{stream}} = \vec{V}_\infty + [U\vec{i} + V\vec{j}] + \Omega(y\vec{i} - x\vec{j}), \tag{6.25}$$

where $-(U\vec{i} + V\vec{j})$ is the translation velocity and Ω is the rotational velocity.

For a deforming airfoil, while the left-hand side of equation (6.24) is the same, the right-hand side should now contain the normal velocity, V_B, of each panel in the airfoil fixed coordinate system (body axis), so that the impermeability condition is verified. Furthermore, the coefficients A and B are now time-dependent. Hence,

$$\begin{aligned}\sum_{j=1}^{N}(A_{ij}^n)_k(q_j)_k + \tau_k\sum_{j=1}^{N}(B_{ij}^n)_k + (\vec{V}_{\text{stream}}\cdot\vec{n}_i)_k + (\tau_w)_k(B_{i,n+1}^n)_k \\ + \sum_{m=1}^{k-1}(C_{i,m}^n)_k(\Gamma_{m-1} - \Gamma_m) = (\vec{V}_{B_i}\cdot\vec{n}_i)_k \qquad i = 1,2,...,N\end{aligned}. \tag{6.26}$$

Equation (6.26) results in a system of algebraic equations that are written as

$$A\vec{q} = \tau_k\cdot\vec{b} + \vec{c}, \tag{6.27}$$

where

$$a_{ij} = (A_{ij}^n)_k, \tag{6.28}$$

$$b_i = \left[\frac{\ell}{\Delta_k} (B^n_{i,n+1})_k - \sum_{j=1}^{N} (B^n_{ij})_k \right], \tag{6.29}$$

and

$$\begin{aligned} c_i = &-(\vec{V}_{\text{stream}} \cdot \vec{n}_i)_k - \frac{\ell}{\Delta_k} \tau_{k-1} (B^n_{i,n+1})_k - \\ &- \sum_{m=1}^{k-1} (C^n_{i,m})_k (\Gamma_{m-1} - \Gamma_m) + (\vec{V}_{B_i} \cdot \vec{n}_i)_k \end{aligned} . \tag{6.30}$$

By having a closer look at the system of equations, we can see that $\vec{b}$ and $\vec{c}$ are known when the vorticity of the additional trailing-edge panel is identified, meaning that Δ_k and Θ_k should also be known. Consequently, to solve such a problem, Teng [30] proposes the iterative solution expressed in Figure 6.2.

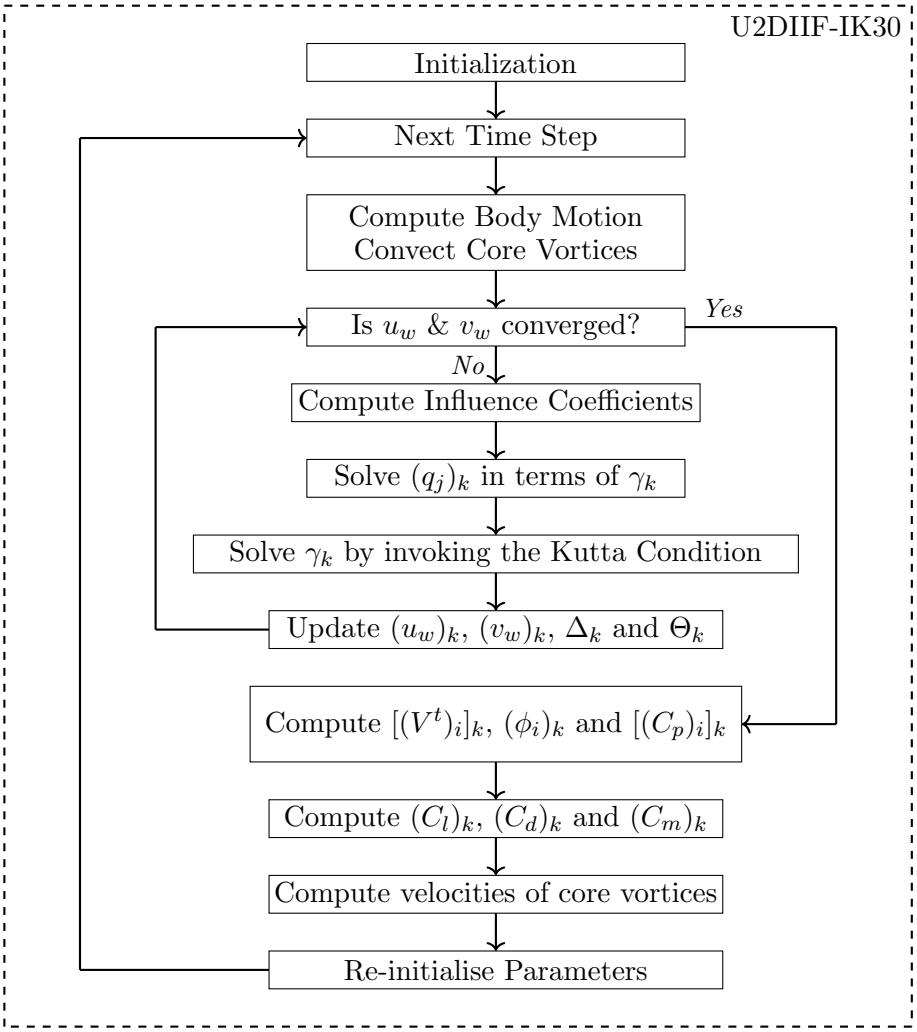

Figure 6.2: Solver methodology adapted from [30].

During the iterative process, we must write the source strength vector, q_j, in terms of τ, so we can later determine τ at the time step k by invoking the Kutta condition. Thus, equation

(6.26) rewritten as

$$A(q_j)_k = B_k\tau + C_k, \tag{6.31}$$

is given in terms of τ as

$$q_j = b1_j\tau + b2_j. \tag{6.32}$$

Using equation (6.32), we can write the tangential velocity at panel i in terms of τ as

$$\begin{aligned}\left[(V^t)_i\right]_k = \sum_{j=1}^{N} A^t_{ij}(q_j)_k + \tau_k \sum_{j=1}^{N} B^t_{ij} + (\vec{V}_{\text{stream}} \cdot \vec{t}_i)_k \\ +(\tau_w)_k \cdot (B^t_{i,n+1})_k + \sum_{m=1}^{k-1} (C^t_{i,m})_k(\Gamma_{m-1} - \Gamma_m) \qquad i = 1, 2, ..., N\end{aligned}, \tag{6.33}$$

with $q_j = b1_j\tau + b2_j$. With some algebraic manipulation, the tangential velocities are expressed as

$$V^t_i = D1_i\tau + D2_i. \tag{6.34}$$

To solve for τ we now use the Kutta condition, which states that

$$\left[(V^t)_1\right]^2_k - \left[(V^t)_N\right]^2_k = 2\ell\frac{\tau_k - \tau_{k-1}}{t_k - t_{k-1}}. \tag{6.35}$$

Using equation (6.34) we obtain

$$(D1_1\tau + D2_1)^2 - (D1_N\tau + D2_N)^2 = 2\ell\frac{\tau - \tau_{k-1}}{\Delta t}, \tag{6.36}$$

$$D1_1^2\tau^2 + 2D1_1D2_1\tau + D2_1^2 - D1_N^2\tau^2 - 2D1_ND2_N\tau - D2_N^2 = \frac{2\ell}{\Delta t}\tau + 2\ell\frac{\tau_{k-1}}{\Delta t}, \tag{6.37}$$

and finally,

$$(D1_1^2 - D1_N^2)\tau^2 + \left(2D1_1D2_1 - 2D1_ND2_N - \frac{2\ell}{\Delta t}\right)\tau + D2_1^2 - D2_N^2 - 2\ell\frac{\tau_{k-1}}{\Delta t} = 0. \tag{6.38}$$

After convergence, the velocities at the center of all core vortices are given in components as

$$(u_h)_k = \sum_{j=1}^{N}(A^x_{hj})_k(q_j)_k + \tau_k\sum_{j=1}^{N}(B^x_{hj})_k + (\vec{V}_\infty\cdot\vec{i})_k + (\tau_w)_k\cdot(B^x_{h,n+1})_k + \sum_{m=1,m\neq h}^{k-1}(C^x_{h,m})_k(\Gamma_{m-1}-\Gamma_m) \qquad i=1,2,...,N \tag{6.39}$$

and

$$(v_h)_k = \sum_{j=1}^{N}(A^y_{hj})_k(q_j)_k + \tau_k\sum_{j=1}^{N}(B^y_{hj})_k + (\vec{V}_\infty\cdot\vec{j})_k + (\tau_w)_k\cdot(B^y_{h,n+1})_k + \sum_{m=1,m\neq h}^{k-1}(C^y_{h,m})_k(\Gamma_{m-1}-\Gamma_m) \qquad i=1,2,...,N \tag{6.40}$$

Equations (6.39) and (6.40) may be use to calculate $(u_w)_k$ and $(v_w)_k$ when the subscript h is replaced with $n+1$.

6.3 Pressure Distribution and Force Calculation

This subsection concerns the calculation of the pressure distribution C_p which is later used to calculate lift and drag coefficients, as well as the pitching moment coefficient.

The pressure coefficient is given by

$$C_p = \frac{p-p_\infty}{\frac{1}{2}\rho U_\infty^2}, \tag{6.41}$$

which can be rewritten as

$$C_p = \left(\frac{V_{\text{stream}}}{V_\infty}\right)^2 - \left(\frac{V}{V_\infty}\right)^2 - \frac{2}{V_\infty^2}\frac{\partial\phi}{\partial t}, \tag{6.42}$$

where

$$V^2 = (V^t)^2 + (V^n)^2, \tag{6.43}$$

is the total velocity concerning the airfoil-fixed coordinate system. Then, using a backward finite-difference approximation, the pressure coefficient at the i-th panel control point is given by

$$[(C_p)_i]_k = \frac{[(V_{\text{stream}})_i]_k^2}{V_\infty^2} - \frac{[V_i]_k^2}{V_\infty^2} - \frac{2}{V_\infty^2}\frac{(\phi_i)_k-(\phi_i)_{k-1}}{t_k-t_{k-1}}. \tag{6.44}$$

At each control point, the velocity potential is calculated by integrating the velocity field from infinity to the leading edge and then from the leading edge to each panel control point. Here, infinity is considered to be at ten chord lengths where induced velocities by singularities can be neglected. Thus, the velocity field is integrated on a straight line from infinity to the leading edge with the U_∞ direction, which then continues along the airfoil surface. This line is discretized into z panels, where the tangential velocities are evaluated. Here, only the velocity contribution due to singularities should be considered. Thus, the tangential velocities at panel f are given by

$$\begin{aligned}[(V_\phi^t)_f]_k = \sum_{j=1}^{N}(A_{fj}^t)_k(q_j)_k + \tau_k\sum_{j=1}^{N}(B_{fj}^t)_k + (\tau_w)_k\cdot(B_{f,n+1}^t)_k \\ + \sum_{m=1}^{k-1}(C_{f,m}^t)_k(\Gamma_{m-1}-\Gamma_m) \qquad f=1,2,...,z\end{aligned}, \tag{6.45}$$

where the influence coefficients $(A_{f,j}^t)_k$, $(B_{f,j}^t)_k$, $(B_{f,n+1}^t)_k$ and $(C_{f,m}^t)_k$ are calculated as before with their subscripts adequately replaced. Moreover, $\cos\theta_i$ should be modified to $-\cos\alpha$ and $\sin\theta_i$ to $-\sin\alpha$.

The velocity potential at the airfoil leading edge, $\phi_{\text{l.e.}}$, is the sum of the induced velocity at each panel f multiplied by their length, expressed as

$$(\phi_{\text{l.e.}})_k = \sum_{f=1}^{z}[(V_\phi^t)_f]_k\sqrt{(x_{f+1}-x_f)^2+(y_{f+1}-y_f)^2}. \tag{6.46}$$

For the line integral over the airfoil surface, the tangential component of the induced velocity at the i-th panel control point is

$$\begin{aligned}\left[(V_\phi^t)_i\right]_k = \sum_{j=1}^{N}(A_{ij}^t)_k(q_j)_k + \tau_k\sum_{j=1}^{N}(B_{ij}^t)_k + (\tau_w)_k\cdot(B_{i,n+1}^t)_k + \\ \sum_{m=1}^{k-1}(C_{i,m}^t)_k(\Gamma_{m-1}-\Gamma_m) \qquad i=1,2,...,N\end{aligned}. \tag{6.47}$$

The velocity potential at i-th boundary point is obtained by

$$(\phi_{\text{node }i}) = (\phi_{\text{l.e.}})_k - \sum_{j=i}^{i_{\text{l.e.}}-1}[(V_\phi^t)_j]_k\sqrt{(x_{j+1}-x_j)^2+(y_{j+1}-y_j)^2}, \tag{6.48}$$

if $1 \leq i \leq i_{\text{l.e.}}$ and

$$(\phi_{\text{node }i}) = (\phi_{\text{l.e.}})_k + \sum_{j=i_{\text{l.e.}}}^{i-1}[(V_\phi^t)_j]_k\sqrt{(x_{j+1}-x_j)^2+(y_{j+1}-y_j)^2}, \tag{6.49}$$

if $i_{\text{l.e.}} \leq i \leq N+1$ and then, the velocity potential is obtained at the i-th panel control point using

$$(\phi_i)_k = \frac{1}{2}[(\phi_{\text{node } i})_k + (\phi_{\text{node } i+1})_k]. \tag{6.50}$$

By integrating the pressure distribution, forces are obtained in the airfoil-coordinate system using equations (6.51) and (6.52).

$$C_x = -\sum_{i=1}^{N}(C_p)_i(y_{i+1} - y_i), \tag{6.51}$$

and

$$C_y = \sum_{i=1}^{N}(C_p)_i(x_{i+1} - x_i). \tag{6.52}$$

The pitching moment coefficient can also be computed with

$$C_m = -\sum_{i=1}^{N}(C_p)_i \left[(x_{i+1} - x_i)x_{m_i} + (y_{i+1} - y_i)y_{m_i}\right]. \tag{6.53}$$

Lift and drag coefficients are then calculated by rotating C_x and C_y so that drag and lift are along and perpendicular to the free stream velocity, respectively, as

$$C_d = C_x \cos\alpha + C_y \sin\alpha, \tag{6.54}$$

and

$$C_l = C_y \cos\alpha - C_x \sin\alpha. \tag{6.55}$$

Although this is a simpler model when compared to CFD, it still presents a considerable challenge regarding storage and computation time. As one can see, the model uses a large amount of influence coefficients that quickly reach large dimensions. As N increases, the number of influence coefficients grows N^2, and for each time step increment, $2N + NTS^2$ influence coefficients are added. To alleviate the computation time, an option was introduced in the code that removes wake vortices older than a certain period. We do this while being clearly aware that such action violates the unchangeability of the flow field's total circulation. However, as will be shown ahead, the removal of vortices past a certain distance from the airfoil will have a negligible influence on the aerodynamic coefficients, meaning that we can sacrifice the total circulation for compute efficiency.

As mentioned before, the airfoil needs to be discretized into panels. For the present study,

the airfoil is divided into N segments using cosine-based spacing, as illustrated in Figure 6.3.

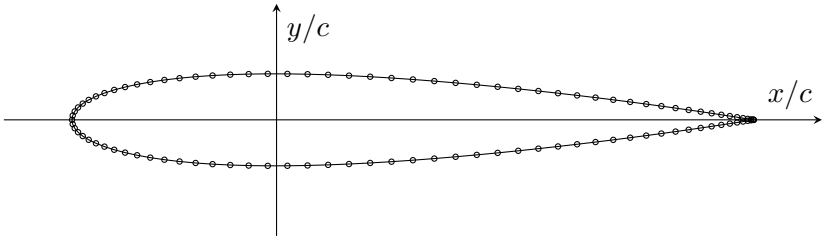

Figure 6.3: Cosine-based spacing.

One aspect of the proposed NACA0012-IK30 airfoil is the fact that it has two discontinuities on its surface, which presents a clear challenge to the panel method. Without any consideration, if we deflect the frontal part some control points may overlap or grossly misrepresent our geometry. To tackle this limitation, we use an optimized sigmoid that provides a smooth transition using 5 % of the airfoil chord to create a continuous deformation. The deformation strategy used to dynamically deflect the leading edge is presented in Figure 6.4.

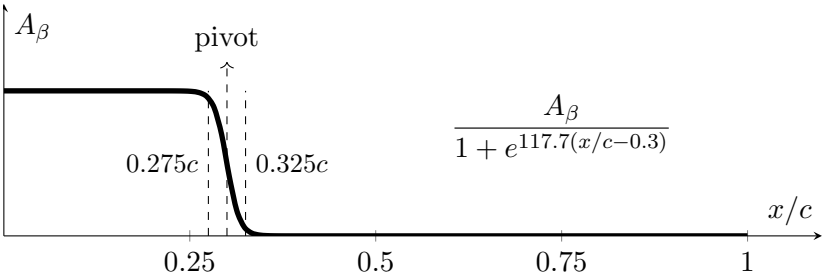

Figure 6.4: Deformation strategy for the leading-edge deflection.

To guarantee that the numerical solution is independent of the number of panels and time steps per period, a brief study is conducted considering the

$$Re = 1 \times 10^4, h = 0.25, k = 4.0 \text{ and } A_\beta = 0^\circ$$

condition. The results are presented in Figure 6.5, showing the desired mesh and time step independence. For the study, we will be using the middle condition ($N+N_{TS}$) where $N = 200$ and $N_{TS} = 200$.

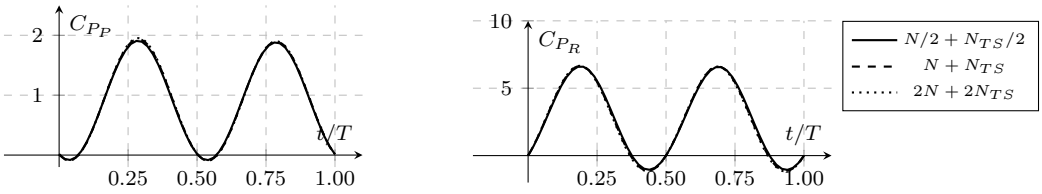

Figure 6.5: Influence of number of panels and time steps per period.

Considering the same condition, a similar study is made regarding the number of vortices that are kept in the wake as a way to improve computational efficiency. Based on the results presented in Figure 6.6, we see that we can maintain only the vortices created in the last four periods without affecting the propulsive coefficients. This assumption holds out throughout

the study since this was the condition with the higher effective angle of attack and where vortices were closer to the airfoil. One should be aware and be always on notice that four periods may not be enough in other conditions.

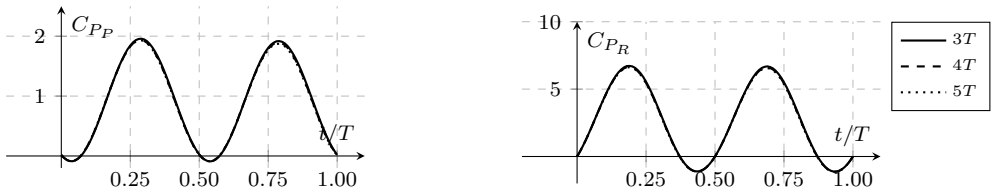

Figure 6.6: Influence of the number of vortices in the wake.

As a final validation step, the present methodology is contrasted with results published by Jones and Platzer [25]. The comparison is shown in Figure 6.7 using the propulsive power coefficient for plunging (left) and pitching (right) motions, proving the correct implementation of the unsteady panel method.

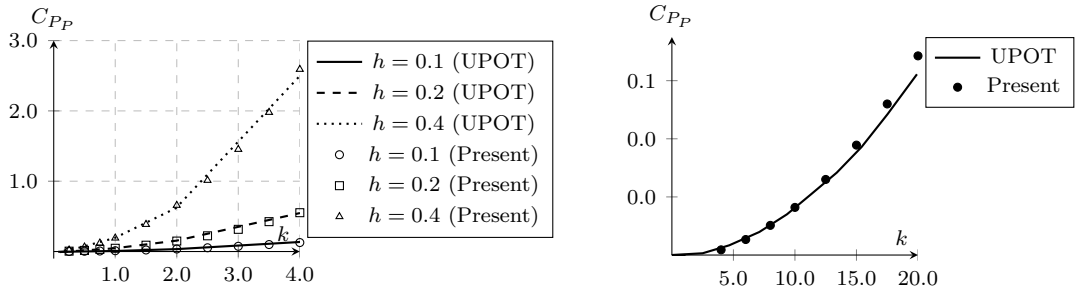

Figure 6.7: Validation using data published by Jones and Platzer [25].

Chapter 7

Optimization

"I always believed that constraints enable great engineering."

Johny Srouji

This chapter builds upon the previous numerical and experimental methodologies and connects them to a central part of the study: the optimization of the NACA0012-IK30 both as an airfoil and a wing. The first section will look into the numerical optimization framework of the airfoil as a propulsor, meaning that we will be focused on the improvement of its propulsive capabilities, mainly thrust generation and propulsive efficiency. Contrarily, the second section presents an optimization methodology that is used at a higher Reynolds number. In these conditions, the optimization is conducted experimentally, and its objective is the improvement of the drag and lift coefficients of a NACA0012-IK30 wing.

7.1 Optimization of the NACA0012-IK30 as a propulsor

As mentioned before, the NACA0012-IK30 has a dynamically activated leading edge, which has the potential to improve the propulsive performance. Finding the adequate leading-edge pitching amplitude may be obtained by studying the influence of the leading-edge kinematics on the propulsive performance parametrically. However, parametric studies cannot guarantee that an optimal value will be achieved, and for that, optimization methods should be used. In this section, the optimal leading-edge pitching amplitude is found using a gradient-based algorithm that suggests a newer amplitude after each oscillation cycle until convergence is verified.

The optimization process is based on the gradient ascent, in which a certain number of iterations/steps in the gradient direction leads to a desired maximum of a function. Mathematically, it is expressed as

$$A_\beta^{n+1} = A_\beta^n \pm \gamma_n \frac{\mathrm{d}F}{\mathrm{d}A_\beta}, \tag{7.1}$$

where F is the objective function that we are looking to maximize, γ_n is the optimization step size, n represents the current iteration, and $n+1$ is the next one. The objective function, F, in the present work, is defined as

$$F = \varphi\overline{C_{P_P}} + (1-\varphi)\eta, \tag{7.2}$$

where φ is a variable that weighs between the maximization of thrust or propulsive efficiency. Unfortunately, the values of F are not known since we do not know its dependence on A_β. This means that the gradient cannot be obtained analytically, thus a backward-finite difference is used to estimate ∇F, as

$$\nabla F = \frac{\mathrm{d}F}{\mathrm{d}A_\beta} \approx \varphi \frac{\overline{C_{P_P}}^{n} - \overline{C_{P_P}}^{n-1}}{A_\beta^n - A_\beta^{n-1}} + (1-\varphi)\frac{\eta_t^n - \eta_t^{n-1}}{A_\beta^n - A_\beta^{n-1}}. \tag{7.3}$$

Using equations (7.1) and (7.3), the new leading-edge pitching amplitude value is expressed by the following recurrence relation

$$A_\beta^{n+1} = A_\beta^n \pm \gamma_n \left(\varphi \frac{\overline{C_{P_P}}^{n} - \overline{C_{P_P}}^{n-1}}{A_\beta^n - A_\beta^{n-1}} + (1-\varphi)\frac{\eta_t^n - \eta_t^{n-1}}{A_\beta^n - A_\beta^{n-1}} \right). \tag{7.4}$$

The optimization step size, γ_n is also an important parameter that dictates the convergence rate to the desired maximum. For the step size calculator, we use the Barzilai-Borwein method [195], which is adapted to the present work as

$$\gamma_n = \frac{\left| (A_\beta^n - A_\beta^{n-1}) \left(\frac{\mathrm{d}F}{\mathrm{d}A_\beta}^{n} - \frac{\mathrm{d}F}{\mathrm{d}A_\beta}^{n-1} \right) \right|}{\left| \frac{\mathrm{d}F}{\mathrm{d}A_\beta}^{n} - \frac{\mathrm{d}F}{\mathrm{d}A_\beta}^{n-1} \right|^2}. \tag{7.5}$$

However, while there is a step size suggestion, the change in the pitching amplitude is limited to 1°. This limiter reduces existing transients between consecutive periods, which allows for a A_β adjustment after each period. Hence, the recurrent equation (7.1) is rewritten as

$$A_\beta^{n+1} = A_\beta^n \pm \max\left(\gamma_n \frac{\mathrm{d}F}{\mathrm{d}A_\beta}, 1^\circ \right). \tag{7.6}$$

The motion of the airfoil parts is achieved by using user-defined functions (UDFs) that are linked to ANSYS Fluent. In these C-programmed codes, equations that govern the airfoil kinematics are implemented. Additionally, in the subroutine that controls the kinematics of the leading edge, a sequence of instructions is developed to conduct the optimization study of the airfoil pitching amplitude.

The overall procedure for the optimization starts by providing an initial guess that is communicated to ANSYS Fluent. During the simulation and at every time step, two data files (kinematics and forces report) are created, which are later used to calculate the propulsive indicators and provide a new leading-edge pitching amplitude. The mean values using the last period, are reported at every optimization step into a data file with some additional infor-

mation. After each oscillation cycle, the optimization kicks in, suggesting a new pitching amplitude depending on the objective function. A pitching amplitude is considered converged when

$$\frac{\left|A_\beta^{n+1} - A_\beta^n\right|}{\left|A_\beta^n\right|} \tag{7.7}$$

is kept under 1 % for five consecutive periods. The optimization framework is shown in Figure 7.1.

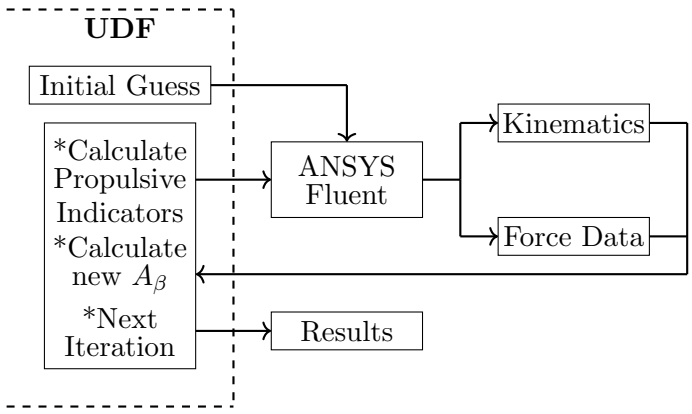

Figure 7.1: Optimization Framework.

Figure 7.2 provides a more visual way to illustrate a hypothetical run of the implemented optimization setup.

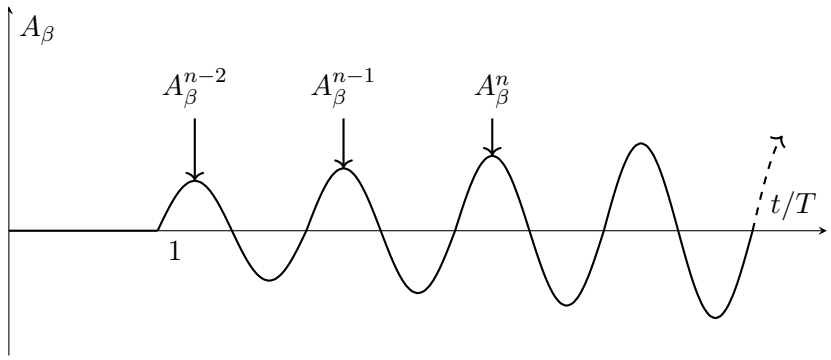

Figure 7.2: Strategy applied for the optimal search of F using A_β.

7.2 Optimization of the NACA0012-IK30 Wing

For the optimization at higher Reynolds numbers, the framework is drastically changed. First of all, instead of optimizing the leading edge position numerically, we will optimize it experimentally, meaning that a new real-time optimization (RTO) framework is developed and implemented to accomplish such a task. Furthermore, at higher Reynolds numbers, oscillating airfoils have significant difficulty regarding thrust production since considerable frequencies or amplitudes are required to pass through the drag-to-thrust transition. Hence, under these conditions, the NACA0012-IK30 will be used for dynamic stall mitigation purposes by

exploring its potential at high angles of attack.

This section describes an RTO strategy for finding optimal Ω values considering a NACA0012-IK30 wing. This strategy uses a gradient-based and model-free optimization algorithm, which looks at reducing drag and improving the lift coefficients by employing the following function:

$$F = \varphi(-C_D) + (1 - \varphi)C_L, \tag{7.8}$$

where φ is a weighting factor.

However, one should consider that in a real-time optimization, the experimental setup is susceptible to vibrations, inevitably yielding noisy measurements. This noisy data creates an enormous challenge to gradient-based methods, especially gradient evaluation.

The effect of the vibrations and other turbulent-flow-associated effects in the measurements of F can be reduced by considering a moving average of equation (7.8). Therefore, this work follows a stochastic methodology capable of overcoming this issue while following a gradient-based approach by considering the following objective function:

$$\mathcal{O} = \frac{1}{j} \sum_{i=n-j+1}^{n} \varphi(-C_{D_i}) + (1 - \varphi)C_{L_i}, \tag{7.9}$$

which uses the last j data points. Although force measurements of $\mathcal{O}$ were not conventionally filtered, the moving average effectively acts as a low-pass filter; therefore, j should be chosen to avoid a considerable phase lag between F and $\mathcal{O}$. The objective function, $\mathcal{O}$, should be maximized in this proposal. In this way, the solution of this optimization problem is given by

$$\underset{\Omega \in [-40^\circ, 40^\circ]}{\operatorname{argmax}} \ \mathcal{O}, \tag{7.10}$$

with the Ω constraints indicating the maximum leading-edge deflection relative to the ψ part.

Since we are using a gradient approach, the search for a leading-edge position that maximizes $\mathcal{O}$ follows the recursive equation

$$\Omega^{t+1} = \Omega^t + \gamma \frac{\mathrm{d}\mathcal{O}}{\mathrm{d}\Omega}, \tag{7.11}$$

where γ is the optimization step size and t indicates the time instant. The previous equation can be rewritten as

$$\Delta\Omega = \gamma \frac{\mathrm{d}\mathcal{O}}{\mathrm{d}\Omega}, \tag{7.12}$$

where $\Delta\Omega = \Omega^{t+1} - \Omega^t$. Equation (7.12) resembles a P-controller (Proportional Gain Control),

where $\Delta\Omega$ is the control output $u(t)$, γ is the proportional gain and $\mathrm{d}\mathcal{O}/\mathrm{d}\Omega$ is the error.

This work extends this understanding to a broader expression considering the I- and D-controller (Integral and Derivative Gain Controls). This approach promotes flexibility for this proposal since the integral gain can account for past data while the derivative gain can capture the tendency of the present information. Therefore, the proposal follows a PID-controller framework.

It is well-known that the general control output $u(t)$ of a PID controller is given by

$$u(t) = K_p e(t) + K_i \int_0^t e(t)\mathrm{d}t + K_d \frac{\mathrm{d}e(t)}{\mathrm{d}t}, \tag{7.13}$$

where K_p, K_i, and K_d are the proportional, integral, and derivative terms. Alternatively, equation (7.13) is rewritten in the following form

$$u(t) = K_p \left(e(t) + \frac{1}{T_i} \int_0^t e(t)\mathrm{d}t + T_d \frac{\mathrm{d}e(t)}{\mathrm{d}t} \right), \tag{7.14}$$

where T_i and T_d are the integral and derivative times.

Considering the proposal, the error value is given by

$$e(t) = \frac{\mathrm{d}\mathcal{O}}{\mathrm{d}\Omega}, \tag{7.15}$$

and the controller output is used as

$$\Omega^{t+1} = \Omega^t + u(t). \tag{7.16}$$

Krishnamoorthy and Skogestad [196] presented a recent and thorough review of real-time optimization as a feedback control problem. They enumerated several strategies to estimate the gradient, considering model-based and model-free methods. Among the strategies considering model-based methods, there are gradient estimation strategies based on transient measurements, the fast Fourier transform (FFT), the Kalman filter, and the least-squares problem. The present work proposes a novel approach using regression techniques and transient measurements. The gradient estimation includes two parts indicated by the superscripts: (1) derived using regression techniques and (2) derived using transient measurements.

As mentioned before, the gradient cannot be directly estimated with real-time data due to the presence of noise. Considering this limitation, our proposal first uses an online local linear modeling strategy based on the method proposed by Hunnekens et al. [197], who exploit a moving linear regression to estimate the gradient.

In this way, as we run the optimization process, we save the last q ordered pairs $(\Omega, \mathcal{O})$ and

for each time step, we use all gathered data to calculate the following linear regression

$$\hat{\mathcal{O}}^{(1)} = \varepsilon_1 \Omega^* + \varepsilon_0, \tag{7.17}$$

where the hat $\hat{}$ and the upper-index (1) indicates an estimated value of $\mathcal{O}$ using regression techniques, $\varepsilon_0, \varepsilon_1$ are the linear-regression parameters obtained using the least squares method, and Ω^* is a perturbed version of Ω to avoid ill-conditioned problems. Using this approach, one can easily obtain an estimate of the gradient given by

$$\frac{\mathrm{d}\hat{\mathcal{O}}^{(1)}}{\mathrm{d}\Omega^*} = \varepsilon_1. \tag{7.18}$$

One particular problem with this formulation is the fact that if the last q values of Ω are very close or even the same, the calculation of ε_1 can easily become a badly or an ill-conditioned problem, compromising the gradient evaluation. One simple way to mitigate this problem is to randomly perturb each Ω before they enter the regression block. The aforementioned modification, Ω^*, is given by

$$\Omega^* = \Omega + U(-\Upsilon, \Upsilon), \tag{7.19}$$

where $U(-\Upsilon, \Upsilon)$ represents a random number generated by a uniform distribution with values between $-\Upsilon$ and Υ. The Υ value must be chosen to avoid overdamping the gradient evaluation.

Although it is a fairly simple way to estimate the gradient, this dither-free extremum-seeking control approach must be used cautiously since a local model, obtained by evaluating the last q ordered pairs, offers only an approximate representation of the vicinity of $\mathcal{O}$ for a given Ω. This behavior yields a non-trivial relation between the controller gains (K_p, K_p/T_i, K_pT_d) and q. Moreover, q must be chosen carefully since a low number of ordered pairs can lead to a noisy gradient estimation. In contrast, too many points will misrepresent the local gradient with data outside the vicinity of Ω^t. One can find further information on these approaches' intricacies and the differences between the dynamic and static map settings at Hunnekens et al. [197].

While the method proposed by Hunnekens et al. [197] is central to the current RTO methodology, we propose an extension by implementing the concept of spatial memory using transient measurements. The method has a temporary memory of the last ωq seconds when using a moving linear regression of the previous q data points, where ω is the data acquisition frequency. This means that after ωq seconds, the measurement system retains no information in the Ω domain.

To implement some level of spatial memory, real-time measurements of $\mathcal{O}$ are used to create a static map between the input, Ω, and the objective function. As illustrated in Figure 7.3, this is accomplished by the vector $\overrightarrow{\mathcal{O}}$ which has eighty-one elements, effectively dividing the

Ω space from $-40°$ to $40°$ with $1°$ intervals.

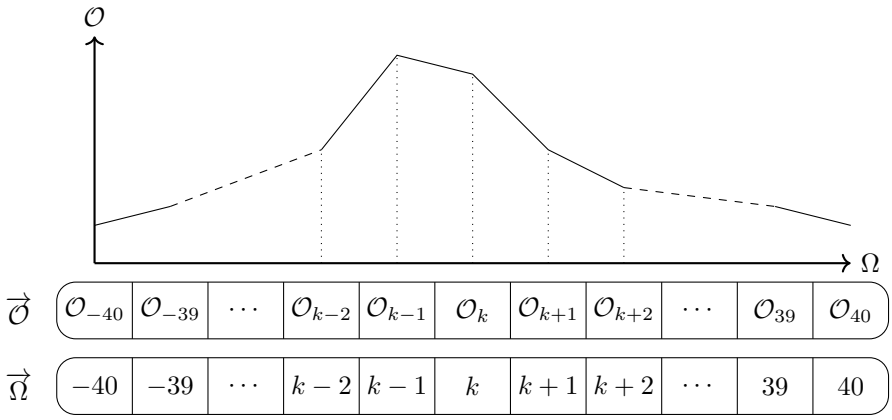

Figure 7.3: Static map from transient measurements.

The static map is built by initializing the vector $\vec{\mathcal{O}}$ with a large negative value when the optimization starts. As the algorithm runs, the term $\mathcal{O}_k$ of the vector $\vec{\mathcal{O}}$ is constantly updated with transient measurements according to,

$$\mathcal{O}_k = \begin{cases} \mathcal{O}_{\text{previous}} & \text{if } \lfloor \Omega_t \rceil \neq k \\ 0.5\left(\mathcal{O}_{\text{actual}} + \mathcal{O}_{\text{previous}}\right) & \text{if } \lfloor \Omega_t \rceil = k \end{cases}, \tag{7.20}$$

which is evaluated recursively at every time step updating the static map.

A limitation of this approach is the fact that to create the static map accurately, the Ω perturbations must occur at a relatively slow rate to guarantee that the entries $(\Omega, \mathcal{O})$ are a viable representation of the steady-state case. In the present study, this is achieved by limiting $\dot{\Omega}$, which is accomplished by saturating the PID output. Since the output was severely saturated, there was no need to implement the derivative part of the controller, which is commonly used to dampen the controller response.

This static map is used for obtaining the gradient estimation using transient measurements, computed as

$$\frac{\mathrm{d}\hat{\mathcal{O}}^{(2)}}{\mathrm{d}\Omega} = \begin{cases} \frac{\mathcal{O}_t - \max \vec{\mathcal{O}}}{\Omega_t - \operatorname{argmax} \vec{\mathcal{O}}} & \text{if } \Omega_t > \operatorname{argmax} \vec{\mathcal{O}} \\ \frac{\max \vec{\mathcal{O}} - \mathcal{O}_t}{\operatorname{argmax} \vec{\mathcal{O}} - \Omega_t} & \text{if } \Omega_t < \operatorname{argmax} \vec{\mathcal{O}} \\ 0 & \text{if } \Omega_t = \operatorname{argmax} \vec{\mathcal{O}} \end{cases}, \tag{7.21}$$

which directly connects the current system state to the $\max \vec{\mathcal{O}}$.

This approach takes into account recent transient measurements as illustrated in Figure 7.4. This figure shows the gradient estimation strategies proposed by Hunnekens et al. [197] (left) and the ones proposed in this work (right).

With this framework, the gradient evaluation using both the moving linear regression and

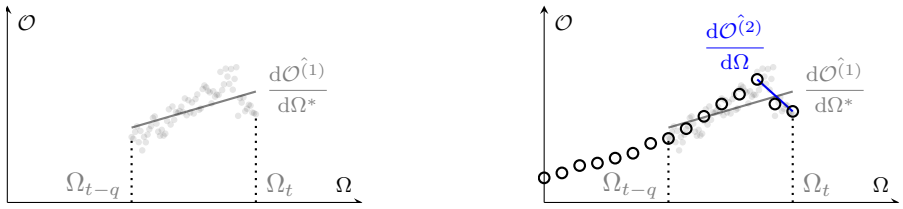

Figure 7.4: Optimization framework proposed by Hunnekens et al. [197] (left) and the extension proposed in the present work (right).

the static map maximum is achieved by

$$\frac{d\mathcal{O}}{d\Omega} \approx \frac{1}{2}\left(\frac{d\hat{\mathcal{O}}^{(1)}}{d\Omega^*} + \frac{d\hat{\mathcal{O}}^{(2)}}{d\Omega}\right), \tag{7.22}$$

which as seen in Figure 7.4, will act against the delay introduced by using older data to estimate the true gradient.

Figure 7.5 illustrates the optimization algorithm with a pseudocode that combines the gradient estimations derived by the moving linear regression strategies and the static map.

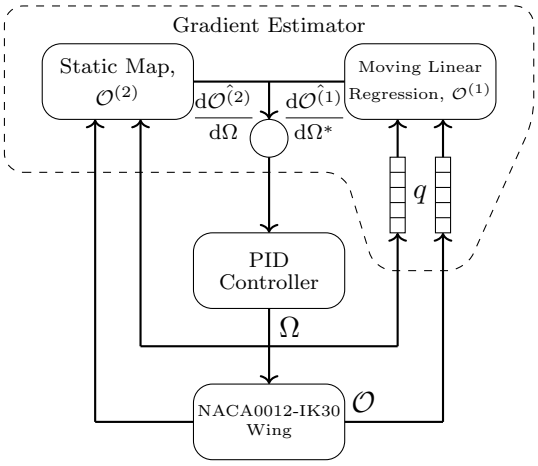

while RTO is activated **do**
Update the delay vector with the latest measurement $[Z_t^{-1}, Z_{t-1}^{-1}, Z_{t-2}^{-1}, \ldots, Z_{t-q}^{-1}]$.
Update the static map, $\mathcal{O}^{(2)}$, using equation (7.20).
Compute the moving linear regression of the delay vector, $\hat{\mathcal{O}^{(1)}}$, using equation (7.17).
Determine first gradient estimation, ε_1, using equation (7.18).
Locate the max and argmax of the static map.
Compute the second gradient estimation based on the static map, using equation (7.21).
Determine the final gradient estimate with equation (7.22).
Feed the gradient estimate to the PID controller, obtaining u as seen in equation (7.14).
Update the leading edge deflection using equation (7.16).
end while

Figure 7.5: RTO Formulation.

Regarding the initial values of the PID gains, we derived them using the Ziegler-Nichols tuning method [198]. Further adjustments were made to achieve an acceptable response, where the maximum is reached somewhat quickly. All parameters used for the optimization using

the local linear static model are presented in Table 7.1. These were tested and calibrated when analyzing the NACA0012-IK30 at $Re = 3.0 \times 10^5$ and $\psi = 30°$.

Table 7.1: Parameters for the optimization of the NACA0012-IK30 wing.

Simulink Model Clock	ω_{Simulink}	$1\,\text{kHz}$
Moving Average Window	j	1000 samples ($1\,\text{s}$)
Proportional Gain	K_p	1.000
Integral Gain	K_i	0.100 ($T_i = 10\,\text{s}$)
Derivative Gain	K_d	0.000 ($T_d = 0\,\text{s}$)
Maximum Ω deflection	$\max \Omega$	$\pm 40°$
Maximum $\dot{\Omega}$	$\max \dot{\Omega}$	$\pm 2\,^\circ\,\text{s}^{-1}$
Anti-windup Scheme	-	Clamping
Delay Vector Size	q	5000 samples ($5\,\text{s}$)
Random Perturbation Parameter	Υ	$0.1°$

Chapter 8

Propulsive Enhancement

"The pursuit of perfection often impedes improvement."

George Will

This chapter explores the operation of the NACA0012-IK30 airfoil at the lower Reynolds number spectrum. At first, flow visualization tests are performed, where we study the broad influence of the movable leading edge on the flow field. Then, the same conditions are reproduced numerically, where we explore the propulsive capabilities of the airfoil under various oscillation conditions. This phase focuses on the influence of the dynamic activation of the leading edge on the propulsive parameters. Furthermore, using the optimization methodology defined before, we compare the proposed geometry with traditional flapping, concluding that the NACA0012-IK30 airfoil can provide meaningful improvements over conventional flapping.

8.1 Flow Visualization

In this section, all experimental data regarding the flow visualization of the IK30 mechanism is presented, with a special focus on the influence of the dynamic leading edge on flow separation. The Reynolds number, reduced frequency, nondimensional amplitude, nondimensional velocity, and leading-edge pitching amplitude are selected as the governing parameters of the flow field. But before moving to the flow visualization results, there is the need to ensure that the kinematics prescribed to the plunging and pitching motors closely follow the sinusoidal wave shown in Chapter 4.

The kinematics validation of the plunging motor is made by operating the motor at its maximum amplitude, $A = 0.1$ m, with a frequency of 1 Hz. The experimental validation of the plunging motion is achieved by tracking the airfoil's trailing edge using the high-speed camera, as illustrated in Figure 8.1.

Trailing-edge tracking is made using the Photron FASTCAM Viewer 4, which offers a manual tracking feature and a calibration tool that converts pixels into length. In the experimental validation, the calibration is achieved using a known reference (ruler) from which we can obtain that a pixel is approximately 3.4×10^{-4} m. In Figure 8.2, the experimental measurements are plotted against the desired sinusoidal wave.

Figure 8.1: Tracking methodology for plunging validation.

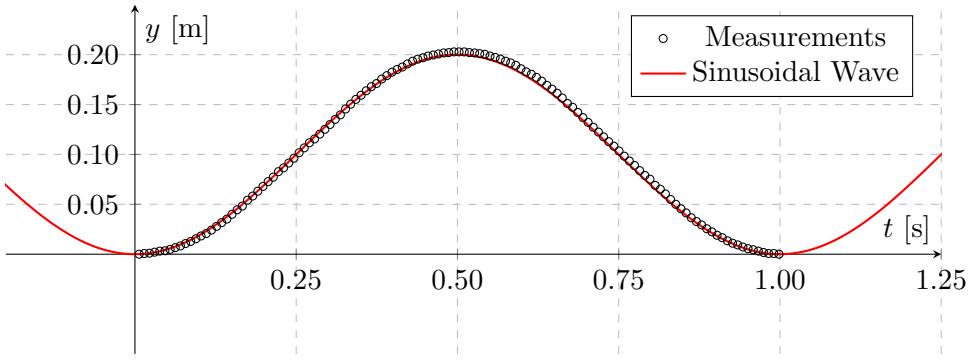

Figure 8.2: Plunging motion validation. Measurements are estimated to have an uncertainty of 3.45×10^{-4} m.

Likewise, the pitching motion is also verified, in this case with a pitching frequency of 1 Hz and an angular amplitude A_β of 20°. Differently from the plunging motion, we track the leading edge position. Then, the dimensions a and b are calculated, which are used to determine the leading-edge angle of attack, β, as illustrated in Figure 8.3.

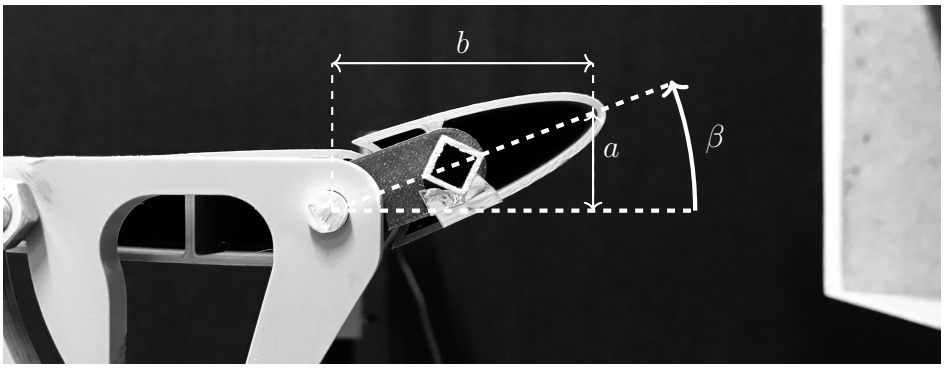

Figure 8.3: Tracking methodology for pitching validation.

In Figure 8.4, experimental measurements are plotted against the desired sinusoidal profile.

Following the kinematics validation, we now move to the analysis of the flow fields surrounding the airfoil. As mentioned in the methodology, images are obtained in a Lagrangian perspective where the camera is attached to the support that holds the wing. In the images, an array of LEDs that illuminates the smoke is visible.

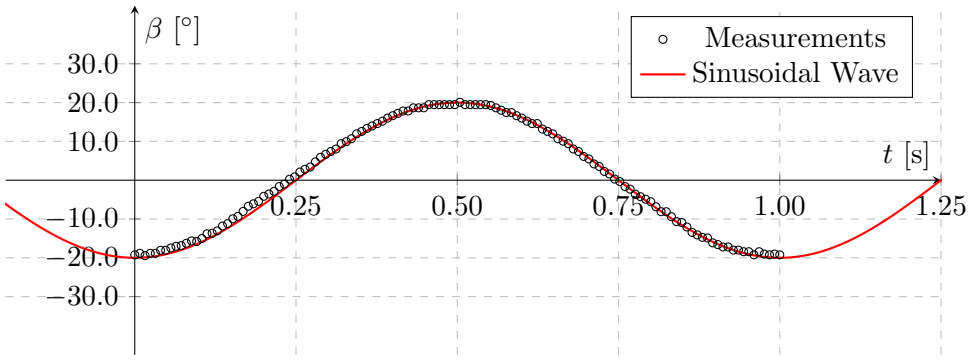

Figure 8.4: Pitching motion validation. Measurements are estimated to have an uncertainty no more than 6.56×10^{-4} degrees.

Data is obtained for a Reynolds number of 1.0×10^4, at two different nondimensional amplitudes, 0.25 and 0.50. At the lower nondimensional amplitude, the reduced frequency is set to 1.0, 2.0, and 4.0, while for the highest, the reduced frequencies tested are 0.5, 1.0, and 2.0, as shown in Figure 8.5. This results on a nondimensional velocity, kh, between 0.25 and 1.00 (Strouhal number between 0.080 and 0.318). This corresponds to a maximum effective angle of attack between $14.1°$ and $45.0°$ when no leading edge deflection is considered.

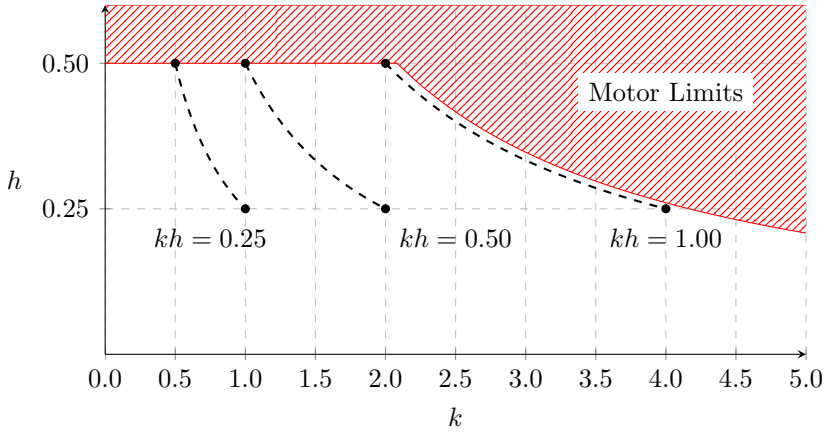

Figure 8.5: Tested conditions in the $k - h$ domain. Values are calculated based on pressure of 930 hPa and a temperature of $18.0\,°$C.

Each (k, h) combination is tested with three leading-edge pitching amplitudes, being these $A_\beta = 0°$, $10°$ and $20°$. Before moving further, let us revisit the kinematics that will be used throughout this study. The plunging motion is given by

$$y = A \sin(2\pi f t), \tag{8.1}$$

while the pitching leading edge is controlled as

$$\beta = A_\beta \sin(2\pi f t + \phi), \tag{8.2}$$

where the phase angle, ϕ, is set at $90°$. Such value causes the leading edge to be maximally deflected when the airfoil experiences maximum plunging velocity, providing the highest effective angle of attack reduction possible. Concerning the back part, it is always fixed at

$\psi = 0°$.

With $A_\beta = 0°$, the airfoil oscillates as a conventional plunging airfoil, but when we change the leading-edge pitching amplitude, the airfoil actively changes its curvature and maximum airfoil thickness position. Figure 8.6 shows such effect, where the m and p parameters, used to quantify the airfoil camber and maximum thickness position in the 4-digit series of NACA airfoils, are plotted against t/T.

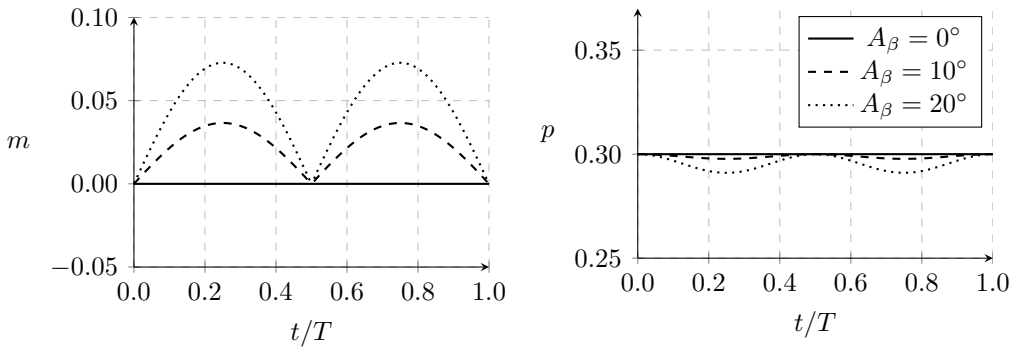

Figure 8.6: Geometric characteristics of NACA0012-IK30.

Consequently, by changing the curvature, we are directly changing the effective angle of attack. In the particular case of this NACA0012-IK30 configuration, deflecting the leading edge down to $-10.0°$ or $-20.0°$ reduces the effective angle of attack of the airfoil by approximately $3.0°$ and $6.0°$, respectively.

The flow visualization results shown ahead as sequences of images have a template presented in Figure 8.7. On the bottom, the t/T and the effective angle of attack are displayed, while on the top left corner, the Π symbol can be $\perp, \top, \uparrow, \downarrow$, meaning the lower, upper, ascending and descending positions, respectively. The oscillation period starts when the airfoil is at its lowest position ($\perp$).

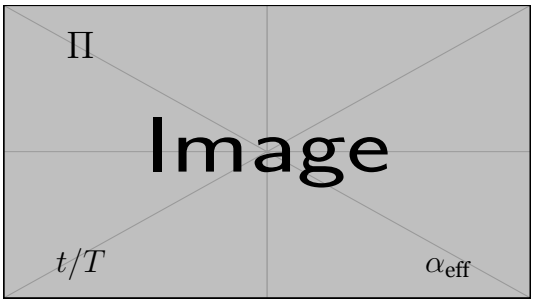

Figure 8.7: Flow visualization results template.

Although images give a good overall idea of the aerodynamic phenomena, videos are available at **https://www.earc96.com/PhD** for a deeper understanding of the results discussion. Moreover, sequences of images are presented in Appendix A1 for further examination.

Flow visualization tests are carried out with a pressure and temperature of $930(1)$ hPa and $18.0(1)$ °C, respectively. The Reynolds number is set constant to $Re = 1.0 \times 10^4$, which in the

literature is at the lower spectrum of the Reynolds number.

The figures shown in the following subsections have the airfoil positioned at the center of the frame, placed at about 2 cm from the wind tunnel exit. All images have the air flowing from right to left.

8.1.1 Flow fields with $h = 0.25$

This subsection concerns the flow fields at the lowest nondimensional amplitude tested ($h = 0.25$). The following images present three different reduced frequencies, each considering three separate leading-edge pitching amplitudes.

This first condition (Figure 8.8) is one of the slower oscillating cases ($k = 1.0$), with a nondimensional velocity of 0.25. Because of this, no extreme flow separation is observed or even expected. However, during descent, there is a small region of separated flow. Yet, it can not be concluded unequivocally from images where this region starts, but it most certainly originates at the gap dividing the leading edge and the ψ part.

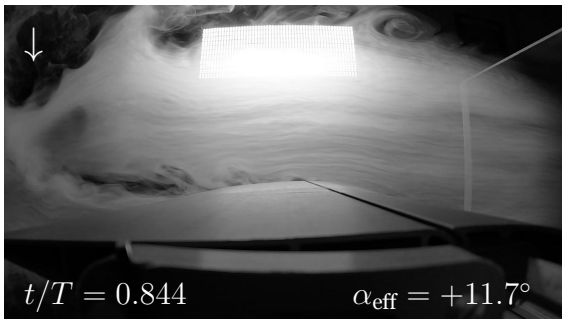

Figure 8.8: Flow visualization at $Re = 1.0 \times 10^4$, $h = 0.25$, $k = 1.0$ and $A_\beta = 0°$ at $t/T = 0.844$.

With the leading-edge pitching amplitude set to $10°$ (Figure 8.9), the flow dynamics barely change compared to the previous case. However, it is now clear that the flow separation during descent starts at the airfoil gap, extending downstream to the trailing edge. This flow separation can have a harmful influence since it creates a low-pressure zone located beyond the maximum thickness position, which does not have enough kinetic energy to reattach.

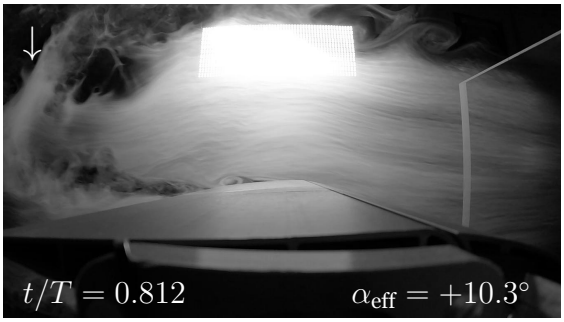

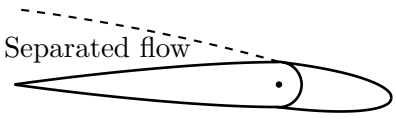

Figure 8.9: Flow visualization at $Re = 1.0 \times 10^4$, $h = 0.25$, $k = 1.0$ and $A_\beta = 10°$ at $t/T = 0.812$.

A leading-edge pitching amplitude of $20°$ (Figure 8.10) presents a new aerodynamic phenomenon that was not seen in this (k, h) condition. The difference resides at the top position,

where the flow separates due to the higher leading-edge pitching velocity. Furthermore, during the descent, the flow detaches right at the start of the ψ part, caused by the excessive camber of the airfoil. This event is typically not desired, as a separated flow region after the maximum thickness region may increase drag. This is a huge alert, reminding us that the leading-edge activation must be used wisely to avoid any aerodynamic performance degradation.

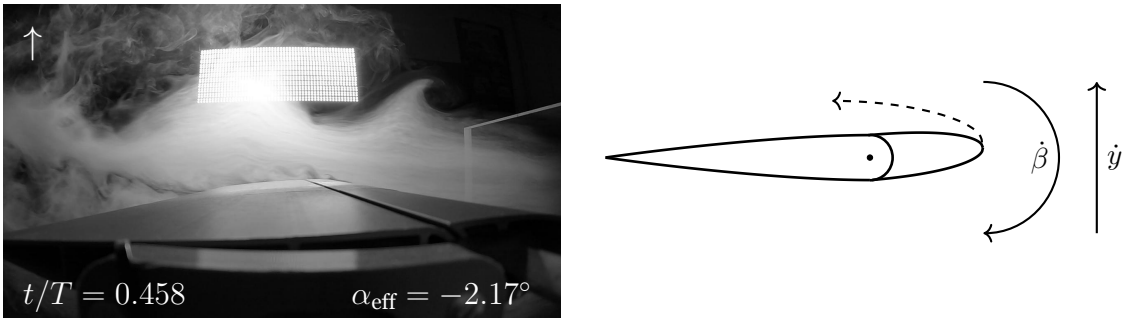

Figure 8.10: Flow visualization at $Re = 1.0 \times 10^4$, $h = 0.25$, $k = 1.0$ and $A_\beta = 20°$ at $t/T = 0.458$.

Flow separation becomes more evident when increasing the reduced frequency to 2.0 (Figure 8.11). During descent, the flow becomes separated at the leading edge, forming for a brief moment a leading-edge vortex that quickly disperses and moves towards the back part of the airfoil.

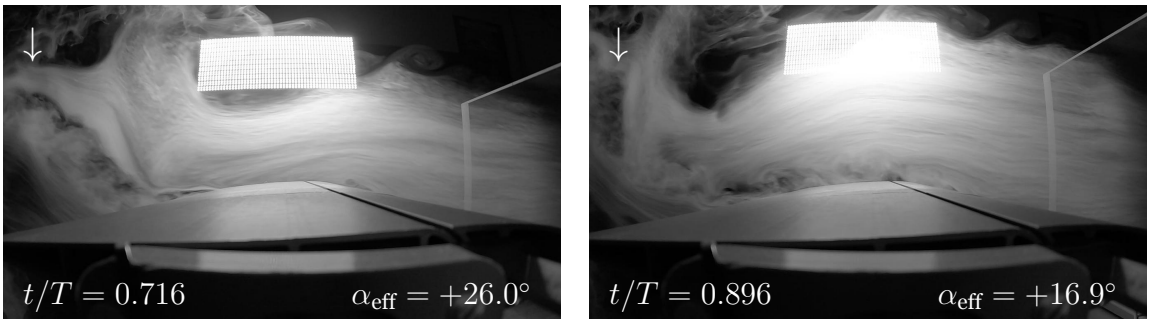

Figure 8.11: Flow visualization at $Re = 1.0 \times 10^4$, $h = 0.25$, $k = 2.0$ and $A_\beta = 0°$ at $t/T = 0.458$ and 0.896.

With $A_\beta = 10°$ (Figure 8.12), the flow dynamics change slightly. Flow still separates at the leading edge, but the detachment process is not as pronounced as in the plunging-only leading edge. Furthermore, the size of the region of the separated flow is slightly smaller when compared to the right image of Figure 8.11.

At the maximum tested leading-edge pitching amplitude (Figure 8.13), separation is reduced to a level where only a small zone of separated flow is seen at the leading edge, meaning that the intense adverse pressure gradient is no longer present. Massive flow separation is only present at the maximum thickness position where the airfoil has its maximum curvature.

At the highest reduced frequency tested, $k = 4$ (Figure 8.14), the aerodynamic phenomena surrounding the airfoil present some extreme features. The flow is detached from the airfoil for the whole period. During the descent, there is LEV formation of considerable size, while

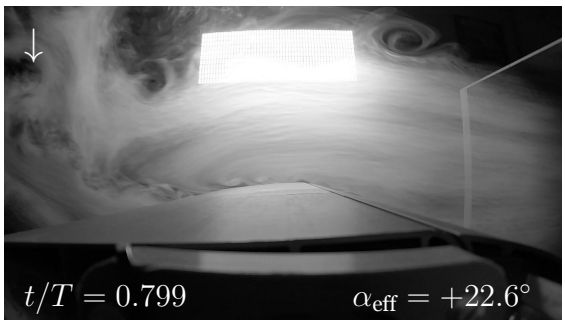

Figure 8.12: Flow visualization at $Re = 1.0 \times 10^4$, $h = 0.25$, $k = 2.0$ and $A_\beta = 10°$ at $t/T = 0.799$.

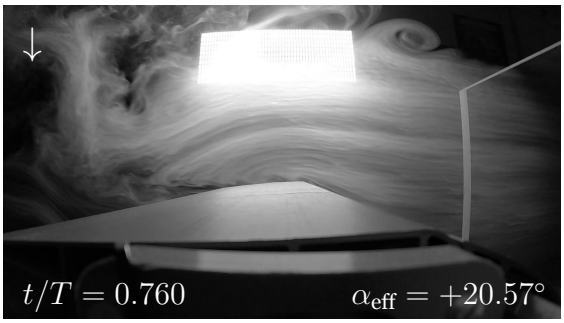

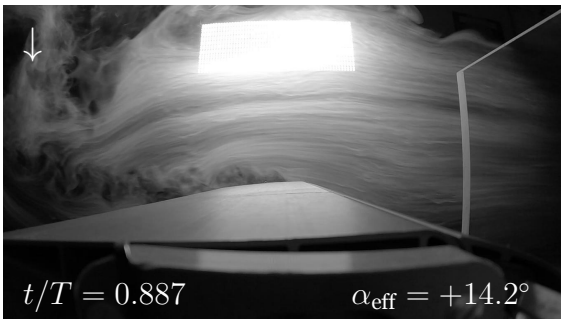

Figure 8.13: Flow visualization at $Re = 1.0 \times 10^4$, $h = 0.25$, $k = 2.0$ and $A_\beta = 20°$ at $t/T = 0.760$ and 0.887.

in the ascending phase, it is convected and dissipated. Due to the wide lens, we can also see the formation of the TEV behind the airfoil, with the typically mushroom-like structure indicating thrust production.

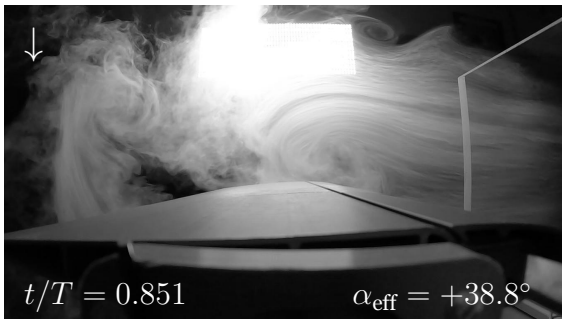

Figure 8.14: Flow visualization at $Re = 1.0 \times 10^4$, $h = 0.25$, $k = 4.0$ and $A_\beta = 0°$ at $t/T = 0.851$.

Deflecting the leading edge at $10°$ (Figure 8.15), flow separation is slightly alleviated. LEV formation is still present, although it breaks down when arriving at the lowest position.

When $A_\beta = 20°$ (Figure 8.16), the stall is reduced considerably. However, flow separation still appears at the leading edge, quickly moving towards the trailing edge. Thus, the separated flow region is convected downstream, clearing the airfoil-upper surface during the ascending phase, where almost no separated flow is observed.

8.1.2 Flow fields with $h = 0.50$

In this subsection, the first condition (Figure 8.17) represents the condition with the slower oscillating velocity at this nondimensional amplitude ($k = 0.5$). Even with a slower motion,

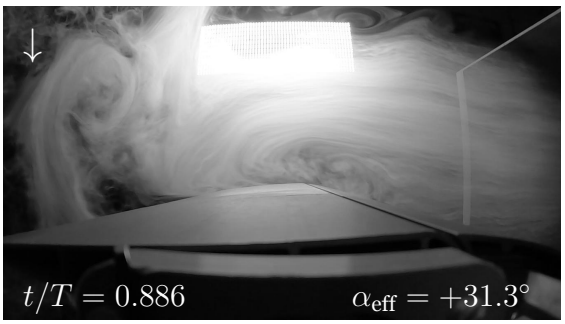

Figure 8.15: Flow visualization at $Re = 1.0 \times 10^4$, $h = 0.25$, $k = 4.0$ and $A_\beta = 10°$ at $t/T = 0.886$.

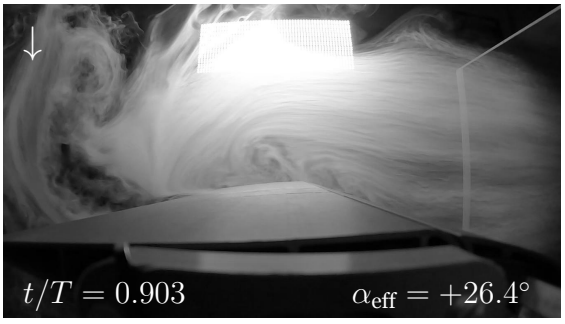

Figure 8.16: Flow visualization at $Re = 1.0 \times 10^4$, $h = 0.25$, $k = 4.0$ and $A_\beta = 20°$ at $t/T = 0.903$.

there is the possibility of flow separation. In fact, during the descending phase, the airfoil becomes stalled, with flow separation starting right at the leading edge.

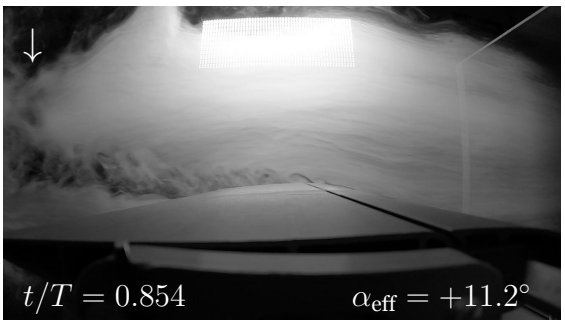

Figure 8.17: Flow visualization at $Re = 1.0 \times 10^4$, $h = 0.50$, $k = 0.5$ and $A_\beta = 0°$ at $t/T = 0.854$.

With a leading-edge pitching amplitude of $10°$ (Figure 8.18), the aerodynamic effects do not change considerably. The main difference is the flow separation starting point, which now starts at the back part and seems to be less intense. Like the conditions observed in the last subsection, this could indicate an increase in the overall drag production.

At the maximum leading-edge pitching amplitude (Figure 8.19), there is one significant effect to be examined. When the airfoil gets to the top position, the leading edge presents flow separation with a positive angle of attack. This comes as a consequence of excessive deflection of the leading edge which could not change the angle of attack quick enough to avoid flow separation. This condition, where clear flow separation occurs on the upper surface of the β part inevitably increases drag. During the descending phase, flow separation starts at the gap, as seen in other conditions.

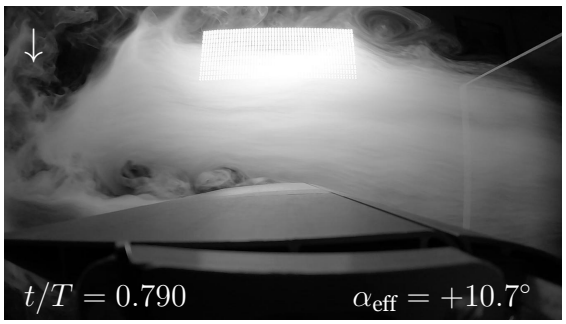

Figure 8.18: Flow visualization at $Re = 1.0 \times 10^4$, $h = 0.50$, $k = 0.5$ and $A_\beta = 10°$ at $t/T = 0.790$.

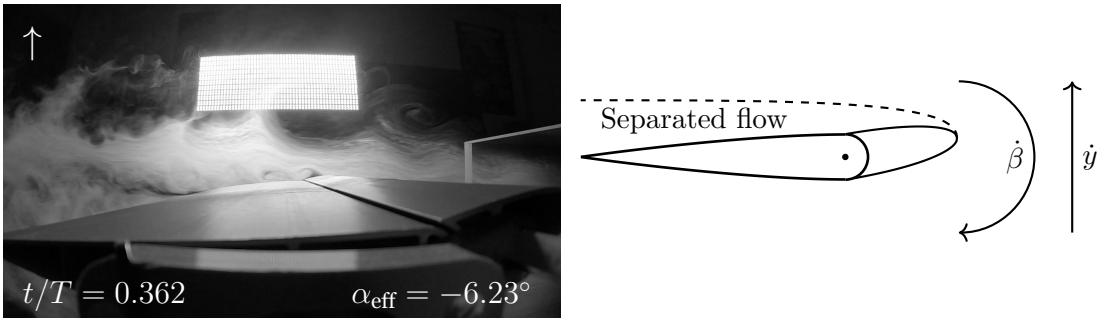

Figure 8.19: Flow visualization at $Re = 1.0 \times 10^4$, $h = 0.50$, $k = 0.5$ and $A_\beta = 20°$ at $t/T = 0.362$.

Increasing the reduced frequency to 1.0 (Figure 8.20), one can only expect the occurrence of stronger flow separation. This is corroborated by the existence of a leading-edge vortex, seen during the descent phase. However, it quickly dissipates and detaches from the airfoil's upper surface. At the ascending stage, flow quickly attaches to the airfoil.

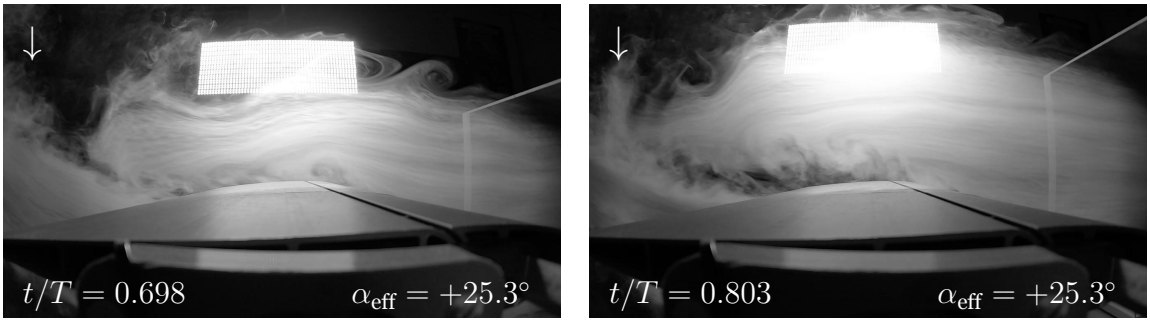

Figure 8.20: Flow visualization at $Re = 1.0 \times 10^4$, $h = 0.50$, $k = 1.0$ and $A_\beta = 0°$ at $t/T = 0.698$.

Setting the leading-edge pitching amplitude to $10°$ (Figure 8.21), as seen in other cases, reduces the strength of flow separation. Even with the leading edge deflecting, the flow still detaches at the leading edge, although at a much lower intensity compared to the non-deflecting case.

With $A_\beta = 20°$ (Figure 8.22) the flow does not separate at the leading edge anymore. However, the airfoil curvature close to the pivot of the leading edge does not assist in maintaining the flow attached to the back part, forming a notable region of separated flow.

When the reduced frequency is set to 2.0 (Figure 8.23), the aerodynamic phenomena sur-

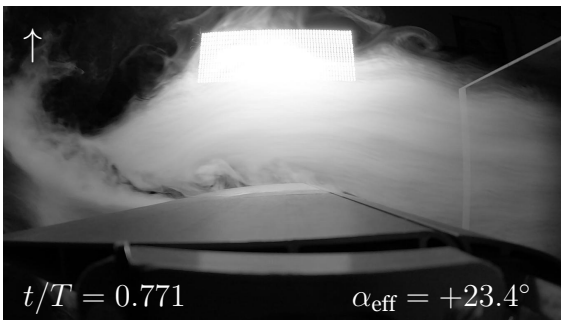

Figure 8.21: Flow visualization at $Re = 1.0 \times 10^4$, $h = 0.50$, $k = 1.0$ and $A_\beta = 10°$ at $t/T = 0.771$.

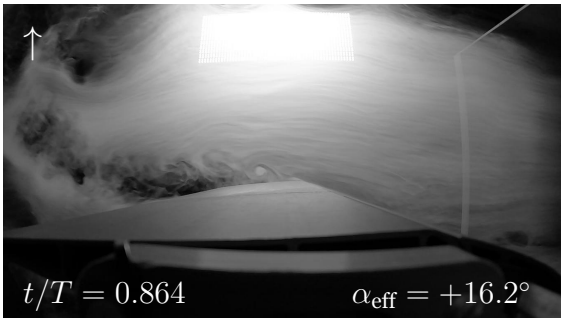

Figure 8.22: Flow visualization at $Re = 1.0 \times 10^4$, $h = 0.50$, $k = 1.0$ and $A_\beta = 20°$ at $t/T = 0.864$.

rounding the airfoil become severe. The flow remains detached at the airfoil for the majority of the period, with a clear LEV structure appearing during descent. This LEV structure is massive, with its diameter approximately the same size as the chord length. During the ascending phase, the LEV is convected downstream and mixed up with the wake.

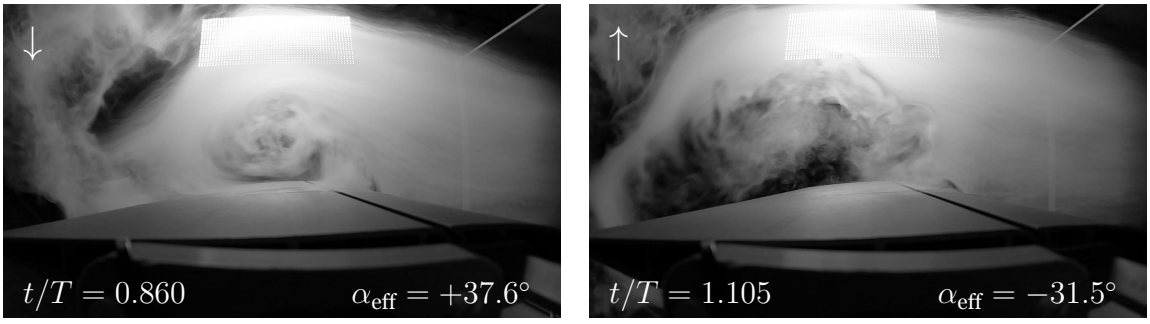

Figure 8.23: Flow visualization at $Re = 1.0 \times 10^4$, $h = 0.50$, $k = 2.0$ and $A_\beta = 0°$ at $t/T = 0.860$ and 1.105.

With $A_\beta = 10°$ (Figure 8.24), the leading-edge vortex is still distinguishable, but its formation occurs later during descent. When we compared the region of separated flow at this condition to the non-deflecting leading-edge case, the LEV has its size reduced by approximately 50 %.

The leading edge pitching at the maximum amplitude (Figure 8.25) further changes the dynamics of the LEV. In this condition, we cannot identify an obvious LEV structure but rather an intense region of detached flow. Moreover, the reduction of separated flow, compared to the nondeflecting leading edge, represents roughly a 75 % decrease.

To summarize the influence of the leading-edge pitching amplitude, Figure 8.26 shows the

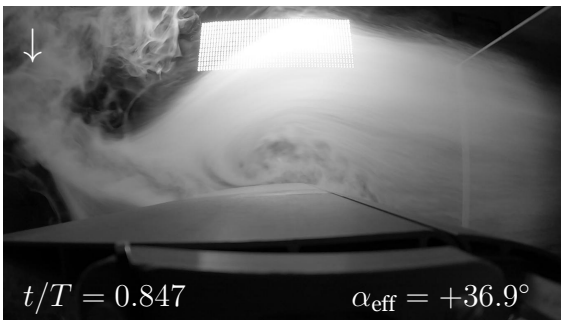

Figure 8.24: Flow visualization at $Re = 1.0 \times 10^4$, $h = 0.50$, $k = 2.0$ and $A_\beta = 10°$ at $t/T = 0.847$.

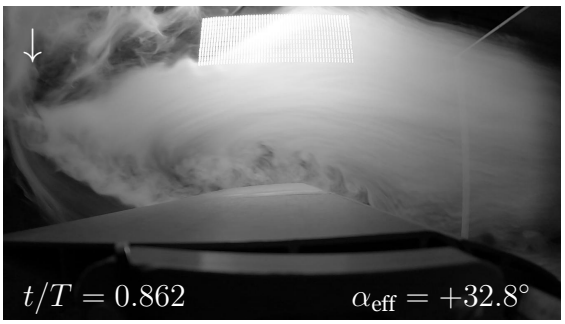

Figure 8.25: Flow visualization at $Re = 1.0 \times 10^4$, $h = 0.50$, $k = 2.0$ and $A_\beta = 20°$ at $t/T = 0.862$.

conditions with the higher nondimensional velocity for the two nondimensional amplitudes where massive flow separation was observed. In these images, we see that the leading-edge pitching amplitude has a crucial impact on the leading-edge vortex size. The LEV has its maximum size for the plunging-only cases, which is reduced as the pitching amplitude increases. It is clear that increasing the leading edge deflection and lowering the effective angle of attack of the β part delivers a reduction of the strength of the local adverse pressure gradient.

However, it is noteworthy that flow visualization cannot give reliable insight regarding force generation, although some conditions observed in this analysis may be good indicators, for instance, of drag production. Hence, it is relevant to correlate force generation with force data to verify, for example, if the LEV reduction is beneficial since there are authors, for instance, Gao et al. [75] who identified the leading-edge vortex as a thrust booster for plunging airfoils.

In the following section, the conditions tested experimentally will be reproduced numerically using a bidimensional CFD approach to study the aerodynamic and propulsive characteristics of the proposed geometry, while correlating them with the flow features observed. Moreover, the NACA012-IK30 airfoil will be compared with what is commonly seen in the field of unsteady aerodynamics so we can verify its potential.

8.2 Numerical Validation

Before advancing to the numerical results, we first conduct the numerical validation, which consists of two separate tasks: a mesh sensitivity study and a comparison with published

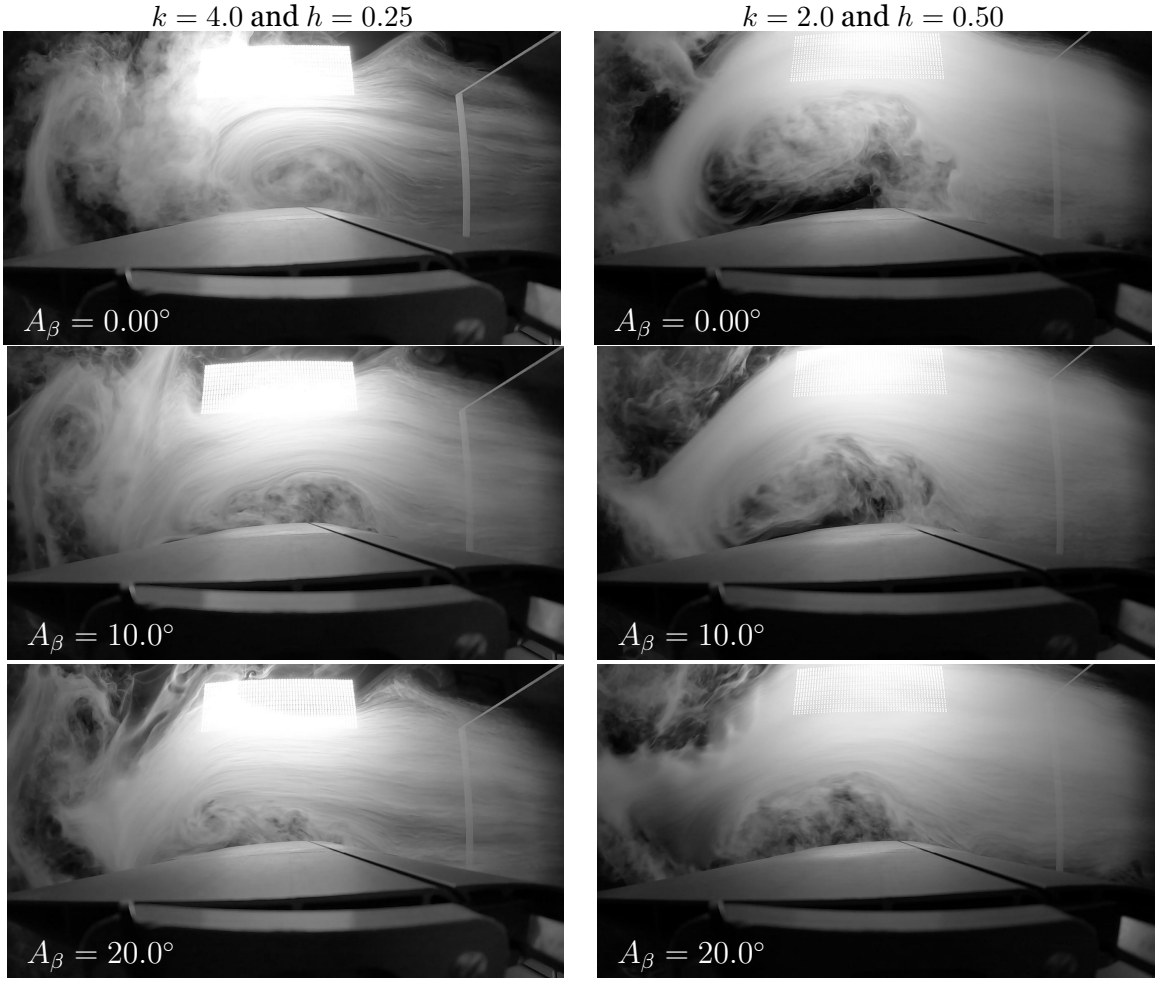

Figure 8.26: Comparison of leading-edge vortex size at $t/T = 1.000$.

data in the literature. As a complement, a qualitative comparison is made between flow visualization data and those obtained carrying out CFD simulations.

Figure 8.27 shows the propulsive power and required power coefficients over time at the lowest Reynolds number, with $h = 0.50,\ k = 1.00$ and $A_\beta = 5.0°$. In this condition, the SST $k-\omega$ is coupled with the Intermittency Transition model, and as required, the mesh elements close to the walls are designed to have a y^+ of approximately 1. First, the mesh sensitivity study consisted of creating a grid that fulfilled the mesh required with one hundred time steps per period. Then, the number of elements was duplicated and quadrupled with the number of time steps per period following the same logic, creating two more meshes with finer time steps. As seen in the aforementioned figure, no considerable differences are seen, indicating that mesh and time step independence were achieved. The propulsive and required power was used as the main focus of this validation, as they will be needed as propulsive indicators.

As seen in Figure 8.27, no considerable differences occurred, indicating that mesh and time step independence were achieved. Additionally, the present methodology is compared against numerical data of a plunging NACA0012 [63], as shown in Figure 8.28. The mean propulsive and required power coefficients are used to verify the reliability of the CFD results at such a

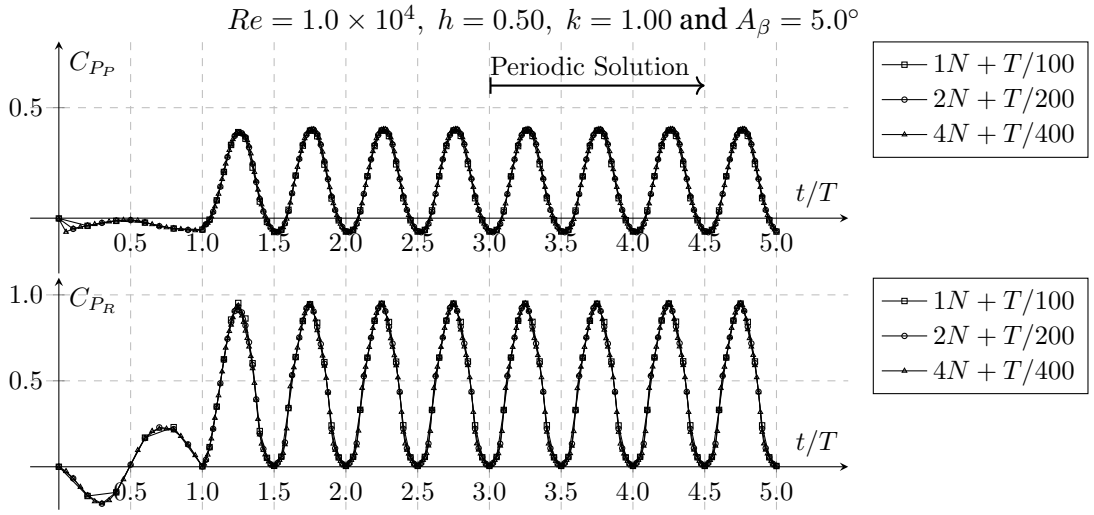

Figure 8.27: Mesh sensitivity analysis (plots are downsampled by a factor of five).

low Reynolds state. Computations are conducted at $Re = 2.0 \times 10^4$, $h = 0.175$ and a Strouhal number, St, between 0.1 and 0.4. Here, the Strouhal number is related to the nondimensional velocity, kh, as $kh = \pi St$.

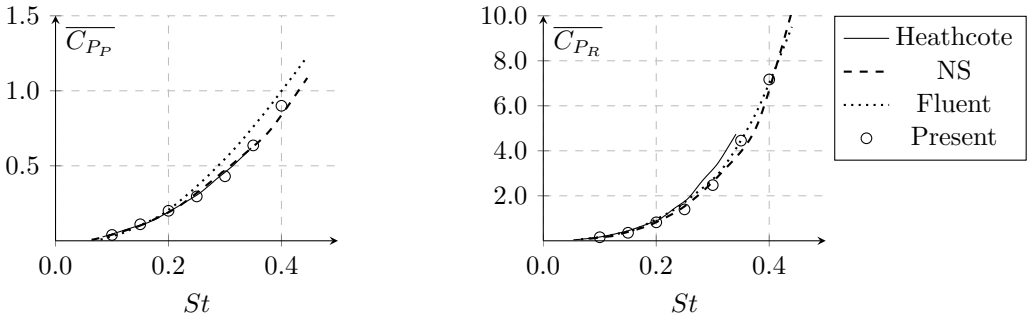

Figure 8.28: Numerical validation using data from [63] (NS and Fluent) and Heathcote et al. [37].

As aforesaid, a qualitative comparison of flow visualization data is made with numerical flow fields. Flow separation is analyzed by comparing the images obtained experimentally and the total pressure contours from CFD computations. The total pressure is used since in separated regions it presents lower values due to associated losses. As this is a qualitative evaluation with a focus on the flow field surrounding the flapping airfoils, the colormap of the images presented on the right is not shown. However, it is important to know that the colormap limits are not the same for different images, meaning that comparisons between different conditions can lead to erroneous conclusions. Hence, the analysis will be exclusively focused on the gradients of the total pressure.

The experimental and numerical flow fields are compared at $t/T = 0.75$ and 1.00, as effects during the ascending phase are the same, but symmetrical, to what is observed during the descending phase. These time instants are chosen to evaluate when the airfoil is at its maximum effective angle of attack ($t/T = 0.75$) and when it is inverting its plunging direction ($t/T = 1.00$), which gives a good idea of the overall flow separation phenomena occurring during the period. While five leading-edge pitching amplitudes were simulated, only the three

tested experimentally ($A_\beta = 5, 10$ and $10°$) are shown. Furthermore, for the two plunging amplitudes, only the lowest and highest reduced frequencies are presented.

8.2.1 Comparisons for $h = 0.25$ and $k = 1.0$ (Figure 8.29)

The first comparison is made for the lower nondimensional amplitude and reduced frequency. When the leading edge is not pitching, there is no significant separation even when the airfoil is at its maximum effective angle of attack ($t/T = 0.75$). From the CFD simulations, we can see a low-pressure zone at the leading edge, which creates a suction force pointing forward in the chordwise direction, resembling a thrust regime. At $t/T = 1.00$, the airfoil has a vortex being convected on the upper surface that is similar to what is seen on the experimental data, although the latter presents flow separation extending to the trailing edge.

With the leading-edge pitching at $10°$, the lowest pressure value is still at the frontal part of the airfoil, with the low-pressure region now extending downstream, beyond the maximum thickness position. Experimental tests show a small region of separated flow at the ψ part of the airfoil, which is also visible in the numerical-obtained flow field (green region). The now-existing curvature due to leading-edge rotation propitiates flow separation, and the existing discontinuity between the two parts seems to further intensify the phenomenon. This results in the flow separation detected close to the trailing edge at $t/T = 1.00$, which was expected as the deflection of the leading edge caused the low-pressure zone to move downstream. Overall, CFD computations agree with experimental data, showing less separate flow compared to when the leading edge is only plunging.

At the maximum leading-edge pitching amplitude ($A_\beta = 20°$), the lowest pressure zone is no longer located at the leading edge, being formed after the maximum airfoil thickness position (blue region). Experimental data agrees, which shows a more visible flow separation starting at the airfoil discontinuity and moving downstream. As the lowest pressure zone is located on the ψ part, pressure drag will inevitably increase. The results are similar with $A_\beta = 10°$ with only a slight increase in the region of separated flow.

8.2.2 Comparisons for $h = 0.25$ and $k = 4.0$ (Figure 8.30)

Keeping the same nondimensional amplitude but increasing the reduced frequency to its maximum value of 4, creates a more prominent flow separation, as expected by the increase of the overall effective angle of attack. With a plunging-only leading edge, there is a stronger and more concentrated vortex at the front seen both experimentally and numerically. At the end of the period ($t/T = 1.00$), the leading-edge vortex seen during descent continues to grow, creating a noticeable low-pressure zone. On the lower surface, there is a low-pressure zone (green region), illustrating the remains of the LEV formed during the ascending phase.

By deflecting the leading edge, the frontal part of the airfoil experiences a lower effective angle of attack, which reduces the intensity of flow detachment. This is verified at $A_\beta = 10°$ by the slightly smaller vorticity region in experimental data and numerical simulations. Al-

though difficult to observe, there is a low-pressure zone being formed at the discontinuity that will grow and be convected. With the dynamic deflection of the leading edge, the LEV seen at $t/T = 1.00$ in the CFD computations has its size reduced, which is also verified experimentally. However, due to the additional curvature, the small low-pressure zone identified before has grown and is roughly in the middle of the ψ part.

A similar result is seen at $A_\beta = 20°$, although experimentally, differences at $t/T = 0.75$ are minimal when compared to when the leading edge pitches at $10°$. Overall, the LEV structures are reduced by approximately 50 % when compared to the no-pitching case. Furthermore, the leading-edge vortex is further reduced, although the low-pressure region (pink region) seen at the back part increases, almost suggesting that the LEV is feeding this vortex formed downstream.

8.2.3 Comparisons for $h = 0.50$ and $k = 0.5$ (Figure 8.31)

In this subsection, the experimental-numerical comparison for the highest nondimensional amplitude is made for the lowest reduced frequency. This condition, in terms of the effective angle of attack, is equal to the first one analyzed at the lowest amplitude, as they have the same nondimensional velocity. However, the phenomena seen are quite different, indicating that the effective angle of attack may be an unreliable parameter when it comes to identifying flow structures and features.

Right at the first condition, where no flow separation was seen with $h = 0.25$ at $t/T = 0.75$, we notice a low-pressure zone already at the airfoil maximum thickness position, with a red region downstream denouncing a higher pressure zone. At the end of the period, the flow separation grows bigger, creating a large wake region.

With $A_\beta = 10°$, flow separation exists but is now located close to the trailing edge, suggesting that it was transported quickly on the airfoil's surface. However, at $t/T = 1.00$, the flow fields are fairly similar to what was seen in the previous condition.

By increasing the leading-edge pitching amplitude to $20°$, the region of separated flow obtained numerically recedes close to where it was in the no-pitching case, which differs from what is seen experimentally, where flow separation seems to extend up to the trailing edge. At the end of the period, the flow field is similar, although being slightly smaller compared to the previous cases.

8.2.4 Comparisons for $h = 0.50$ and $k = 2.0$ (Figure 8.32)

At the highest reduced frequency for a nondimensional amplitude of 0.50, flow features become more prominent in the flow field, suggesting that a higher nondimensional amplitude creates larger length-scale structures. Similarly to what was seen in $h = 0.25$ and $k = 4.0$ condition, which has the same nondimensional velocity and thus the same maximum effective angle of attack, there is LEV formation as denounced by the concentrated lower pressure

zone seen during descent.

With a plunging-only leading edge, the LEV is visible during descent. Such phenomenon is seen both numerically and experimentally, although smoke density makes it hard to identify the vortical structure accurately. At the end of the period, the LEV has grown to a considerable size.

During descent, as the leading-edge pitching amplitude increases up to $20°$, the leading-edge vortex size decreases as expected by the decrease in the effective angle of attack of the β part. However, as seen in $h = 0.25$ and $k = 4.00$, a low-pressure zone appears beyond the maximum airfoil thickness position. At this nondimensional amplitude, this region is much more visible. One could argue, based on these images, that the LEV is being transformed into this vortical region as the leading-edge pitching amplitude increases.

Experimentally, we see leading-edge vortices with approximately the chord size, although their shape is slightly different depending on the leading-edge pitching amplitude. Flow fields obtained numerically give a clearer idea of the influence of A_β in which higher pitching amplitudes change the LEV from a circular form to a more oval shape that stays closer to the airfoil.

Area left intentionally blank.

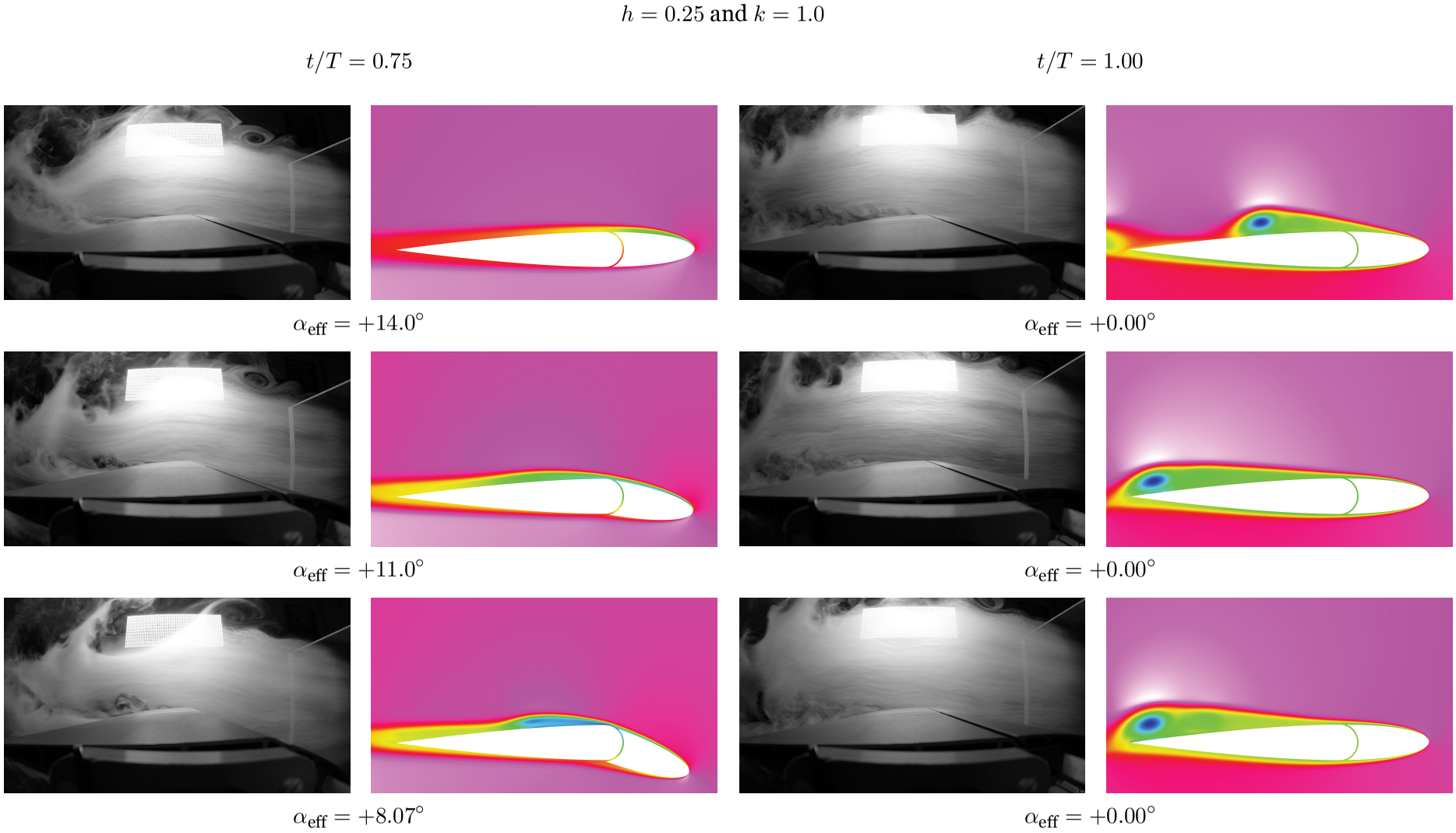

Figure 8.29: Experimental *Vs* Numerical comparisons at $h = 0.25$ and $k = 1.0$.

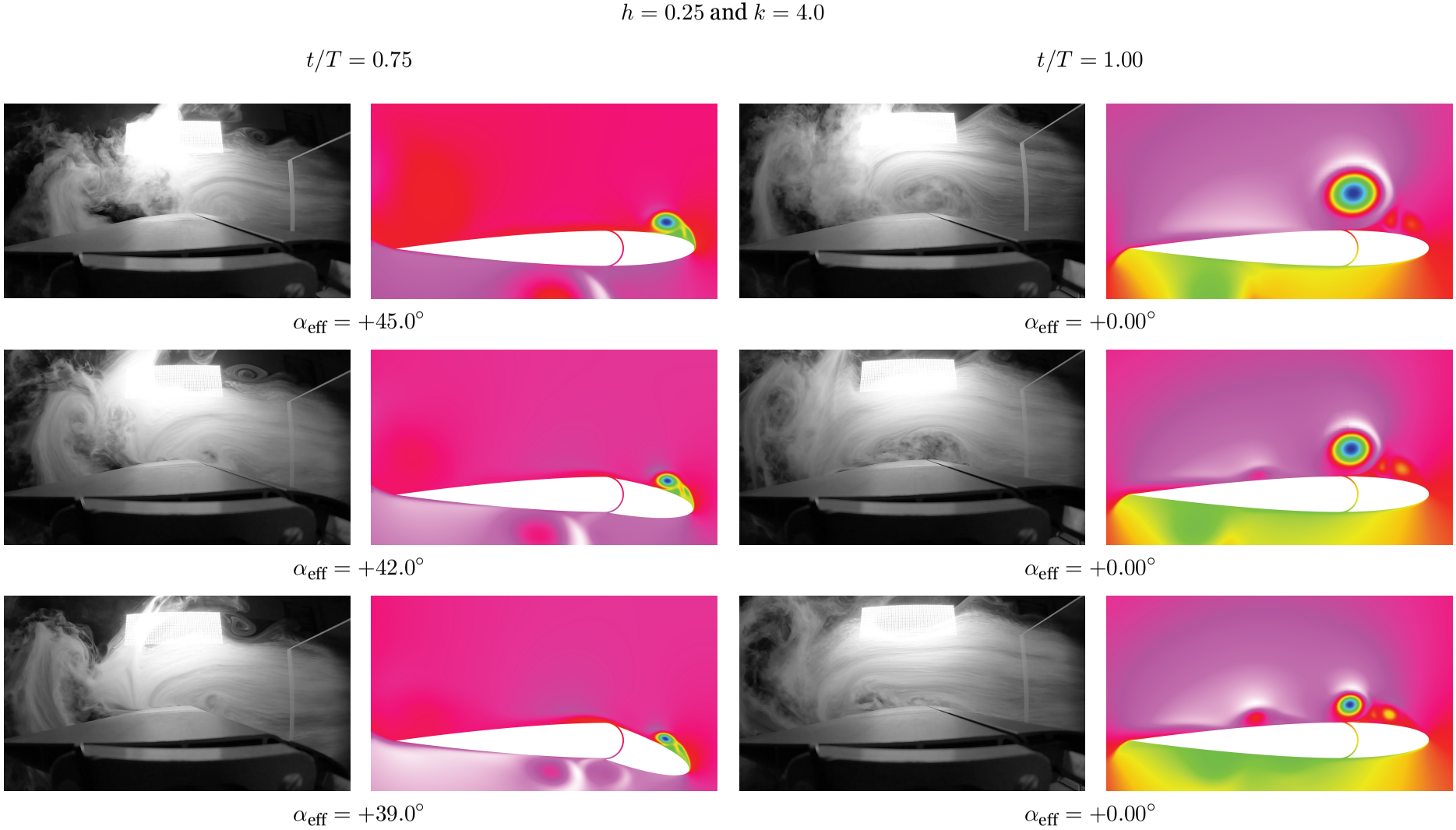

Figure 8.30: Experimental *Vs* Numerical comparisons at $h = 0.25$ and $k = 4.0$.

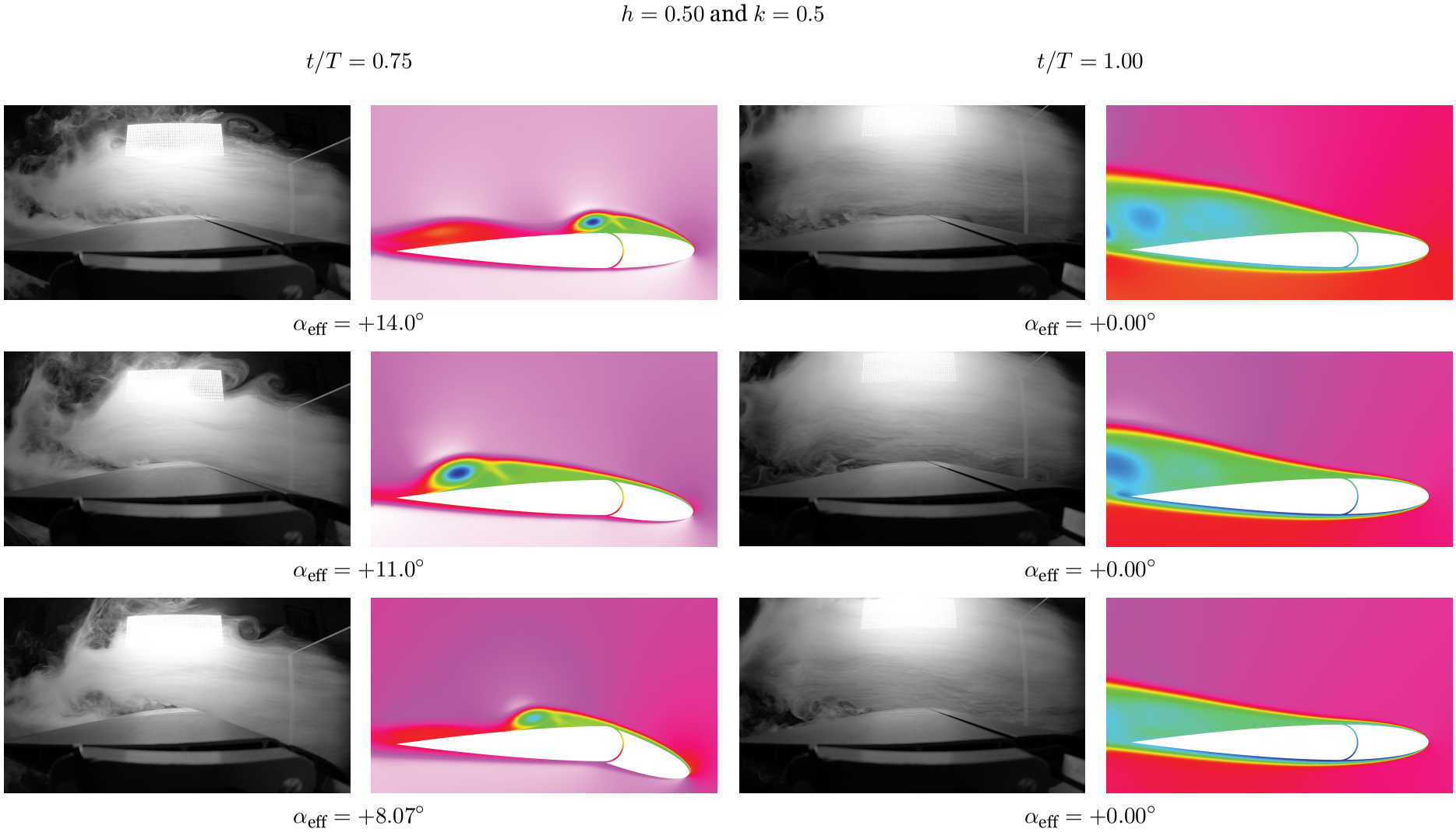

Figure 8.31: Experimental *Vs* Numerical comparisons at $h = 0.50$ and $k = 0.5$.

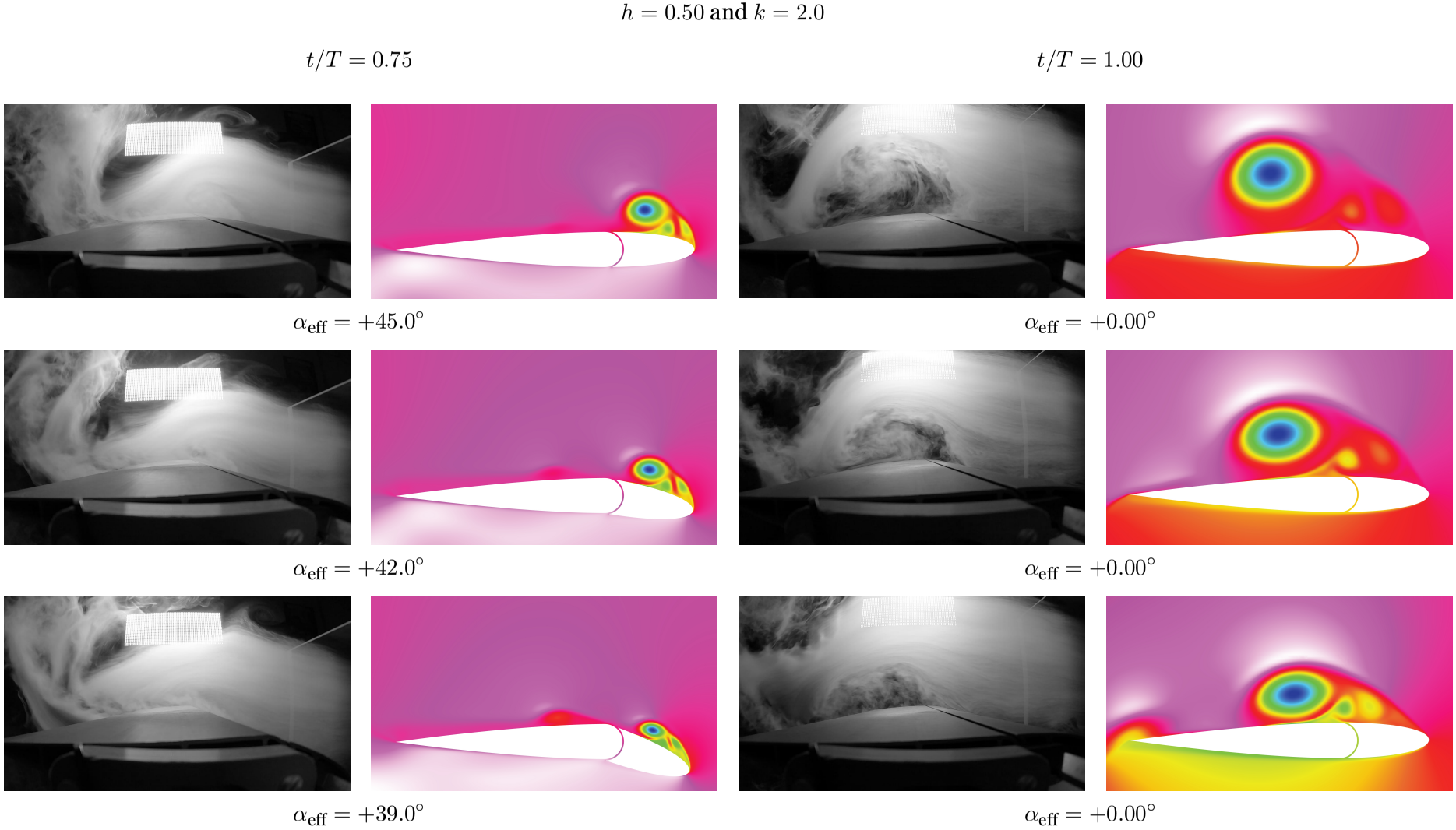

Figure 8.32: Experimental *Vs* Numerical comparisons at $h = 0.50$ and $k = 2.0$.

8.3 Propulsive Performance

Although some of the CFD results seen in the section before are slightly different from those obtained experimental, mainly the tardiness of predicting some of the flow separation, the overall performance of the established CFD methodology predicts the flow field characteristics fairly accurately.

Based on what is considered a valid numerical validation, we can move toward the analysis of the propulsive performance of the NACA0012-IK30 airfoil for the 30 cases simulated. The propulsive performance is evaluated using three parameters: the mean propulsive power, the mean required power, and the propulsive efficiency.

The analysis consists of discussing these three propulsive indicators for the two nondimensional amplitudes. In each graph, all nondimensional velocities are plotted, as a function of the leading-edge pitching amplitude. Compared to the conditions tested experimentally, two additional leading-edge pitching amplitudes are tested: $5°$ and $15°$.

In Figure 8.33, the mean propulsive power coefficient is plotted for the three nondimensional velocities considered. Overall, increasing the pitching amplitude is beneficial up to a certain value where $\overline{C_{P_P}}$ starts decreasing, except when $kh = 1.00$, a condition where we did not reach the maximum. Results also show that the slower flapping condition does not benefit from the dynamic leading edge or presents good propulsive capabilities, being very close to a drag-producing regime. While both nondimensional amplitudes have fairly similar behavior, with $h = 0.50$, improvements in terms of magnitude are much more significant. When it comes to the mean propulsive power, improvements of up to $177.4\,\%$ relative to the plunging-only case can be achieved. Based on the shape of the graphs we see that, at this nondimensional amplitude, the β amplitudes that generate higher mean propulsive power coefficients move to the right as the reduced frequency increases. This suggests that kinematics that generate higher effective angles of attack require higher leading-edge pitching amplitudes to maximize the mean propulsive power coefficient.

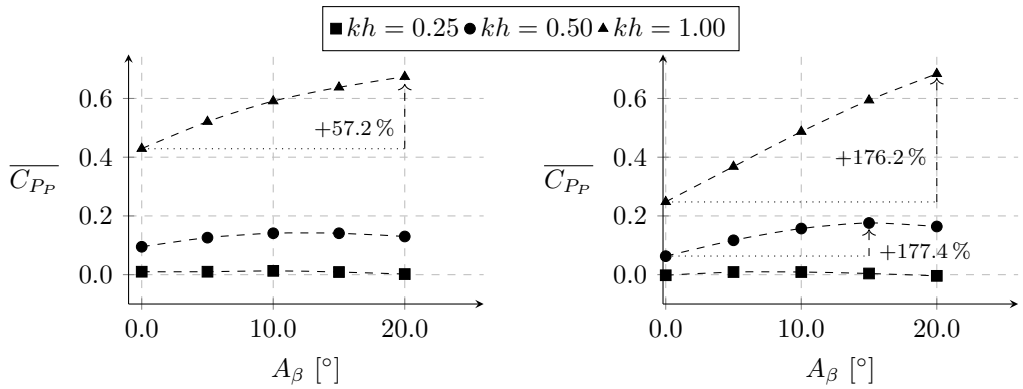

Figure 8.33: Mean propulsive power coefficient with $h = 0.25$ (left) and $h = 0.50$ (right).

When it comes to the mean required power coefficient, shown in Figure 8.34, the influence of the dynamically activated leading edge is overall beneficial but rather small, except for the

case with the lower amplitude and highest nondimensional velocity. In this specific case, the required power decreases linearly as A_β increases, with a $13.0\,\%$ reduction compared to the plunging-only leading edge.

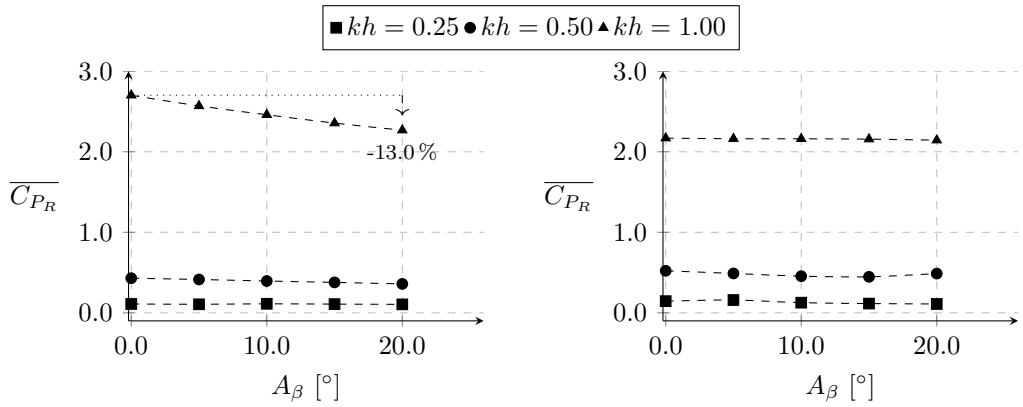

Figure 8.34: Mean required power coefficient with $h = 0.25$ (left) and $h = 0.50$ (right).

Combining the two propulsive coefficients results in the propulsive efficiency shown in Figure 8.35. By basically keeping the mean required power coefficient constant and increasing the propulsive power, there is an inevitable increase in the propulsive efficiency. The graphs indicate that when the leading edge is deflected, great improvements are achieved for both nondimensional amplitudes with astonishing increases of up to $229.8\,\%$. Overall, higher propulsive efficiency is seen for the middle nondimensional velocity, although it is not clear if $kh = 1.00$ could offer better efficiency at larger pitching amplitudes since no larger values were studied in this parametric analysis.

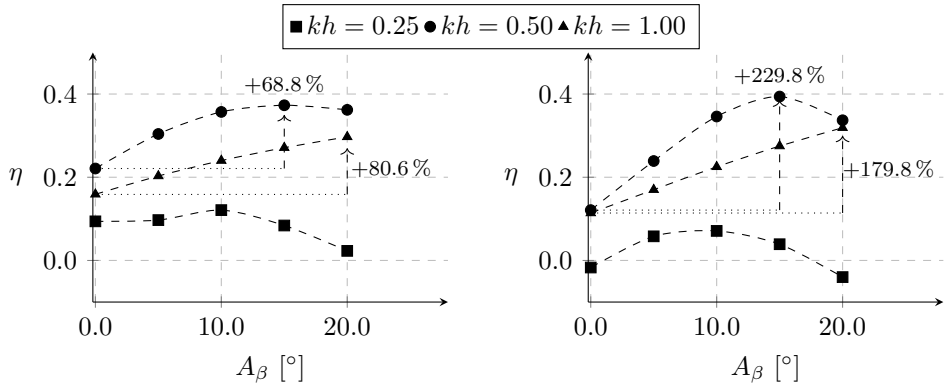

Figure 8.35: Propulsive efficiency with $h = 0.25$ (left) and $h = 0.50$ (right).

8.4 Correlation of Propulsive Indicators with Flow Features

The differences observed in the propulsive indicators come from the changes induced in the flow field surrounding the airfoil by the proposed geometry. To better understand the impact of the dynamically activated leading edge, this section presents several snapshots of the flapping airfoil at its lowest position ($t/T = 1.00$), considered a cumulative representation of what occurred during the period. The grid layout shown in figures 8.36 and 8.37 shows

the influence of both reduced frequency and leading-edge pitching amplitude for the two nondimensional amplitudes by using the total pressure contours.

As the reduced frequency increases, the presence of the leading-edge vortex becomes more evident and moves upstream. This is expected as a higher reduced frequency means that a critical effective angle of attack that triggers separation is reached quicker, and thus the LEV formation starts earlier. In a plunging airfoil, the leading-edge vortex only works as a thrust enhancement feature when located upstream of the maximum thickness position. Interestingly, the NACA0012-IK30 airfoil follows the same principle even though it cannot be considered to be a simple plunging airfoil.

For the lower nondimensional amplitude, at the lowest reduced frequency, the deflection of the leading edge simply moves the LEV downstream with no major differences between the pitching cases. This is backed up by previous graphs where the mean propulsive power did not show a significant dependence on the leading-edge pitching amplitude.

However, for the other two reduced frequencies ($k = 2.0$ and 4.0), there is a stronger dependence on A_β, which can be correlated to what is seen in the flow field. Starting with $k = 2.0$, we see that when increasing the leading-edge pitching amplitude, the LEV present in $A_\beta = 0.0°$ becomes smaller and feeds another vortex that appears beyond the maximum thickness position.

At the same time, looking at the mean propulsive coefficient we see that its concave-shaped function means that there is an optimal value of pitching amplitude that maximizes the mean propulsive power. That value is somewhere between $10°$ and $15°$. When comparing the mean propulsive power coefficient and the flow fields, we see that to obtain good performance one should reduce the LEV intensity but only up to a certain point.

This result is central to the analysis of this mechanism because it clearly states that we are not pursuing the total elimination of the LEV, instead, we are looking for a way to exploit its presence. This means that understanding the LEV dynamics (its position, intensity, and residence time on the airfoil) is crucial to optimally use the NACA0012-IK30 as a thrust enhancement mechanism. Nonetheless, when the leading edge is pitching at its maximum amplitude, where no LEV is seen, the airfoil can still provide better performance than the plunging-only leading edge.

The same is seen for $k = 4.0$, although at $A_\beta = 20.0°$ there is still a clear leading-edge vortex. This denounces that the leading-edge pitching amplitude is not able to greatly reduce the LEV size, the reason why $\overline{C_{P_P}}$ is still increasing at such an angle of attack.

The same effects are seen for the highest nondimensional amplitude ($h = 0.50$), although in a more intense way, as one sees by the LEV sizes shown in Figure 8.37. Even though the nondimensional velocities are kept the same, meaning that the effective angle of attack is the

same, higher nondimensional amplitudes enlarge the flow-separated zones.

However, even with all these differences, we can conclude that if there is no leading-edge vortex present, there is no real improvement concerning the thrust performance, making the NACA0012-IK30 mechanism an LEV exploiting mechanism. Keeping in mind that the leading-edge vortex will eventually pass the maximum thickness position, one should strive to find the LEV intensity that enhances thrust, while at the same time, minimizing its influence when the LEV is at the ψ part, which the proposed geometry showed it can do.

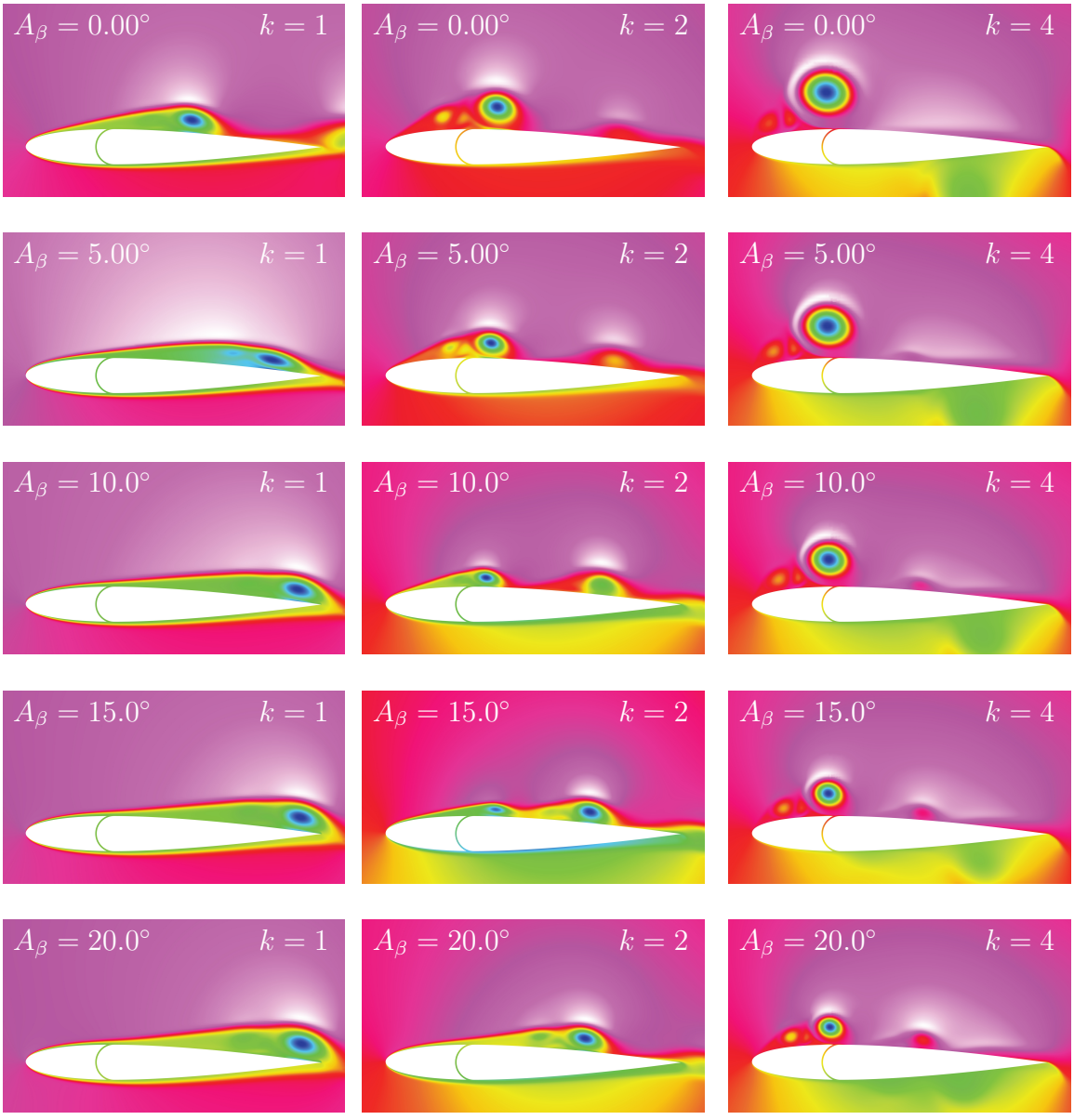

Figure 8.36: Total pressure contour at $h = 0.25$ at $t/T = 1.00$.

8.5 Instantaneous Coefficients

While the propulsive parameters and flow fields are important to understanding the overall performance of flapping airfoils, they fail to explain the most fundamental reasons that justify

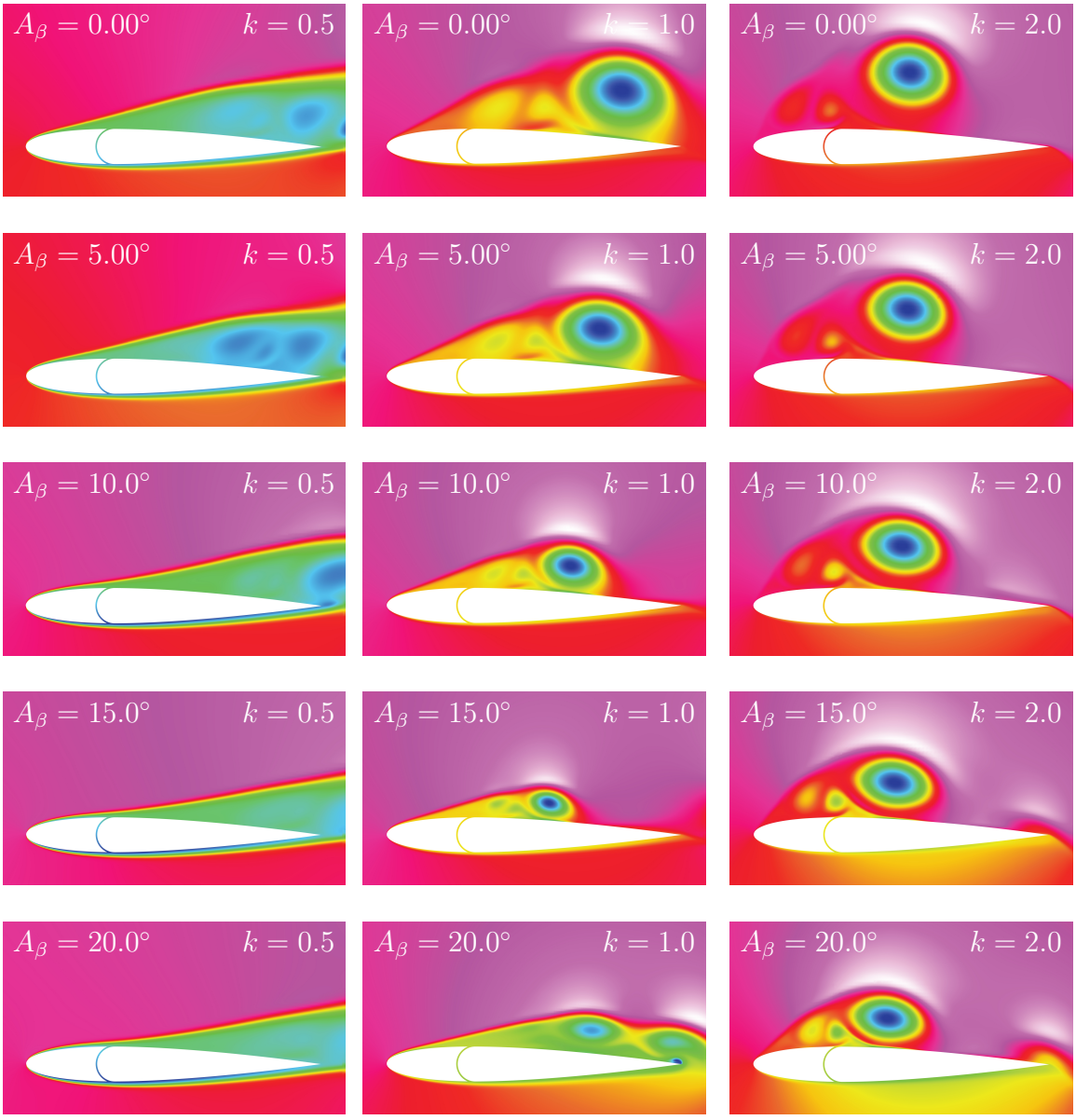

Figure 8.37: Total pressure contour at $h = 0.50$ at $t/T = 1.00$.

the changes seen in the propulsive indicators. Thus, this section aims to offer a deeper understanding of the results presented before by analyzing the propulsive power and required power coefficients as a function of time. For a brief comparison, CFD results are contrasted against the ones obtained with the unsteady panel method presented in Chapter 6. This approach identifies the influence of the NACA0012-IK30 mechanism, more specifically the time frames that impact the mean coefficients. The following graphs are focused only on the conditions that show good propulsive characteristics and a clear dependence on the leading-edge pitching amplitude, $kh = 0.50$ and 1.00.

In Figure 8.38, the propulsive power is shown as a function of t/T for a nondimensional velocity of 0.50. To simplify the analysis, only three leading-edge pitching amplitudes are presented. Deflecting the leading edge improves the propulsive power for the vast majority of the oscillating period, with the greatest improvements seen when the airfoil has its maximum

effective angle of attack ($t/T = 0.25$ and $t/T = 0.75$). However, results also show that the continuous increase of A_β may not be beneficial, where the pitching amplitude can lead to the degradation of the propulsive power, as observed in $t/T = 0.50$.

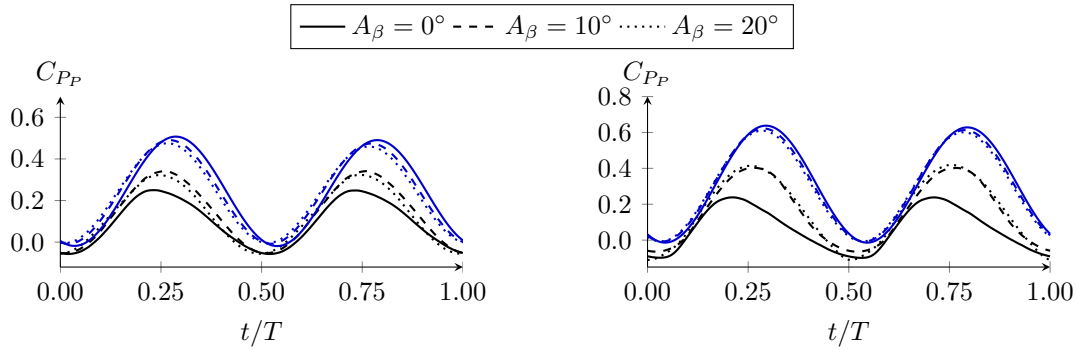

Figure 8.38: C_{P_P} as a function of t/T with $kh = 0.50$ for $h = 0.25$ (left) and $h = 0.50$ (right). CFD and UPM results in black and blue, respectively.

When looking at the UPM results, it is clear that there is an overestimation of the thrust production, mainly due to the lack of separated flow, as seen ahead. Furthermore, deflecting the leading edge will lead to a slight thrust decrease that is caused by the reduction of the suction located at the frontal part of the airfoil, also shown afterward.

At the highest nondimensional velocity, shown in Figure 8.39, propulsive power is highly favored by the leading-edge pitching amplitude. Once again, bigger improvements are seen when the airfoil is at its maximum plunging velocity. This coincides with the instant where the leading edge has its maximum angle of attack, enlarging the frontal area of the airfoil, which leads to an increase in thrust. This will be presented ahead using the pressure distribution around the airfoil. For the range studied, higher pitching amplitudes lead to higher propulsive power, although a pitching ceiling similar to the $kh = 0.50$ case is expected since excessive deflection presents no real benefit.

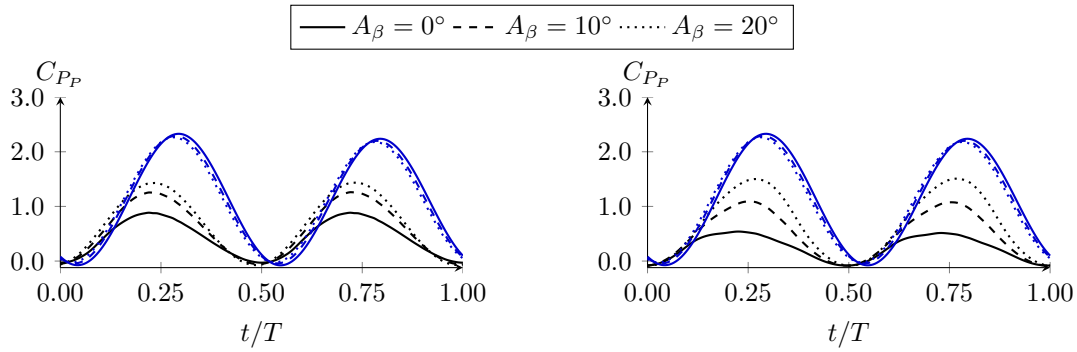

Figure 8.39: C_{P_P} as a function of t/T with $kh = 1.00$ for $h = 0.25$ (left) and $h = 0.50$ (right). CFD and UPM results in black and blue, respectively.

This ceiling was solely not observed due to the relative importance between the plunging and pitching terms in the effective angle of attack. The reduction in α_{eff} that the leading edge can provide is limited to $6°$ when the pitching amplitude is set at $20°$. This means that increasing

the kh reinforces the dominance of plunging over pitching. In fact, if we consider the ratio

$$\frac{\arctan(kh)}{\arctan\left(\dfrac{c_\beta \sin A_\beta}{c_\beta \cos A_\beta + c_\psi}\right)}, \tag{8.3}$$

it shows that the contribution of plunging to the effective angle of attack goes from 4.5 to 7.5 times the pitching contribution when the nondimensional velocity increases from 0.50 to 1.00. This is why we need higher pitching amplitudes at higher nondimensional velocities to achieve better propulsive power, as we saw in Figure 8.33.

In this condition, it is interesting to see how deflecting the leading edge pushes the CFD results closer to the inviscid solution. This may be because deflecting the leading edge in real flow can lead to the minimization of the flow separation, which is a regime where potential flow truly stands out. Additionally, it is worth mentioning that during the accelerating phases, $0.00 - 0.25$ and $0.50 - 0.75$, the panel method provides a good approximation, which may denounce that this is a time window where none or negligible separation is present.

Concerning the required power, it was seen that its mean value decreases with the leading-edge pitching, although showing an overall small dependence on it, excepting some cases at the lowest nondimensional amplitude. This is reinforced in Figure 8.40, which shows that the deflection of the leading edge causes indeed a reduction of power consumption during the acceleration phases of the period.

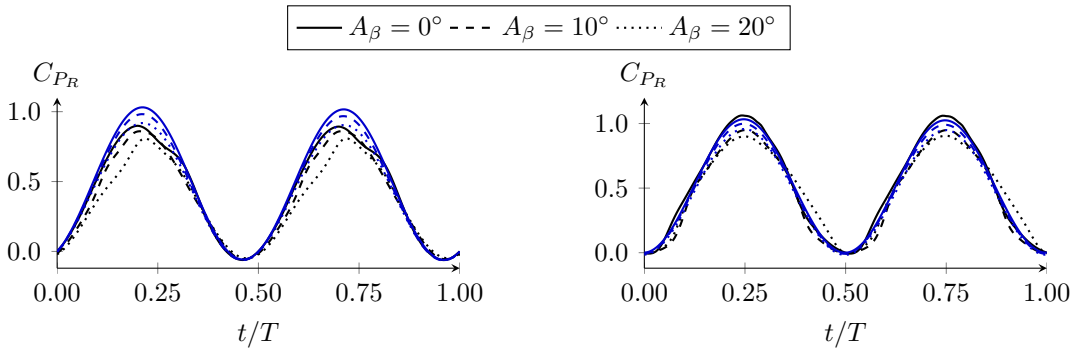

Figure 8.40: C_{P_R} as a function of t/T with $kh = 0.50$ for $h = 0.25$ (left) and $h = 0.50$ (right). CFD and UPM results in black and blue, respectively.

Contrarily to the propulsive power, the panel code provides a very good prediction of the consumed power for the two amplitudes. Additionally, as in the CFD computations, deflecting the leading edge provides a slight reduction in the required power, due to lowering the effective angle of attack that consequently reduces lift.

In Figure 8.41, the power consumption for the highest nondimensional velocity is shown. Overall, the required power coefficient is similar to the previous case, having its biggest reduction at $t/T = 0.25$ and $t/T = 0.75$, where compared to the baseline case, the airfoil experiences a smaller effective angle of attack. Although this is also verified for $h = 0.50$, for the rest of the period, the leading-edge deflection slightly increases power consumption, counter-

acting those gains. This is why some of the cases analyzed in the mean power consumption are almost independent of the pitching amplitude.

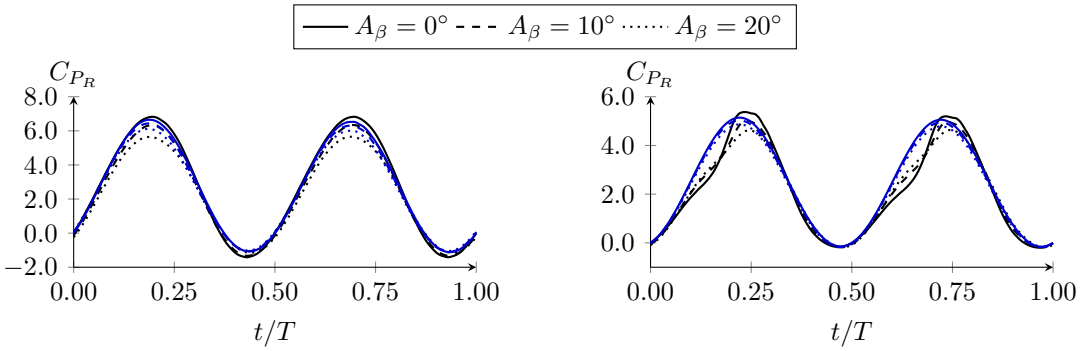

Figure 8.41: C_{P_R} as a function of t/T with $kh = 1.00$ for $h = 0.25$ (left) and $h = 0.50$ (right). CFD and UPM results in black and blue, respectively.

Once again, the panel code provides an adequate approximation, being a very interesting result since this is a condition where severe flow separation is present, and still, the potential flow approach can predict quite accurately the lifting forces, and thus consumed power.

To better understand the impact of the dynamically activated leading edge, some snapshots of the numerical flow field are presented, together with the airfoil pressure distribution. Also, a brief comparison is made between the CFD results and the pressure distribution obtained by the unsteady panel method. The flow fields are shown only for $h = 0.50$ at $t/T = 0.75$, where satisfactory propulsive improvements were seen for $kh = 0.50$ and 1.00. Flow visualization data is also provided for additional comparisons.

In Figure 8.42, the condition $h = 0.50$ and $kh = 0.50$ is presented. The influence of the movable leading edge on the flow field is clear, especially regarding the dynamics of the leading-edge vortex and the pressure distribution around the airfoil. By increasing the leading-edge pitching amplitude, the suction peak located at the front decreases. Not only that, a low-pressure zone located beyond the maximum thickness position grows in intensity. For $A_\beta = 20°$, its intensity approaches the suction level present at the leading edge, but interestingly, it does not reduce propulsion as seen in Figure 8.38 (right). This can only be justified by the enlarged frontal area provided by the leading-edge deflection, which increases the horizontal component of the aerodynamic force (resultant force) of the airfoil.

Regarding the panel method results, as expected, it presents an extremely high suction peak at the leading edge, which cannot be sustained in real flow, confirmed by the presence of a leading-edge vortex in the numerical flow field. Additionally, it is also seen that a low-pressure zone is present at the back part, where CFD shows a bump in the pressure coefficient. Interestingly enough, the panel code also has this C_p prominence, although for a much different reason. Due to the leading-edge deflection, the whole airfoil presents a dynamic curvature close to the pivot point ($0.3c$). With this curvature, a low-pressure zone is needed around the pivot to guarantee that the air remains attached to the surface. This is

the reason why the UPM presents this C_p bump and not because of highly nonlinear effects such as vortex shedding. Also worth mentioning is the fact that, as the leading-edge pitching amplitude increases, the UPM starts offering a better aerodynamic representation of the pressure distribution, especially at the frontal part. This may be attributed to the absence of extreme flow separation.

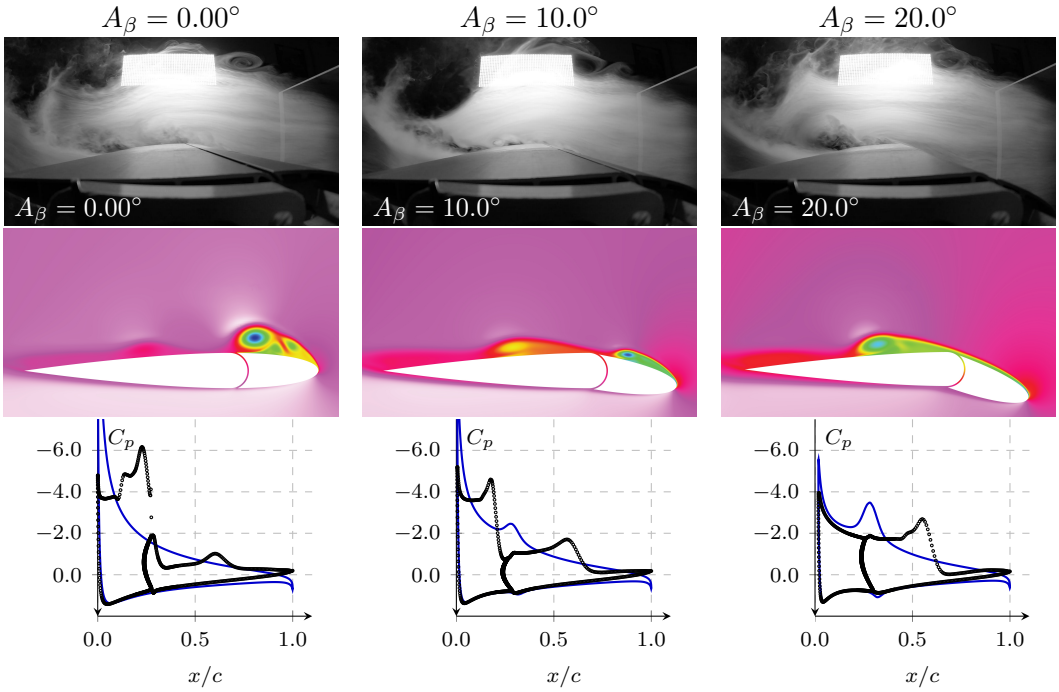

Figure 8.42: Flow fields with $h = 0.50$ and $kh = 0.50$ at $t/T = 0.75$. CFD and UPM results in black and blue, respectively.

In Figure 8.43, the same plunging amplitude is considered while the nondimensional velocity is increased to 1.00. Results are similar to $kh = 0.50$ but effects are magnified, as expected by the higher effective angle of attack imposed by the larger nondimensional velocity. However, contrary to the previous case, the suction peak is not greatly influenced by the leading-edge deflection, reinforcing the fact that propulsive augmentation mainly comes from the increase in the frontal area created by the pitching of the frontal part. Unlike the previous case, the leading-edge pitching amplitudes considered could not mitigate LEV formation. For that, a higher A_β needs to be considered. Moreover, the small influence that the leading-edge pitching amplitude has on the pressure distribution shows once again that the plunging component dominates the effective angle of attack.

Concerning the UPM results, similar effects are observed. Results show the same limitations that arise from a potential flow approach, but some regions of the airfoil, for instance, the lower surface, are well represented by its solution.

The presence of the leading-edge vortex is justified by a strong adverse pressure gradient located right at the leading edge, which is seen in the pressure distribution graphs close to $x/c = 0.00$, where there is a rapid increase in pressure. This pressure gradient at the leading edge can be greatly alleviated using the leading-edge deflection, as verified in Figure 8.42

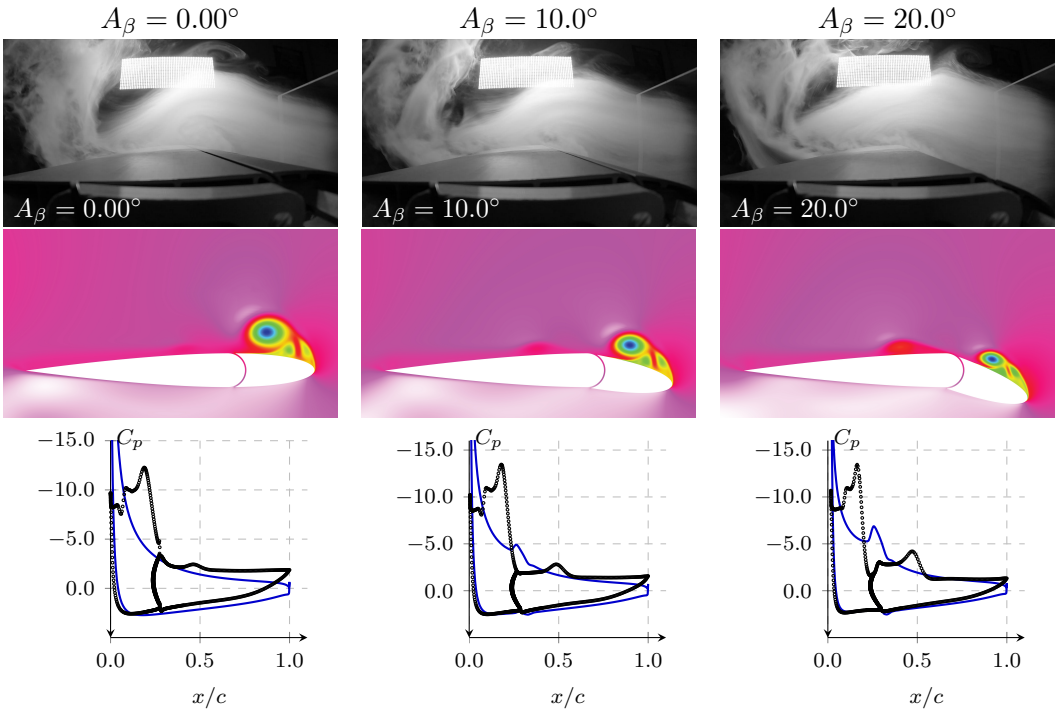

Figure 8.43: Flow fields with $h = 0.50$ and $kh = 1.00$ at $t/T = 0.75$. CFD and UPM results in black and blue, respectively.

when $A_\beta = 20°$. However, it comes at the expense of enlarging the suction at the back part of the airfoil. Meanwhile, the vortex size is not controlled by the existing pressure gradient, instead, it is governed by the angular deviation between the shear layer that appears following separation and the leading-edge chord direction, as illustrated in Figure 8.44

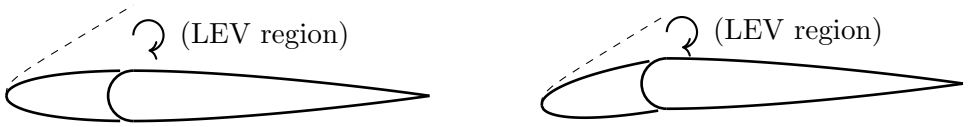

Figure 8.44: The growing mechanism of the leading-edge vortex. The shear layer is illustrated as the dashed line.

Figure 8.45 summarizes the influence of the pitching amplitude in the leading-edge vortex size and its intensity at the highest nondimensional amplitude and velocity. Here, the frames are taken at the end of the oscillation period ($t/T = 1.00$) when the LEV is fully developed, presenting a cumulative representation of what occurred during the full period.

Although the size of the leading-edge vortex is reduced considerably, up to 50 % as mentioned before, its intensity stays fairly unchanged, judging by similar pressure distributions. This was also observed during the descending phase, shown in Figure 8.43. However, it is worth mentioning that this is a plunging-dominated condition where the suction remains somewhat unaffected until a critical pitching amplitude is reached, from there on, the suction starts shrinking, as seen in Figure 8.42. Once again, the panel method adequately produces good results for the regions where the flow stays attached.

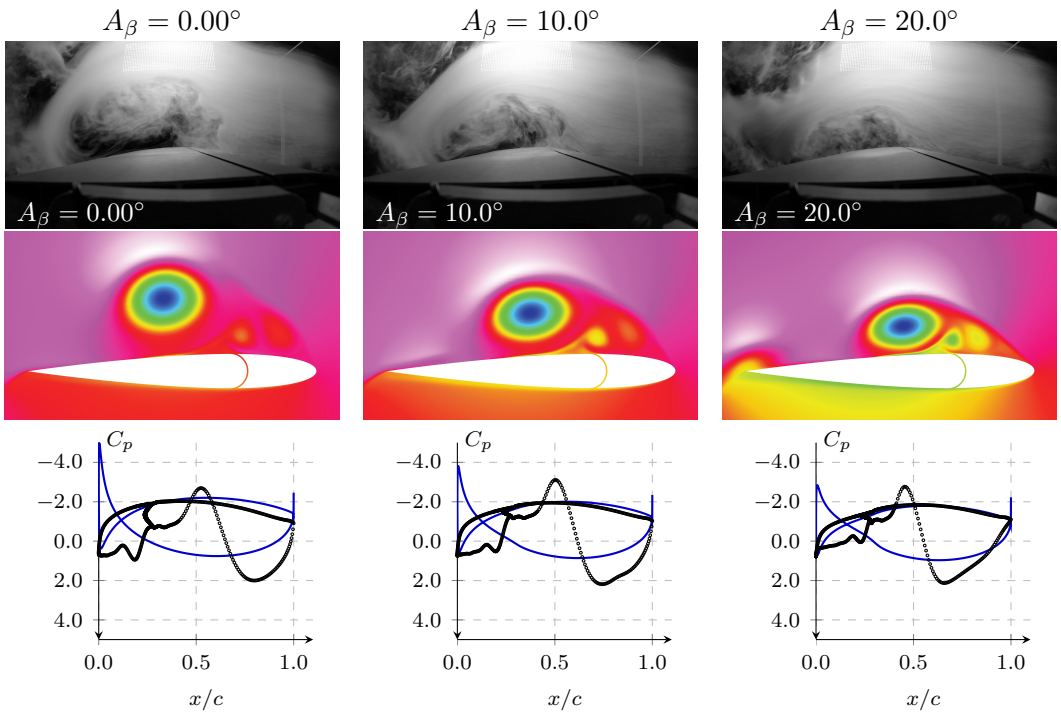

Figure 8.45: Flow fields with $h = 0.50$ and $kh = 1.00$ at $t/T = 1.00$. CFD and UPM results in black and blue, respectively.

Based on what was shown in this section, we must now present a summary of the results and draw the main conclusions of the proposed leading-edge mechanism at a Reynolds number of 1×10^4. In general, as we have seen with the mean propulsive coefficients, the dynamic leading edge offers good improvements mainly by exploiting the LEV presence. However, in some particular cases, the NACA0012-IK30 mechanism creates unsatisfactory results, where additional flow separation can increase drag and/or lift production.

However, when it comes to explaining thrust improvements, basing it only on the commonly used concept of mitigation of flow separation is not only simplistic but incorrect. The proposed mechanism shows that instead of mitigating flow separation, we should find ways to exploit the leading-edge vortex.

Hence, the main advantage of the NACA0012-IK30 airfoil comes from considering that the lower pressure linked to the flow separation zone may be used as a thrust-enhancing mechanism. By deflecting the leading edge, one can increase the frontal area of the airfoil, and when a low-pressure zone appears at the leading edge, increases the thrust force. However, as seen in the cases with lower reduced frequencies where flow separation is less intense, the mechanism is not adequate since the deflection of the leading edge at such conditions creates two main problems: it reduces the pressure differential at the leading edge, which is responsible for thrust enhancement, and increases flow separation beyond the maximum thickness position which may lead to higher drag.

Since the NACA0012-IK30 mechanism was demonstrated to be a good way to improve the

propulsive capabilities of oscillating airfoils, a question that may arise is how its performance can be compared to conventional flapping, where the whole airfoil is pitching and not only the leading edge. The following section will focus on that comparison by understanding whether or not the leading edge has the primary role when it comes to thrust improvements.

8.6 NACA0012-IK30 Vs Conventional Flapping

Comparing the NACA0012-IK30 mechanism with conventional flapping requires setting a base of conditions and understanding the limitations to make this a valid comparison. An obvious difference is the fact that conventional flapping airfoils do not present a dynamic curvature, as the NACA0012-IK30 does, which will undoubtedly change how the flow passes over the airfoil. But we will leave out the geometrical differences and will only compare the two situations in terms of kinematics.

So to make a valid comparison, the effective angle of attack of both configurations must be the same. As the plunging parameters are kept equal for the two configurations, to achieve the same effective angle of attack, what we need to do in practice is match the angle of attack waveform. The geometrical solution for such a problem at a given instant is shown in Figure 8.46.

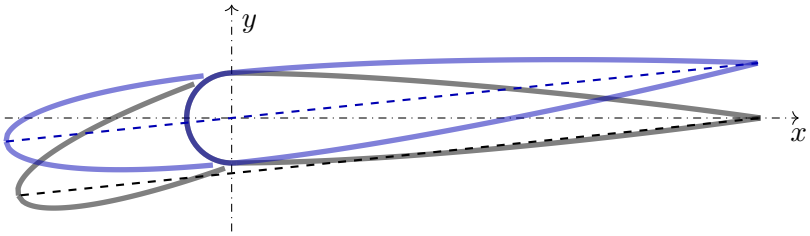

Figure 8.46: NACA0012-IK30 airfoil Vs Conventional Flapping.

In conventional flapping, as with the NACA0012-IK30, pitching is obtained by following a sinusoidal wave generally expressed as

$$A_\alpha \sin(2\pi f t). \tag{8.4}$$

As these two flapping modes have different expressions for their angle of attack, then the question becomes: what is the value of A_α that approximates $\alpha(t)$ for the two configurations? It turns out that A_α can take the maximum angle of attack value of the NACA0012-IK30 for a given A_β. Hence A_α may be calculated as

$$A_\alpha = \arctan\left(\frac{c_\beta \sin A_\beta}{c_\beta \cos A_\beta + c_\psi}\right), \tag{8.5}$$

making the approximation

$$A_\alpha \sin(2\pi f t) \approx \arctan\left(\frac{c_\beta \sin(A_\beta \sin(2\pi f t))}{c_\beta \cos(A_\beta \sin(2\pi f t)) + c_\psi}\right), \tag{8.6}$$

valid as seen in Figure 8.47, where the left-hand side and right-hand side of equation (8.6) are plotted for a leading-edge pitching amplitude of $20°$.

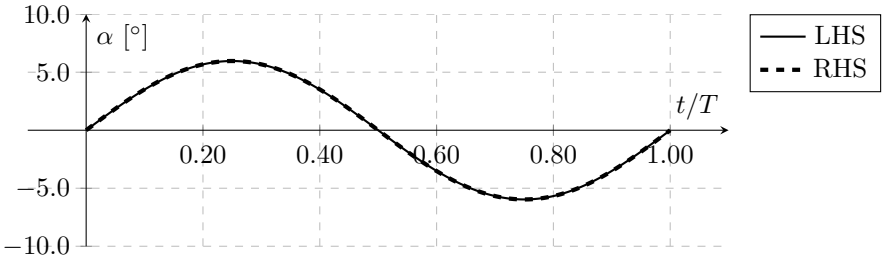

Figure 8.47: Effective angle of attack of NACA0012-IK30 airfoil Vs Conventional Flapping.

Based on this framework, we now compare the two flapping modes for the conditions shown in the previous sections. The comparison is made simple by only considering the mean propulsive coefficients and propulsive efficiency since comparing the instantaneous coefficients would create lots of graphs with unwanted complexity. Furthermore, the mean coefficients offer central knowledge when studying the propulsive performance of oscillating airfoils.

Unlike previous sections, the two nondimensional amplitudes are shown side by side. Instead of using the reduced frequency, we now use the kh (the nondimensional velocity) to facilitate the comparison. In Figure 8.48, the mean propulsive power coefficient is shown as a function of the airfoil pitching amplitude with (P) and (C) representing the proposed geometry and conventional flapping, respectively.

Overall, without focusing on the nondimensional amplitude, the NACA0012-IK30 airfoil offers more propulsive power when compared to conventional flapping except at lower nondimensional velocities. However, in these low oscillating conditions, the improvements of conventional flapping are negligible. Furthermore, higher increases are seen for the highest amplitude.

The main difference between the two ways of flapping occurs at $k = 0.50$ where after reaching its maximum, $\overline{C_{P_P}}$ starts decreasing, while conventional flapping is still increasing. This is not observed at $k = 1.00$, suggesting that the range of pitching amplitudes where the NACA0012-IK30 airfoil offers greater performance over conventional flapping depends on the pitching amplitude and the $k - h$ combination.

When it comes to power consumption, shown in Figure 8.49, conventional flapping consumes less power, except when $kh = 1.00$ at the lowest nondimensional amplitude. This condition may appear counterintuitive as the leading edge and back parts individually have

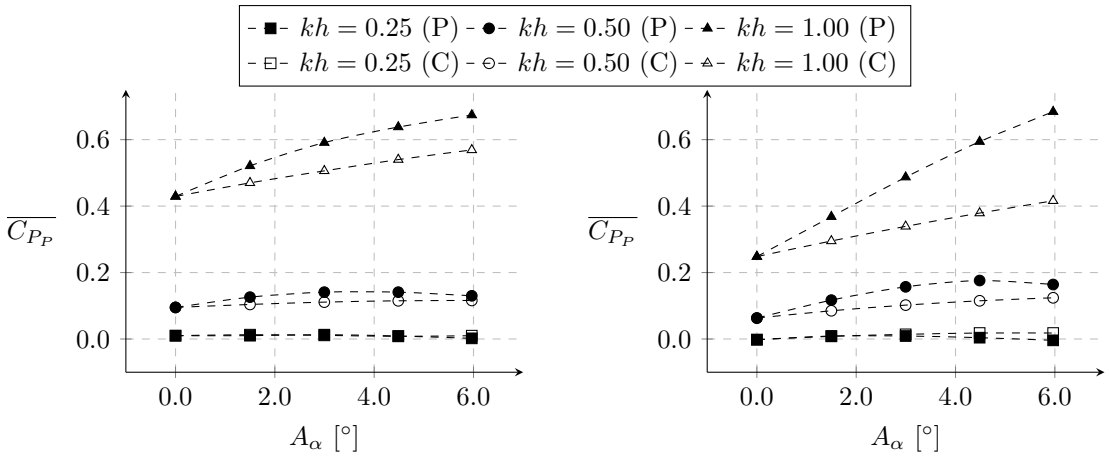

Figure 8.48: Mean propulsive power coefficient for $h = 0.25$ (left) and $h = 0.50$ (right).

a lower effective angle of attack, which in general, should reduce power consumption.

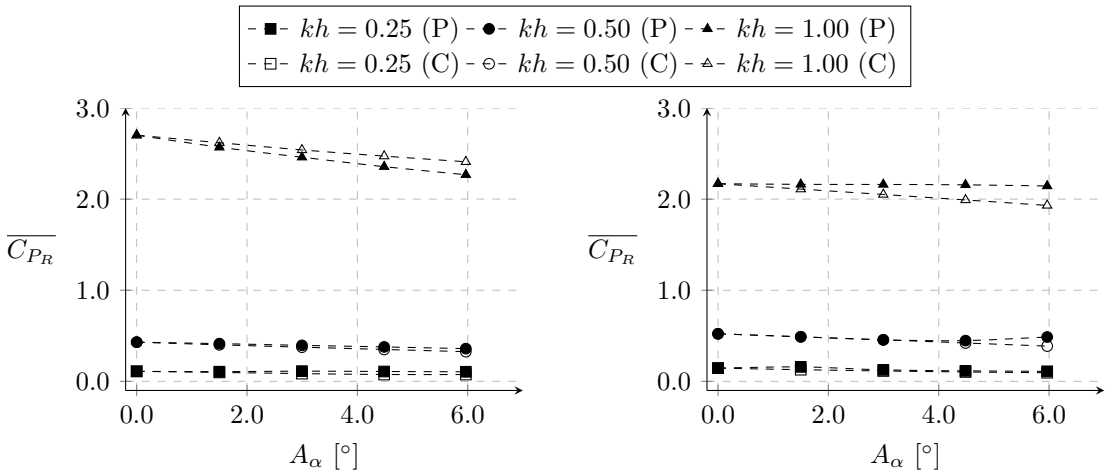

Figure 8.49: Mean required power coefficient for $h = 0.25$ (left) and $h = 0.50$ (right).

Propulsive efficiency follows a different behavior when compared to the other propulsive indicators (propulsive and required power), as shown in Figure 8.50. With $kh = 0.25$, conventional flapping is superior as it can provide better thrust production at a lower power demand, although at the lowest amplitude, it shows a dip close to $A_\alpha = 4.5°$. With $h = 0.50$ we see two branches where one increases continually and the other, the NACA0012-IK30, has its efficiency quickly degraded.

Results seen at $kh = 0.50$ become different as the NACA0012-IK30 airfoil now offers better propulsive efficiency for the range studied, although the trends observed indicate that conventional flapping will surpass the IK30 after $6°$. With $kh = 1.00$, the proposed airfoil has better propulsive efficiency with no clear sign of performance degradation in the vicinity of $A_\alpha = 6°$.

This analysis aimed to answer the question raised in the previous section of whether or not the proposed mechanism could offer improved propulsive performance. This was an important

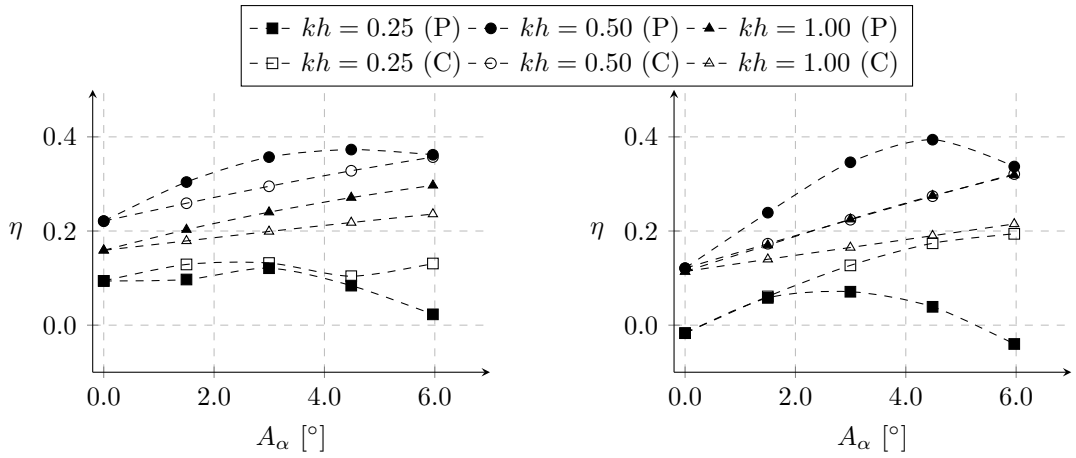

Figure 8.50: Propulsive efficiency for $h = 0.25$ (left) and $h = 0.50$ (right).

question since there is interest in comparing it with conventional flapping, which is the norm in the majority of research.

In short, both the NACA0012-IK30 and conventional flapping have advantages and disadvantages that are highly dependent on the prescribed kinematics. Overall, at the lower nondimensional velocity tested, conventional flapping is preferable while at the highest, the proposed geometry works best. At the intermediate nondimensional velocity ($kh = 0.50$), the NACA0012-IK30 airfoil offers superior propulsive performance, but results indicate that for higher pitching amplitudes (higher than $6°$), it will not be desirable when compared to conventional flapping.

By comparing the two flapping modes in terms of kinematics, we are indirectly studying the influence of an underlying curvature variable, which is key to understanding the results presented. The vast majority of published work is focused on symmetrical airfoils, and the ones that consider camber do not study it *per se*. As seen in this analysis, it is an important parameter to be considered, especially when it varies over time. Nonetheless, the proposed geometry is simply a particular and non-optimized solution to change the airfoil camber, which on one hand can offer superior performance but at the same time, can quickly degrade it.

One could argue that the range studied in this section is rather small as the pitching amplitude of the airfoils is kept under $10°$. As observed, data shows that the NACA0012-IK30 airfoil, for some conditions, is an excellent alternative to conventional flapping, but its overall performance in higher angles of attack is not captured. This is the purpose of the next section, where a wider study is presented.

8.7 Optimal Study of the NACA0012-IK30 Airfoil

In this section, we will extend the comparison initiated in the previous study, and extend it to higher angles of attack. However, the comparison will not be conducted parametrically

but optimally, using the methodology defined in chapter 7.

The Reynolds number is kept at 1.0×10^4, but only the highest nondimensional amplitude, $h = 0.5$, is tested. An additional reduced frequency ($k = 1.5$) is added to this study. Moreover, as stated in the optimization methodology, the change in the leading-edge pitching amplitude is limited to 1° after each iteration. This limiter reduces existing transients between consecutive periods, which allows for a A_α adjustment after each period.

8.7.1 Optimization of $\overline{C_{P_P}}$

The first part of the optimization process is focused on maximizing the propulsive power, meaning that $\varphi = 1$ in equation (7.2). Moreover, for the specific case of the proposed flapping, where the IK30 mechanism is considered, it is important to mention that we use the leading-edge pitching amplitude and not the global airfoil pitching amplitude, as in standard flapping.

In Figure 8.51, the mean propulsive power is shown as a function of the airfoil pitching amplitude, with each data point representing an iteration step. Additionally, a parametric study (P) for the highest nondimensional velocity, where higher transients are expected, shows that the limiter mentioned above works appropriately.

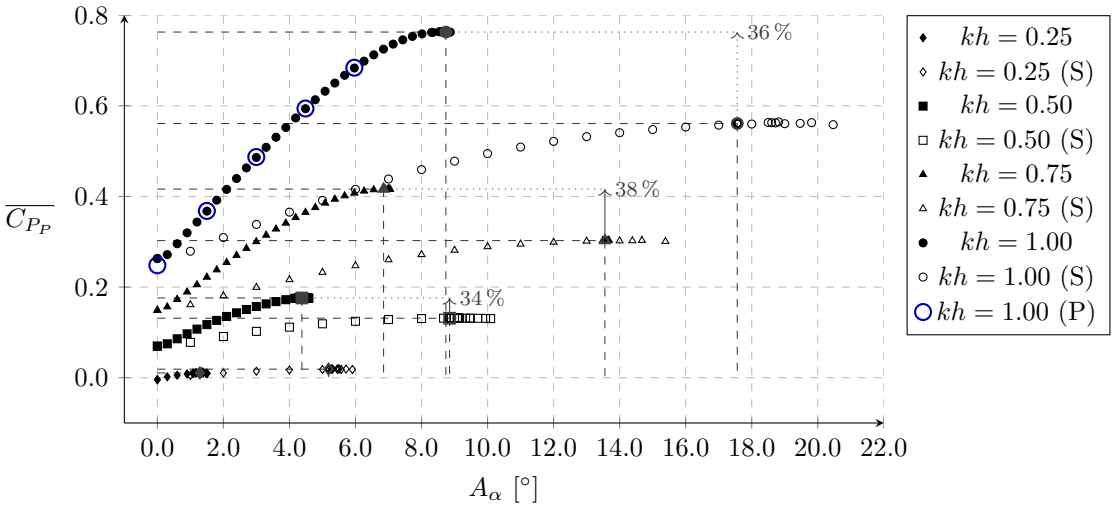

Figure 8.51: $\overline{C_{P_P}}$ as a function of A_α during the optimization of the propulsive power ($\varphi = 1.0$). Standard flapping is represented by (S).

The mean propulsive power increases with the nondimensional velocity regardless of the flapping mode. Moreover, for each kh, there is a pitching amplitude that maximizes thrust. These are global maximums since null or excessive deflection holds no real benefit. At the lowest nondimensional velocity, $kh = 0.25$, both flapping methodologies offer no significant advantage. As verified in the parametric study, this is a slow flapping condition causing the airfoil to be very close to the drag-producing regime. However, for kh greater than 0.5, the pitching amplitude influences the mean propulsive power. Results show that by only deflecting the leading edge, much higher propulsive power is achieved compared to standard

flapping, considering the same angle of attack. Comparing peak performance, the proposed mechanism can offer an increase of up to 38 % at a much lower pitching amplitude. Moreover, as kh increases, the A_β that maximizes the propulsive power also increases for both ways of flapping, though this growth is thought to be asymptotic.

To understand the thrust enhancement mechanism for the two flapping modes, we provide some snapshots of the total pressure field plus the pressure coefficient of the airfoil surface. The total pressure is only used as a qualitative parameter to identify flow-separated regions. In Figure 8.52, the $\overline{C_{P_P}}$ optimization process is shown for $kh = 1.00$ at two instants, $t/T = 0.75$ and $t/T = 1.00$. Other kh conditions are similar, although effects are scaled down.

Analyzing the images of both flapping configurations, although having broadly different geometries, they present the same flow patterns. At the beginning of the optimization process (0.00 % of max F), the flow separates right at the leading edge during the descent, creating a massive separated region at the end of the period. As the optimization process progresses, we observe that the LEV has its size reduced, although not being completely cleared. This indicates that the maximization of the propulsive power is accomplished together with the presence of the LEV. One could expect such a result since the LEV is a low-pressure region that effectively works as a suction force in the β part. An additional result that differentiates the two modes is that the proposed flapping creates an additional vortex at the ψ part, close to the pivot point, which is enlarged as the leading-edge pitching amplitude increases. As will be seen ahead, this vortex will be the main reason why the required power increases when compared to standard flapping.

In Figure 8.53, five snapshots of the descending phase (the ascending phase is similar but symmetrical) are shown at maximum $\overline{C_{P_P}}$. The pressure coefficient at the airfoil surface is also provided for both standard and proposed flapping. As seen in Figure 8.52, the maximization of the propulsive power requires the presence of a LEV, which being a low-pressure zone, acts as a thrust booster for both flapping modes. As the airfoil accelerates downwards ($t/T = 0.625$), a suction zone appears on the frontal part of the upper surface, which has a peak right at the leading edge. Following this peak is an adverse pressure gradient that is the cause of the flow separation and subsequent LEV formation.

Furthermore, for the proposed flapping, we see an additional adverse pressure gradient appearing at the pivot point due to the dynamic curvature of the NACA0012-IK30, which results in flow separating at two different places, as captured at $t/T = 0.75$. Looking at C_p, although the suction zone at the β part is similar for both flapping modes, the ψ part of the proposed flapping presents an additional suction zone that majorly contributes to lift, leading to an increase in consumed power. As the airfoil continues its descent, these low-pressure zones are diluted until reaching the bottom position, where the pressure distribution is virtually the same for both flapping configurations.

In addition to the pressure distribution, we also present the propulsive coefficients over time

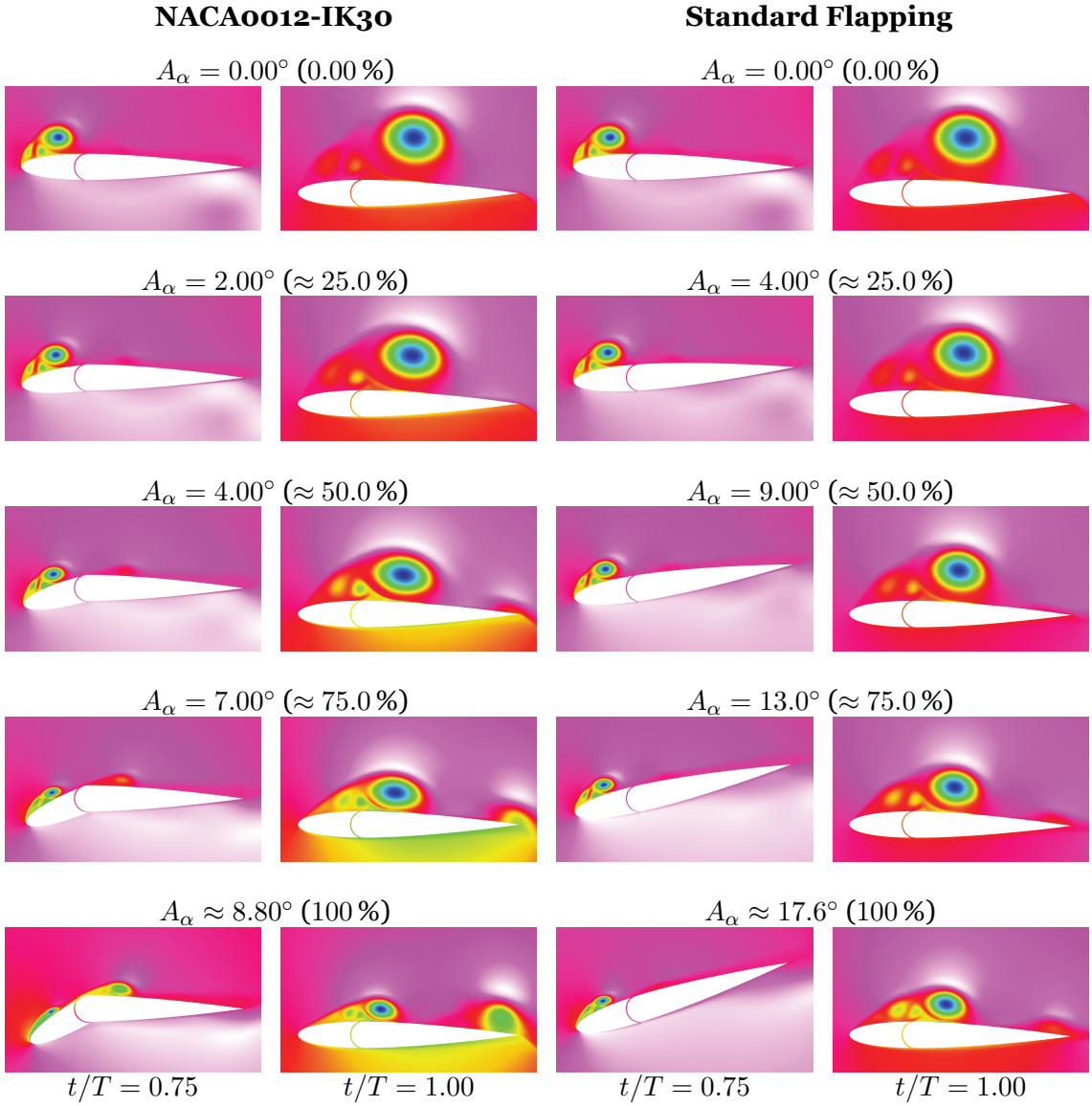

Figure 8.52: Optimization progress with $\varphi = 1.0$.

to comprehend why the proposed flapping offers more thrust and the contributions of each airfoil part in these coefficients. In Figure 8.54, the C_{P_P} decomposition is provided, where we see that the leading edge is the main contributor, with the proposed geometry providing an approximate $50\,\%$ increase compared to standard flapping while at peak performance. The ψ part is similar to conventional flapping, offering a slight improvement.

It is worth stopping here and questioning how the proposed flapping methodology outperforms conventional flapping regarding thrust production. The root cause of such improvements is uncovered by revisiting the distribution of the pressure coefficient and by looking at the overall frontal area of the airfoil during the oscillation cycle (Figure 8.53). As one can see, while both flapping modes have similar pressure coefficient distributions, the frontal part in the proposed flapping has a larger deflection than in the standard configuration. This larger deflection combined with the suction peak located at the leading edge, increases the resultant force in the streamwise direction, in this case thrust. This is how conventional flapping can

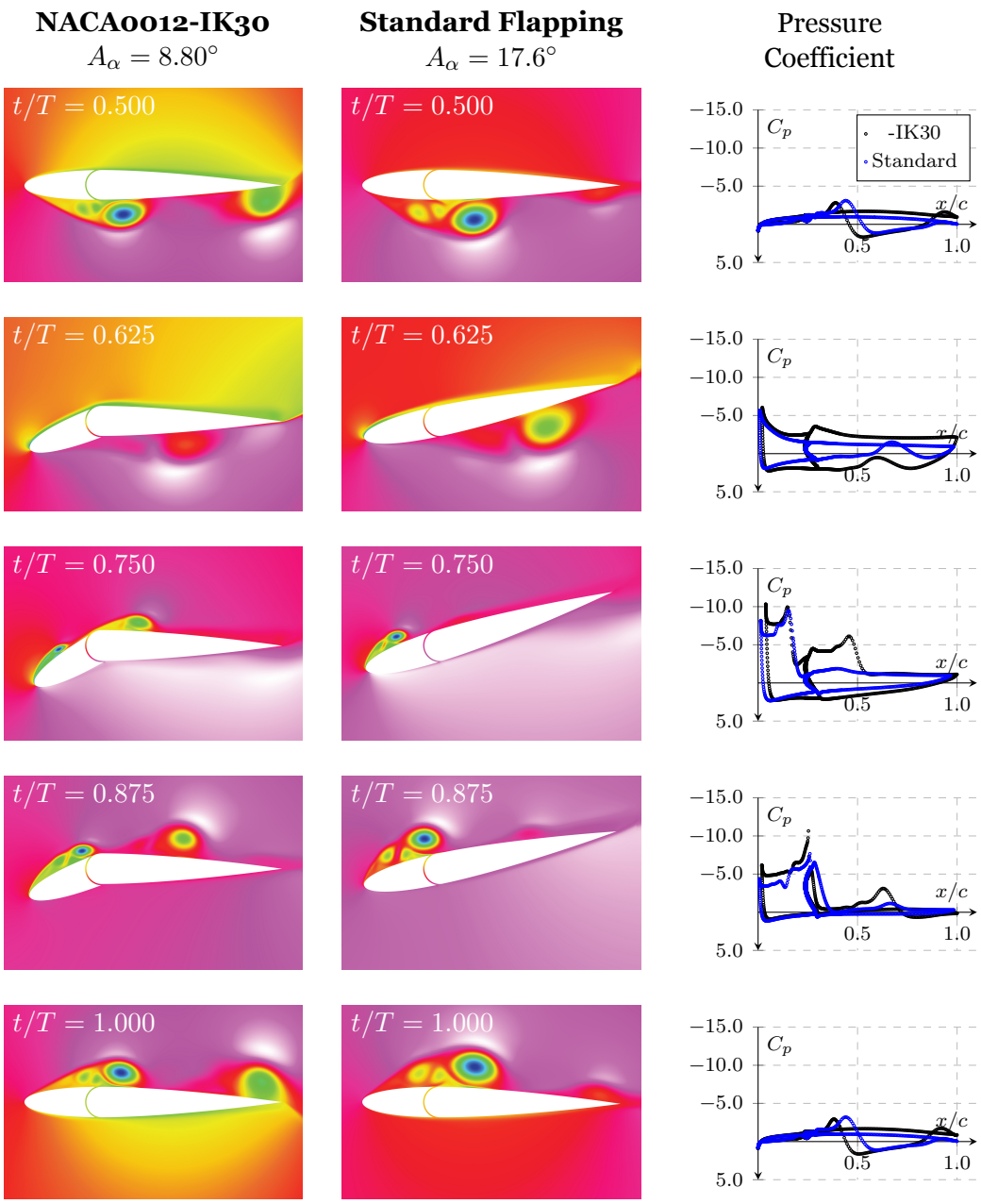

Figure 8.53: Pressure distribution for the two flapping modes at maximum propulsive power.

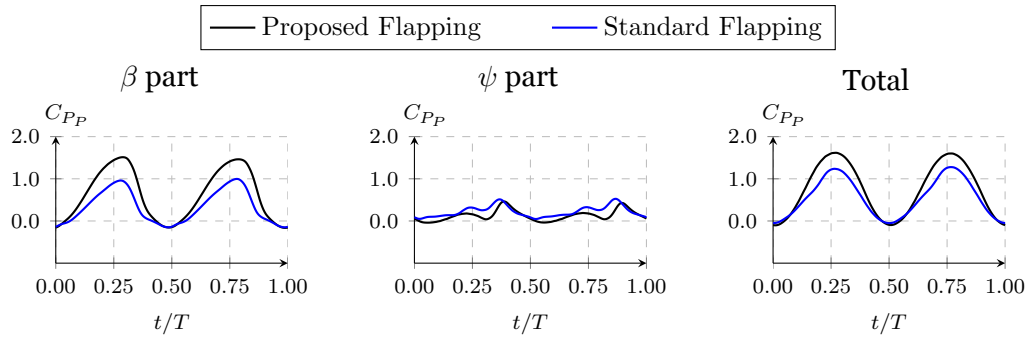

Figure 8.54: Propulsive power coefficient decomposition when $\varphi = 1.0$.

be surpassed by the IK30 mechanism.

Contrary to C_{P_P}, the consumed power by the β part of the airfoil for both flapping configurations is nearly the same as observed in Figure 8.55. However, when looking at the ψ part, it is clear that standard flapping consumes considerably less power, mainly because it does not have that vortex seen in the proposed configuration that is responsible for a higher lift and thus, more required power.

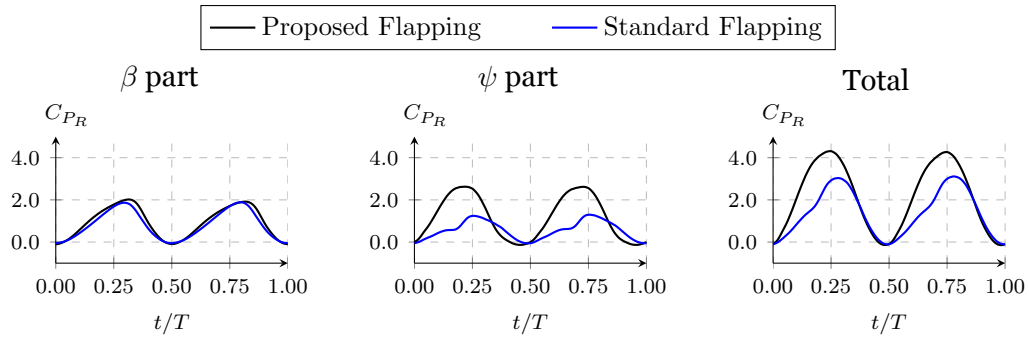

Figure 8.55: Required power coefficient decomposition when $\varphi = 1.0$.

This is why the two flapping modes present very different power requirements at maximum propulsive power. In Figure 8.56, the mean propulsive power coefficient is shown as a function of the mean required power coefficient.

The IK30 mechanism, while providing more thrust, consumes more power than standard flapping. Considering $kh = 1.00$, when at peak propulsive power, the proposed geometry requires up to 36 % more power than the conventional way of flapping. At lower nondimensional velocities, it goes down to 27 % if we neglect the smallest kh.

Before moving to the optimization of propulsive efficiency, it is vital to remember that we are maximizing the propulsive power while maintaining the phase angle constant at $90°$. By doing this, we are looking exclusively at the influence of the pitching amplitude, by restricting the known influence that the phase angle has on thrust production. The impact of the latter is a crucial matter for future research. However, this limitation does not interfere when we are looking for the optimization of the propulsive efficiency, which is known to reach its

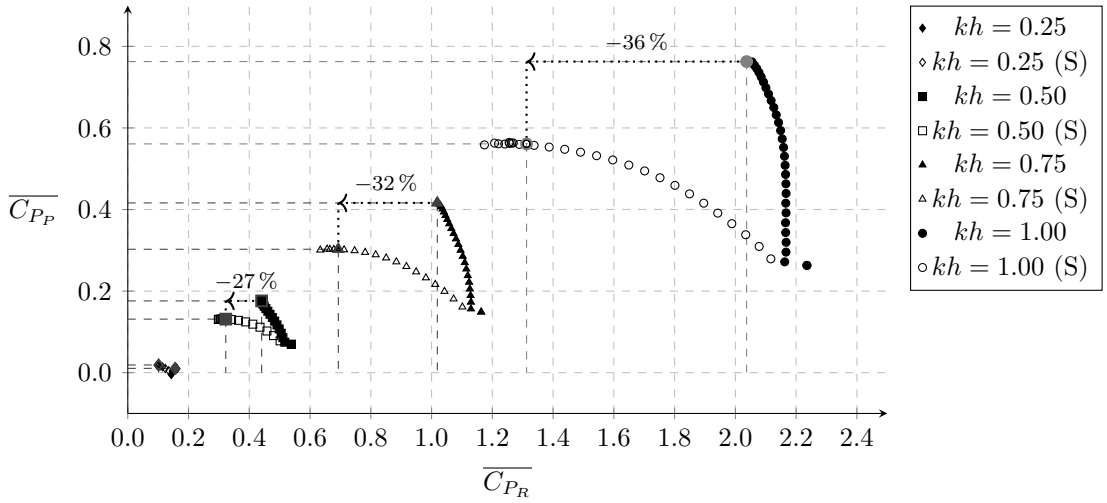

Figure 8.56: $\overline{C_{P_P}}$ as a function of $\overline{C_{P_R}}$ during the optimization of the propulsive power ($\varphi = 1.0$). Standard flapping is represented by (S).

maximum when the phase angle is $90°$.

8.7.2 Optimization of η

The optimization methodology is extended to the propulsive efficiency ($\varphi = 0.0$) in Figure 8.57. Higher efficiency is achieved by standard flapping mainly due to the lower power demand it requires. At $kh = 0.25$, efficiency is pretty low for both flapping modes, mainly due to the insignificant propulsive power generated. For other nondimensional velocities, the pitching component offers noticeable enhancements, with conventional flapping achieving propulsive efficiencies close to $60\,\%$. Maximum efficiency is achieved for $kh = 0.75$ regardless of flapping methodology, showing that, unlike propulsive power, efficiency does not increase continuously with kh.

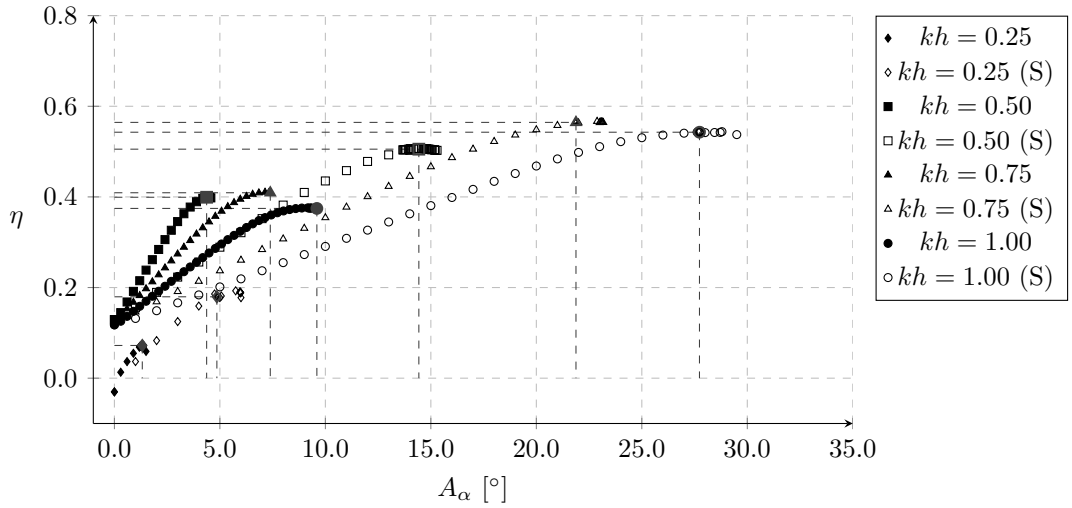

Figure 8.57: η as a function of A_α during the optimization of the propulsive efficiency ($\varphi = 0.0$). Standard flapping is represented by (S).

While standard flapping offers better efficiency, the IK30 mechanism offers a unique feature.

The pitching amplitude that maximizes the mean propulsive power also offers near-optimal propulsive efficiency, making this a central outcome of the present study. The justification for such a feature is the fact that the power consumed by proposed flapping does not vary as much as standard flapping when the leading edge pitching amplitude changes. This means that if $\overline{C_{P_R}}$ is kept fairly constant, when we maximize for $\overline{C_{P_P}}$ we will also be finding an efficiency maximum, as one can see by the propulsive efficiency definition. This is not achievable with conventional flapping airfoils. On the one hand, plunging airfoils present good thrust production, but propulsive efficiency typically takes a hit, while on the other hand, flapping, where plunging and pitching are combined, offers better efficiency at the expense of lower thrust [77].

Figure 8.61 shows the efficiency as a function of the mean propulsive power. In standard flapping, the airfoil passes through maximum thrust generation, sacrificing it to reach optimal efficiency, as one can see by the curved paths created during optimization. In contrast, the proposed airfoil reaches optimal propulsive efficiency following a linear path in the $\overline{C_{P_P}}$ direction. Moreover, when we look at the same propulsive efficiency envelope, the IK30 mechanism offers much-improved thrust performance, rendering standard flapping for these regimes impractical.

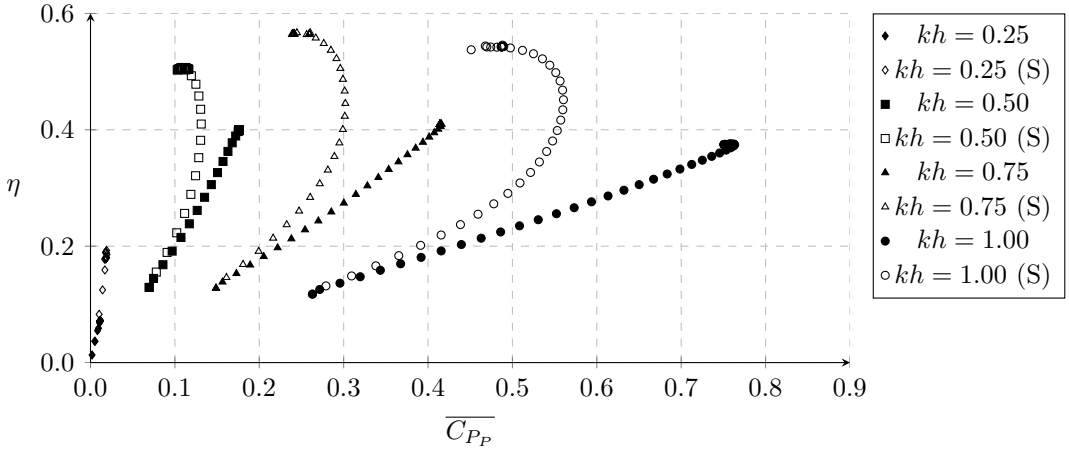

Figure 8.58: η as a function of $\overline{C_{P_P}}$ during the optimization of the propulsive efficiency ($\varphi = 0.0$). Standard flapping is represented by (S).

To supplement these graphs, Figure 8.59 shows the total pressure contour during the optimization progress of η, similar to what was presented for the mean propulsive power. An overall look at the snapshots leads to the primary conclusion that optimizing propulsive efficiency requires the nearly complete removal of the leading-edge vortex, regardless of flapping mode. This is verified halfway down ($t/T = 0.50$), where the LEV becomes smaller and smaller until its formation is minimal. Still, there is a suction zone that then separates and creates a slight separation region beyond the pivot point ($t/T = 1.00$).

In Figure 8.60, a closer view of the descent phase is given together with the pressure coefficient distribution for the two flapping modes. In the first half of the descent ($t/T = 0.625$), the flow on the upperside remains attached with the proposed flapping having two clear suction

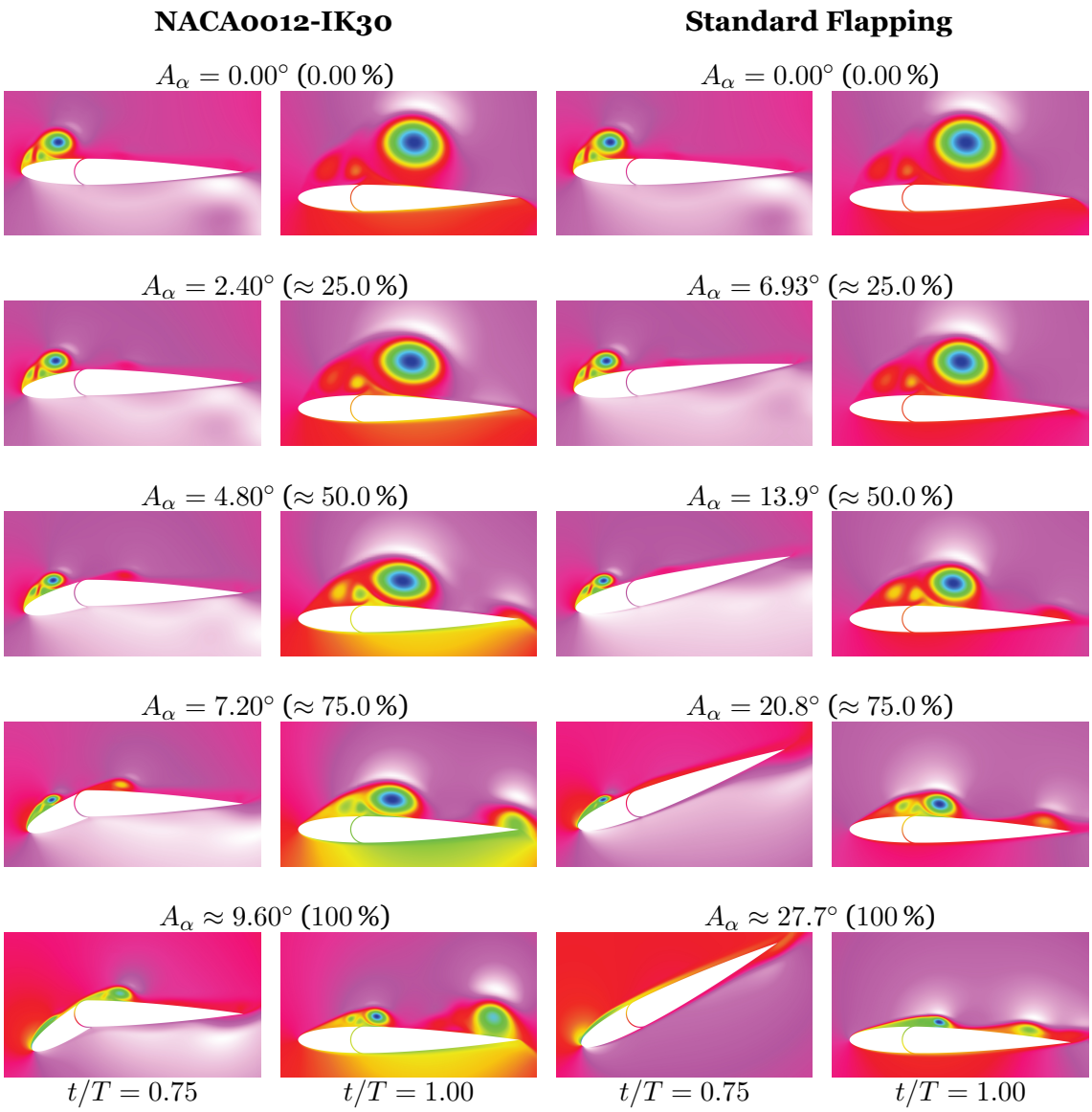

Figure 8.59: Optimization progress with $\varphi = 0.0$.

zones. These two regions then become separated ($t/T = 0.75$) judging by the interruption of the adverse pressure gradient seen at $t/T = 0.625$. In contrast, conventional flapping still has the flow attached but not for long since at $t/T = 0.875$, its adverse pressure gradient is also affected. The pressure distribution graphs reaffirm that the proposed geometry can provide more thrust but consume more power.

This is corroborated by Figure 8.61, where the proposed flapping offers more propulsive power, with the major contributor being the β part. In contrast, thrust in conventional flapping is greatly influenced by the ψ part.

However, as seen before, the higher thrust comes at the cost of higher power consumption, where the proposed flapping can require two times more energy, as shown in Figure 8.62. Nonetheless, as we saw in Figure 8.58, although conventional flapping achieves significant propulsive efficiencies with low power demand, it sacrifices the propulsive power to achieve

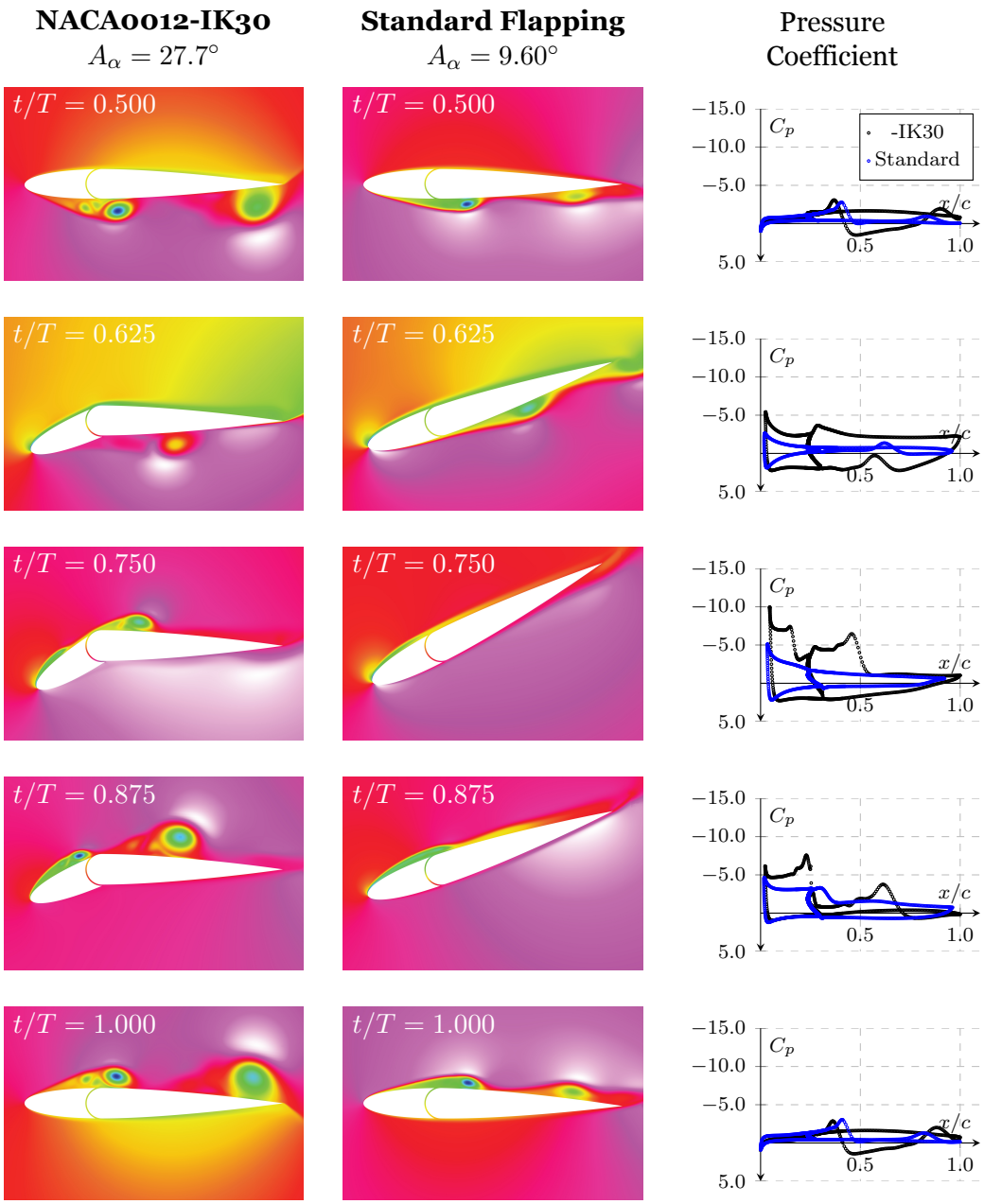

Figure 8.60: Pressure distribution for the two flapping modes at maximum propulsive efficiency ($\varphi = 0.0$).

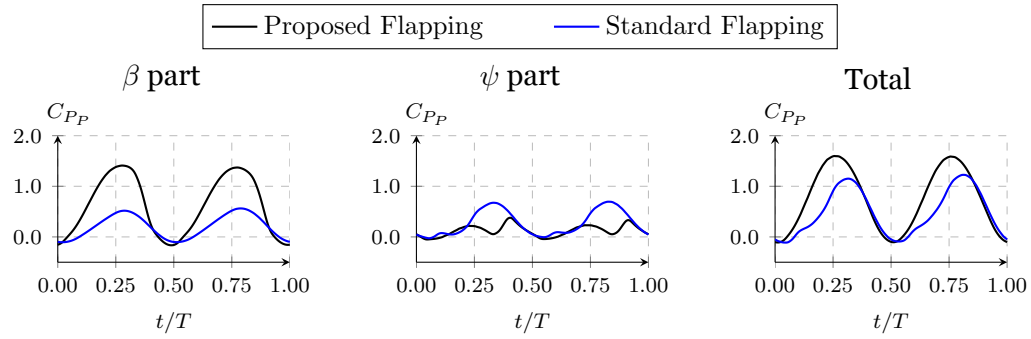

Figure 8.61: Propulsive power coefficient decomposition when $\varphi = 0.0$.

it.

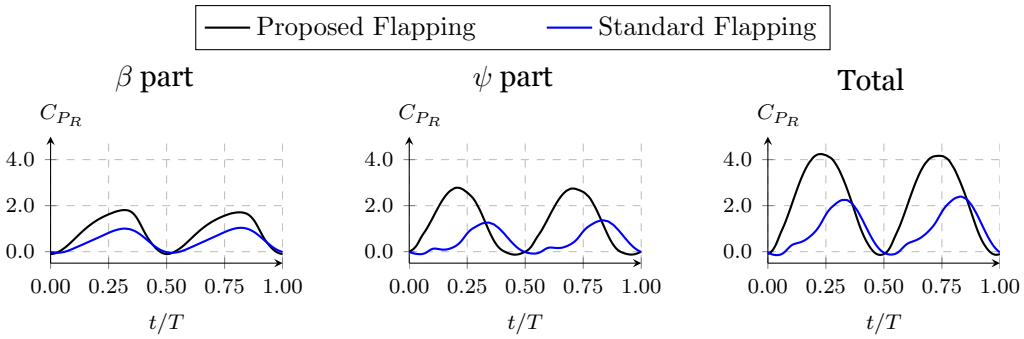

Figure 8.62: Required power coefficient decomposition when $\varphi = 0.0$.

This marks the end of the studies where the proposed geometry is used as a propulsor. All data shown here may be found at **https://www.earc96.com/PhD** and is openly accessible, editable, and may be shared by anyone. Additional information can be found in the database, for instance, uncertainties and other propulsive and kinematic variables, which were not included in the current manuscript.

The next chapter will present the results where the IK30 mechanism is used to mainly mitigate the adverse effects of dynamic stall, at a much higher Reynolds number.

Chapter 9

Dynamic Stall Mitigation

"Development is an endurance exercise with incremental improvements."

Sri Mulyani Indrawati

In this chapter, we move to a higher Reynolds number regime where a NACA0012-IK30 wing is used as a stall mitigation system. Unlike chapter 8, the proposed geometry is no longer considered a propulsive device, as the allowable kinematics could not induce the required momentum excess in the wake. The forces and moments acting on the wing are obtained for different static and dynamic configurations. Also in the chapter are CFD results for static conditions where the influence of the leading edge position on the overall wing performance is analyzed.

9.1 Static Force Measurements

Force measurements are conducted using a blower wind tunnel with an open test section, at a Reynolds number of 2.0×10^5. The primary reason for such a configuration was to remove any wall effects that could appear during oscillations. In fact, considering an angle of attack of 20° would result in a blockage ratio close to $14\,\%$. However, this decision leads to the inevitable emergence of three-dimensional effects, which creates a considerable difference when compared to bidimensional wind tunnel experiments. Overall, 3D effects reduce lift, increase drag, and delay wing stall. Nonetheless, the effectiveness of the proposed mechanism is not questionable as will be shown in force and stall visualization data.

9.1.1 Flap Configuration

Before exploring the dynamic conditions (plunging and pitching), the NACA0012-IK30 wing is tested under several static conditions using three basic configurations.

The first configuration considers a plain flap with the leading edge fixed at $\beta = 0^\circ$. Then, the angle of attack of the back part, ψ, is varied between 0° and 30°, as shown in Figure 9.1.

In Figure 9.2, the drag and lift coefficients of the flap configuration are plotted against the angle of attack, as is the standard NACA0012 ($\Omega = 0^\circ$). In addition, for a quick comparison, the bidimensional lift is also shown. By deflecting just the back part, there is slightly more drag compared to the standard configuration, however, with the plus of having more lift. Something worth mentioning is that although the back part moves as a plain flap, it does not

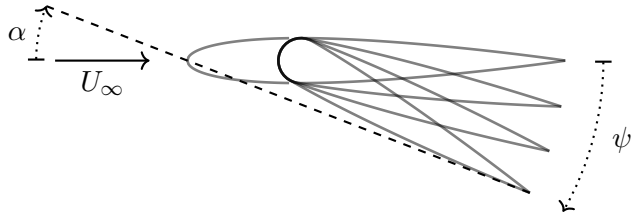

Figure 9.1: Flap configuration for steady tests.

behave as one. The deflection of a plain flap translates the lift curve upwards, which is not seen in the present case, where only the lift slope is changed.

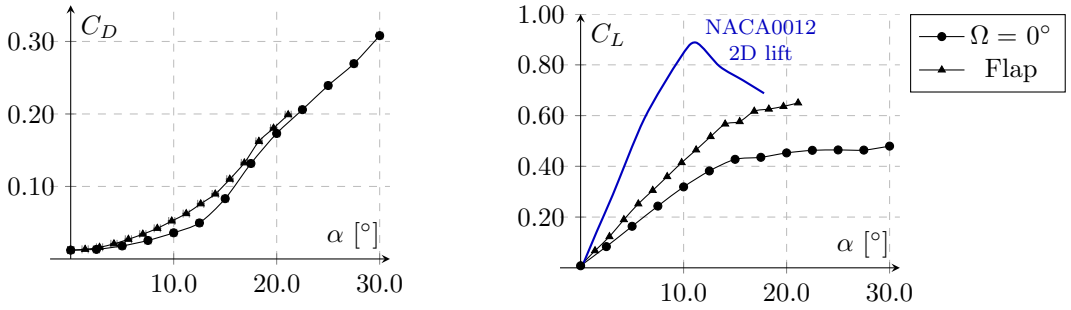

Figure 9.2: Drag and lift coefficients as a function of α. The NACA0012 bidimensional lift was obtain from [199].

Concerning the moment coefficient (Figure 9.3), the main difference is centered around the intensity of the pitch-up moment, which is much less intense when compared to the standard configuration. The moment is measured at 30 % of the chord for all tests, coinciding with the leading edge pivot point.

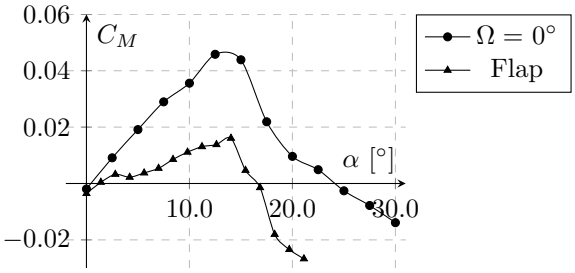

Figure 9.3: Moment coefficient ($0.3c$) as a function of α.

After hitting the maximum at around $15°$, the moment coefficient decreases due to the onset of flow separation. If we reexamine the lift coefficient, that coincides with the interruption of the linear region. Moreover, the stall phenomenon is much less abrupt when compared to the 2D case. To better understand the relationship between the aerodynamic coefficients and the onset of flow separation, a sequence of images is shown where a series of tufts were attached to the wing. Images are the result of the image processing methodology explained in section 4.3.

In Figure 9.4 the upper surface from $\psi = 10°$ ($\alpha = 7.00°$) to $\psi = 30°$ ($\alpha = 21.1°$) is shown. In the following images, the horizontal black lines show the wing's center. The results indicate

that until $\alpha = 14.0°$, the flow remains attached with a particularity: a spanwise pressure gradient is present and becomes stronger with the angle of attack. This is verified by the tips of the tufts which are pushed toward the center of the wing.

When $\alpha = 15.4°$, it is clear that tufts are shuddering more than in previous conditions, meaning the onset of flow separation occurred. It is also clear that the stall begins at the wing's center as the outer tufts still stick to the surface. From here on, the continuous increase of ψ leads to the magnification of flow separation phenomena. Interestingly enough, when $\alpha = 21.1°$, the two most outer strings that are closer to the trailing edge still indicate that the flow at that region is not fully detached.

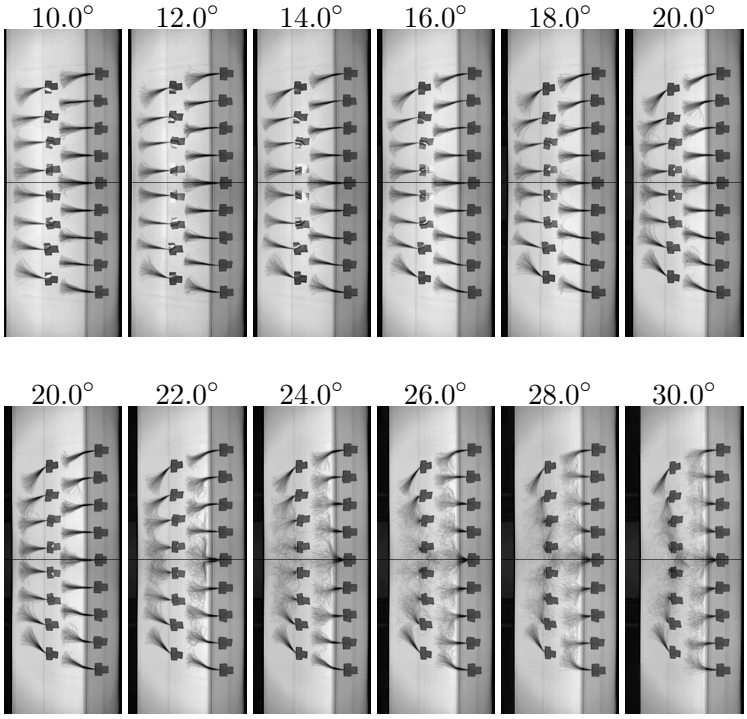

Figure 9.4: Stall visualization at the upper surface for the flap configuration. Values indicate the ψ angle.

9.1.2 Fixed Leading-Edge Configuration

The second configuration considers a fixed leading-edge position relative to the back part, which means that we are intrinsically studying the effects of wing curvature. The angular deviation between the two parts is calculated as

$$\Omega = \beta - \psi, \tag{9.1}$$

with the present study considering three conditions: $0°$, $-10°$ and $-20°$, with all configurations having the leading edge pointing downwards when the back part is at $0°$. The parametric study is conducted by varying ψ from $0°$ to $30°$, as illustrated in Figure 9.5.

By looking at the aerodynamics of this configuration, it immediately resembles a leading-edge flap, where the frontal area of the airfoil is deflected. As shown in Figure 9.6, while drag

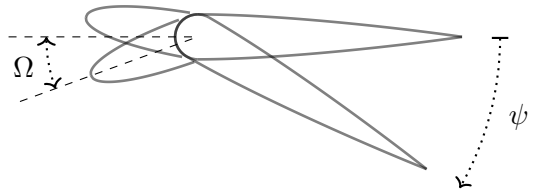

Figure 9.5: Fixed leading-edge configuration for steady tests.

is overall the same for all leading-edge deflections, lift goes up for the same angle of attack, and the onset of the stall is delayed, being pushed towards higher angles of attack.

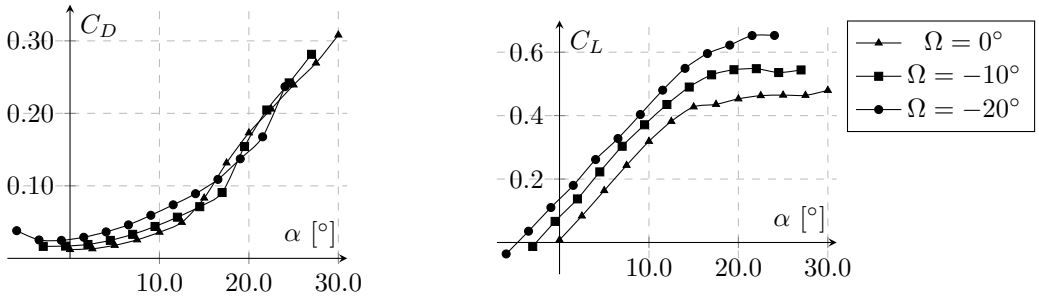

Figure 9.6: Drag and lift coefficients as a function of α.

Regarding the moment coefficient, shown in Figure 9.7, we see that the primary effect of the leading-edge deflection is increasing the nose-down moment intensity, as one could expect when deflecting the frontal back downwards. Also, the stall onset delay is visible on the moment coefficient by looking at the angle of attack where C_M reaches its maximum. This maximum occurs at the angle of attack where the flow starts to separate.

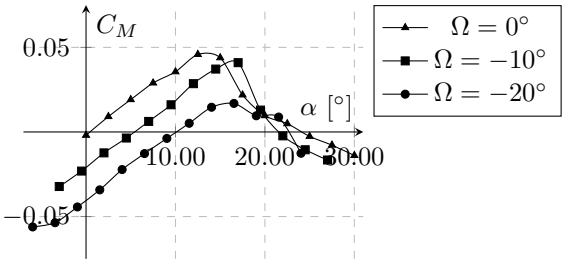

Figure 9.7: Moment coefficient as a function of α.

As shown in the flap configuration, a series of images are provided to visualize how the flow behaves at the wing surface, adding a new level of knowledge regarding the behavior of the aerodynamic coefficients. In Figure 9.8, when $\Omega = 0°$, the flow remains attached until $16°$, which agrees with F/T data where stall occurs in the vicinity of $15°$.

With $\Omega = -10°$ (Figure 9.9), the onset of the stall is pushed for higher angles of attack, starting somewhere between $18°$ and $20°$. However, it is important to mention that the way stall occurs is different. In the first case, when $\Omega = 0°$ (conventional NACA0012), flow separation affects the whole wing surface, judging by the oscillations of both the upstream and downstream tufts. With the frontal deflection, we observe that flow separation now starts downstream, clearly identified when ψ = $20°$.

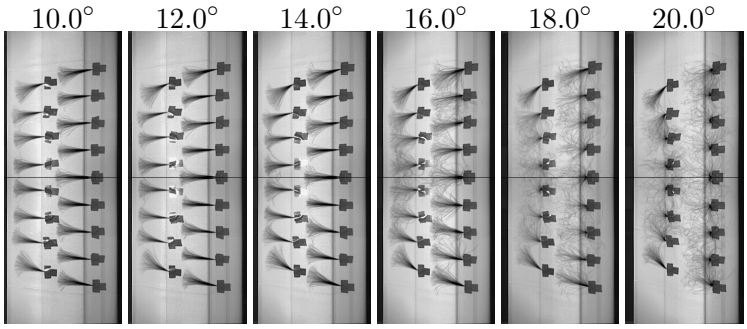

Figure 9.8: Stall visualization at the upper side considering $\Omega = 0°$. Values indicate ψ values.

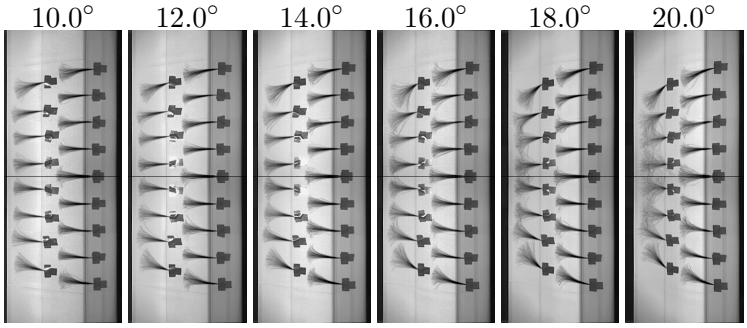

Figure 9.9: Stall visualization at the upper side considering $\Omega = -10°$. Values indicate ψ values.

The same effect is seen in Figure 9.10, where $\Omega = -20°$. When $\psi = 22°$, the flow is already separated at the ψ part, while the tufts placed at the frontal part still do not present a considerably high standard deviation. When the angle of attack is further increased, flow separation grows, especially at the central section of the wing.

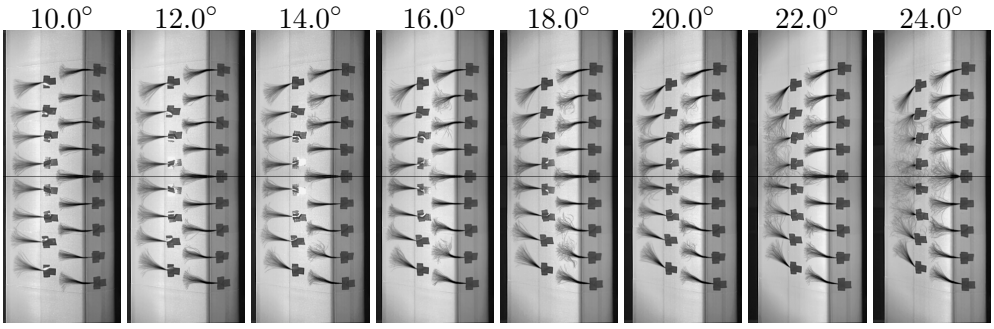

Figure 9.10: Stall visualization at the upper side considering $\Omega = -20°$. Values indicate ψ values.

9.1.3 Variable Leading-Edge Configuration

In the third configuration chosen for the static tests, the back part is fixed, while we change the leading-edge angle of attack. Its value is then changed from $\beta = \psi$ down to $0°$, as shown in Figure 9.11.

While in the second configuration, we were studying the curvature induced by the frontal

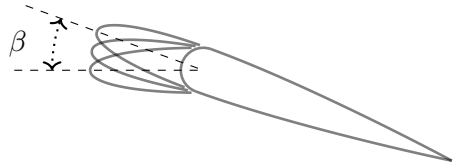

Figure 9.11: Variable leading-edge configuration for steady tests.

deflection, in this particular configuration, we are directly observing the influence of leading-edge deflection on the overall performance of the wing. Figure 9.12 shows the lift and drag coefficients plotted against the leading-edge angle of attack for five different ψ. With $\psi = 10°$, it is clear that the leading-edge deflection holds no real influence. Increasing ψ to $15°$ results in a slight modification in the aerodynamic coefficients, in particular when β is reduced by $5°$. A small reduction in drag accompanied by a lift increase is observed, but after that angle of attack, no significant changes are obtained. For ψ higher than $15°$, decreasing the leading-edge angle of attack leads to a drag reduction until it reaches a plateau. At the same time, lift increases with the β reduction. However, continuously lowering the leading-edge angle of attack can lead to lift degradation, as observed by the subtle reduction at $\psi = 25°$ that becomes more evident for $\psi = 30°$.

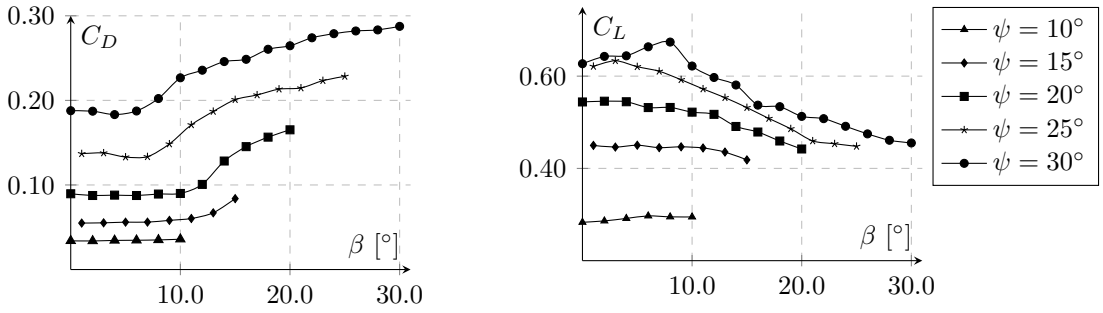

Figure 9.12: Drag and lift coefficients as a function of β.

Regarding the moment coefficient, shown in Figure 9.13, we see that it is considerably influenced by the leading-edge position. With $\psi = 10°$, the deflection of the leading edge reduced the pitch-up moment that the wing experiences, without affecting drag or lift, as seen before. However, at $15°$ and more evidently at $20°$, decreasing the leading-edge angle of attack leads to an increase in the pitch-up tendency until β is close to $12°$ from where the pitch-up moment starts declining. Similar trends are observed with $\psi = 25°$ and $30°$ but with a visible plateau at higher leading-edge angles of attack. This tendency, where the C_M first intensifies its nose-up moment and then has its value lowered as β decreases, is a consequence of the reattachment of the flow.

In Figure 9.14, the $\psi = 20°$ case is selected to show the influence of the movable leading edge, although the effects of the other conditions are somewhat similar. Here, we can split the snapshots at $\beta = 10°$. Starting at $\beta = 20°$, the airfoil is fully stalled, with the tufts vibrating rapidly. By deflecting the leading edge down to $10°$, the flow starts to attach from the outer areas of the wing to the central section and from the leading edge to the ψ part, which leads to a reduction in drag and an increase in the lift as seen before. Furthermore, the pitch-

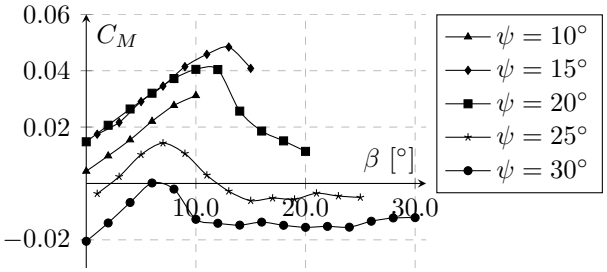

Figure 9.13: Moment coefficient as a function of β.

up tendency of the wing increases, as one could expect. This trend is then inverted as β continues its way down to $0°$, with the flow becoming fully attached. The lift continues to increase, although very slowly, and drag stays virtually constant.

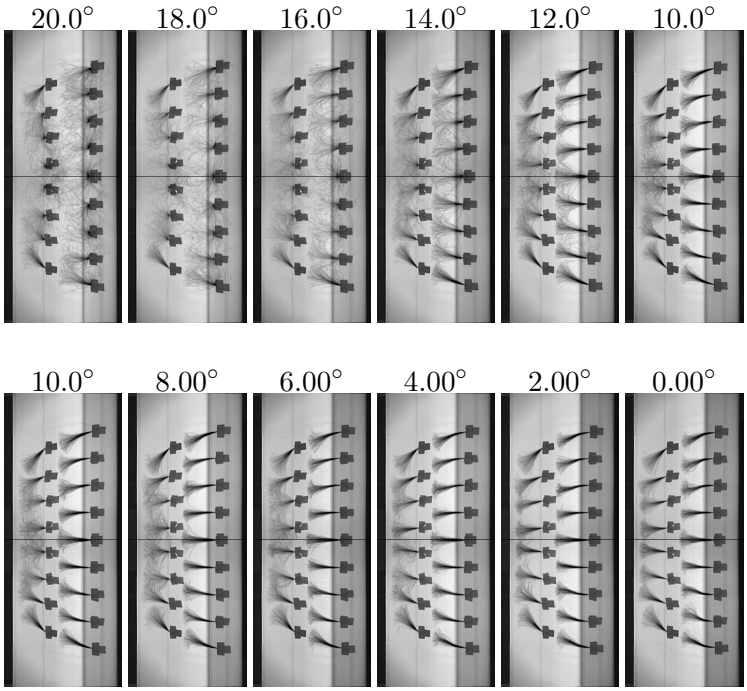

Figure 9.14: Stall visualization at the upper side considering the leading-edge flap configuration. Values indicate β values.

9.2 CFD Computations

To comprehend the influence of the leading edge deflection on the aerodynamic coefficients, a small set of cases is simulated using CFD. The main objective of such simulations is to have direct access to the pressure distribution and understand how the pressure distribution is altered. These simulations include two groups: the first one contains the results of the NACA0012-IK30 airfoil used as a conventional NACA0012 airfoil meaning that α is varied without modifying Ω, while the second one, fixes the ψ at $15°$ and changes Ω.

The first configuration has the purpose of analyzing the pressure distribution but also validating the numerical setup by comparing it with the experimental data. Simulations are

conducted only up to $15°$ where no extreme flow separation is detected. This decision was made to keep the methodology framework fairly simple so we would not need to extend the computations to a transient formulation. Furthermore, we will only be looking at steady conditions due to restricted computational power.

Before moving to the results, we first conduct some early testing regarding the computational mesh and setup. A brief mesh sensitivity study, illustrated in Figure 9.15, is done at $Re = 2 \times 10^5$ and at the maximum angle of attack, $\alpha = 15°$, to assure that the results would be grid independent. These graphs contain the pressure distribution at the wing center section and were obtained using the interpolation feature available within Tecplot software. The three meshes used for the sensitivity study were created based on an element size factor of $\sqrt[3]{2}$, with the mesh used for final simulations (Basic) having approximately 5 million elements. Moreover, due to the SST $k - \omega$ turbulence model, all meshes were designed to keep the y^+ parameter ideally close to 1, although values up to 5 were admissible. This was achieved with preliminary computations to determine the correct element size that would respect the model imposition.

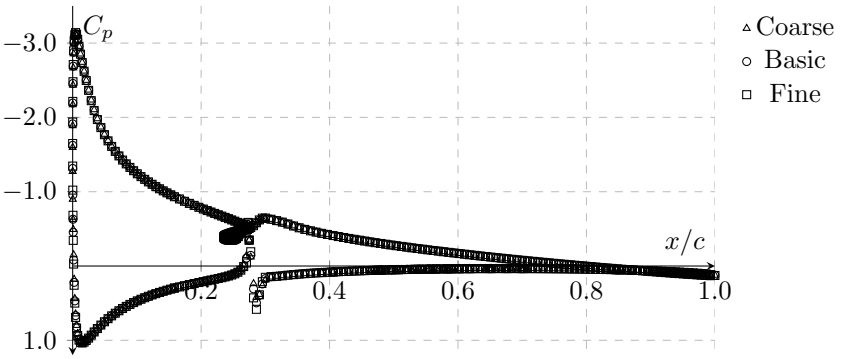

Figure 9.15: Mesh sensitivity study. Pressure coefficient at the wing center section.

Although a slight discrepancy close to the pivot point may be observed, the overall pressure distribution is fairly the same for all meshes considered. Further analysis of the pressure coefficient will be made below, using the pressure coefficient contour over the wing surface. Before that, further validation tests are conducted by comparing the aerodynamic coefficients obtained by CFD and experiments to ensure that the numerical formulation offers a good enough approximation of the experimental setup.

Starting with Figure 9.16, we have the drag (left) and lift (right) coefficients as a function of α. In these graphs, computational results are plotted against experimental data. For the range selected for CFD computations, we observe a good agreement between the two coefficients and data sets. However, one can see a disparity that starts at around $12.5°$ and indicates an overestimation of lift, which often occurs where conventional turbulence modeling is late to estimate the onset of stall [200]. However, these differences can go further than turbulence modeling since many flow parameters were not available, and geometrical aspects, such as the servo motor hub in the experimental tests, were not considered in the CFD model.

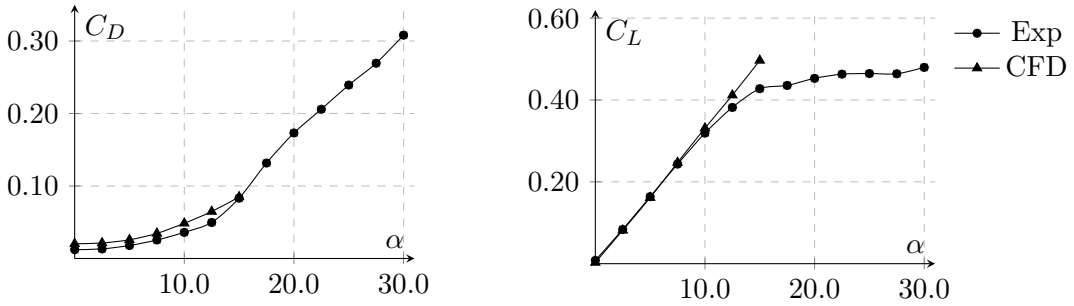

Figure 9.16: Drag and lift coefficients as a function of α.

An additional comparison is made using the pitching moment, as presented in Figure 9.17. This is an important parameter that conveys force information together with where it is applied. Although indirectly, this coefficient provides insightful information regarding the location of the suction peak region. Once again, CFD computations overall agree with experimental data, although overestimating the peak pitching moment due to the delay in predicting the onset of stall.

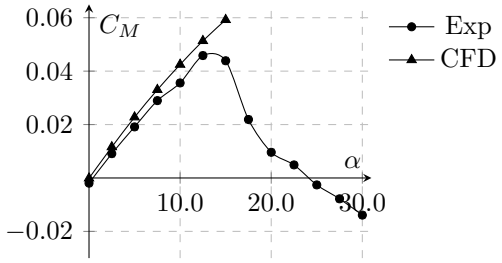

Figure 9.17: Moment coefficient as a function of α.

Let us now look at the CFD results. We start with the NACA0012 configuration, here shown in Figure 9.18, where the angle of attack is varied while keeping $\Omega = 0°$, meaning that there is no leading edge deflection relative to the ψ part. In the following figures, the pressure coefficient contour is shown on the suction side (left column) and pressure side (right column) of the wing.

Starting with the first row, where $\alpha = 0°$ is presented, no differences are seen between the two sides, as expected. The stagnation region is located right at the leading edge, with the peak suction forming on the β part.

When increasing the angle of attack to $5°$, the pressure differential becomes visible, from which three main effects should be analyzed. The first point is recognizing that there is a pressure gradient not only in the flow-wise direction but also in the wing span direction, where

$$\frac{\partial C_p}{\partial z} < 0, \tag{9.2}$$

going from the wing center section to its tips. This is a consequence of the experimental rig three three-dimensionality, which cannot prevent pressure from leaking towards the wing

tips, as in a 2D approach. Three dimensionality also leads to totally different stall characteristics, since the whole wing will not enter the stall at the same time, as confirmed by the stall visualization tests. This is obvious when looking at the contour plots (figures 9.18 and 9.19), as the wing center section will experience the intensest adverse pressure gradient and thus reach $\max C_L$ first.

The second point to be noted is the fact that the suction peak becomes more intense and moves upstream towards the leading edge. As commonly known, this provides a lift increase with an increase in the nose-up pitching moment, a trend that stops as soon as the airfoil enters the stall region.

The final aspect to be analyzed, which is specific to the wing under study, is the pressure discontinuity seen where the wing was divided. This effect was also visible in Figure 9.15 at around $x/c = 0.30$ where we observe that at the suction side, a small adverse pressure gradient is formed while at the pressure side, a favorable pressure gradient appears. These two effects combined will inevitably contribute to a small drag increase, although being an acceptable trade-off for the simpler design.

For the $\alpha = 10°$ and $15°$, the results show similar effects, with the suction peak becoming more intense and moving even further upstream. Although not simulated, going further than $15°$ will lead to the suction region burst, creating complex shear layer structures between the attached flow at the extremities and the stalled region at the center, as verified experimentally.

The other configuration simulated was the fixed ψ, at $15°$, with variable β. In Figure 9.19, the contour plots are shown for $\beta = 15°$, $12.5°$, $10°$ and $7.5°$.

Results start at $\psi = 15°$ with $\Omega = 0°$, condition shown on the first row. The suction peak is located right at the leading edge, with the pressure discontinuity being visible on both sides of the wing, as discussed before. When lowering the leading edge to $\beta = 12.5°$, two important effects appear. The first one to be noted is the reduction of the maximum $-C_p$ intensity, which is justified by a lower leading edge angle of attack. The other difference relative to the first row is the appearance of a stronger secondary suction region formed right at the start of the ψ part. This is the result of the curvature induced by the β change where the pressure becomes smaller.

These effects become even more visible when $\beta = 10°$ and $7.5°$ with the upstream suction region donating its intensity to the one close to $x/c = 0.30$. Regarding the pressure side of the airfoil, it remains fairly constant for all conditions. This pressure migration is responsible for the reduction of nose-up moment observed in force data while keeping the lift force fairly constant (revisit Figures 9.6 and 9.7). It is important to remember that these were only verified for experiments where the flow is fully attached.

These effects will be crucial for interpreting the dynamic tests presented in the following

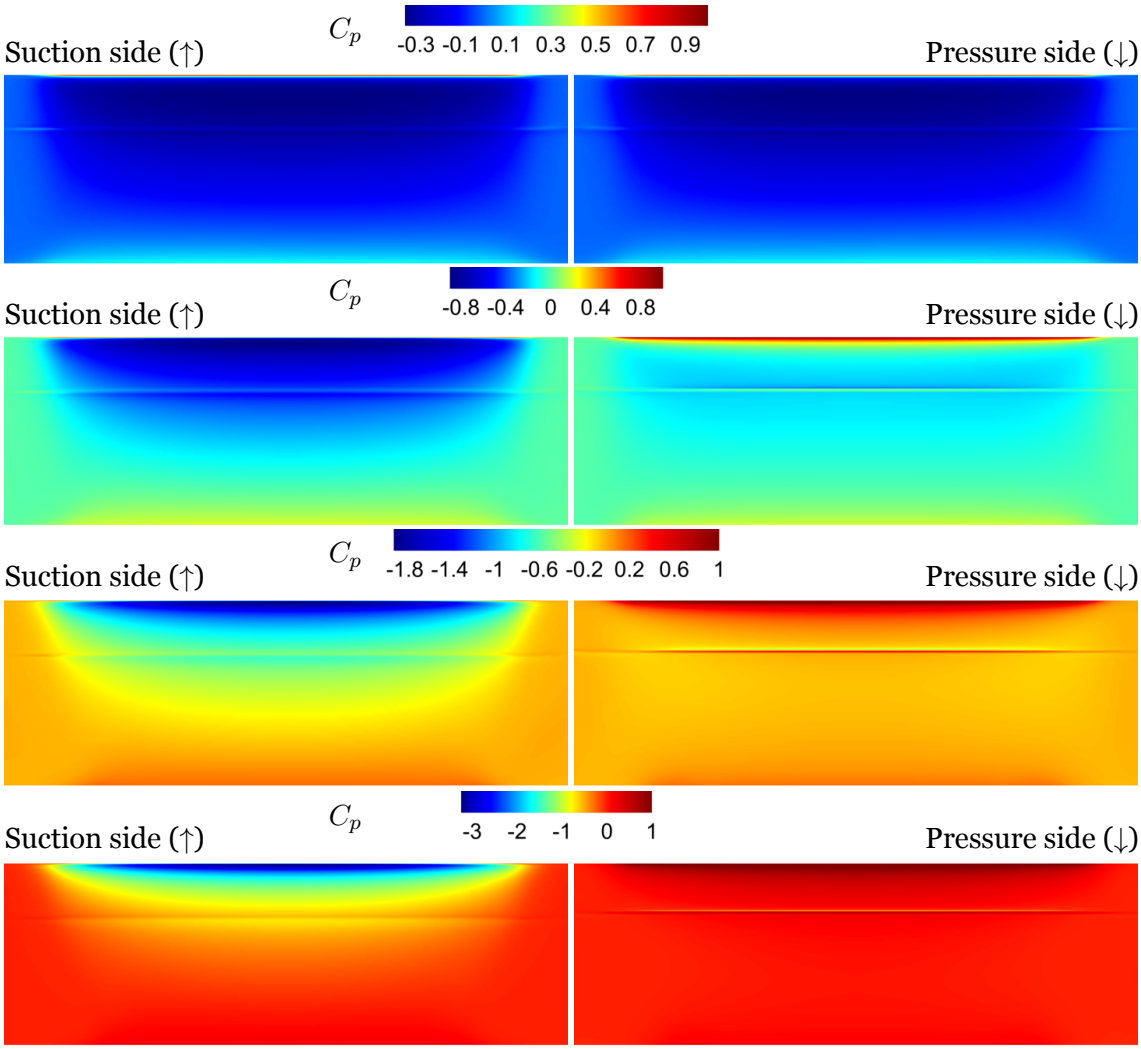

Figure 9.18: NACA0012-IK30 airfoil $Re = 2 \times 10^5$.

sections, in particular, the lift and pitching moment variations.

9.3 Optimization of the NACA0012-IK30 Wing

Yet, before moving to the dynamic cases, the NACA0012-IK30 wing is coupled with the optimization methodology described in Chapter 7 to truly reveal the efficacy of a movable leading edge.

The optimization consists of studying the NACA0012-IK30 wing at a Reynolds number of $Re = 3.0 \times 10^5$ with five different ψ, $10°$, $15°$, $20°$, $25°$ and $30°$. Based on the objective function, $\mathcal{O}$, the real-time optimization will look into the minimization of drag ($\varphi = 1$) and the maximization of lift ($\varphi = 0$). Additionally, the influence of the leading edge position on the moment coefficient and aerodynamic efficiency, C_L/C_D, are presented.

The optimization process starts with the airfoil at $\alpha = \psi$, meaning that there is no leading edge deflection ($\Omega = 0°$). Then, it runs for 60 s, implying that max $\mathcal{O}$ is expected to be reached

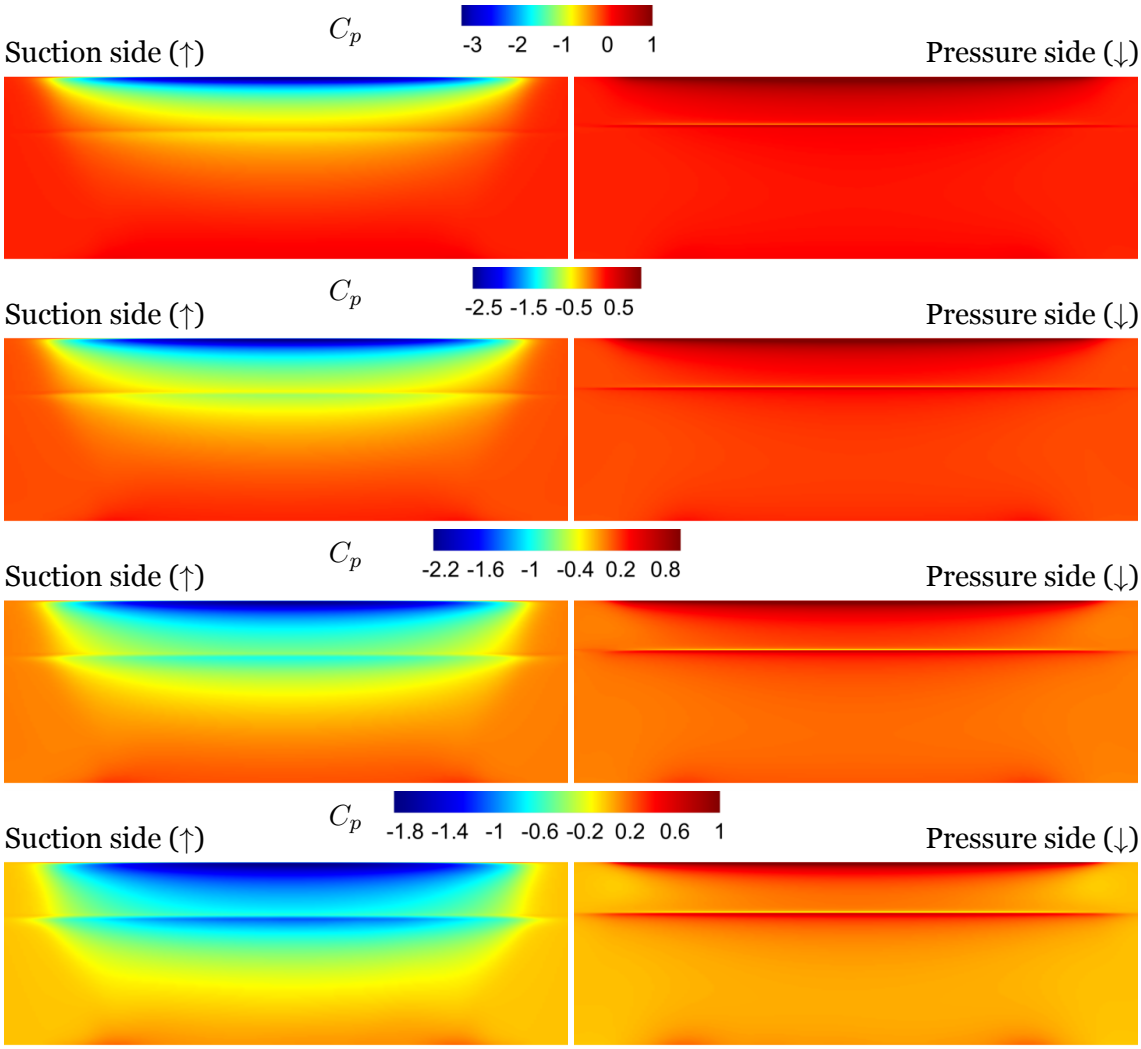

Figure 9.19: NACA0012-IK30 airfoil with movable leading edge $Re = 2 \times 10^5$.

in under one minute, although it is typically quicker, as seen in the results. Force measurements start at $t = -5$ s but the optimization only starts when $t = 0$ s. The first 5 s are used as a reference to calculate relative improvements.

The analysis starts by presenting the real-time minimization of drag, shown in Figure 9.20. The drag coefficient and the airfoil angle of attack are plotted side by side as a function of time for the five ψ cases.

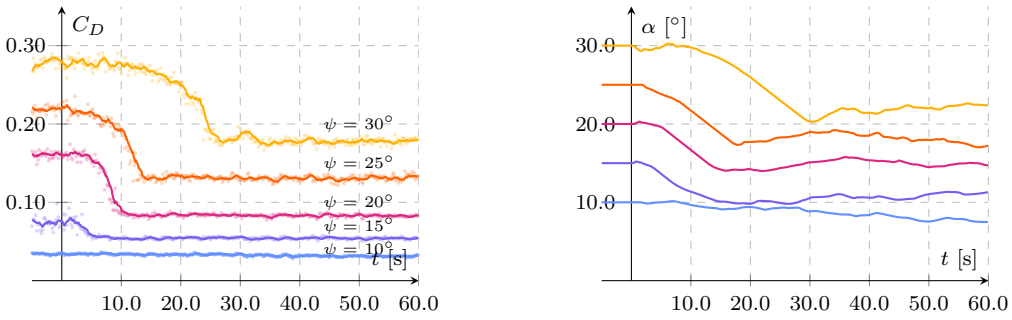

Figure 9.20: RTO of drag: Drag coefficient (left) and wing's angle of attack (right)

Starting with $\psi = 10°$, the optimization results in a constant drag coefficient over time, indicating that the search was initiated closer to the minimum. At $\alpha = 10°$, the airfoil is not expected to experience significant flow separation, a condition in which moving the leading edge does not bring any considerable benefit. This changes with $\psi = 15°$, where the optimization process finds a lower drag condition. Yet, the reduction is not as significant as in the following conditions. When ψ is set at $20°$, the wing is already undergoing extensive stall. In these conditions, the movable leading edge shows its real potential. The real-time optimization provides a substantial reduction in drag, bringing the wing to the drag level experienced when at $\alpha = 15°$ and $\Omega = 0°$.

These improvements happen due to the following physical phenomena. When ψ = $20°$, as mentioned above, the wing is at its stall region, meaning that the airflow on its surface was subjected to an adverse pressure gradient strong enough to reverse the flow direction. With $\psi = 15°$, the effects were not as visible since a substantial stall had not been reached yet. As soon as the RTO starts, and the downward motion of the leading edge is detected as advantageous, the suction peak and adverse pressure gradient start becoming less intense. It is important to highlight that lowering β yields changes in the wing's curvature and angle of attack. All these combined lead to the flow becoming more attached, reducing the wake and therefore, reducing drag.

With $\psi = 25°$ and $30°$, identical effects are identified, with the latter case being able to go down as close as to when the airfoil is at $20°$ with no leading edge deflection. Looking at the evolution of the wing angle of attack, it is clear that the leading edge position converges to an interval rather than to a definite value. This is justified firstly by the noisy measurements that induce oscillations to the gradient estimate, but also due to the existence of drag buckets in the β domain, as will be seen when plotting C_D against the leading edge angle of attack.

Regarding the optimization of the lift coefficient, presented in Figure 9.21, the movable leading edge shows its prospect of improving lift generation when the airfoil is in a deep stall.

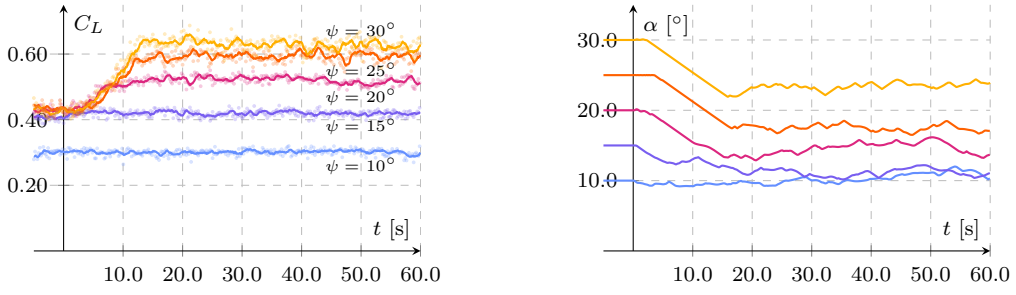

Figure 9.21: RTO of lift: Lift coefficient (left) and wing's angle of attack (right).

Similarly to the drag minimization, when $\psi = 10°$, deflecting the leading edge holds no considerable effect. The same is seen with $\psi = 15°$, and although the angle of attack changes over time for these two cases, as seen on the right graph, the lift coefficient remains fairly constant. For the next three conditions ($\psi = 20°$, $25°$ and $30°$) the wing starts the optimization with similar lift coefficients which indicates that the onset of the stall is somewhere close

to $15°$. However, they branch out into various lift coefficients that result from the flow reattaching to the wing, since the adverse pressure gradient located at the frontal part becomes less and less intense as the leading edge droops. Once again, a singular angle of attack cannot be reached as the gradient estimation is bumpy, but the control is still strong enough to keep the wing at a high lift level. This lift increase, accompanied by a drag reduction, is a typical characteristic of mitigating or recovering from a stall. As seen ahead, these two effects combined will offer a noticeable aerodynamic efficiency boost.

In contrast to the previous graph, Figure 9.22 shows the optimization process's history against the leading-edge attack angle, β, for both C_D and C_L. These graphs show the point cloud measured during the RTO together with the static map built during the optimization for all ψ cases. Looking at $\psi = 10°$, both drag and lift coefficients start at flat and wide regions where the gradient is close to zero. The fluctuations during the gradient estimation process make the leading edge search away from $\beta = 10°$ but have shown no influence in the gradient, indicating that we started very close to minimal drag and maximum lift coefficients. The same is seen for the lift coefficient when $\psi = 15°$ but not for drag. As observed on the left graph, the overall airfoil benefits from a β reduction, indicating that some flow separation is present and that lowering the leading edge may reduce or eliminate it. For the last three cases, $\psi = 20°$, $25°$ and $30°$, a similar behavior is seen. The drag coefficient starts relatively high, as expected in these angles of attack, and starts decreasing as β drops. In these cases, somewhere between $8°$ and $13°$, a rapid drag reduction is observed, which can mainly be justified by a significant flow reattachment on the wing surface. The lift does not exhibit the same behavior on the right graph, growing steadily as the leading edge pitches down. Similarly to the drag coefficient, the optimization finds a wide region of maximum lift instead of a single point.

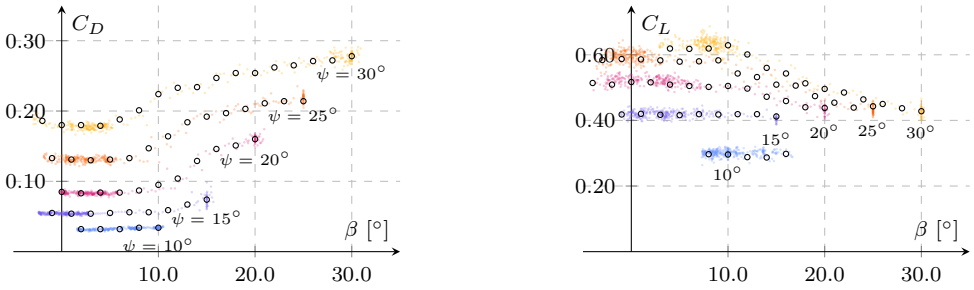

Figure 9.22: Drag minimization (left) and lift maximization (right) in the β domain.

To summarize the optimization results, Figure 9.23 presents the relative improvements obtained from the RTO implementation. Both graphs present the wing with no leading edge deflection ($\Omega = 0°$) and the optimal leading edge position found for both drag and lift. The calculations were made by averaging the first and last five seconds and calculating their relative variation. Regarding drag generation, it is observed that by just deflecting the leading edge, great improvements can be achieved with drag reductions that can go near $47\,\%$. Its true potential is seen at higher angles of attack where extreme flow separation is present. This is also verified for lift production, which sees its maximum gain at $\psi = 30°$ with an increase

of $45\,\%$. Additionally, something unique is the fact that it is not only capable of enhancing lift but also delaying the onset of stall. When looking at the $\Omega = 0°$ curve, where there is no leading edge deflection, the onset of stall starts around $\alpha = 15°$ where a stagnation is seen in the lift coefficient rise. By using the optimal leading edge position, the onset of the stall is pushed to higher angles of attack while providing much higher lift coefficients, adding enormous flexibility to this modified NACA0012 wing.

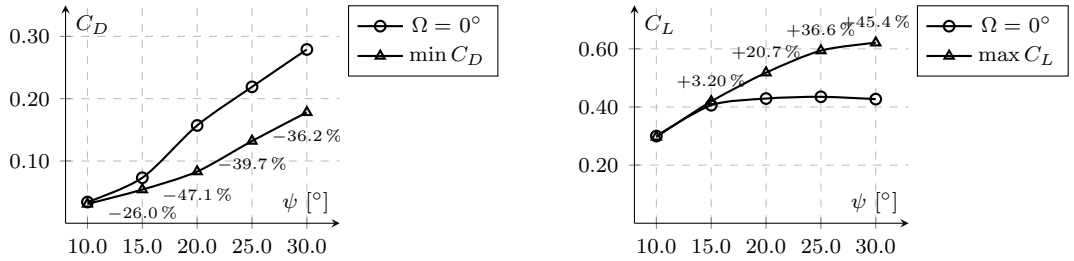

Figure 9.23: Improvements of drag minimization (left) and lift maximization (right).

Even though the optimization was focused on drag and lift forces, it is also important to analyze how other parameters are affected by the moving leading edge. Figure 9.24 shows the moment coefficient and aerodynamic efficiency as a function of β using data from both the drag minimization and maximization of C_L.

Looking at the moment coefficient for the $\psi = 10°$, we observe that moving the leading edge has a linear influence on the pitching moment, which does not occur for the other cases. With $\psi = 15°$, a nonlinear behavior is detected close to $\beta = 15°$ where the moment slightly increases as the leading-edge pitches down. Revisiting Figure 9.22, this slight increase was accompanied by a reduction in drag. This becomes much more evident when $\psi = 20°$, where reducing the leading edge angle of attack increases the moment initially. This increase is justified by a flow reattachment, which inevitably reduces drag and increases lift, ending up pushing the center of pressure forward and increasing the nose-up tendency. However, as the leading edge continues to go down, the center of pressure will travel downstream since the suction zone located at the leading edge will lose its density. This leads to the pitching moment reduction when β is less than $10°$. With $\psi = 25°$ and $30°$, the effects are similar, but the data shows an interesting particularity. In these cases, it is clear that before there is an increase in the moment as β goes down, the wing has a flat region where the moment is not affected even with drag and lift changing. This indicates that the wing's aerodynamic center is very close to the pivot point, where the sensors are positioned.

Concerning aerodynamic efficiency, regardless of the ψ condition, the influence of the leading edge angle of attack is the same, offering considerable improvements relative to the $\Omega = 0°$ configuration. As expected, increasing ψ decreases the lift-to-drag ratio, yet the graph indicates that using the leading edge angle of attack as a variable can mitigate its effects. Indeed, one can achieve higher aerodynamic efficiency than a lower ψ case with the advantage of producing more lift. For instance, the wing at $\psi = 20°$ with optimal β produces more lift with similar efficiency compared to when the wing is at $\psi = 10°$ and $\Omega = 0°$. This is the true

versatility of the proposed NACA0012-IK30 geometry.

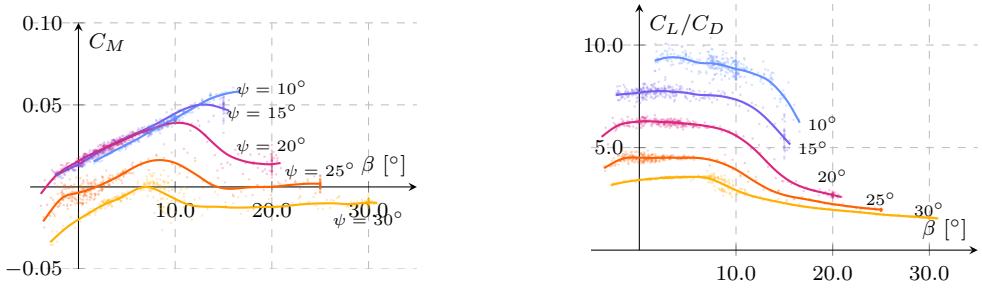

Figure 9.24: Moment coefficient at $0.3c$ (left) and aerodynamic efficiency (right)

9.4 NACA0012-IK30 Wing Under Ramps

After studying the wing under static conditions and optimizing it for minimal drag and maximum lift, the NACA0012-IK30 wing is subjected to a series of dynamic tests, starting with ramps. This section is focused exclusively on pitching ramps with constant Ω, following the sigmoid-based kinematics defined in subsection 4.2.6.

In Figure 9.25, all pitching ramp conditions tested are shown. The software limit is computed based on a Reynolds number of 2×10^5 with a pressure of 915 hPa and a temperature of $25\,°$C. These values were chosen as the typical air properties at the LABDIN laboratory (EESC-USP) during experimental tests.

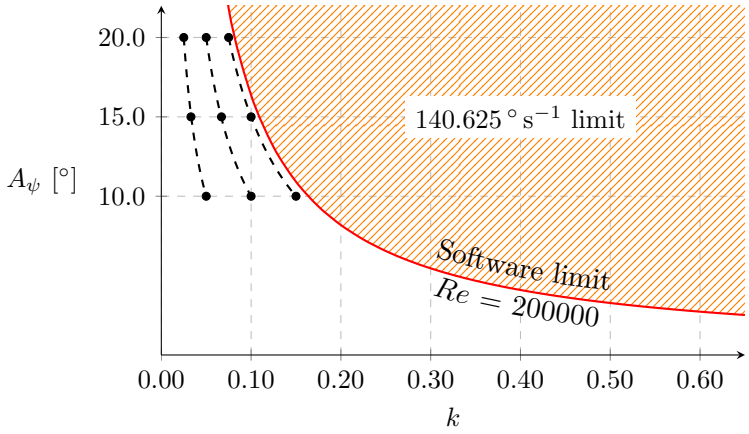

Figure 9.25: Tested conditions in the $k - A_\psi$ domain. Values are calculated based on pressure of 915 hPa and a temperature of $25.0\,°$C.

Before moving to the results, it is worth taking a pause and analyzing the filtering process of raw data, especially in dynamic cases. In Figure 9.26, the discrete Fourier transform (DFT) of (raw) C_L is shown for four static conditions with different α, all with $\Omega = 0°$. Frequencies higher than 100 Hz are not shown as they are quite small.

This graph is shown to have a better grasp regarding several phenomena present in the force data. As observed in the graph, there is a range of frequencies between approximately 5 Hz and 40 Hz which provide, in this case, a contribution to the lift coefficient. These frequen-

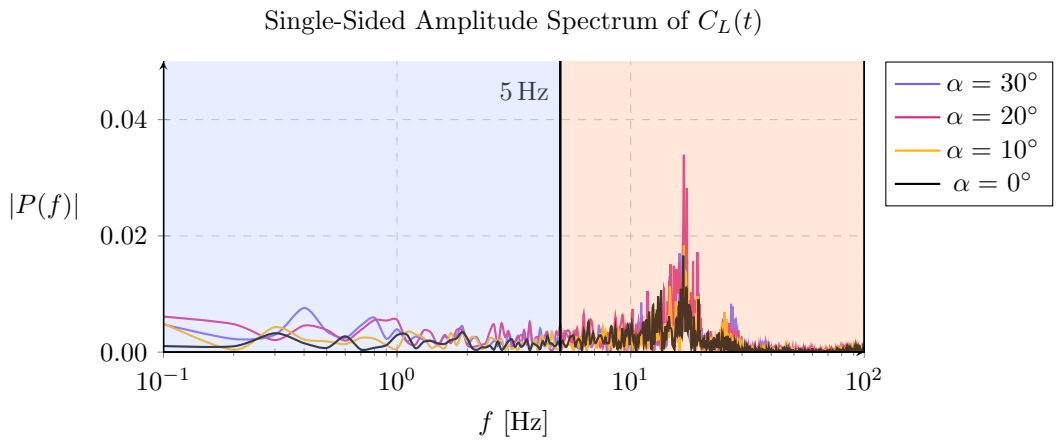

Figure 9.26: Frequency spectrum of C_L for four angles of attack with $Re = 2 \times 10^5$.

cies are mainly the result of turbulent-induced effects exerted on the structure coupled with vortex-shedding phenomena. Since these effects are not central to the present study, the designed Butterworth filter uses a cutoff frequency of 5 Hz to filter raw data. This value is chosen carefully, so it does not affect or remove the frequency spectrum dominated by the motion frequencies tested. Nevertheless, future work shall look into the frequency domain and how it changes with the leading edge mechanism.

Let us now focus on the results by observing Figure 9.27, where the results are shown for all ramp conditions. The three aerodynamic coefficients are plotted against the nondimensional time, t^*, defined as time, t, divided by 15 s, which is the duration of the ramps experiments. Graphs are centered at $t^* = 0.33$, which coincides with the inflection point of the ramps.

When looking at all the graphs simultaneously, the first obvious conclusion is that for the ramps tests, the reduced frequency does not greatly influence the results, as the amplitude does. With $A_\psi = 10°$ the ramps elevate the drag of $\Omega = 0°$ and $-10°$. On the other side, the $\Omega = -20°$ has its drag slightly reduced, with an abrupt spike when the wing is at its maximum angular velocity.

With a ramp amplitude of $A_\psi = 15°$, the advantages of deflecting the β part start appearing. With no leading edge deflection, the wing produces slightly more drag compared to the other cases, yet not considerable. Similarly to what was observed in the static cases, having the β part deflected lowers the overall angle of attack of the wing, which can reduce drag. This becomes even clearer with $A_\psi = 20°$, where $\Omega = 0°$ leads to approximately double the drag relative to the $\Omega = -10°$ and $-20°$ conditions.

Regarding lift, for a ramp amplitude of $10°$, the wing with no leading edge deflection has slightly more lift. Once again, the reduced frequency presents no considerable effect on the aerodynamics of the wing. With $A_\psi = 15°$, the ramp elevates all configurations to a similar lift level with no visible differences. The main disparity appears when ψ goes up to $20°$, in which the conditions where the leading edge is deflected downwards produce more lift due

to the mitigation of a possible stall. For this ramp amplitude, something worth mentioning is the fact that the $\Omega = 0^\circ$ case reaches a lift coefficient close to 0.6 but quickly crashes below 0.5, something that becomes more visible at the higher reduced frequencies. This occurs because the airfoil moves faster than the shedding process of the leading-edge vortex, thus enjoying the presence of a low-pressure zone.

Concerning the moment coefficient, we see that decreasing Ω intensifies the nose-down tendency, something well known where the leading edge is deflected as a flap. For the ramp amplitudes of 10° and 15° the effects and magnitudes of C_M are quite similar, with the ramp increasing the nose-up tendency. For the highest ramp amplitude, we have two distinct results. When $\Omega = 0^\circ$, we follow the whole process of going through the onset of stall, in which the nose-up tendency intensifies as the angle of attack increases up to the angle when it quickly drops. This quick drop in pitching moment occurs together with the aforementioned lift crash, a result of the dissolution of the suction zone located at the β part. By deflecting the leading edge with $\Omega = -10^\circ$ or -20°, all stall effects are delayed, where no pitching moment drop is observed, drag is kept at a lower level and no lift crash is detected.

Area left intentionally blank.

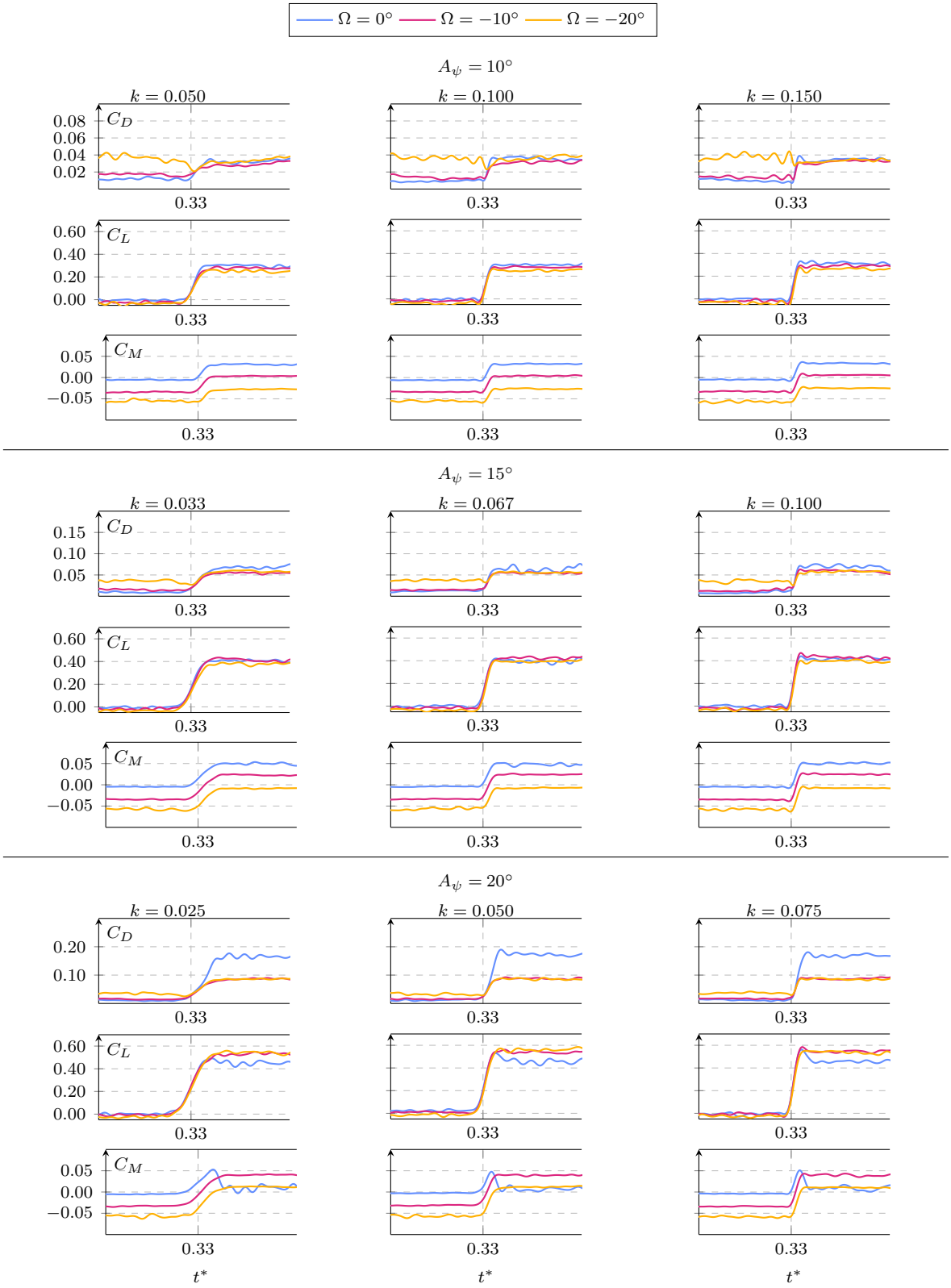

Figure 9.27: Aerodynamic coefficients for all pitching ramps with $Re = 2.0 \times 10^5$.

9.5 NACA0012-IK30 Wing Under Plunging

After exploring the aerodynamic characteristics of the NACA0012-IK30 wing under different static and ramp cases, we now move to the study of periodic conditions, starting with the investigation of plunging kinematics. The wing is tested considering a Reynolds number of 2.0×10^5 never exceeding a maximum plunging velocity of $2\pi f A = 0.7\,\mathrm{m\,s^{-1}}$ dictated by the software limitations.

In Figure 9.28, the plunging motor limit is presented based on a representative pressure of $915\,\mathrm{hPa}$ and temperature of $25.0\,^{\circ}\mathrm{C}$. Air properties were slightly different during testing, although the motor curve stayed virtually the same. The warning sign indicates a condition that the stepper failed to execute, due to lack of available torque. Two nondimensional amplitudes are considered (0.25 & 0.50), each with the nondimensional velocities of 0.0125, 0.025 and 0.0375. Based on these three nondimensional velocities, one can easily calculate the effective angle of attack over time as

$$\alpha_{\text{eff}} = \arctan(kh\sin(2\pi ft)) + \alpha(\beta, \psi, t), \tag{9.3}$$

where the first term represents the plunging contribution to the effective angle of attack. Looking exclusively at this term and using the values prescribed for the study, we see that the plunging motion adds by itself up to $0.72°$, $1.43°$ and $2.15°$ for the three kh, respectively.

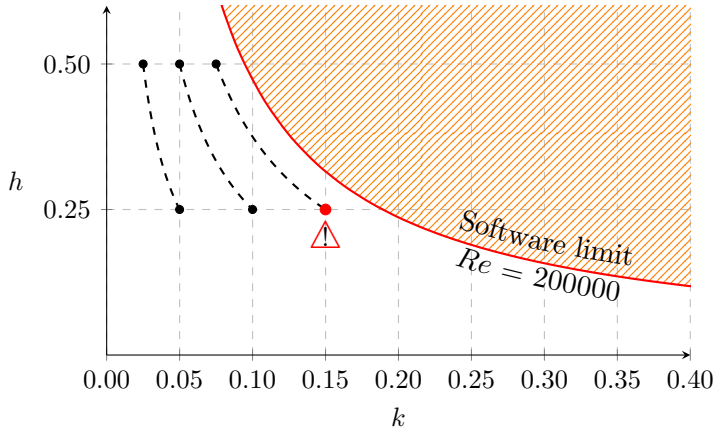

Figure 9.28: Tested conditions in the $k - h$ domain. Values are calculated based on pressure of $915\,\mathrm{hPa}$ and a temperature of $25.0\,^{\circ}\mathrm{C}$.

As explained before, the plunging motion considers a wing with the back part fixed at an angle of attack, ψ, and a pitching leading edge that never surpasses ψ. This condition ensures that we do not exceed the angle of attack more than ψ, which would inevitably degrade the aerodynamic performance. Such kinematics are accomplished by the plunging sinusoidal wave

$$y(t) = A\sin\left(2\pi ft\right), \tag{9.4}$$

and the pitching waveform prescribed to the leading edge given by

$$\beta = \overline{\beta} + A_\beta \sin\left(2\pi f t + \phi\right), \tag{9.5}$$

where ϕ is fixed at $90°$. To ensure that $\beta \leq \psi$ throughout the period, we use the

$$\overline{\beta} = \psi - A_\beta \tag{9.6}$$

constraint. Figure 9.29 illustrates some snapshots of the prescribed kinematics for the plunging cases.

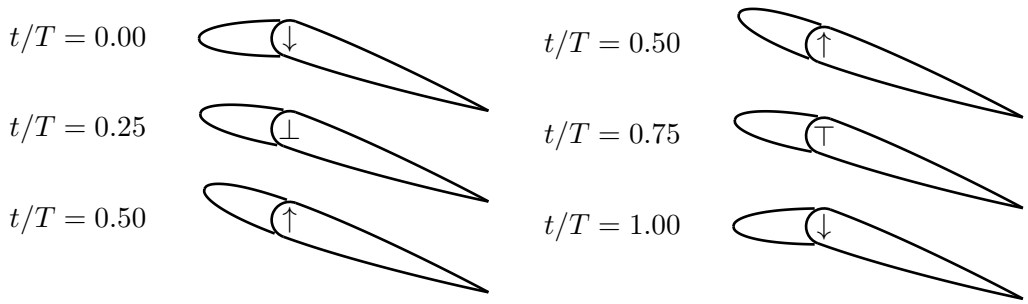

Figure 9.29: Plunging kinematics.

Each data point in the graph of Figure 9.28 is tested for $\psi = 10°$, $15°$ and $20°$. In all these conditions, the pure plunging condition ($\beta = \psi$ and $\dot{\beta} = 0$) is considered and taken as a reference. For the dynamic actuation of the leading edge, we have

- $A_\beta = 5.0°$ for $\psi = 10°$,
- $A_\beta = 7.5°$ for $\psi = 15°$, and
- $A_\beta = 5.0°$ and $10°$ for $\psi = 20°$.

In this section, only the cases with a nondimensional amplitude of 0.50 are presented since the $h = 0.25$ conditions present very similar results and conclusions. If you want to have access to the results concerning the lowest nondimensional amplitude, please see Appendix A2.

9.5.1 Plunging with $\psi = 10°$

The first case of this section considers the ψ part set at $10°$, shown in Figure 9.30. The following graphs show the aerodynamic coefficients as a function of the t/T and α_{eff} for two leading-edge pitching amplitudes and reduced frequencies, corresponding to the three nondimensional velocities considered. Throughout the study, the moment coefficient is calculated at 30 % of the chord, coinciding with the pivot point where the F/T sensors are located.

Starting with the drag coefficient, we see that activating the leading edge has a rather small effect, regardless of the reduced frequency. The reduction comes primarily from lowering

pressure drag at the frontal part of the wing and not from mitigating flow separation. No massive flow separation is expected as the maximum effective angle of attack experienced during the oscillation does not come near the static stall angle (around $15°$, as seen in Figure 9.2).

Concerning lift, it remains fairly independent regardless of A_β. This implies that the same lift coefficient can be obtained at a lower effective angle of attack, as observed. But once again, in terms of lift gain and drag reduction, we see that deflecting the leading edge when $\psi = 10°$ does not produce a significant difference. This result indicates that when flow separation is nonexistent, no considerable gains in either lift or drag are expected when pitching the leading edge.

However, when it comes to the moment coefficient, we see a considerable reduction in its mean value while activating the leading edge. Since drag and lift stay nearly the same, the reduction of the pitching moment can only be caused by the shift of the pressure center. The change in the pressure center is dictated by the location of the suction peak zone: when the leading edge has no pitching, the suction zone stays closer to the leading edge of the wing, while when the β part drops down, this low-pressure zone moves downstream closer to the pivot point, thus reducing the pitching moment. This is an interesting result that can offer some real-world applications, for instance, reducing moment loads in oscillating rotor blades without compromising the aerodynamic performance in terms of drag and lift.

All the aforementioned effects are quantified in Table 9.1, where we observe the relative changes of the mean aerodynamic coefficients, considering $A_\beta = 0°$ as the reference case. The mean aerodynamic coefficients are used as they are useful indicators that govern the real-world operation and performance of systems that use flapping airfoils. Results reinforce the fact that, at this ψ configuration, drag slightly improves, lift is kept nearly constant while the pitching moment sees noticeable reductions of almost $70\,\%$.

Table 9.1: Overview of plunging improvements for $\overline{\psi} = 10°$ considering $A_\beta = 0°$ the reference.

$\overline{\psi}$	A_β	k	$\Delta\overline{C_D}$ (%)	$\Delta\overline{C_L}$ (%)	$\Delta\overline{C_M}$ (%)
$10°$	$5°$	0.025	$-5.5\,\%$	$-0.1\,\%$	$-68.4\,\%$
$10°$	$5°$	0.050	$-6.9\,\%$	$-0.4\,\%$	$-67.2\,\%$
$10°$	$5°$	0.075	$-6.8\,\%$	$-1.3\,\%$	$-64.1\,\%$

9.5.2 Plunging with $\psi = 15°$

With the back part fixed at $15°$, illustrated in Figure 9.31, we now have some differences compared to the previous ψ case. The discrepancies come from the fact that when the wing is placed at $15°$, it is right at the limit where the stall begins. As expected, when adding the plunging motion to the equation, the wing will transit to a deeper stall region due to the increase in the effective angle of attack created by the vertical motion. Again, the reduced frequency does not change the overall effects but slightly intensifies them because a higher k will lead to the experience of a higher effective angle of attack.

Regarding drag, it is clear that having a pitching leading edge offers good improvements, especially during the descending phase, which by lowering the leading edge, the wing distances itself from the onset stall region. This is seen in the graphs where the aerodynamic coefficients are plotted against α_{eff}. In the present case, we now see the true potential of the proposed airfoil, for instance, there are phases of the period where the $A_\alpha = 7.5°$ condition provides an almost $50\,\%$ reduction compared to the reference case.

Concerning lift, the leading edge deflection also offers some improvements, although not as considerable. Still, the wing can achieve a slightly higher lift coefficient, which appears as a result of flow reattachment created by the dynamic leading edge. This is corroborated by graphs where the lift is a function of α_{eff}, which have a similar or slightly higher lift with a lower effective angle of attack.

Contrarily to the previous condition, here the moment coefficient does not present major differences aside from the initial and final phases of the period, where the lower angle of attack of the leading edge reduces the nose-up tendency by shifting the suction peak zone.

In Table 9.2, we corroborate the previous analysis by seeing respectful drag and pitching moment reductions while the lift is not considerably affected by the pitching leading edge.

Table 9.2: Overview of plunging improvements for $\overline{\psi} = 15°$ considering $A_\beta = 0°$ the reference.

$\overline{\psi}$	A_β	k	$\Delta\overline{C_D}$ (%)	$\Delta\overline{C_L}$ (%)	$\Delta\overline{C_M}$ (%)
$15°$	$7.5°$	0.025	$-37.8\,\%$	$4.5\,\%$	$-20.1\,\%$
$15°$	$7.5°$	0.050	$-40.3\,\%$	$5.0\,\%$	$-20.9\,\%$
$15°$	$7.5°$	0.075	$-45.3\,\%$	$4.1\,\%$	$-14.1\,\%$

9.5.3 Plunging with $\psi = 20°$

With $\psi = 20°$, the wing is at an angle of attack where it is now fully stalled, and for this specific condition, three leading-edge pitching amplitudes are considered. In the presence of a stall, the movable leading edge truly shows its potential, presenting an enormous impact on the aerodynamic performance, as shown in Figure 9.32.

Looking at the drag coefficient, we see that regardless of reduced frequency, the plunging-only condition produces a substantial amount of drag. With a leading-edge pitching amplitude of $A_\beta = 5°$, a considerable drag reduction is obtained, going further when $A_\beta = 10°$ is imposed. As we saw previously in the stall visualization tests, more specifically in Figure 9.14, deflecting the leading edge can fully reattach the flow to the wing, which leads to a drastic reduction of pressure drag created by the wake.

These improvements are also observed in the lift, where the pitching leading edge increases lift production, being a clear indication that the stall phenomenon is being relieved. The mean lift goes up when $A_\beta = 5°$ and $10°$ with instantaneous values being even larger.

When combining drag, lift, and the alleviation of stall, the moment coefficient becomes very

different from the conditions analyzed before, where the flow was for the most part attached to the wing. The difference here resides in the fact that activating the leading edge now does not reduce the nose-up tendency of the airfoil, instead, it increases it. This is justified by the flow reattachment, which gradually makes the pressure center move upstream and farther from the location where the moment is measured.

With the resurgence and migration of the suction zone, the pitching moment, in particular the nose-up tendency, sees increases that go up to $59\,\%$, as seen in Table 9.3. This may be seen as a disadvantageous, yet, such effect comes as a byproduct created by the flow reattachment that, on the other hand, provides good lift increases coupled with a considerable drag reduction, in some cases more than $50\,\%$.

Table 9.3: Overview of plunging improvements for $\overline{\psi} = 20^\circ$ considering $A_\beta = 0^\circ$ the reference.

$\overline{\psi}$	A_β	k	$\Delta\overline{C_D}$ (%)	$\Delta\overline{C_L}$ (%)	$\Delta\overline{C_M}$ (%)
20°	5°	0.025	$-22.8\,\%$	$10.4\,\%$	$54.5\,\%$
20°	10°	0.025	$-47.5\,\%$	$14.7\,\%$	$58.7\,\%$
20°	5°	0.050	$-19.7\,\%$	$9.1\,\%$	$38.5\,\%$
20°	10°	0.050	$-49.3\,\%$	$14.9\,\%$	$57.0\,\%$
20°	5°	0.075	$-21.3\,\%$	$8.5\,\%$	$39.9\,\%$
20°	10°	0.075	$-53.6\,\%$	$14.6\,\%$	$57.1\,\%$

Area left intentionally blank.

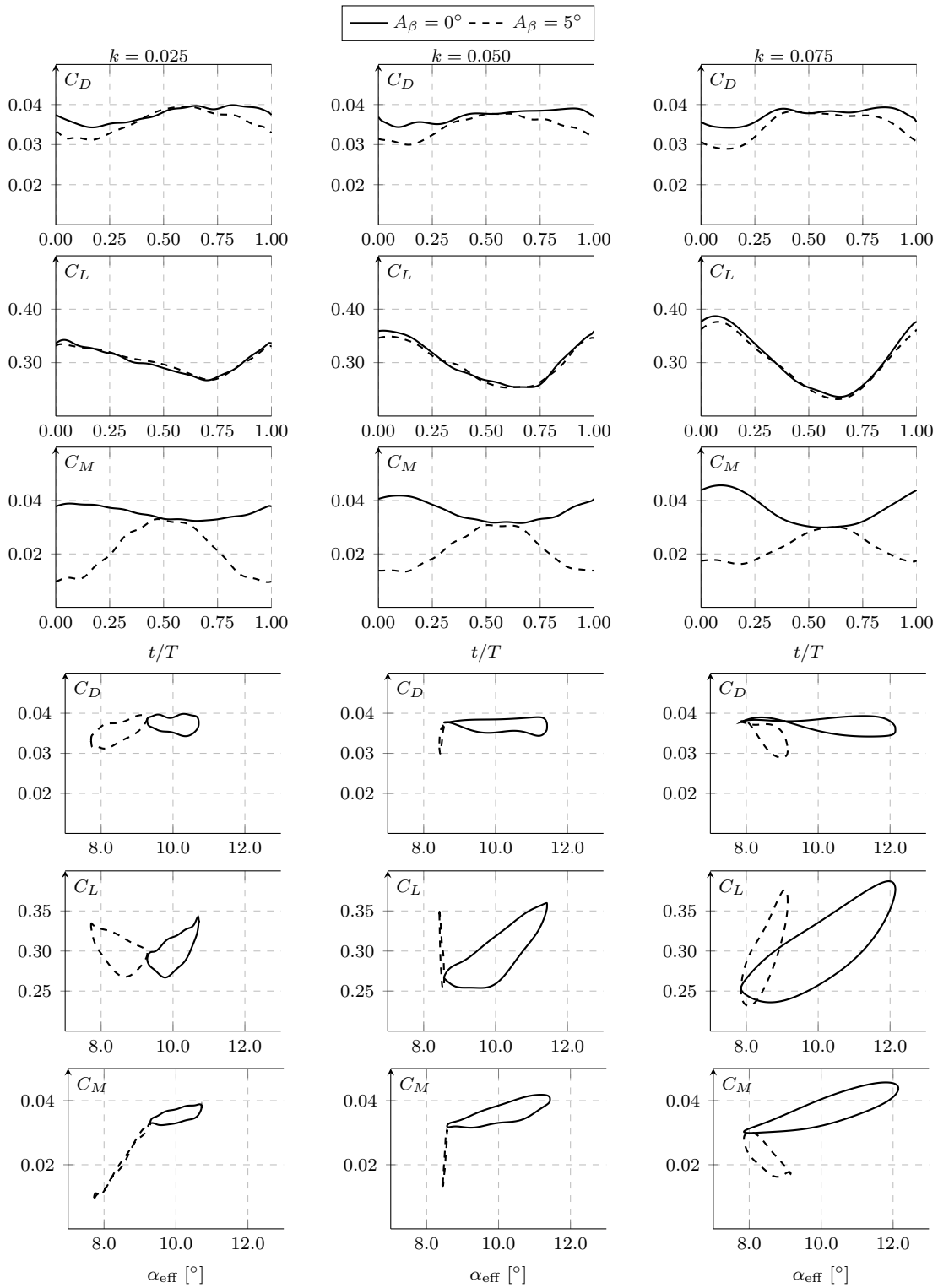

Figure 9.30: Aerodynamic coefficients with $h = 0.50$ and $\overline{\psi} = 10°$ ($\dot{\psi} = 0$).

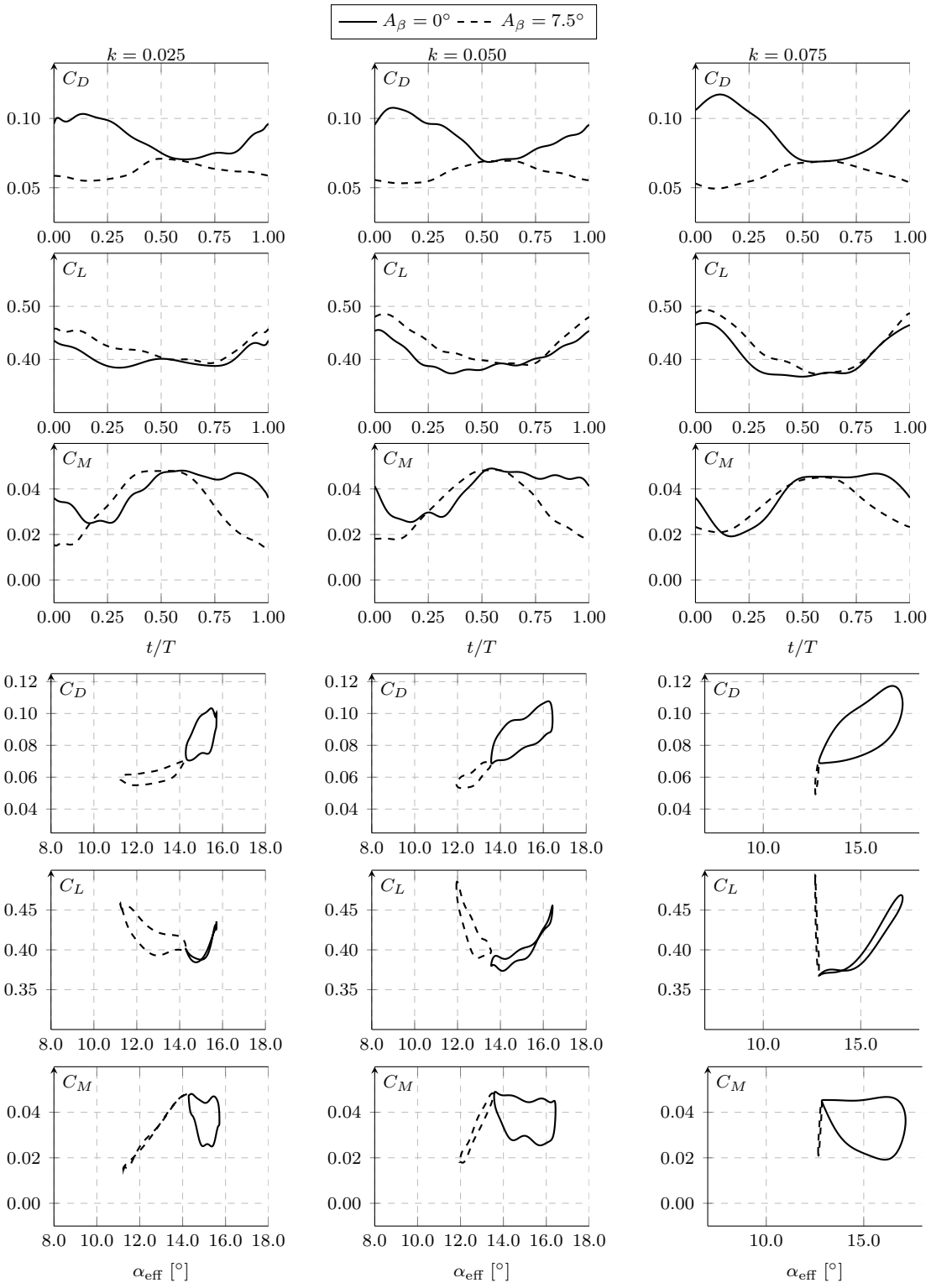

Figure 9.31: Aerodynamic coefficients with $h = 0.50$ and $\overline{\psi} = 15°$ ($\dot{\psi} = 0$).

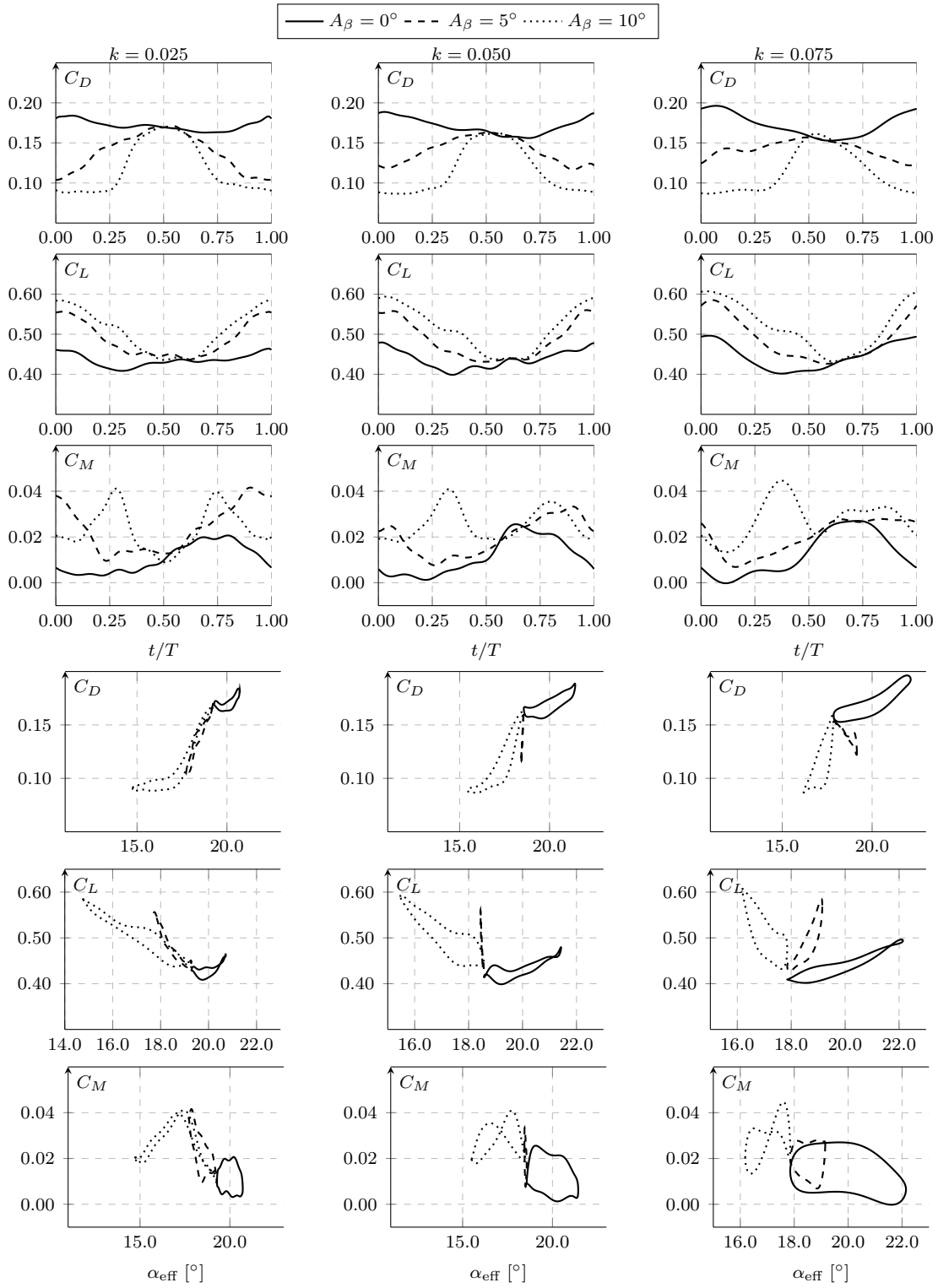

Figure 9.32: Aerodynamic coefficients with $h = 0.50$ and $\overline{\psi} = 20°$ ($\dot{\psi} = 0$).

9.6 NACA0012-IK30 Wing Under Pitching

Following the plunging conditions, the wing is tested under pitching considering two arrangements. As noted before, the difference in resolution between the pitching (stepper) and servo motors creates a wobbling effect that renders their simultaneous use impractical. Therefore we only consider the activation of each motor separately.

9.6.1 Movable Leading-Edge

In this subsection, the wing is fixed with the same $\psi = 10°$, $15°$ and $20°$ as we saw in the previous section but now, we only pitch the leading edge, removing any plunging effects seen before. In Figure 9.33, the conditions considered for this study are presented.

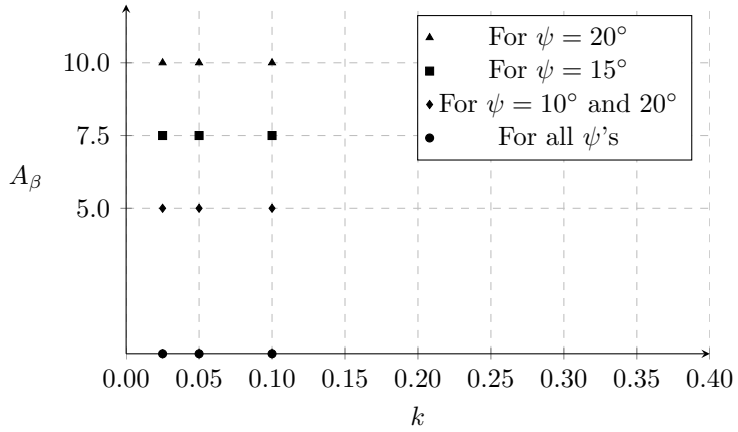

Figure 9.33: Tested conditions in the $k - A_\beta$ domain. Values are calculated based on pressure of 915 hPa and a temperature of 25.0 °C.

The leading edge follows similar kinematics as before defined as

$$\beta = \overline{\beta} + A_\beta \sin(2\pi f t), \tag{9.7}$$

and to once again ensure that $\beta \leq \psi$ throughout the period, we use the

$$\overline{\beta} = \psi - A_\beta \tag{9.8}$$

constraint. This means that the leading edge is kept between $\psi - 2A_\beta$ and ψ, as illustrated in Figure 9.34. This pitching mode will present strong similarities with the plunging cases since it has the same leading-edge kinematics without the plunging component, which did not induce considerable changes in the effective angle of attack.

The first condition illustrated in Figure 9.35 fixed the ψ part at $10°$ with two leading-edge pitching amplitudes: $0°$ and $5°$. The conditions where $A_\beta = 0°$, for the present and following conditions, are represented by a single point in the graphs where the independent variable is α_{eff}, indicating mean aerodynamic coefficients, as these are static conditions.

As one can verify, the activation of the leading edge when $\psi = 10°$ has a small to no im-

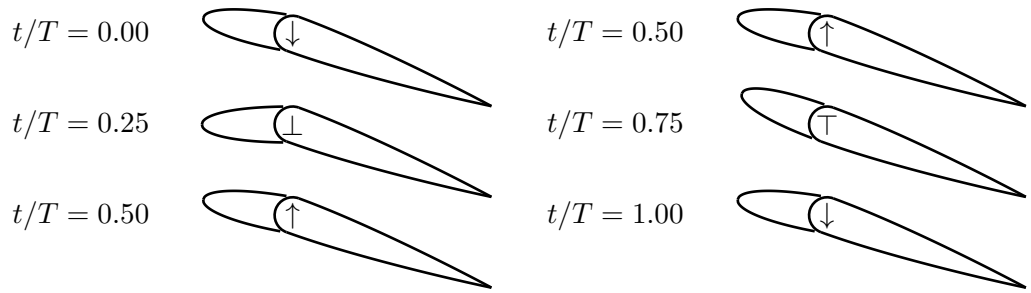

Figure 9.34: Pitching leading edge with fixed ψ.

pact on both drag and lift. Even though it can reduce the effective angle of attack, these two coefficients are kept nearly constant. The same cannot be said of the moment coefficient, which reduces its nose-up tendency as the effective angle of attack decreases. Similar to what was observed before, this is caused by the migration of the suction zone downstream, which moves the pressure center closer to the location where the moment is measured. The reduced frequency does not hold any noticeable differences.

We see all these effects summarized in Table 9.4, where the relative changes of the mean aerodynamic coefficients are presented. Deflecting the leading edge, which reduces the angle of attack, leads to a small lift reduction, a modest improvement of drag, and a considerable pitching moment alleviation.

Table 9.4: Overview of pitching improvements for $\overline{\psi} = 10^\circ$ considering $A_\beta = 0^\circ$ the reference.

$\overline{\psi}$	A_β	k	$\Delta\overline{C_D}$ (%)	$\Delta\overline{C_L}$ (%)	$\Delta\overline{C_M}$ (%)
10°	5°	0.025	$-5.2\,\%$	$-1.6\,\%$	$-74.6\,\%$
10°	5°	0.050	$-7.0\,\%$	$-2.9\,\%$	$-73.0\,\%$
10°	5°	0.100	$-6.9\,\%$	$-2.4\,\%$	$-75.8\,\%$

With $\psi = 15^\circ$, shown in Figure 9.36, effects stay virtually the same, with drag and lift being slightly affected by the leading edge motion and the moment following the same tendency as before. This is an interesting condition that can be compared with the analogous plunging case presented in Figure 9.31. The small yet strong enough contribution of the plunging motion pushed the wing into the stall region, whose contribution is not present here, making this condition very similar to when $\psi = 10^\circ$.

Nevertheless, Table 9.5 shows that even if this condition cannot reach the improvements of the homologous plunging case, we still accomplish a drag reduction up $20\,\%$, a slight lift boost and a useful pitching moment reduction.

Table 9.5: Overview of pitching improvements for $\overline{\psi} = 15^\circ$ considering $A_\beta = 0^\circ$ the reference.

$\overline{\psi}$	A_β	k	$\Delta\overline{C_D}$ (%)	$\Delta\overline{C_L}$ (%)	$\Delta\overline{C_M}$ (%)
15°	7.5°	0.025	$-16.0\,\%$	$2.7\,\%$	$-52.4\,\%$
15°	7.5°	0.050	$-19.8\,\%$	$2.1\,\%$	$-52.4\,\%$
15°	7.5°	0.100	$-19.1\,\%$	$3.0\,\%$	$-49.2\,\%$

Results are radically changed when the wing is at $\psi = 20^\circ$, as shown in Figure 9.37, where

three leading-edge pitching amplitudes are analyzed. Concerning the drag coefficient, we see that it is very much improved by lowering the leading edge for $A_\alpha = 5°$ and $10°$ with both amplitudes being able to achieve an identical minimum drag level. Nevertheless, when $A_\alpha = 10°$, the wing stays at a lower drag level for a larger fraction of the period, thus offering a better result. As soon as the leading edge approaches ψ, the performance quickly degrades, a synonym for the onset of dynamic stall.

Regarding lift, not only does the bigger leading-edge pitching amplitude provide more force for a higher percentage of the period, but it also offers it at a lower angle of attack. Here, the reduced frequency plays a role in expanding the distance between the lift levels during descending and ascending phases of the period.

The moment coefficient has a similar behavior seen before regarding the reattachment of the flow to the wing surface. As the effective angle of attack decreases, the flow reattaches, judging by the drag reduction and lift increase, which moves the pressure center upstream and intensifies the nose-up tendency of the wing. When the effective angle of attack goes up again, this tendency disappears as the airfoil enters its stall phase again.

All of this is quantified in Table 9.6 where appreciable lift enhancements are obtained together with considerable drag improvements, especially for the highest leading edge pitching amplitude. Nevertheless, as seen before, this comes with the cost of a higher nose-up pitching moment.

Table 9.6: Overview of pitching improvements for $\overline{\psi} = 20°$ considering $A_\beta = 0°$ the reference.

$\overline{\psi}$	A_β	k	$\Delta\overline{C_D}$ (%)	$\Delta\overline{C_L}$ (%)	$\Delta\overline{C_M}$ (%)
$20°$	$5°$	0.025	$-26.6\,\%$	$8.4\,\%$	$55.2\,\%$
$20°$	$10°$	0.025	$-48.5\,\%$	$12.0\,\%$	$54.9\,\%$
$20°$	$5°$	0.050	$-30.5\,\%$	$8.1\,\%$	$63.4\,\%$
$20°$	$10°$	0.050	$-52.3\,\%$	$12.1\,\%$	$62.7\,\%$
$20°$	$5°$	0.100	$-28.2\,\%$	$8.2\,\%$	$61.1\,\%$
$20°$	$10°$	0.100	$-48.4\,\%$	$12.1\,\%$	$59.1\,\%$

Area left intentionally blank.

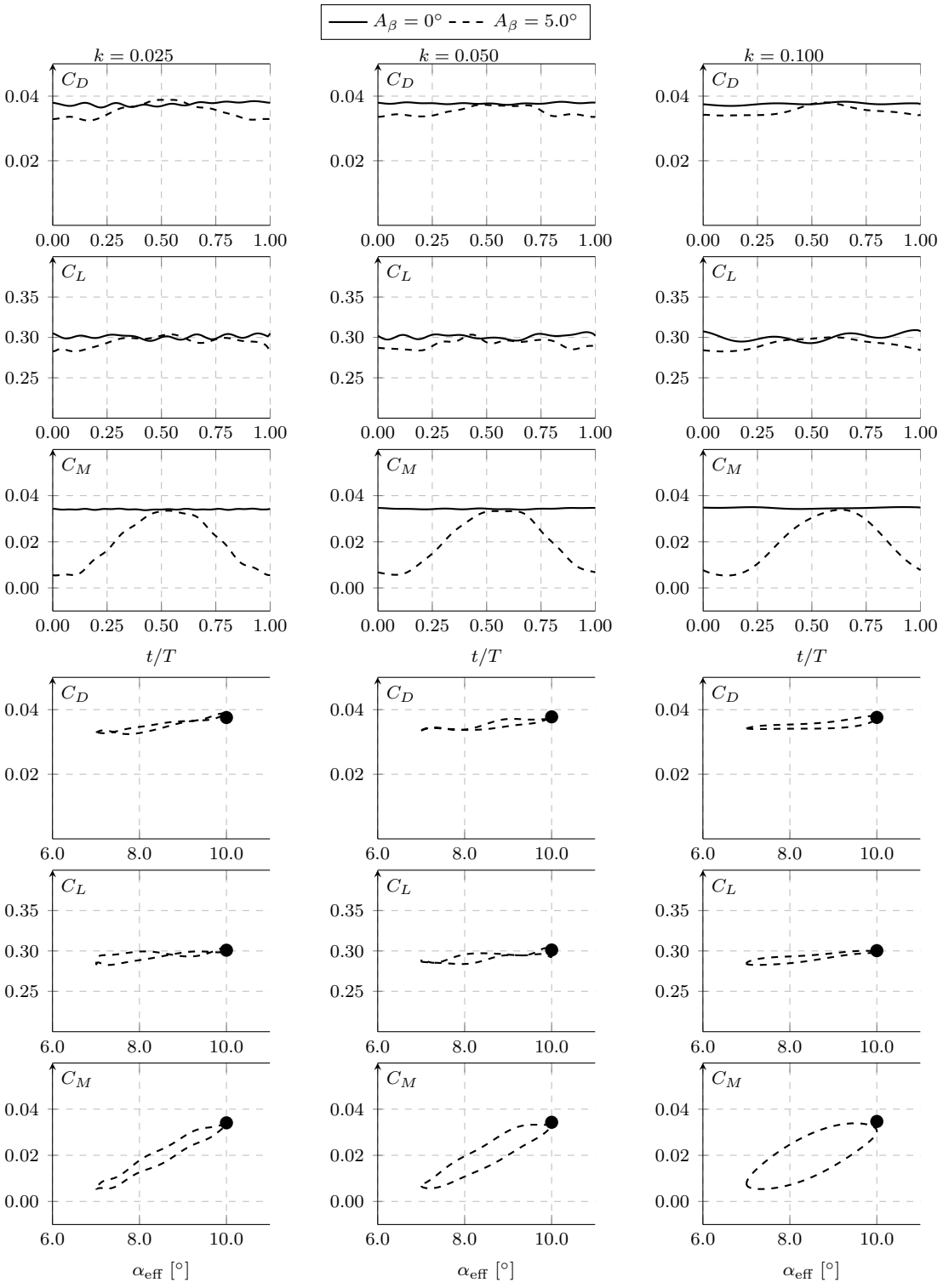

Figure 9.35: Aerodynamic coefficients with $\overline{\psi} = 10°$ ($\dot{\psi} = 0$).

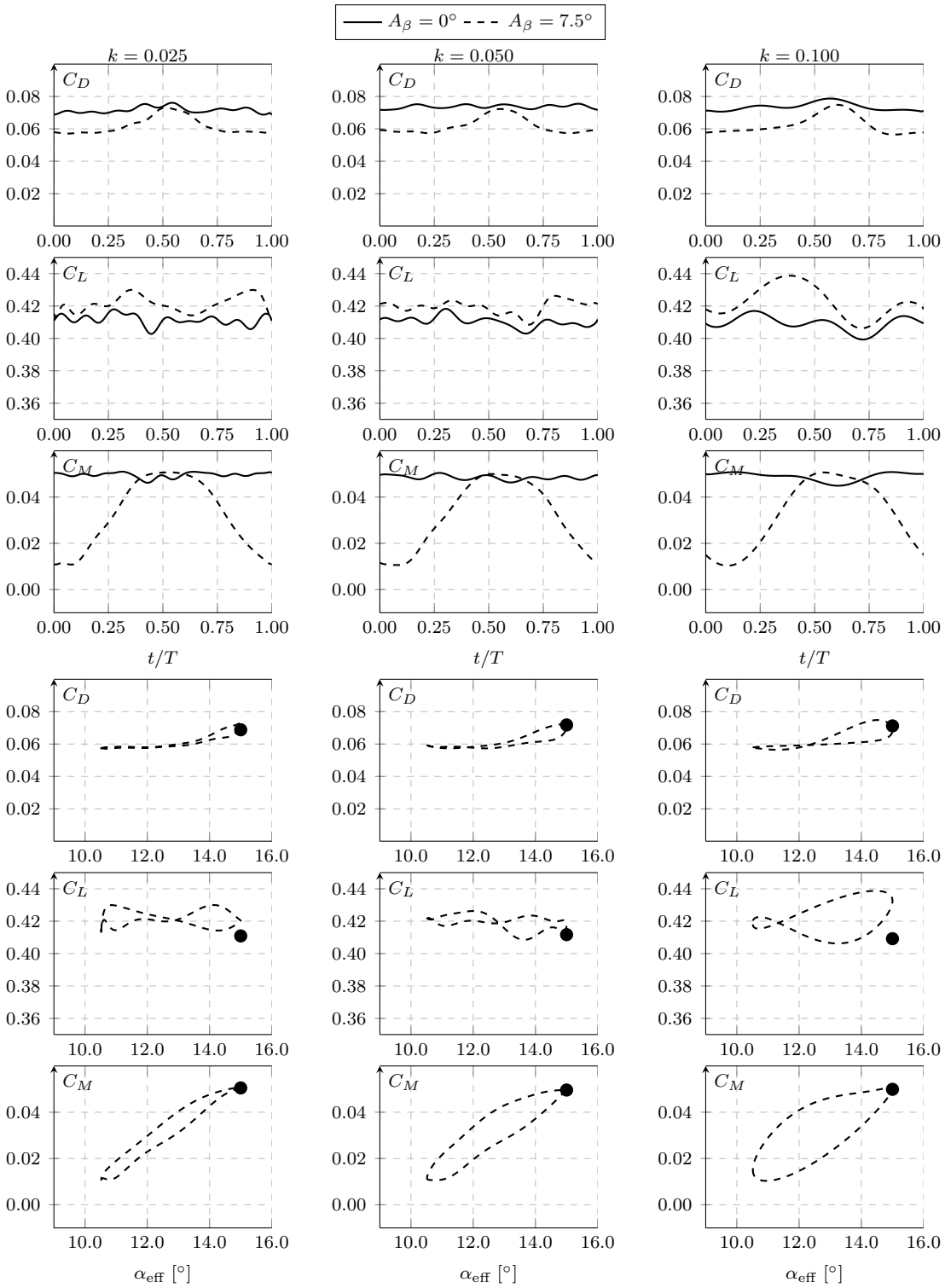

Figure 9.36: Aerodynamic coefficients with $\overline{\psi} = 15°$ ($\dot{\psi} = 0$).

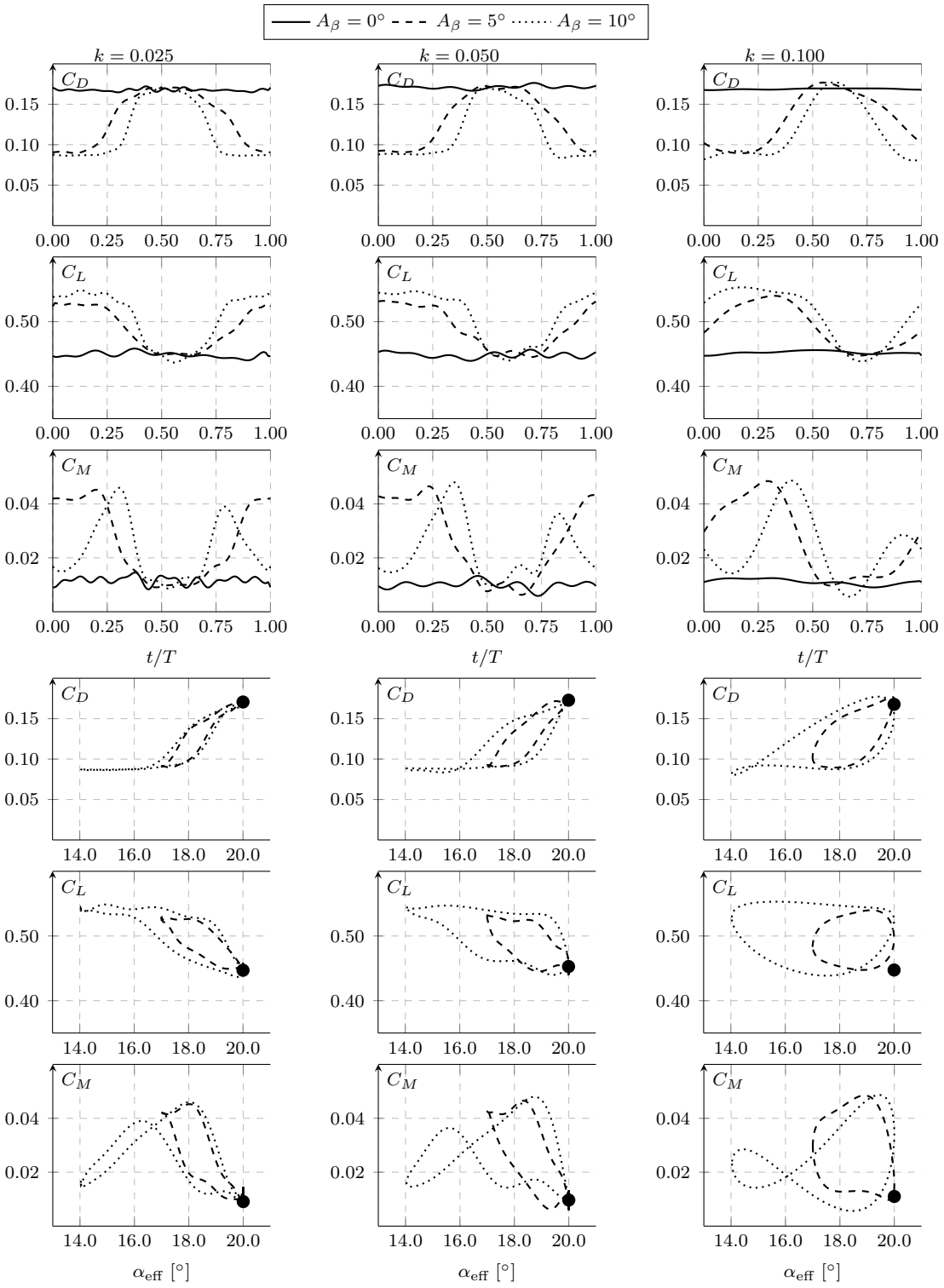

Figure 9.37: Aerodynamic coefficients with $\overline{\psi} = 20°$ ($\dot{\psi} = 0$).

9.6.2 Pitching with Constant Ω

The second pitching mode uses the NACA0012-IK30 with the leading edge fixed as a flap. Three positions are considered: $\Omega = 0°$, $-10°$ and $-20°$. Then, the angle of attack of the back part is changed sinusoidally as

$$\psi = A_\psi + A_\psi \sin(2\pi f t), \tag{9.9}$$

in which the ψ part oscillates between $0°$ and $2A_\psi$ and, consequently, the leading edge between Ω and $\Omega + 2A_\psi$, as illustrated in Figure 9.38.

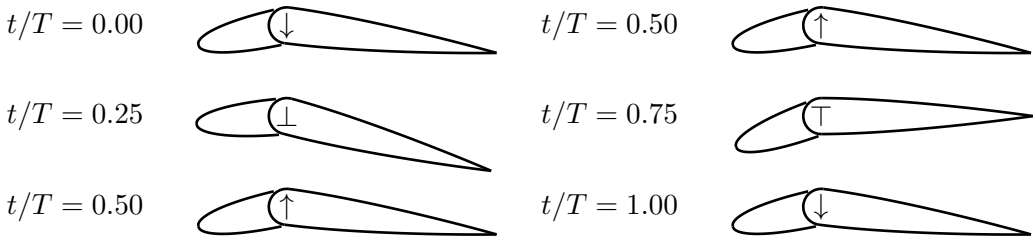

Figure 9.38: Pitching kinematics with fixed Ω.

While the previous pitching mode focused on the dynamic curvature of the wing and its impact on the aerodynamic performance, here we will focus our attention on the airfoil fixed curvature created by a fixed leading edge deflection relative to the ψ part. The study of this pitching mode considers three kA_ψ curves, each with three pitching amplitudes, $A_\psi = 5°$, $7.5°$ and $10°$. These are shown in Figure 9.39 considering the same air properties as before. The software limit is also presented, where a maximum pitching velocity of $140.625°$ was admissible.

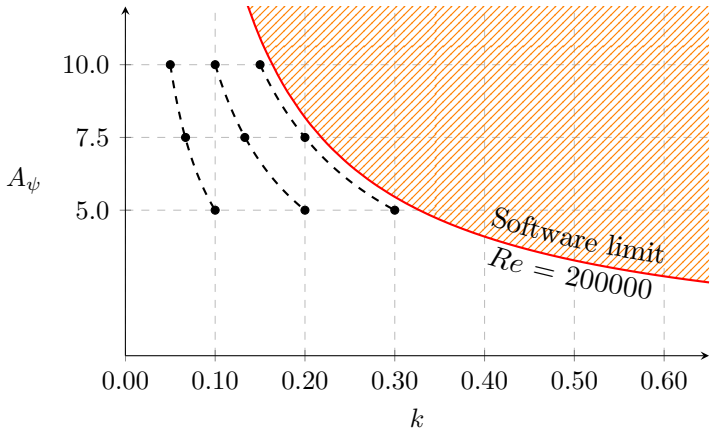

Figure 9.39: Tested conditions in the $k - A_\psi$ domain. Values are calculated based on pressure of 915 hPa and a temperature of 25.0 °C.

Beginning at the lowest pitching amplitude, $A_\psi = 5°$, shown in Figure 9.40, we observe that drag is kept lower with the no-flap and $\Omega = -10°$ configurations. With $\Omega = -20°$, where the leading edge angle of attack is higher than the pitching amplitude, we see a degradation of performance, especially when the airfoil is at $t/T = 0.25$.

The deflection of the β part is also nonbeneficial for lift, which as expected, has its value reduced with the drooping of the leading edge by the overall reduction of the wing's angle of attack. Nevertheless, the curvature of the wing provides an advantage, since it provides more lift for the same angle of attack but does not improve the maximum angle of attack.

Additionally, the highest reduced frequency creates a very small region of negative lift at lower effective angles of attack for $\Omega = 0°$ and amplifies the negative area for the other two configurations, something witnessed for the other pitching amplitudes too. This is likely due to the intensification of the existent lag between kinematics and aerodynamics that becomes more evident as k increases.

The moment coefficient is one of the aerodynamic coefficients that are more affected due to the great influence that the β deflection has on the suction peak location. As observed, when Ω is reduced, the curve corresponding to $\Omega = 0°$ is translated downwards. This means that there is an intensification of the nose-down tendency of the wing, which can be considered a disadvantage.

Table 9.7 illustrates all these misfortunes where drag goes up and lift goes down considerably, as is the pitching moment. It is worth mentioning that these significant reductions in the pitching moment (much higher than $100\,\%$) come from the fact that the Ω deflection shifts the moment from a nose-up to a nose-down tendency.

Table 9.7: Overview of pitching improvements for $A_\psi = 5°$ considering $\Omega = 0°$ the reference.

A_ψ	Ω	k	$\Delta\overline{C_D}$ (%)	$\Delta\overline{C_L}$ (%)	$\Delta\overline{C_M}$ (%)
$5°$	$-10°$	0.100	$3.0\,\%$	$-24.9\,\%$	$-173.5\,\%$
$5°$	$-10°$	0.200	$2.6\,\%$	$-22.3\,\%$	$-162.5\,\%$
$5°$	$-10°$	0.300	$1.5\,\%$	$-19.9\,\%$	$-168.7\,\%$
$5°$	$-20°$	0.100	$28.6\,\%$	$-41.7\,\%$	$-330.5\,\%$
$5°$	$-20°$	0.200	$26.7\,\%$	$-44.1\,\%$	$-306.4\,\%$
$5°$	$-20°$	0.300	$27.2\,\%$	$-47.4\,\%$	$-317.0\,\%$

Similar effects are verified when $A_\psi = 7.5°$ (Figure 9.41), but there are slight differences that should be addressed, mainly because we are now closer to the stall region of the wing. The obvious difference is the fact that now the larger pitching amplitude offers higher lift and more drag while maintaining a similar moment coefficient when $A_\psi = 5°$. Furthermore, we now see an almost independence of lift when $\Omega = -10°$, something that cannot be said for drag. With $k = 0.067$ and $\Omega = 0°$, a subtle difference is observed when the wing is close to its maximum effective angle of attack, $\alpha_{\text{eff}} = 15°$ ($t/T = 0.75$), where a rapid increase in drag and a tiny reduction in both lift and moment are noticed, indicating that the wing is on the brink of stall. This phenomenon vanishes at the other reduced frequencies where kinematics start dominating the flow field.

All of this is shown in Table 9.8 where we now have the $\Omega = -10°$ case providing fair drag improvements with no major differences in lift. As in the previously pitching amplitude, the highest leading-edge deflection still degrades the aerodynamic performance.

Table 9.8: Overview of pitching improvements for $A_\psi = 7.5°$ considering $\Omega = 0°$ the reference.

A_ψ	Ω	k	$\Delta\overline{C_D}$ (%)	$\Delta\overline{C_L}$ (%)	$\Delta\overline{C_M}$ (%)
$7.5°$	$-10°$	0.067	$-4.9\,\%$	$0.2\,\%$	$-122.6\,\%$
$7.5°$	$-10°$	0.133	$-7.0\,\%$	$-0.7\,\%$	$-118.9\,\%$
$7.5°$	$-10°$	0.200	$-8.1\,\%$	$2.3\,\%$	$-111.3\,\%$
$7.5°$	$-20°$	0.067	$12.7\,\%$	$-10.9\,\%$	$-242.5\,\%$
$7.5°$	$-20°$	0.133	$8.4\,\%$	$-16.3\,\%$	$-234.2\,\%$
$7.5°$	$-20°$	0.200	$10.7\,\%$	$-12.8\,\%$	$-227.1\,\%$

With $A_\psi = 10°$, shown in Figure 9.42, the presence of stall becomes inevitable when Ω is fixed at zero degrees. There is an evident and quick increase in drag when the wing passes the $\alpha_{\text{eff}} = 15°$ threshold together with a lift decline as the wing reaches its maximum angle of attack. These effects are echoed in the pitching moment, which displays a sharp decline at the onset of the stall. Once again, at the higher reduced frequency, these impacts in the aerodynamics coefficients are smoothed out by kinematics. All these effects caused by the occurrence of stall, are circumvented when we deflect the leading-edge flap, which offers more lift and similar drag for an equal angle of attack while removing unwanted fluctuations in the pitching moment. Once again, when the dynamic stall is present, the deflection of the leading edge truly shines, showing that it can attack the main fronts of the dynamic stall.

This is upheld by the mean relative changes shown in Table 9.9, where drag is reduced down to $45\,\%$, lift can be slightly higher for the $\Omega = -10°$ configuration, and the pitching moment is reduced but much less aggressively.

Table 9.9: Overview of pitching improvements for $A_\psi = 10°$ considering $\Omega = 0°$ the reference.

A_ψ	Ω	k	$\Delta\overline{C_D}$ (%)	$\Delta\overline{C_L}$ (%)	$\Delta\overline{C_M}$ (%)
$10°$	$-10°$	0.050	$-45.0\,\%$	$6.1\,\%$	$-76.3\,\%$
$10°$	$-10°$	0.100	$-41.4\,\%$	$5.5\,\%$	$-78.3\,\%$
$10°$	$-10°$	0.150	$-42.7\,\%$	$2.8\,\%$	$-81.9\,\%$
$10°$	$-20°$	0.050	$-28.0\,\%$	$-1.5\,\%$	$-211.2\,\%$
$10°$	$-20°$	0.100	$-27.6\,\%$	$-2.8\,\%$	$-205.6\,\%$
$10°$	$-20°$	0.150	$-24.8\,\%$	$-2.1\,\%$	$-208.8\,\%$

This marks the end of the exposition and analysis of the results. All data presented here may be found at **https://www.earc96.com/PhD** and is openly accessible, editable, and may be shared by anyone. Additional information can be found in the database, for instance, uncertainties and other kinematic variables, which were not included in the current manuscript for simplicity.

The next and final chapter will provide an overview of the entire project and migrate the discussion of the results to a more futuristic perspective. Several hypotheses will be raised, together with suggestions given on how to approach and explore such opportunities.

Area left intentionally blank.

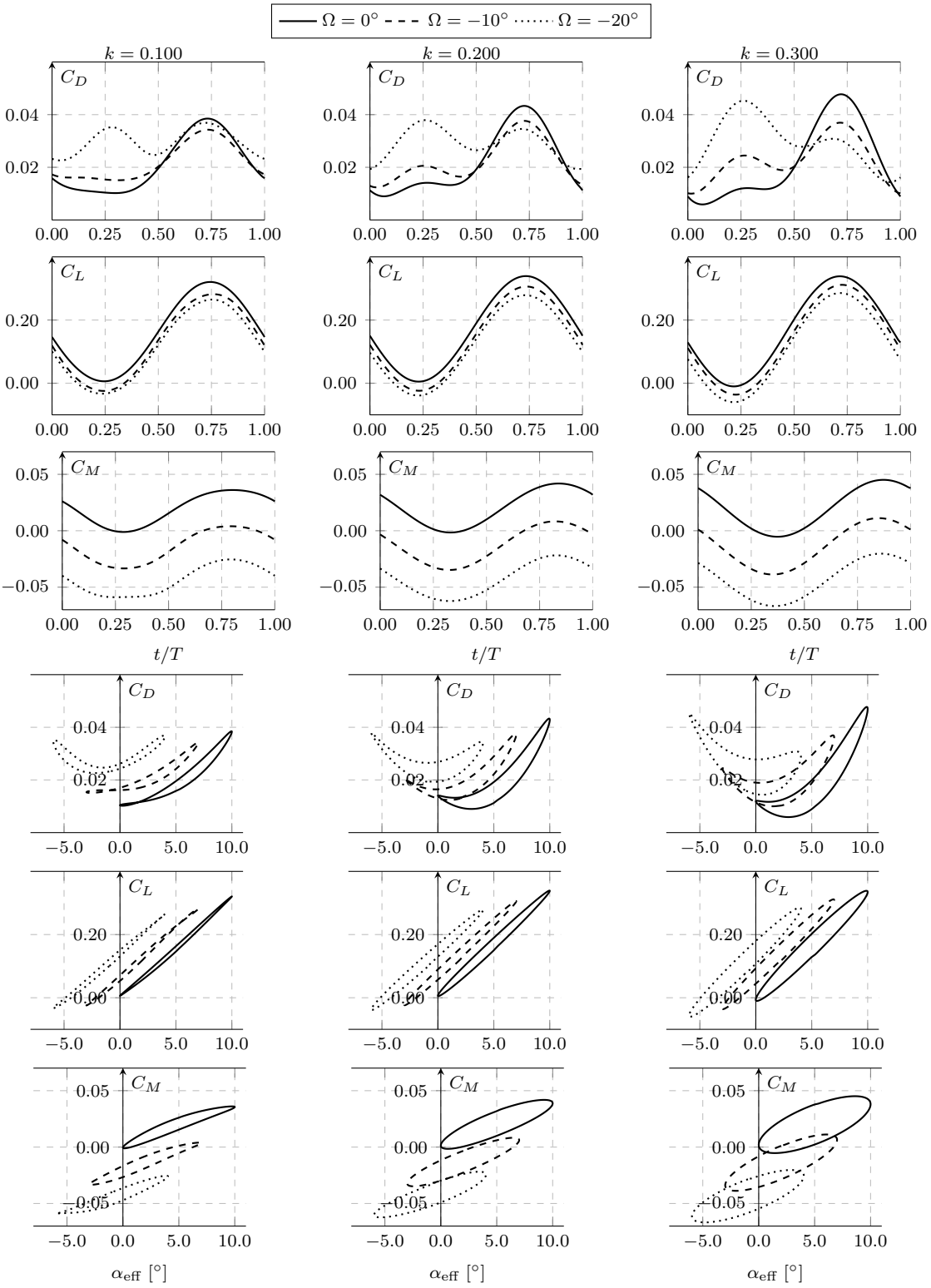

Figure 9.40: Aerodynamic coefficients with $A_\psi = 5°$ at different leading edge positions.

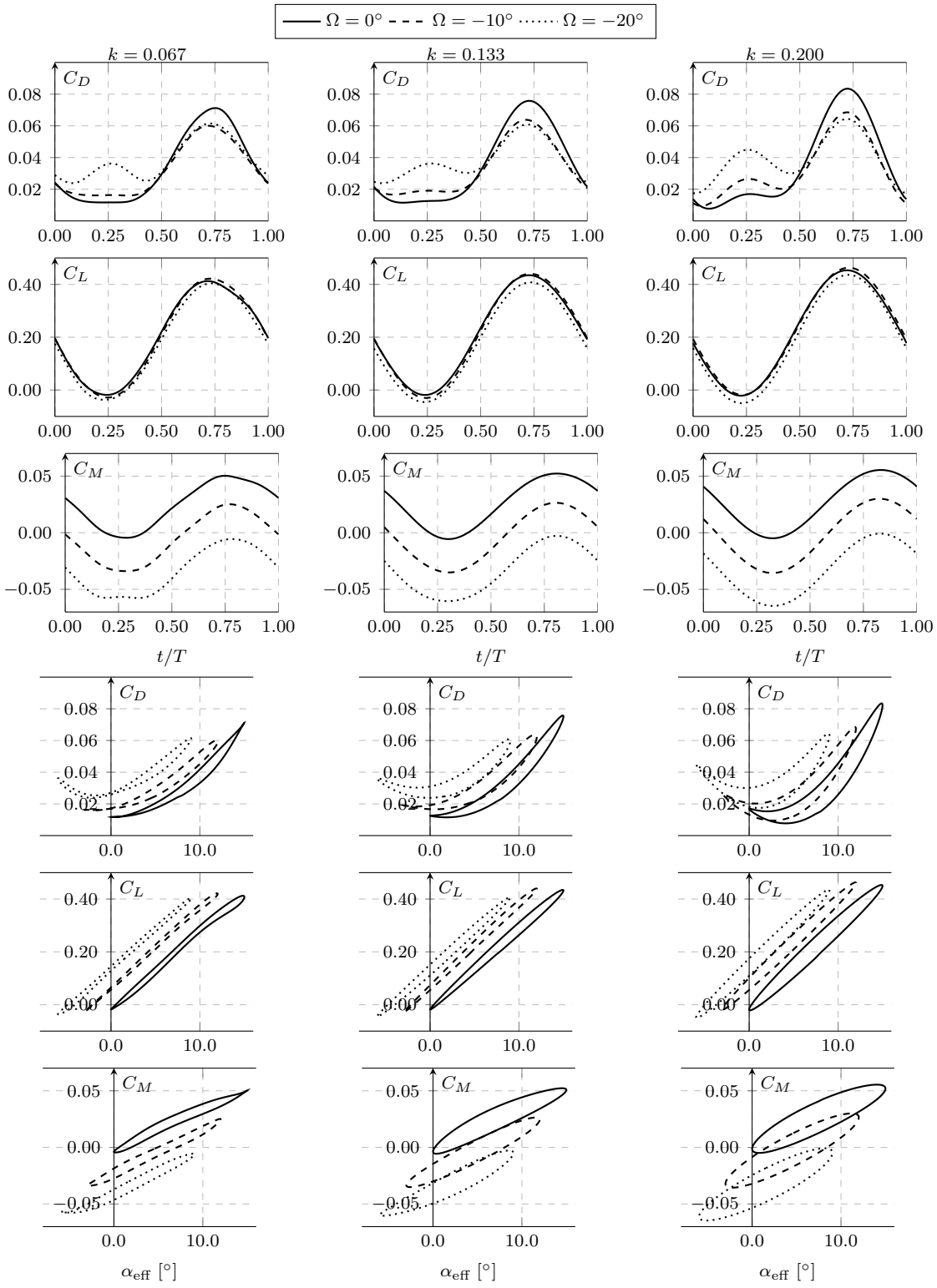

Figure 9.41: Aerodynamic coefficients with $A_\psi = 7.5°$ at different leading edge positions.

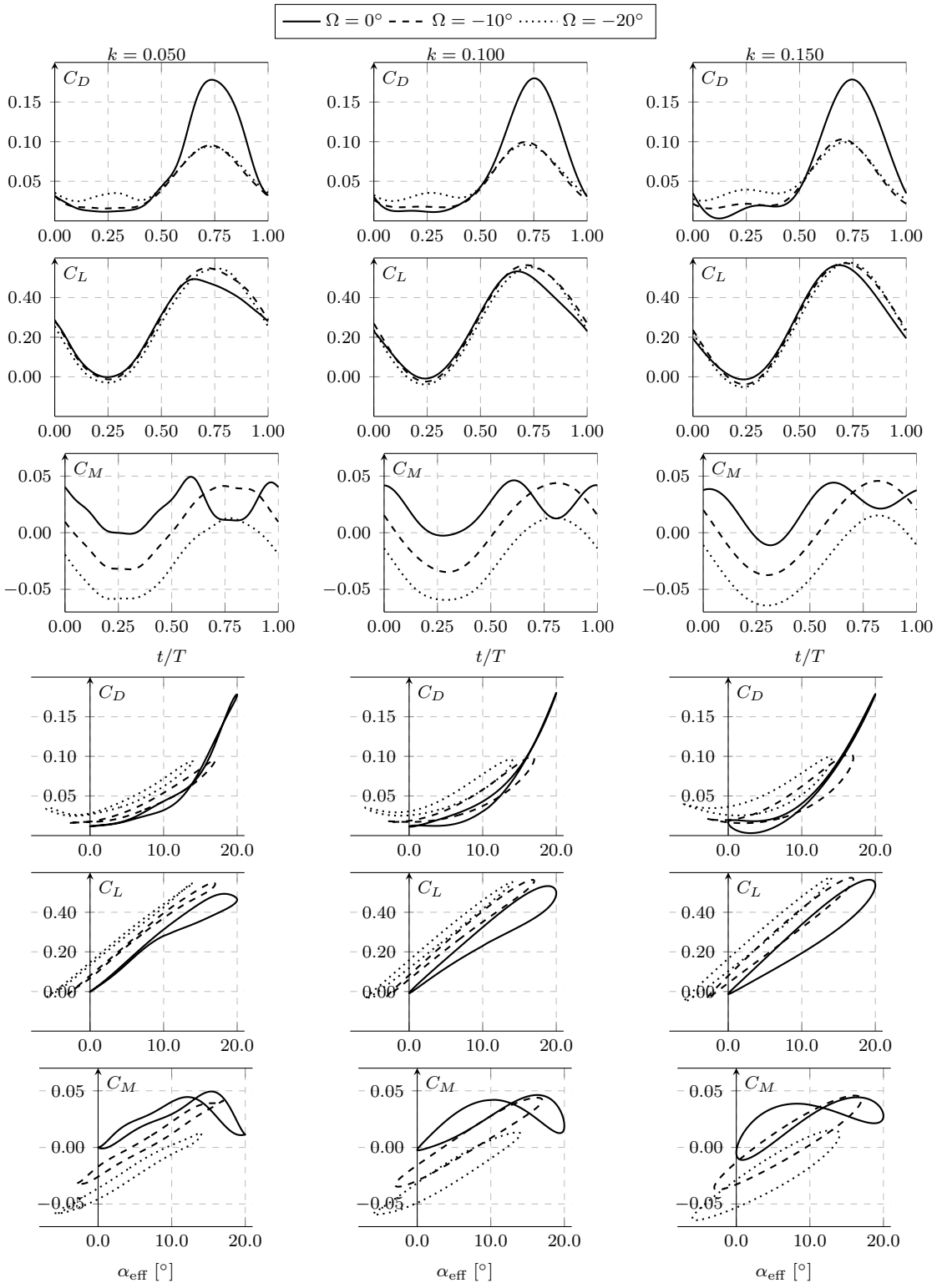

Figure 9.42: Aerodynamic coefficients with $A_\psi = 10°$ at different leading edge positions.

Chapter 10

Conclusions & Future Research

"Humans fly commercially or recreationally, but animals fly professionally."

McMasters & Henderson

In this last chapter, we will look at an overview of the work where we revisit some of the most important outcomes, identify a few of the project's shortcomings, and suggest improved investigation paths for future analysis of the proposed NACA0012-IK30 airfoil. More than promoting the accomplishments, this chapter has the necessary mission of being not a closing chapter but a starting point for the scientific community that wishes to explore innovative geometries in unsteady airfoils. This thesis has made significant contributions to the field through several publications in international conferences and peer-reviewed journals, demonstrating the research's impact and relevance in advancing knowledge within the discipline [68–70, 201–216].

The project had the primordial objective of proposing a straightforward yet innovative bio-inspired geometry, which could offer propulsive enhancements at the lower Reynolds region and bring some stall mitigation capabilities for the higher Reynolds spectrum. Just by examining the last two chapters, it is unambiguous that the study achieved its purpose, yet some particularities still need to be addressed. Let us start by revisiting the lower Reynolds region presented in Chapter 8, where the proposed airfoil acted as a propulsive device.

10.1 Propulsive Capabilities of the NACA0012-IK30 Airfoil

The study opens up with a series of flow visualization tests designed to explore the influence that a pitching leading edge has on the flow field surrounding a flapping airfoil. Tests considered a Reynolds number of 1.0×10^4 which allowed the flapping airfoil to experience really high effective angles of attack, well beyond the static stall angle.

Results showed that the leading edge has an enormous impact on the flow field phenomena, especially on the leading-edge vortex size. Furthermore, it was also seen that the deflection of the leading edge should be used but always keeping in mind the effective angle of attack created due to the plunging motion. This is central to mitigating unwanted flow separation that degrades thrust production, which was observed in some conditions where flow separation occurs due to excessive leading-edge deflection.

While flow visualization tests provided a great starting point to discuss the effectiveness of a movable leading edge, only the propulsive analysis of the airfoil could dictate the true enhancements that it could provide. Since force measurements were not available, a numerical setup was prepared to reproduce the experimental conditions. The results turned out to be quite impressive: by just deflecting the leading edge, the propulsive power could be raised $177.4\,\%$, and the propulsive efficiency easily doubled. Later on, such improvements were correlated with the flow features where it is concluded that without the presence of the leading-edge vortex, the NACA0012-IK30 does not have a clear path to improve the propulsive power. This implies that the proposed geometry is effectively a LEV exploiting system, from which it can extract additional thrust that would otherwise be lost to lift generation. This is why curvature, in this case time-varying curvature, is a key parameter to improve thrust production.

After proving that the proposed airfoil could indeed improve the propulsive capabilities of oscillating airfoils, one should ask the question of how this flapping mode compares to conventional flapping widely reported in the literature. That question was answered by implementing an optimization method coupled with the CFD software and the results were clear: while the proposed flapping consumed more power, it provided more thrust at a much lower angle of attack, again illustrating the importance of dynamic curvature. Furthermore, while standard flapping offered better efficiency, the NACA0012-IK30 mechanism presented a unique feature: the pitching amplitude that maximized the propulsive power also offered near-optimal propulsive efficiency which is not achievable with conventional flapping airfoils. This is a major improvement over conventional flapping since the proposed geometry can get around the problem of sacrificing efficiency for thrust production, as standard flapping does.

10.2 What is next for the NACA0012-IK30 airfoil as a propulsion device?

Based on the results, no major question can be raised about the efficacy of the proposed airfoil in the context of enhancing flapping propulsion. However, one should recognize that the analysis domain selected for the study is still small and that so much needs to be explored.

In fact, when looking at the NACA0012-IK30 airfoil, from the four degrees of freedom, x, y, β and ψ, only two, y and β were investigated. Instead of looking at this as a limitation, this should serve as a motivation to keep opening new doors that can improve the already high enhancements achieved.

Hence, from the several kinematics that can be applied, special attention should be made regarding the activation of ψ, where we could explore the simultaneous use of β and ψ. This would extend the dynamic curvature concept of the airfoil and create newer ways to manipulate the effective angle of attack, pushing the design closer to a bird's wing. All of this can be

accomplished by expanding the optimization algorithm to include additional variables, for instance, the ψ pitching amplitude and phase angle, ϕ. The results will unlock newer operational states which will exploit even further the presence of a leading-edge vortex by changing ψ.

However, achieving improvements without any visible path for real-world applications limits the motivation and true success of designing an innovative system. Hence, an important question emerges:

Can the NACA0012-IK30 design be used in a future propulsion system?

The improvements presented by this project suggest that the proposed design should at a minimum provide some inspiration for newer propulsive systems. However, to accurately address this question we need to divide the answer into the two most common applications: micro-aerial vehicle design and naval engineering.

When it comes to MAV flight, the proposed geometry is extremely far from the demanding requirements of micro-aerial vehicle design. The required miniaturization of the suggested airfoil is a much more complex problem that will involve, apart from aerodynamics, material science, and innovative control systems. Even if the system, as presented in the document, cannot be implemented right away, it can still provide useful insights and stimulate the study of dynamic curvature and active wing deformation.

Ironically, the NACA0012-IK30 airfoil is much closer to a real-world application in the realm of naval engineering where it could be a replacement for traditional propellers. In such an application, the suggested airfoil and its paraphernalia could be easily scaled up and incorporated, for example in a ship, without profound modifications.

Although the study was conducted in the air, we see major advantages when discussing its hypothetical operation in water, mainly due to the lack of rigid weight requirements needed for aeronautical applications. This means that there is a higher leverage regarding, for instance, the choosing of the chord length, c, which plays a particularly important role in the reduced frequency, and consequently in thrust generation.

Hence, as a final remark, it is recommended that the attention be directed to the investigation of the hydrodynamic performance of the geometry by exploring it, either parametrically or optimally. Modifications to the geometry must be encouraged, where the airfoil could be updated with newer morphing structures, which could be subjected to kinematics similar to the major locomotion methods used by fish.

10.3 Dynamic Stall Mitigation using a NACA0012-IK30 Wing

After exploring the propulsive capabilities of the NACA0012-IK30 airfoil, we transitioned to a higher Reynolds number regime where the movable leading edge was used as a stall mitigation system. Let us revisit Chapter 9 and recapitulate its main outcomes.

The proposed airfoil was built into a 2.5 aspect ratio wing that was tested under various conditions. The first phase of studies examined static cases where three configurations were considered. These were focused on understanding the use of the back part as a plain trailing-edge flap, how the leading edge performs while acting as a leading-edge flap, and finally, understanding how dropping the leading edge improves the aerodynamic performance.

Results show unequivocally that the proposed geometry is operationally flexible to provide drag, lift, and moment enhancements relative to the traditional NACA0012 airfoil. All improvements were validated by a brief stall visualization study in which we saw that deflecting the leading edge does mitigate aerodynamic stall in a significant way. CFD computations are also carried out to understand how the pressure distribution changes when dropping the leading edge.

After finishing the static conditions, a question emerged: how could we push the NACA0012-IK30 wing to the limit and what could we really extract from it? The question was answered by implementing an innovative real-time optimization that could find minimal drag and maximum lift. Impressive results were obtained, where drag was improved up to $47\,\%$ and lift, up to $45\,\%$. Furthermore, the optimal states found by the RTO methodology delayed the stall angle by more than $10°$.

The static conditions end with the optimization study, followed by the dynamic cases, which start with pitching ramps where the leading edge was fixed as a flap. The ramps showed the smooth transition between the two states and provided an initial view of how the wing enters the stall region and how the leading edge deflection can delay such a phenomenon. Moreover, it shows how to use Ω without sacrificing aerodynamic performance.

Ramps were followed by the plunging conditions where the wing has a fixed mean angle of attack while dynamically activating the leading edge according to the effective angle of attack induced by the plunging motion. Results show that when the wing does not experience dynamic stall in plunging, drag and lift are kept almost the same, while the pitching moment is improved by reducing the nose-up tendency of the wing. Contrarily, when the wing experiences extensive dynamic stall, the movable leading edge can provide more than a $50\,\%$ reduction in drag, a respectful increase in lift but with the side effect of intensifying the nose-up moment.

The study finishes with the pitching cases which are divided into two phases: the first phase fixes the airfoil at a mean angle of attack and moves the leading edge while the second phase

fixes Ω and then the whole airfoil is subjected to pitching. The first configuration resembles the plunging cases but without the plunging contribution, which leads to similar outcomes. The second pitching configuration shows the importance of having an adequate leading-edge deflection and helps us understand when we may be causing the wrong interaction between kinematics and aerodynamics. This was clear in the results where having a leading edge flap could mitigate the adverse effects of dynamic stall at higher pitching amplitudes but quickly degrade the aerodynamic performance at lower angles of attack.

10.4 What is next for the NACA0012-IK30 airfoil as a stall mitigation device?

One thing is clear: the NACA0012-IK30 airfoil is a remarkable system to delay, mitigate, or even suppress the aerodynamic stall and its adverse effects. However, we must recognize that the analysis of this system is still in its infancy phase and that so much remains to be explored and uncovered.

Looking retrospectively at the results, one thing that comes to mind is that the results are as good as the prescribed kinematics. This means that while the system showed its effectiveness in mitigating dynamic stall with rather decent improvements, without exploring the kinematics domain, we will not reach new highs in terms of performance.

One could propose an extensive parametric study where a deeper analysis of the motion parameters was made. Instead, let us go right to the nuclear option and extract everything we can get from the NACA0012-IK30 airfoil, by extending the real-time optimization to the dynamic cases.

In retrospect, and starting with the plunging conditions, one of the shortcomings was imposing the condition

$$\beta \leq \overline{\psi} \rightarrow \overline{\beta} = \overline{\psi} - A_{\beta}, \tag{10.1}$$

which deviated the attention from studying $\overline{\beta}$ individually. If we had studied plunging with a constant Ω, the results would have been even higher than the ones presented in this document.

Hence, to optimally use the leading edge while the airfoil experiences plunging, we may still apply the kinematics used, where

$$y = A\sin(2\pi f t) \tag{10.2}$$

with

$$\psi = \overline{\psi} \tag{10.3}$$

and

$$\beta = \overline{\beta} + A_\beta \sin(2\pi f t + \phi) \tag{10.4}$$

but treat $\overline{\beta}$ and A_β as dynamic variables that need to be optimized. The phase angle ϕ can also be used for the optimization, especially if there is considerable lag between kinematics and dominant aerodynamic effects. This was not observed in the conditions allowed by the experimental setup, as seen by the small influence that the reduced frequency had on the results.

Concerning the optimization framework, it could follow a real-time and periodic optimization where the recurrent expression

$$\overrightarrow{x}^{k+1} = \overrightarrow{x}^{k} \pm \gamma^k \nabla \mathcal{O}(\overrightarrow{x}^{k}) \tag{10.5}$$

could be called after each period, where $\overrightarrow{x}$ is the vector of variables used for optimization and $\mathcal{O}$ is the objective function which in the context of unsteady airfoils and dynamic stall could be the mean period drag and lift coefficients. For the specific case of the plunging conditions, the control variables could be written as

$$\overrightarrow{x} = \begin{bmatrix} \overline{\beta} & A_\beta \end{bmatrix}^T. \tag{10.6}$$

The same strategy can be extended for the pitching cases, where we can apply the waveform

$$\psi = \overline{\psi} + A_\psi \sin(2\pi f t) \tag{10.7}$$

to the back part while the leading edge is subjected to the waveform shown in equation (10.4) with the same state vector of equation (10.6) for optimal search. It is important to mention that the experimental rig presented in this study would need to be updated for such an optimization study since the simultaneous control of ψ and Ω was unusable. This would result in the better use of the leading edge, in which we could exploit the improvements of deflecting it at higher angles of attack without sacrificing performance at the lower angles.

With these optimal studies, we can truly unlock what the NACA0012-IK30 airfoil can provide regarding dynamic stall improvements. However, it is important to keep in mind that this is a first-generation design which has its challenges and limitations. Moving away from kinematics, questions about the geometry still remain unanswered:

What is the influence of the pivot point?

What about other airfoils and wing geometries?

Should we be worried about the airfoil surface discontinuity?

Could the second-generation design be a continuous morphing structure?

And can these systems be easily applicable in the context of rotor blade dynamics?

These and other questions must be asked incessantly so we keep pushing the goal post further and further, where we truly obtain operational flexible and robust systems that can meet the challenges of dynamic stall.

Bibliography

[1] The Biomimicry Institute, "Biomimicry is an approach to innovation that seeks sustainable solutions to human challenges by emulating nature's time-tested patterns and strategies." 2019, last accessed 21 December 2019 [**Link**]. [Online]. Available: https://biomimicry.org/what-is-biomimicry/ 1

[2] C. Darwin, *The Origin of Species*. Cambridge University Press, 2009, [**Crossref**]. 1

[3] Airbus, "An airbus futuristic conceptual airliner "takes flight" to inspire next-generation engineers," 2019, last accessed 7 November 2019 [**Link**]. [Online]. Available: https://www.airbus.com/newsroom/news/en/2019/07/airbus-conceptual-airliner-to-inspire-new-generation-engineers.html xvii, 2, 3

[4] Airbus, "Biomimicry: engineering in nature's style," 2018, last accessed 13 November 2019 [**Link**]. [Online]. Available: https://www.airbus.com/newsroom/news/en/2018/01/biomimicry--engineering-in-nature-s-style.html 3

[5] Airbus, "How the albatross is inspiring next generation of aircraft wings," 2019, last accessed 13 November 2019 [**Link**]. [Online]. Available: https://www.airbus.com/newsroom/press-releases/en/2019/06/how-the-albatross-is-inspiring-next-generation-of-aircraft-wings.html xvii, 3, 4

[6] Airbus, "The albatross is inspiring tomorrow's aircraft wings," 2019, last accessed 13 November 2019 [**Link**]. [Online]. Available: https://www.airbus.com/en/newsroom/stories/2019-07-the-albatross-is-inspiring-tomorrows-aircraft-wings 3

[7] Airbus, "Airbus inspired by nature to boost aircraft environmental performance," 2019, last accessed 16 December 2019 [**Link**]. [Online]. Available: https://www.airbus.com/newsroom/press-releases/en/2019/11/airbus-inspired-by-nature-to-boost-aircraft-environmental-performance.html xvii, 4

[8] Airbus, "Airlines are looking to reduce fuel consumption. wake-energy retrieval could help," 2019, last accessed 16 December 2019 [**Link**]. [Online]. Available: https://www.airbus.com/en/newsroom/stories/2019-11-airlines-are-looking-to-reduce-fuel-consumption-wake-energy-retrieval 4

[9] H. Liu, H. Aono, and H. Tanaka, "Bioinspired Air Vehicles Designed for Mars Exploration," *Acta Futura*, pp. 81–95, 2013, [**Crossref**]. 5

[10] MARIN, "Foil design," 2022, last accessed 7 February 2022 [**Link**]. [Online]. Available: https://www.marin.nl/en/jips/foil-design xvii, 5, 6

[11] M. M. Koochesfahani, "Vortical patterns in the wake of an oscillating airfoil," *AIAA Journal*, vol. 27, no. 9, pp. 1200–1205, sep 1989, [**Crossref**]. xvii, 9, 23

[12] I. H. Tuncer and M. F. Platzer, "Computational Study of Flapping Airfoil Aerodynamics," *Journal of Aircraft*, vol. 37, no. 3, pp. 514–520, may 2000, [**Crossref**]. 9, 16

[13] X. Wu, X. Zhang, X. Tian, X. Li, and W. Lu, "A review on fluid dynamics of flapping foils," *Ocean Engineering*, vol. 195, p. 106712, jan 2020, [**Crossref**]. 9, 27, 32, 34, 35, 83

[14] W. Birnbaum, "Das ebene Problem des schlagenden Flügels," *ZAMM - Zeitschrift für Angewandte Mathematik und Mechanik*, vol. 4, no. 4, pp. 277–292, 1924, [**Crossref**]. 9, 12

[15] W. Birnbaum, "Der schlagflügelpropeller und die kleinen schwingungen elastisch befestigter tragflügel," *Zeitschrift für Flugtechnik und Motorluftschiffahrt*, vol. 15, no. 11/12, pp. 128–134, 1924. 9

[16] R. Knoller, "Die gesetzedes luftwiderstandes," *Flug-und Motortechnik (Wien)*, vol. 3, no. 21, pp. 1–7, 1909. 9

[17] A. Betz, "Ein beitrag zur erklaerung segelfluges," *Z Flugtech Motorluftschiffahrt*, vol. 3, pp. 269–272, 1912. 9

[18] T. von Kármán and J. M. Burgers, *General aerodynamic theory: perfect fluids*. Springer, 1935. 9, 10, 15

[19] D. F. Kurtulus, L. David, A. Farcy, and N. Alemdaroglu, "Aerodynamic characteristics of flapping motion in hover," *Experiments in Fluids*, vol. 44, no. 1, pp. 23–36, aug 2007, [**Crossref**]. 10, 23

[20] T. Cebeci, M. Platzer, H. Chen, K.-C. Chang, and J. P. Shao, *Analysis of Low-Speed Unsteady Airfoil Flows*. Springer Berlin Heidelberg, 2005, [**Crossref**]. 12

[21] R. Katzmayr, "Effect of periodic changes of angle of attack on behavior of airfoils," *NACA Technical Report*, 1922, [**Crossref**]. 14

[22] T. Theodorsen, "General theory of aerodynamic instability and the mechanism of flutter," *NACA Technical Report*, 1935, [**Crossref**]. 15

[23] I. E. Garrick, "Propulsion of a flapping and oscillating airfoil," *Report National Advisory Committee for Aeronautics, NACA Report 567*, pp. 419–427, 1936, [**Crossref**]. 15

[24] M. F. Platzer, K. D. Jones, J. Young, and J. C. S. Lai, "Flapping Wing Aerodynamics: Progress and Challenges," *AIAA Journal*, vol. 46, no. 9, pp. 2136–2149, sep 2008, [**Crossref**]. 15, 28, 29, 33

[25] K. Jones and M. Platzer, "Numerical computation of flapping-wing propulsion and power extraction," in *35th Aerospace Sciences Meeting and Exhibit*. American Institute of Aeronautics and Astronautics, jan 1997, [**Crossref**]. xix, 15, 35, 112

[26] K. Jones and M. Platzer, "An experimental and numerical investigation of flapping-wing propulsion," in *37th Aerospace Sciences Meeting and Exhibit*. American Institute of Aeronautics and Astronautics, jan 1999, [**Crossref**]. 15

[27] P. Freymuth, "Propulsive vortical signature of plunging and pitching airfoils," *AIAA Journal*, vol. 26, no. 7, pp. 881–883, jul 1988, [**Crossref**]. 15

[28] I. H. Tuncer and M. F. Platzer, "Thrust generation due to airfoil flapping," *AIAA Journal*, vol. 34, no. 2, pp. 324–331, feb 1996, [**Crossref**]. 15

[29] K. D. Jones, C. M. Dohring, and M. F. Platzer, "Experimental and Computational Investigation of the Knoller-Betz Effect," *AIAA Journal*, vol. 36, no. 7, pp. 1240–1246, jul 1998, [**Crossref**]. xvii, 15, 16

[30] N.-H. Teng, "The Development of a Computer Code (U2DIIF) for the Numerical Solution of Unsteady, Inviscid and Incompressible Flow Over an Airfoil," Naval Postgraduate School Monterey CA, Tech. Rep., 1987, [**Crossref**]. xix, 15, 31, 101, 106

[31] J. M. Anderson, K. Streitlien, D. S. Barrett, and M. S. Triantafyllou, "Oscillating foils of high propulsive efficiency," *Journal of Fluid Mechanics*, vol. 360, pp. 41–72, apr 1998, [**Crossref**]. 15, 16, 17

[32] J. C. S. Lai and M. F. Platzer, "Jet Characteristics of a Plunging Airfoil," *AIAA Journal*, vol. 37, no. 12, pp. 1529–1537, dec 1999, [**Crossref**]. 16

[33] G. K. Taylor, R. L. Nudds, and A. L. R. Thomas, "Flying and swimming animals cruise at a Strouhal number tuned for high power efficiency," *Nature*, vol. 425, no. 6959, pp. 707–711, oct 2003, [**Crossref**]. xvii, 16, 17

[34] K. D. von Ellenrieder, K. Parker, and J. Soria, "Flow structures behind a heaving and pitching finite-span wing," *Journal of Fluid Mechanics*, vol. 490, pp. 129–138, sep 2003, [**Crossref**]. 17, 34

[35] J. Young and J. C. S. Lai, "Oscillation Frequency and Amplitude Effects on the Wake of a Plunging Airfoil," *AIAA Journal*, vol. 42, no. 10, pp. 2042–2052, oct 2004, [**Cross-**

ref]. xvii, 17, 18

[36] S. Yang, S. Luo, F. Liu, and H.-M. Tsai, "Optimization of Unstalled Pitching and Plunging Motion of an Airfoil," in *44th AIAA Aerospace Sciences Meeting and Exhibit*. American Institute of Aeronautics and Astronautics, jan 2006, [**Crossref**]. 17

[37] S. Heathcote, Z. Wang, and I. Gursul, "Effect of spanwise flexibility on flapping wing propulsion," *Journal of Fluids and Structures*, vol. 24, no. 2, pp. 183–199, feb 2008, [**Crossref**]. xvii, xx, 17, 30, 31, 135

[38] K. B. Lua, T. T. Lim, and K. S. Yeo, "Aerodynamic forces and flow fields of a two-dimensional hovering wing," *Experiments in Fluids*, vol. 45, no. 6, pp. 1047–1065, jul 2008, [**Crossref**]. 17, 24

[39] M. Yu, Z. J. Wang, and H. Hu, "High fidelity numerical simulation of airfoil thickness and kinematics effects on flapping airfoil propulsion," *Journal of Fluids and Structures*, vol. 42, pp. 166–186, oct 2013, [**Crossref**]. 17, 25, 28

[40] M. R. Visbal, "High-Fidelity Simulation of Transitional Flows past a Plunging Airfoil," *AIAA Journal*, vol. 47, no. 11, pp. 2685–2697, nov 2009, [**Crossref**]. 17

[41] C. Liang, K. Ou, S. Premasuthan, A. Jameson, and Z. J. Wang, "High-order accurate simulations of unsteady flow past plunging and pitching airfoils," *Computers & Fluids*, vol. 40, no. 1, pp. 236–248, jan 2011, [**Crossref**]. 17, 27

[42] A. Ashraf, J. Young, J. Lai, and M. Platzer, "Aerodynamic Analysis of Flapping-Wing Propellers for HALE Aircraft," in *47th AIAA Aerospace Sciences Meeting including The New Horizons Forum and Aerospace Exposition*. American Institute of Aeronautics and Astronautics, jan 2009, [**Crossref**]. 18

[43] M. Ashraf, J. Lai, and J. Young, "Numerical analysis of flapping wing aerodynamics," *16th Australasian Fluid Mechanics Conference*, 2007. 18

[44] K. Lu, Y. H. Xie, D. Zhang, and J. B. Lan, "Numerical investigations into the asymmetric effects on the aerodynamic response of a pitching airfoil," *Journal of Fluids and Structures*, vol. 39, pp. 76–86, may 2013, [**Crossref**]. 18, 83

[45] K. Lu, Y. H. Xie, and D. Zhang, "Numerical study of large amplitude, nonsinusoidal motion and camber effects on pitching airfoil propulsion," *Journal of Fluids and Structures*, vol. 36, pp. 184–194, jan 2013, [**Crossref**]. xvii, 19, 20, 83

[46] A. Das, R. K. Shukla, and R. N. Govardhan, "Existence of a sharp transition in the peak propulsive efficiency of a low-re pitching foil," *Journal of Fluid Mechanics*, vol. 800,

pp. 307–326, jul 2016, [Crossref]. xvii, 19, 21

[47] P. Luo, X. Zhang, P. Huang, and L. Xie, "A study on the aerodynamic characteristics of airfoil in the flapping adjustment stage during forward flight," *Journal of Physics: Conference Series*, vol. 916, p. 012009, oct 2017, [Crossref]. 20

[48] J. Hu, H. Xuan, Y. Yu, and J. Zhang, "Effects of continuously increasing pitching and plunging amplitudes on the aerodynamic forces of flapping airfoils," *AIP Advances*, vol. 9, no. 8, p. 085008, aug 2019, [Crossref]. 21

[49] X. Lin, J. Wu, and T. Zhang, "Performance investigation of a self-propelled foil with combined oscillating motion in stationary fluid," *Ocean Engineering*, vol. 175, pp. 33–49, mar 2019, [Crossref]. 21

[50] U. Senturk and A. J. Smits, "Reynolds Number Scaling of the Propulsive Performance of a Pitching Airfoil," *AIAA Journal*, vol. 57, no. 7, pp. 2663–2669, jul 2019, [Crossref]. xvii, 21, 22

[51] T. Wang, L.-H. Feng, and Z.-Y. Li, "Effect of leading-edge protuberances on unsteady airfoil performance at low Reynolds number," *Experiments in Fluids*, vol. 62, no. 10, oct 2021, [Crossref]. 21, 38

[52] W. Tian, A. Bodling, H. Liu, J. C. Wu, G. He, and H. Hu, "An experimental study of the effects of pitch-pivot-point location on the propulsion performance of a pitching airfoil," *Journal of Fluids and Structures*, vol. 60, pp. 130–142, jan 2016, [Crossref]. 22

[53] A. W. Mackowski and C. H. K. Williamson, "Effect of pivot location and passive heave on propulsion from a pitching airfoil," *Physical Review Fluids*, vol. 2, no. 1, p. 013101, jan 2017, [Crossref]. 22

[54] T. V. Buren, D. Floryan, D. Quinn, and A. J. Smits, "Nonsinusoidal gaits for unsteady propulsion," *Physical Review Fluids*, vol. 2, no. 5, p. 053101, may 2017, [Crossref]. 22

[55] S. M. Dash, K. B. Lua, T. T. Lim, and K. S. Yeo, "Enhanced thrust performance of a two dimensional elliptic airfoil at high flapping frequency in a forward flight," *Journal of Fluids and Structures*, vol. 76, pp. 37–59, jan 2018, [Crossref]. 22

[56] M. Boudreau, K. Gunther, and G. Dumas, "Investigation of the energy-extraction regime of a novel semi-passive flapping-foil turbine concept with a prescribed heave motion and a passive pitch motion," *Journal of Fluids and Structures*, vol. 84, pp. 368–390, jan 2019, [Crossref]. 22

[57] M. Boudreau, K. Gunther, and G. Dumas, "Free-pitching flapping-foil turbines with imposed sinusoidal heave," *Journal of Fluids and Structures*, vol. 90, pp. 110–138, oct 2019, [**Crossref**]. 22

[58] V. Tsarsitalidis and G. Politis, "Simulating biomimetic propulsors under spring loading and/or active control for the pitching motion of the wings," in *Proceedings of Fourth International Symposium on Marine Propulsors, SMP'15, Austin, Texas, USA*, 2015, [**Crossref**]. 22

[59] E. Bøckmann and S. Steen, "Experiments with actively pitch-controlled and spring-loaded oscillating foils," *Applied Ocean Research*, vol. 48, pp. 227–235, oct 2014, [**Crossref**]. 22

[60] K. Ohmi, M. Coutanceau, T. P. Loc, and A. Dulieu, "Vortex formation around an oscillating and translating airfoil at large incidences," *Journal of Fluid Mechanics*, vol. 211, pp. 37–60, feb 1990, [**Crossref**]. 23, 27

[61] G. C. Lewin and H. Haj-Hariri, "Modelling thrust generation of a two-dimensional heaving airfoil in a viscous flow," *Journal of Fluid Mechanics*, vol. 492, pp. 339–362, oct 2003, [**Crossref**]. 23

[62] S. Yang, C. Liu, and J. Wu, "Effect of motion trajectory on the aerodynamic performance of a flapping airfoil," *Journal of Fluids and Structures*, vol. 75, pp. 213–232, nov 2017, [**Crossref**]. 23

[63] J. Young and J. C. S. Lai, "Mechanisms Influencing the Efficiency of Oscillating Airfoil Propulsion," *AIAA Journal*, vol. 45, no. 7, pp. 1695–1702, jul 2007, [**Crossref**]. xx, 23, 134, 135

[64] J. Young and J. C. S. Lai, "Vortex Lock-In Phenomenon in the Wake of a Plunging Airfoil," *AIAA Journal*, vol. 45, no. 2, pp. 485–490, feb 2007, [**Crossref**]. 24

[65] K. B. Lua, T. T. Lim, K. S. Yeo, and G. Y. Oo, "Wake-Structure Formation of a Heaving Two-Dimensional Elliptic Airfoil," *AIAA Journal*, vol. 45, no. 7, pp. 1571–1583, jul 2007, [**Crossref**]. 24

[66] M. Ol, H. Dong, and C. Webb, "Motion Kinematics vs. Angle of Attack Effects in High-Frequency Airfoil Pitch/Plunge," in *38th Fluid Dynamics Conference and Exhibit*. American Institute of Aeronautics and Astronautics, jun 2008, [**Crossref**]. xvii, 24

[67] R. Lopes, E. Camacho, F. Neves, A. R. R. Silva, and J. M. M. Barata, "Numerical and experimental study of a plunging airfoil," in *Proceeding of 4th Thermal and Fluids Engineering Conference*. Begellhouse, 2019, pp. 1869–1872, [**Crossref**]. 24

[68] E. Camacho, F. Neves, A. Silva, and J. Barata, "Numerical investigation of frequency and amplitude influence on a plunging naca0012," *Energies*, vol. 13, no. 8, p. 1861, Apr. 2020, [**Crossref**]. 24, 209

[69] D. Rodrigues, E. A. Camacho, F. Neves, J. Barata, and A. R. Silva, "Plunging airfoil motion: Effects of unequal ascending and descending velocities," in *AIAA AVIATION 2020 FORUM*. American Institute of Aeronautics and Astronautics, Jun. 2020, [**Crossref**]. 24

[70] S. B. Gonçalves, E. A. Camacho, and A. R. Silva, "Influence of trailing-edge shape on the propulsive performance of a plunging flat plate," in *AIAA AVIATION 2022 Forum*. American Institute of Aeronautics and Astronautics, Jun. 2022, [**Crossref**]. 24, 209

[71] H. Li, Q. Qu, and R. K. Agarwal, "Aerodynamics of a Flapping Airfoil in Forward Flight in Proximity of Ground," in *35th AIAA Applied Aerodynamics Conference*. American Institute of Aeronautics and Astronautics, jun 2017, [**Crossref**]. 25

[72] A. Andersen, T. Bohr, T. Schnipper, and J. H. Walther, "Wake structure and thrust generation of a flapping foil in two-dimensional flow," *Journal of Fluid Mechanics*, vol. 812, dec 2016, [**Crossref**]. 25

[73] M. Yu, B. Wang, Z. J. Wang, and S. Farokhi, "Evolution of vortex structures over flapping foils in shear flows and its impact on aerodynamic performance," *Journal of Fluids and Structures*, vol. 76, pp. 116–134, jan 2018, [**Crossref**]. xvii, 25, 26

[74] M. Moriche, M. Raiola, S. Discetti, A. Ianiro, O. Flores, and M. García-Villalba, "Assessing aerodynamic force estimation with experiments and simulations of flapping-airfoil flows on the verge of three-dimensionality," *Proceedings of the Institution of Mechanical Engineers, Part G: Journal of Aerospace Engineering*, vol. 234, no. 2, pp. 428–444, aug 2019, [**Crossref**]. 25

[75] A.-K. Gao, S.-F. Zou, Y. Shi, and J. Z. Wu, "Passing-over leading-edge vortex: The thrust booster in heaving airfoil," *AIP Advances*, vol. 9, no. 3, p. 035314, mar 2019, [**Crossref**]. 26, 133

[76] A. Rahman and D. Tafti, "The role of vortex–vortex interactions in thrust production for a plunging flat plate," *Journal of Fluids and Structures*, vol. 96, p. 103011, jul 2020, [**Crossref**]. 26

[77] I. Gursul and D. Cleaver, "Plunging Oscillations of Airfoils and Wings: Progress, Opportunities, and Challenges," *AIAA Journal*, vol. 57, no. 9, pp. 3648–3665, sep 2019, [**Crossref**]. 26, 164

[78] C. Kang, Y. Baik, L. Bernal, M. Ol, and W. Shyy, "Fluid Dynamics of Pitching and Plunging Airfoils of Reynolds Number between 1×10^4 and 6×10^4," in *47th AIAA Aerospace Sciences Meeting including The New Horizons Forum and Aerospace Exposition*. American Institute of Aeronautics and Astronautics, jan 2009, [**Crossref**]. 27

[79] D. G. Bohl and M. M. Koochesfahani, "MTV measurements of the vortical field in the wake of an airfoil oscillating at high reduced frequency," *Journal of Fluid Mechanics*, vol. 620, pp. 63–88, feb 2009, [**Crossref**]. 27

[80] W. Medjroubi, B. Stoevesandt, and J. Peinke, "Wake classification of heaving airfoils using the spectral/hp element method," *Journal of Computational and Applied Mathematics*, vol. 236, no. 15, pp. 3774–3782, sep 2012, [**Crossref**].

[81] J. M. Moubogha, U. Ehrenstein, and J. A. Astolfi, "Forces on a pitching plate: An experimental and numerical study," *Applied Ocean Research*, vol. 69, pp. 27–37, dec 2017, [**Crossref**]. 27

[82] A. E. Panah and J. H. J. Buchholz, "Parameter dependence of vortex interactions on a two-dimensional plunging plate," *Experiments in Fluids*, vol. 55, no. 3, feb 2014, [**Crossref**]. 27

[83] A. E. Panah and J. Buchholz, "Vortex Shedding and Wake Structure of a Plunging Wing," in *50th AIAA Aerospace Sciences Meeting including the New Horizons Forum and Aerospace Exposition*. American Institute of Aeronautics and Astronautics, jan 2012, [**Crossref**]. 27

[84] J.-S. Lee, C. Kim, and K. H. Kim, "Design of Flapping Airfoil for Optimal Aerodynamic Performance in Low-Reynolds Number Flows," *AIAA Journal*, vol. 44, no. 9, pp. 1960–1972, sep 2006, [**Crossref**]. xvii, 28

[85] S. I. Benton and M. R. Visbal, "Effects of Leading-Edge Geometry on the Onset of Dynamic Stall," *AIAA Journal*, vol. 56, no. 10, pp. 4195–4198, oct 2018, [**Crossref**]. 28

[86] A. J. Smits, "Undulatory and oscillatory swimming," *Journal of Fluid Mechanics*, vol. 874, jul 2019, [**Crossref**]. 28, 32, 34

[87] W. B. Tay and K. B. Lim, "Analysis of non-symmetrical flapping airfoils," *Acta Mechanica Sinica*, vol. 25, no. 4, pp. 433–450, may 2009, [**Crossref**]. xvii, 28, 29

[88] L. E. Muscutt, G. D. Weymouth, and B. Ganapathisubramani, "Performance augmentation mechanism of in-line tandem flapping foils," *Journal of Fluid Mechanics*, vol. 827, pp. 484–505, aug 2017, [**Crossref**]. xvii, 29

[89] J.-M. Miao and M.-H. Ho, "Effect of flexure on aerodynamic propulsive efficiency of flapping flexible airfoil," *Journal of Fluids and Structures*, vol. 22, no. 3, pp. 401–419, apr 2006, [**Crossref**]. 30

[90] S. Heathcote and I. Gursul, "Flexible Flapping Airfoil Propulsion at Low Reynolds Numbers," *AIAA Journal*, vol. 45, no. 5, pp. 1066–1079, may 2007, [**Crossref**]. xvii, 30

[91] Z. Zhang, J. Qian, S. Luo, and F. Liu, "Numerical Study of the Aerodynamic Characteristics of a Plunging Rigid Airfoil with Elastic Trailing-Edge Plate," in *20th AIAA Computational Fluid Dynamics Conference*. American Institute of Aeronautics and Astronautics, jun 2011, [**Crossref**]. xvii, 30, 31

[92] J. M. Akkala, A. E. Panah, and J. H. J. Buchholz, "Vortex dynamics and performance of flexible and rigid plunging airfoils," *Journal of Fluids and Structures*, vol. 54, pp. 103–121, apr 2015, [**Crossref**]. 32

[93] C. Zhou, Y. Zhang, and J. Wu, "Effect of flexibility on unsteady aerodynamics forces of a purely plunging airfoil," *Chinese Journal of Aeronautics*, vol. 33, no. 1, pp. 88–101, jan 2020, [**Crossref**]. 32

[94] P. A. Dewey, B. M. Boschitsch, K. W. Moored, H. A. Stone, and A. J. Smits, "Scaling laws for the thrust production of flexible pitching panels," *Journal of Fluid Mechanics*, vol. 732, pp. 29–46, aug 2013, [**Crossref**]. 32

[95] K. Jones, B. Castro, O. Mahmoud, S. Pollard, M. Platzer, M. Neef, K. Gonet, and D. Hummel, "A collaborative numerical and experimental investigation of flapping-wing propulsion," in *40th AIAA Aerospace Sciences Meeting & Exhibit*. American Institute of Aeronautics and Astronautics, jan 2002, [**Crossref**]. xvii, 32, 33

[96] W. Shyy and H. Liu, "Flapping Wings and Aerodynamic Lift: The Role of Leading-Edge Vortices," *AIAA Journal*, vol. 45, no. 12, pp. 2817–2819, dec 2007, [**Crossref**]. 33

[97] M. Visbal, T. O. Yilmaz, and D. Rockwell, "Three-dimensional vortex formation on a heaving low-aspect-ratio wing: Computations and experiments," *Journal of Fluids and Structures*, vol. 38, pp. 58–76, apr 2013, [**Crossref**]. 33

[98] T. Kozłowski and H. Kudela, "Flow patters generated by a flapping airfoil," *3rd Polish Congress of Mechanics & 21st Computer Methods in Mechanics, Gdańsk, Poland*, 2015, [**Crossref**]. 33

[99] K. Parker, K. D. von Ellenrieder, and J. Soria, "Morphology of the forced oscillatory flow past a finite-span wing at low Reynolds number," *Journal of Fluid Mechanics*,

vol. 571, pp. 327–357, jan 2007, [Crossref]. 34

[100] J. A. Esfahani, E. Barati, and H. R. Karbasian, "Comparative investigations in the effect of angle of attack profile on hydrodynamic performance of bio-inspired foil, (corrected)," *Journal of Naval Architecture and Marine Engineering*, vol. 10, no. 2, pp. 99–108, dec 2013, [Crossref]. 34

[101] W. Geissler, "Flapping wing energy harvesting: aerodynamic aspects," *CEAS Aeronautical Journal*, vol. 11, no. 2, pp. 379–389, apr 2019, [Crossref]. 34, 35

[102] B. Wang, B. Zhu, and W. Zhang, "New type of motion trajectory for increasing the power extraction efficiency of flapping wing devices," *Energy*, vol. 189, p. 116072, dec 2019, [Crossref]. 34, 35

[103] Q. Xiao and Q. Zhu, "A review on flow energy harvesters based on flapping foils," *Journal of Fluids and Structures*, vol. 46, pp. 174–191, apr 2014, [Crossref]. 34

[104] Y. L. Wang, W. Jiang, and Y. H. Xie, "Numerical Investigation Into the Effects of Motion Parameters on Energy Extraction of the Parallel Foils," *Journal of Fluids Engineering*, vol. 141, no. 6, dec 2018, [Crossref]. 34

[105] B. Zhu, W. Zhang, and Y. Huang, "Energy extraction properties of a flapping wing with a deformable airfoil," *IET Renewable Power Generation*, vol. 13, no. 11, pp. 1823–1832, may 2019, [Crossref]. 34

[106] G. Jeanmonod and M. Olivier, "Effects of chordwise flexibility on 2d flapping foils used as an energy extraction device," *Journal of Fluids and Structures*, vol. 70, pp. 327–345, apr 2017, [Crossref]. 34

[107] B. J. Simpson, S. Licht, F. S. Hover, and M. S. Triantafyllou, "Energy Extraction Through Flapping Foils," in *27th International Conference on Offshore Mechanics and Arctic Engineering*. ASMEDC, jan 2008, [Crossref]. 34

[108] D. Kim, B. Strom, S. Mandre, and K. Breuer, "Energy harvesting performance and flow structure of an oscillating hydrofoil with finite span," *Journal of Fluids and Structures*, vol. 70, pp. 314–326, apr 2017, [Crossref]. 34

[109] Q. Zhu, "Optimal frequency for flow energy harvesting of a flapping foil," *Journal of Fluid Mechanics*, vol. 675, pp. 495–517, mar 2011, [Crossref]. 34

[110] M. T. Bouzaher, N. Drias, and B. Guerira, "Improvement of Energy Extraction Efficiency for Flapping Airfoils by Using Oscillating Gurney Flaps," *Arabian Journal for Science and Engineering*, vol. 44, no. 2, pp. 809–819, may 2018, [Crossref]. 34

[111] P. Soni, A. Bharadwaj, and S. Ghosh, "Optimization of the Thrust to Lift Ratio using Camber Morphing in Flapping Airfoil," in *AIAA Scitech 2020 Forum*. American Institute of Aeronautics and Astronautics, jan 2020, [Crossref]. 35

[112] A. Boudis, A. C. Bayeul-Lainé, A. Benzaoui, H. Oualli, O. Guerri, and O. Coutier-Delgosha, "Numerical Investigation of the Effects of Nonsinusoidal Motion Trajectory on the Propulsion Mechanisms of a Flapping Airfoil," *Journal of Fluids Engineering*, vol. 141, no. 4, jan 2019, [Crossref]. 35

[113] S. M. Dash, K. B. Lua, and T. T. Lim, "Thrust Enhancement On A Two Dimensional Elliptic Airfoil In A Forward Flight," *International Journal of Mechanical, Industrial and Aerospace Sciences*, 2016, [Crossref]. 35

[114] H. F. Müller-Vahl, G. Pechlivanoglou, C. N. Nayeri, C. O. Paschereit, and D. Greenblatt, "Matched pitch rate extensions to dynamic stall on rotor blades," *Renewable Energy*, vol. 105, pp. 505–519, may 2017, [Crossref]. 35

[115] R. Dunne and B. J. McKeon, "Dynamic stall on a pitching and surging airfoil," *Experiments in Fluids*, vol. 56, no. 8, jul 2015, [Crossref]. 35

[116] N. D. Ham, "Aerodynamic loading on a two-dimensional airfoil during dynamic stall." *AIAA Journal*, vol. 6, no. 10, pp. 1927–1934, Oct. 1968, [Crossref]. 35

[117] W. McCroskey, L. Carr, and K. McAlister, "Dynamic stall experiments on oscillating airfoils," *AIAA Journal*, vol. 14, no. 1, pp. 57–63, Jan. 1976, [Crossref]. 35

[118] T. C. Corke and F. O. Thomas, "Dynamic stall in pitching airfoils: Aerodynamic damping and compressibility effects," *Annual Review of Fluid Mechanics*, vol. 47, no. 1, pp. 479–505, Jan. 2015, [Crossref]. 35

[119] M. S. Francis and J. E. Keesee, "Airfoil dynamic stall performance with large-amplitude motions," *AIAA Journal*, vol. 23, no. 11, pp. 1653–1659, nov 1985, [Crossref]. xvii, 35, 36

[120] D. Favier, A. Agnes, C. Barbi, and C. Maresca, "Combined translation/pitch motion - a new airfoil dynamic stall simulation," *Journal of Aircraft*, vol. 25, no. 9, pp. 805–814, sep 1988, [Crossref]. 36

[121] P. F. Lorber and F. O. Carta, "Airfoil dynamic stall at constant pitch rate and high reynolds number," *Journal of Aircraft*, vol. 25, no. 6, pp. 548–556, jun 1988, [Crossref]. 36

[122] M. R. Visbal, "Dynamic stall of a constant-rate pitching airfoil," *Journal of Aircraft*,

vol. 27, no. 5, pp. 400–407, may 1990, [Crossref]. 36

[123] P. Wernert, W. Geissler, M. Raffel, and J. Kompenhans, "Experimental and numerical investigations of dynamic stall on a pitching airfoil," *AIAA Journal*, vol. 34, no. 5, pp. 982–989, may 1996, [Crossref]. 36

[124] K. Mulleners and M. Raffel, "The onset of dynamic stall revisited," *Experiments in Fluids*, vol. 52, no. 3, pp. 779–793, may 2011, [Crossref]. 36

[125] W. Geissler and H. Haselmeyer, "Investigation of dynamic stall onset," *Aerospace Science and Technology*, vol. 10, no. 7, pp. 590–600, oct 2006, [Crossref]. 36

[126] J. Kiefer, C. E. Brunner, M. O. L. Hansen, and M. Hultmark, "Dynamic stall at high reynolds numbers induced by ramp-type pitching motions," *Journal of Fluid Mechanics*, vol. 938, mar 2022, [Crossref]. 36

[127] K. Isogai, Y. Shinmoto, and Y. Watanabe, "Effects of Dynamic Stall on Propulsive Efficiency and Thrust of Flapping Airfoil," *AIAA Journal*, vol. 37, no. 10, pp. 1145–1151, oct 1999, [Crossref]. 37

[128] N. Savage, "Aerodynamics: Vortices and robobees," *Nature*, vol. 521, no. 7552, pp. S64–S65, May 2015, [Crossref]. 37

[129] I. H. Tuncer and M. Kaya, "Optimization of Flapping Airfoils For Maximum Thrust and Propulsive Efficiency," *AIAA Journal*, vol. 43, no. 11, pp. 2329–2336, nov 2005, [Crossref]. 37

[130] J. Wang and J. Wu, "Aerodynamic performance improvement of a pitching airfoil via a synthetic jet," *European Journal of Mechanics - B/Fluids*, vol. 83, pp. 73–85, sep 2020, [Crossref]. 37

[131] M. R. Visbal and D. J. Garmann, "Mitigation of dynamic stall over a pitching finite wing using high-frequency actuation," *AIAA Journal*, vol. 58, no. 1, pp. 6–15, Jan. 2020, [Crossref]. 37

[132] D. J. Garmann and M. R. Visbal, "Control of dynamic stall on swept finite wings," *AIAA Journal*, vol. 60, no. 9, pp. 5262–5272, Sep. 2022, [Crossref]. 37

[133] H. Bao, W. Yang, D. Ma, W. Song, and B. Song, "Numerical simulation of flapping airfoil with alula," *International Journal of Micro Air Vehicles*, vol. 12, p. 175682932097798, jan 2020, [Crossref]. xvii, 37, 38

[134] T. Ullah, A. Javed, A. Abdullah, M. Ali, and E. Uddin, "Computational evaluation of an

optimum leading-edge slat deflection angle for dynamic stall control in a novel urban-scale vertical axis wind turbine for low wind speed operation," *Sustainable Energy Technologies and Assessments*, vol. 40, p. 100748, aug 2020, [**Crossref**]. 38

[135] D. O. D. Izquierdo and F. D. Marques, "Experimental analysis of passive bio-inspired covert feathers for stall and post-stall performance enhancement," *Meccanica*, vol. 56, no. 11, pp. 2671–2689, jul 2021, [**Crossref**]. 38, 41

[136] A. Z. Al-Garni, A. M. Al-Garni, S. A. Ahmed, and A. Z. Sahin, "Flow control for an airfoil with leading-edge rotation: An experimental study," *Journal of Aircraft*, vol. 37, no. 4, pp. 617–622, jul 2000, [**Crossref**]. xvii, 38

[137] V. M. Kumar and C.-C. Wang, "Active Flow Control of Flapping Airfoil Using Openfoam," *Journal of Mechanics*, vol. 36, no. 3, pp. 361–372, dec 2019, [**Crossref**]. 38

[138] W. W. Huebsch, P. D. Gall, S. D. Hamburg, and A. P. Rothmayer, "Dynamic Roughness as a Means of Leading-Edge Separation Flow Control," *Journal of Aircraft*, vol. 49, no. 1, pp. 108–115, jan 2012, [**Crossref**]. 38

[139] X.-D. Bai, J.-S. Zhang, J.-H. Zheng, and Y. Wang, "Energy extraction performance of a flapping wing with active elastic airbag deformation at the leading edge," *Ocean Engineering*, vol. 228, p. 108901, may 2021, [**Crossref**]. 38

[140] J. Niu, J. Lei, and T. Lu, "Numerical research on the effect of variable droop leading-edge on oscillating NACA 0012 airfoil dynamic stall," *Aerospace Science and Technology*, vol. 72, pp. 476–485, jan 2018, [**Crossref**]. 39

[141] S. Jia, Z. Zhang, H. Zhang, C. Song, and C. Yang, "Wind tunnel tests of 3d-printed variable camber morphing wing," *Aerospace*, vol. 9, no. 11, p. 699, Nov. 2022, [**Crossref**]. 39

[142] D. Liu, W. Yang, and B. Song, "Numerical simulation on aerodynamic performance of bird-like flapping wing with slotted-tip," in *32nd Congress of the International Council of the Aeronautical Sciences, ICAS 2021*, 2021, Conference paper, [**Crossref**]. 39

[143] B. K. Sreejith and A. Sathyabhama, "Experimental and numerical study of laminar separation bubble formation on low Reynolds number airfoil with leading-edge tubercles," *Journal of the Brazilian Society of Mechanical Sciences and Engineering*, vol. 42, no. 4, mar 2020, [**Crossref**]. 39

[144] A. Asghar, R. E. Perez, P. W. Jansen, and W. D. E. Allan, "Application of Leading-Edge Tubercles to Enhance Propeller Performance," *AIAA Journal*, vol. 58, no. 11, pp. 4659–4671, nov 2020, [**Crossref**]. 39

[145] S.-L. Xing, H.-Y. Xu, Z.-Y. Ye, M.-S. Ma, and Y. Xu, "Dynamic stall control using inflatable leading edge," *International Journal of Modern Physics B*, vol. 34, no. 14n16, p. 2040108, jun 2020, [**Crossref**]. 39

[146] M. Sahin, L. N. Sankar, M. S. Chandrasekhara, and C. Tung, "Dynamic Stall Alleviation Using a Deformable Leading Edge Concept-A Numerical Study," *Journal of Aircraft*, vol. 40, no. 1, pp. 77–85, jan 2003, [**Crossref**]. 39

[147] S. Lee, J. Kim, H. Park, P. G. Jabłoński, and H. Choi, "The Function of the Alula in Avian Flight," *Scientific Reports*, vol. 5, no. 1, may 2015, [**Crossref**]. 39

[148] W. Geissler and B. G. van der Wall, "Dynamic stall control on flapping wing airfoils," *Aerospace Science and Technology*, vol. 62, pp. 1–10, mar 2017, [**Crossref**]. xvii, 39, 40

[149] F. Serralunga, M. C. Mussati, and P. A. Aguirre, "An alternative real-time optimization algorithm with modifier adaptation," in *Computer Aided Chemical Engineering*. Elsevier, 2012, pp. 367–371, [**Crossref**]. 40

[150] P. de Azevedo Delou, J. Matias, J. Jäschke, M. B. de Souza, and A. R. Secchi, "Steady-state real-time optimization using transient measurements and approximated hammerstein dynamic model: A proof of concept in an experimental rig," *Journal of Process Control*, vol. 132, p. 103111, Dec. 2023, [**Crossref**]. 40

[151] D. Krishnamoorthy, "Optimizing surplus heat recovery using fast fourier transform-based extremum seeking control," *IFAC-PapersOnLine*, vol. 56, no. 2, pp. 7178–7183, 2023, [**Crossref**]. 40

[152] D. Krishnamoorthy, "A distributed feedback-based online process optimization framework for optimal resource sharing," *Journal of Process Control*, vol. 97, pp. 72–83, Jan. 2021, [**Crossref**]. 40

[153] S. L. Brunton, J. N. Kutz, K. Manohar, A. Y. Aravkin, K. Morgansen, J. Klemisch, N. Goebel, J. Buttrick, J. Poskin, A. W. Blom-Schieber, T. Hogan, and D. McDonald, "Data-Driven Aerospace Engineering: Reframing the Industry with Machine Learning," *AIAA Journal*, pp. 1–26, jul 2021, [**Crossref**]. 40

[154] N. Precup, M. Mor, and E. Livne, "An Active Variable Camber Continuous Trailing Edge Flapped Wing Wind Tunnel Model for Aeroelastic "In-Flight" Shape Optimization Tests," in *2018 Multidisciplinary Analysis and Optimization Conference*. American Institute of Aeronautics and Astronautics, jun 2018, [**Crossref**]. 40

[155] N. T. Nguyen, N. B. Cramer, K. E. Hashemi, E. Ting, M. Drew, R. Wise, J. Boskovic,

N. Precup, T. Mundt, and E. Livne, "Real-Time Adaptive Drag Minimization Wind Tunnel Investigation of a Flexible Wing with Variable Camber Continuous Trailing Edge Flap System," in *AIAA Aviation 2019 Forum*. American Institute of Aeronautics and Astronautics, jun 2019, [**Crossref**]. 40

[156] T. A. Reist, D. Koo, and D. W. Zingg, "Aircraft cruise drag reduction through variable camber using existing control surfaces," *Journal of Aircraft*, vol. 59, no. 6, pp. 1406–1415, Nov. 2022, [**Crossref**]. 40

[157] C. Forte, N. T. Nguyen, J. Xiong, and J. Sager, "Real-time drag optimization and maneuver load alleviation control for a high aspect ratio wing wind tunnel model," in *AIAA SCITECH 2022 Forum*, 2022, [**Crossref**]. [Online]. Available: https://arc.aiaa.org/doi/abs/10.2514/6.2022-0715 41

[158] H. Li, Y. Zhang, and H. Chen, "Optimization of supercritical airfoil considering the ice-accretion effects," *AIAA Journal*, vol. 57, no. 11, pp. 4650–4669, Nov. 2019, [**Crossref**]. 41

[159] R. Wang, X. Ma, G. Zhang, P. Ying, and X. Wang, "Numerical simulation of continuous morphing wing with leading edge and trailing edge parabolic flaps," *Journal of Aerospace Engineering*, vol. 36, no. 5, Sep. 2023, [**Crossref**]. 41

[160] M. Jentys and C. Breitsamter, "Aerodynamic drag reduction through a hybrid laminar flow control and variable camber coupled wing," *Aerospace Science and Technology*, vol. 142, p. 108652, Nov. 2023, [**Crossref**]. 41

[161] S. A. Tran, A. Fisher, D. A. Corson, and O. Sahni, "Dynamic stall alleviation for an SC1095 airfoil using synthetic jets," in *53rd AIAA Aerospace Sciences Meeting*. American Institute of Aeronautics and Astronautics, jan 2015, [**Crossref**]. 41

[162] R. Duvigneau and M. Visonneau, "Optimization of a synthetic jet actuator for aerodynamic stall control," *Computers & Fluids*, vol. 35, no. 6, pp. 624–638, jul 2006, [**Crossref**]. 41

[163] T. C. Corke, M. L. Post, and D. M. Orlov, "SDBD plasma enhanced aerodynamics: concepts, optimization and applications," *Progress in Aerospace Sciences*, vol. 43, no. 7-8, pp. 193–217, oct 2007, [**Crossref**]. 41

[164] A. Starikovskiy, K. Meehan, N. Persikov, and R. Miles, "Static and dynamic stall control by NS SDBD actuators," *Plasma Sources Science and Technology*, vol. 28, no. 5, p. 054001, may 2019, [**Crossref**].

[165] H. Zong, Y. Wu, H. Liang, and Z. Su, "Experimental investigation and intelligent op-

timization of airfoil zero-lift drag reduction with plasma actuators," *AIAA Journal*, vol. 61, no. 1, pp. 223–240, Jan. 2023, [Crossref]. 41

[166] M. Zhao, L. Xu, Z. Tang, X. Zhang, B. Zhao, Z. Liu, and Z. Wei, "Onset of dynamic stall of tubercled wings," *Physics of Fluids*, vol. 33, no. 8, Aug. 2021, [Crossref]. 41

[167] M. Zhao, L. Xu, X. Li, Y. Zhao, and Z. Liu, "Dynamic stall of pitching tubercled wings in vortical wake flowfield," *Physics of Fluids*, vol. 35, no. 1, Jan. 2023, [Crossref]. 41

[168] K. Arunkumar, G. Sravanthi, A. U. Deepika, and M. Srikanth, "Optimization of uav by using tubercles wing configuration," in *AIP Conference Proceedings*. AIP Publishing, 2023, [Crossref]. 41

[169] Y. Lu, Z. Li, X. Chang, Z. Chuang, and J. Xing, "An aerodynamic optimization design study on the bio-inspired airfoil with leading-edge tubercles," *Engineering Applications of Computational Fluid Mechanics*, vol. 15, no. 1, pp. 292–312, Jan. 2021, [Crossref]. 41

[170] G. Chen, B. Chen, X. Yang, X. Tang, J. Ding, and P. Weng, "Noise reduction for high-lift devices on a swept wing model by droop nose," *Aerospace Science and Technology*, vol. 143, p. 108702, Dec. 2023, [Crossref]. 41

[171] M. A. R. Mohamed, K. S. K. Reddy, and S. S. S. Vishnu, "Bio-inspired optimization of leading edge slat," *Aircraft Engineering and Aerospace Technology*, vol. 95, no. 5, pp. 725–733, dec 2022, [Crossref]. 41

[172] V. T. Gopinathan and J. B. R. Rose, "Aerodynamic performance characterization of bio-inspired wings with leading edge tubercles at low reynolds number," *Proceedings of the Institution of Mechanical Engineers, Part G: Journal of Aerospace Engineering*, vol. 237, no. 3, pp. 561–586, jun 2022, [Crossref]. 41

[173] Y. Zhang, M. Zhao, and M. Zhang, "Research on the aerodynamic performance of the wind turbine blades with leading-edge protuberances," *Ocean Engineering*, vol. 280, p. 114615, jul 2023, [Crossref]. 41

[174] D. S. Miklosovic, M. M. Murray, and L. E. Howle, "Experimental evaluation of sinusoidal leading edges," *Journal of Aircraft*, vol. 44, no. 4, pp. 1404–1408, jul 2007, [Crossref]. xvii, 41, 42

[175] C. R. Colletti and P. J. Ansell, "Airfoil morphed leading-edge design for high-lift applications using genetic algorithm," *Journal of Aircraft*, vol. 60, no. 1, pp. 160–171, jan 2023, [Crossref]. 41

[176] M. Kintscher, M. Wiedemann, H. P. Monner, O. Heintze, and T. Kühn, "Design of a smart leading edge device for low speed wind tunnel tests in the european project SADE," *International Journal of Structural Integrity*, vol. 2, no. 4, pp. 383–405, nov 2011, [**Crossref**]. 42

[177] H. Monner, M. Kintscher, T. Lorkowski, and S. Storm, "Design of a smart droop nose as leading edge high lift system for transportation aircrafts," in *Collection of Technical Papers - AIAA/ASME/ASCE/AHS/ASC Structures, Structural Dynamics and Materials Conference*, 2009, Conference paper, [**Crossref**]. [Online]. Available: https://www.scopus.com/inward/record.uri?eid=2-s2.0-84855624336&partnerID=40&md5=80ea13f6fc19b0695582d87e1fb3dfe3 42

[178] R. J. Raj and J. B. R. Rose, "Flow physics and boundary layer optimization over a NACA airfoil by camber morphing at subsonic speeds," *International Journal of Modern Physics C*, vol. 34, no. 06, dec 2022, [**Crossref**]. 42

[179] J. D. Anderson, S. Corda, and D. M. V. Wie, "Numerical lifting line theory applied to drooped leading-edge wings below and above stall," *Journal of Aircraft*, vol. 17, no. 12, pp. 898–904, dec 1980, [**Crossref**]. 42

[180] M. S. Chandrasekhara, P. B. Martin, and C. Tung, "Compressible dynamic stall control using a variable droop leading edge airfoil," *Journal of Aircraft*, vol. 41, no. 4, pp. 862–869, jul 2004, [**Crossref**]. 42

[181] M. Burnazzi and R. Radespiel, "Design and analysis of a droop nose for coanda flap applications," *Journal of Aircraft*, vol. 51, no. 5, pp. 1567–1579, sep 2014, [**Crossref**]. 42

[182] Dantec Dynamics, "Measurement Principles of LDA," 2022, last accessed 13 April 2022 [**Link**]. [Online]. Available: https://www.dantecdynamics.com/solutions-applications/solutions/fluid-mechanics/laser-doppler-anemometry-lda/measurement-principles-of-lda/ xviii, 50

[183] D. Vieira, "Twin impinging jets inline with a low-velocity crossflow," Ph.D. dissertation, University of Beira Interior, 2017, [**Crossref**]. 51

[184] Oriental Motor, "Easm4xd020arac," https://catalog.orientalmotor.com/item/all-categories-components/ll-categories-y-components-motorized-linear-slides/easm4xd020arac, 2021, last accessed 02.11.2021 [**Link**]. 55

[185] Oriental Motor, "Pke543ac-ps50," https://catalog.orientalmotor.com/item/rkii-series-5-phase-stepper-motors/shop-5-phase-rkii-series-stepper-motors/pke543ac-ps50, 2021, last accessed 02.11.2021 [**Link**]. 56

[186] Oriental Motor, "Ard-cd controller," https://catalog.orientalmotor.com/item/s-short-range-servo-motor-drivers/-drivers-with-built-in-controller-stored-data-type/ard-cd, 2021, last accessed 03.11.2021 [**Link**]. 56

[187] Oriental Motor, "Rksd503-cd controller," https://catalog.orientalmotor.com/item/rksd-5-phase-ac-input-stepper-drivers/rksd-5-phase-stepper-motor-drivers-stored-data/rksd503-cd, 2021, last accessed 03.11.2021 [**Link**]. 56

[188] J. R. Taylor, *Introduction to error analysis, the study of uncertainties in physical measurements*, 2nd ed. University Science Books, 1997. 61, 76

[189] ANSYS, *ANSYS® Fluent Theory Guide (Release 2021 R2)*, Ansys, Inc., 2021. 82, 88, 97

[190] B. Zhu, W. Han, X. Sun, Y. Wang, Y. Cao, G. Wu, D. Huang, and Z. C. Zheng, "Research on energy extraction characteristics of an adaptive deformation oscillating-wing," *Journal of Renewable and Sustainable Energy*, vol. 7, no. 2, p. 023101, mar 2015, [**Crossref**]. 83

[191] T. Kinsey and G. Dumas, "Optimal Tandem Configuration for Oscillating-Foils Hydrokinetic Turbine," *Journal of Fluids Engineering*, vol. 134, no. 3, mar 2012, [**Crossref**]. 83

[192] F. R. Menter, "Two-equation eddy-viscosity turbulence models for engineering applications," *AIAA Journal*, vol. 32, no. 8, pp. 1598–1605, aug 1994, [**Crossref**]. 83

[193] NASA, "2dn00: 2d naca 0012 airfoil validation case," https://turbmodels.larc.nasa.gov/naca0012_val.html, 2014, last accessed 13.07.2021 [**Link**]. 91

[194] B. C. Basu and G. J. Hancock, "The unsteady motion of a two-dimensional aerofoil in incompressible inviscid flow," *Journal of Fluid Mechanics*, vol. 87, no. 1, pp. 159–178, jul 1978, [**Crossref**]. 102

[195] J. Barzilai and J. M. Borwein, "Two-Point Step Size Gradient Methods," *IMA Journal of Numerical Analysis*, vol. 8, no. 1, pp. 141–148, 1988, [**Crossref**]. 114

[196] D. Krishnamoorthy and S. Skogestad, "Real-Time optimization as a feedback control problem – A review," *Computers & Chemical Engineering*, vol. 161, p. 107723, may 2022, [**Crossref**]. 117

[197] B. Hunnekens, M. Haring, N. van de Wouw, and H. Nijmeijer, "A dither-free

extremum-seeking control approach using 1st-order least-squares fits for gradient estimation," in *53rd IEEE Conference on Decision and Control*. IEEE, dec 2014, [Crossref]. xix, 117, 118, 119, 120

[198] J. G. Ziegler and N. B. Nichols, "Optimum Settings for Automatic Controllers," *Journal of Dynamic Systems, Measurement, and Control*, vol. 115, no. 2B, pp. 220–222, jun 1993, [Crossref]. 120

[199] W. D. Musial and D. E. Cromack, "Influence of reynolds number on performance modeling of horizontal axis wind rotors," *Journal of Solar Energy Engineering*, vol. 110, no. 2, pp. 139–144, May 1988, [Crossref]. xxi, 170

[200] S. Eftekhari and A. S. M. Al-Obaidi, "Investigation of a NACA0012 finite wing aerodynamics at low reynold's numbers and 0° to 90° angle of attack," *Journal of Aerospace Technology and Management*, 2019, [Crossref]. 176

[201] E. A. Camacho, F. Neves, J. Barata, and A. R. Silva, "Plunging airfoil: Reynolds number and angle of attack effects," in *AIAA AVIATION 2020 FORUM*. American Institute of Aeronautics and Astronautics, Jun. 2020, [Crossref]. 209

[202] E. A. Camacho, F. M. Neves, F. D. Marques, J. M. Barata, and A. R. Silva, "Effects of a Dynamic Leading Edge on a Plunging Airfoil," in *AIAA AVIATION 2021 FORUM*. American Institute of Aeronautics and Astronautics, jul 2021, [Crossref].

[203] E. A. R. Camacho, F. M. S. P. Neves, A. R. R. Silva, and J. M. M. Barata, "Plunging airfoil: Reynolds number and angle of attack effects," *Aerospace*, vol. 8, no. 8, p. 216, Aug. 2021, [Crossref].

[204] G. L. Torres, E. A. Camacho, F. D. Marques, and A. R. Silva, "Simulations of a plunging airfoil undergoing unequal ascending and descending velocities at low reynolds numbers," in *AIAA Scitech 2021 Forum*. American Institute of Aeronautics and Astronautics, Jan. 2021, [Crossref].

[205] E. A. Camacho, F. D. Marques, A. R. Silva, and J. M. Barata, "Leading-edge parametric study of the naca0012-ik30 airfoil," in *AIAA AVIATION 2022 Forum*. American Institute of Aeronautics and Astronautics, Jun. 2022, [Crossref].

[206] G. Torres, E. A. Camacho, F. D. Marques, and A. R. Silva, "Theoretical and numerical analysis of oscillating airfoil including viscous effects," in *AIAA SCITECH 2022 Forum*. American Institute of Aeronautics and Astronautics, Jan. 2022, [Crossref].

[207] E. A. R. Camacho, F. D. Marques, and A. R. R. Silva, "Influence of a Deflectable Leading-Edge on a Flapping Airfoil," *Aerospace*, vol. 10, no. 7, p. 615, jul 2023, [Cross-

ref].

[208] E. A. Camacho, A. R. Silva, and F. D. Marques, "Optimal leading-edge deflection for flapping airfoil propulsion," *Proceedings of the Institution of Mechanical Engineers, Part G: Journal of Aerospace Engineering*, vol. 237, no. 16, pp. 3640–3653, Sep. 2023, [**Crossref**].

[209] E. A. R. Camacho, F. D. Marques, and A. R. R. Silva, "Predicting the naca0012-ik30 airfoil propulsive capabilities with a panel method," in *The 4th International Electronic Conference on Applied Sciences*, ser. ASEC 2023. MDPI, Nov. 2023, p. 193, [**Crossref**].

[210] E. A. Camacho, A. R. Silva, and F. D. Marques, "Optimal operation of the naca0012-ik30 airfoil," in *AIAA AVIATION 2023 Forum*. American Institute of Aeronautics and Astronautics, Jun. 2023, [**Crossref**].

[211] J. A. F. Pereira, E. A. R. Camacho, F. D. Marques, and A. R. R. Silva, "Fast flapping aerodynamics prediction using a recurrent neural network," in *The 4th International Electronic Conference on Applied Sciences*, ser. ASEC 2023. MDPI, Nov. 2023, p. 219, [**Crossref**].

[212] J. Pinho, E. A. Camacho, and A. R. Silva, "Design and testing of a wing with a morphing trailing edge," in *AIAA AVIATION 2023 Forum*. American Institute of Aeronautics and Astronautics, Jun. 2023, [**Crossref**].

[213] J. G. Silva, E. A. Camacho, and A. R. Silva, "Investigation of asymmetric plunging of a naca0012 airfoil," in *AIAA SCITECH 2023 Forum*. American Institute of Aeronautics and Astronautics, Jan. 2023, [**Crossref**].

[214] E. A. R. Camacho, M. M. da Silva, A. R. R. Silva, and F. D. Marques, "Real-time optimization of wing drag and lift performance using a movable leading edge," *Physics of Fluids*, vol. 36, no. 1, Jan. 2024, [**Crossref**].

[215] E. A. Camacho, A. R. Silva, and F. D. Marques, "Dynamic stall mitigation using a deflectable leading edge: The ik30 mechanism," *Journal of Aerospace Engineering (Accepted, now in production)*, 2024, [**Crossref**].

[216] E. A. R. Camacho, A. R. R. Silva, and F. D. Marques, "Mitigating dynamic stall with a movable leading-edge: The naca0012-ik30 wing," in *ICAS Proceedings*, 2024, Conference paper, [**Link**]. 209

Appendixes

Appendix A1 - Flow Visualization

Images start on the next page.

Videos may be found at **https://www.earc96.com/PhD**.

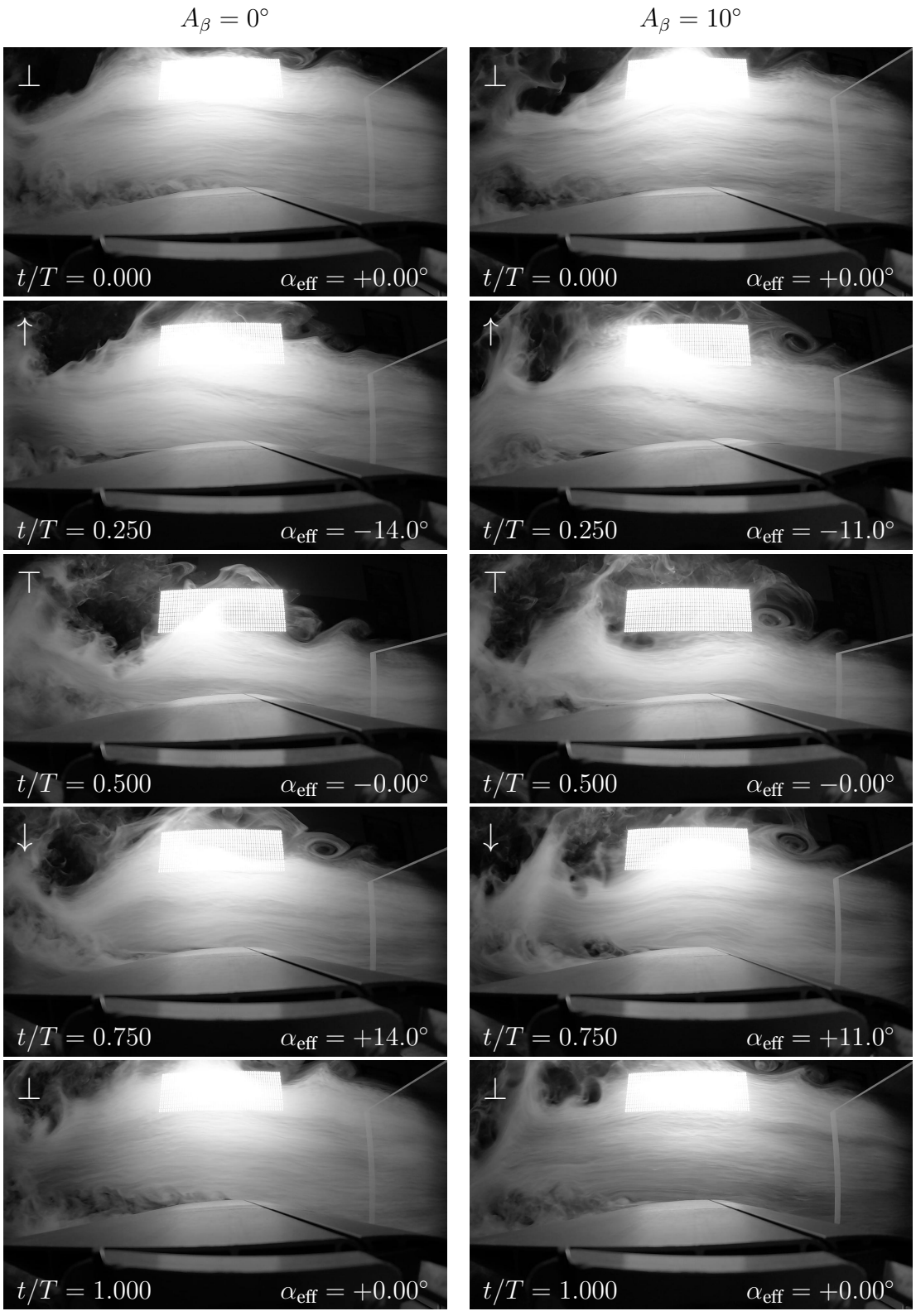

Figure 10.1: Flow visualization at $Re = 1.0 \times 10^4$, $h = 0.25$ and $k = 1.0$.

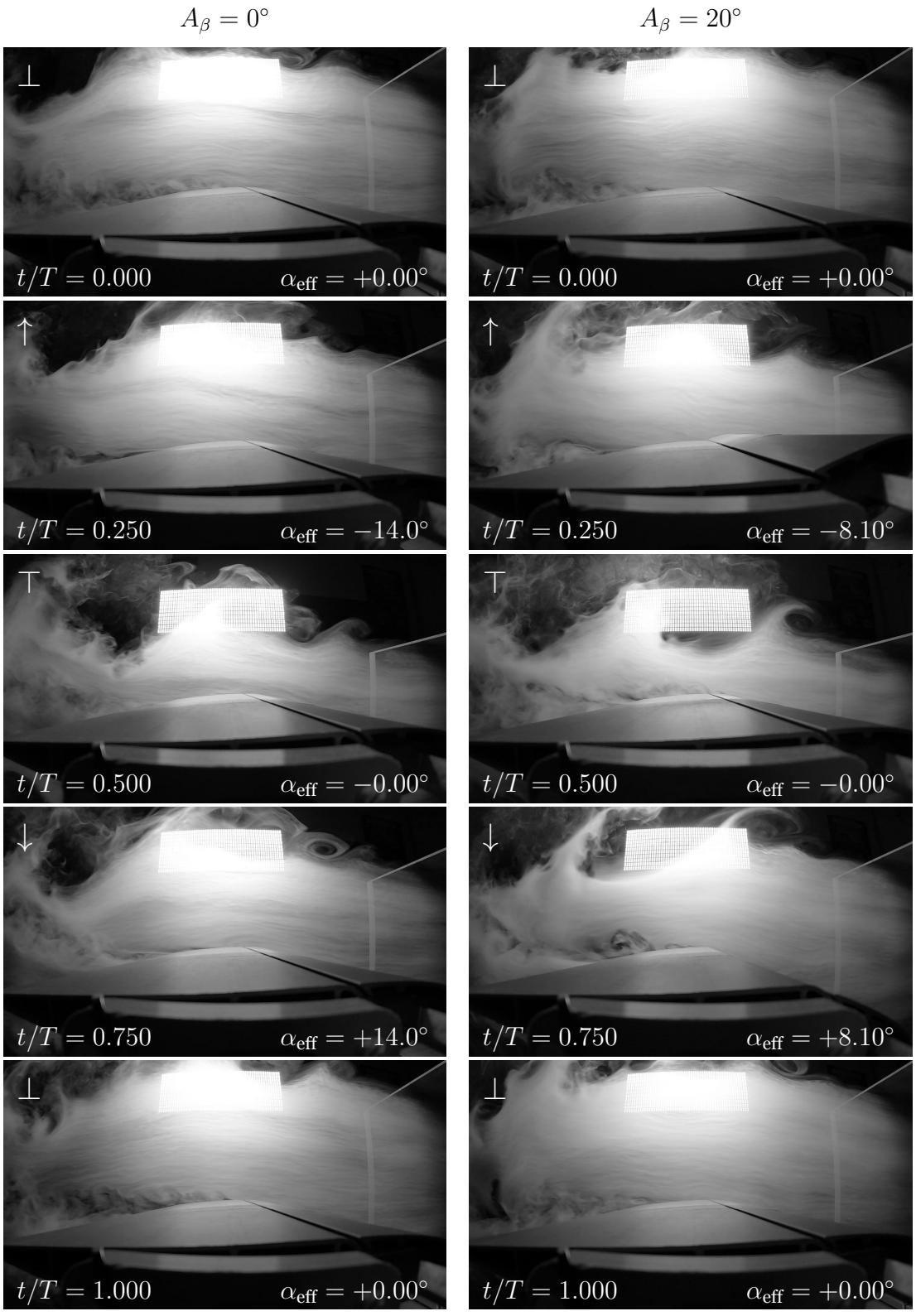

Figure 10.2: Flow visualization at $Re = 1.0 \times 10^4$, $h = 0.25$ and $k = 1.0$.

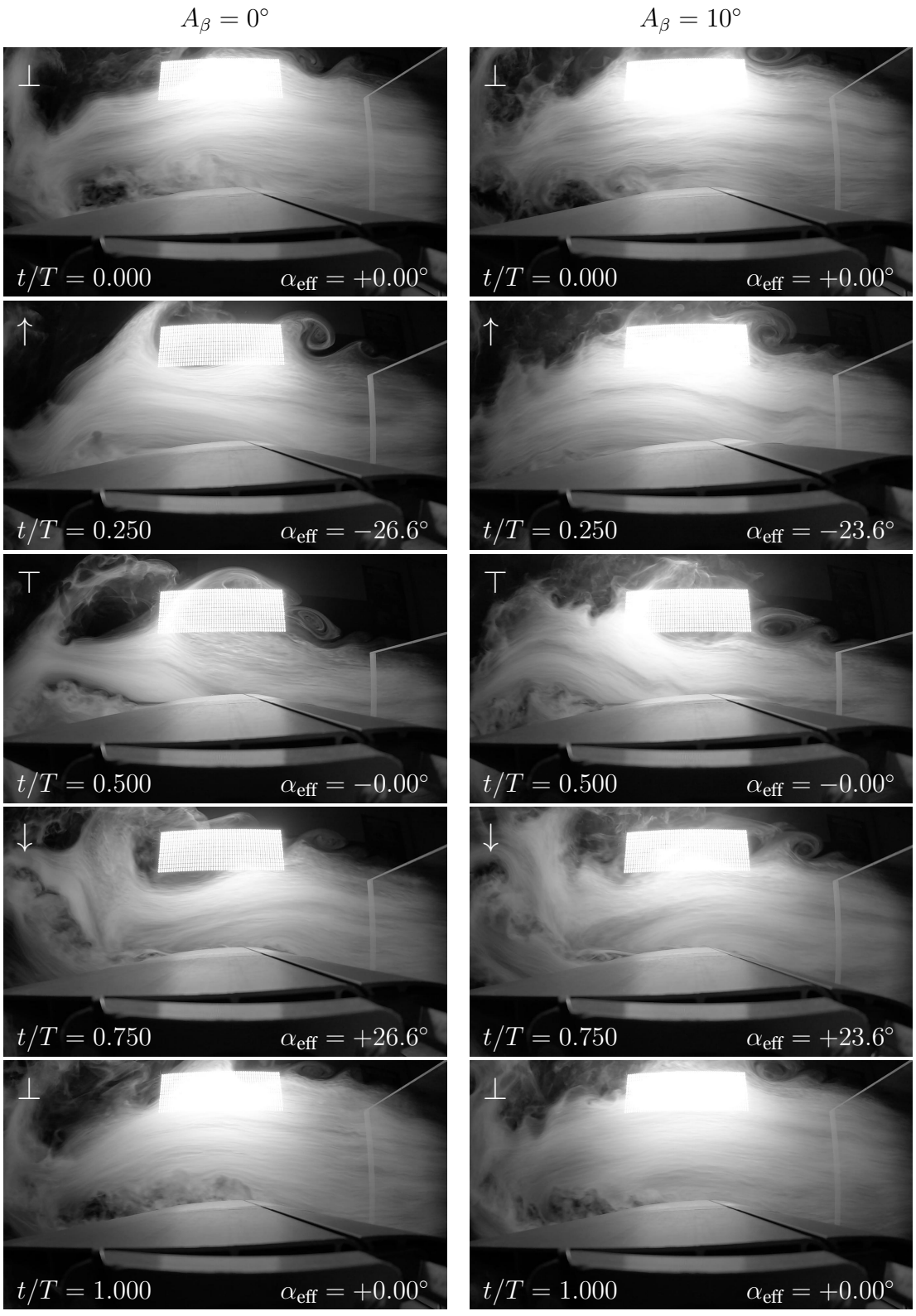

Figure 10.3: Flow visualization at $Re = 1.0 \times 10^4$, $h = 0.25$ and $k = 2.0$.

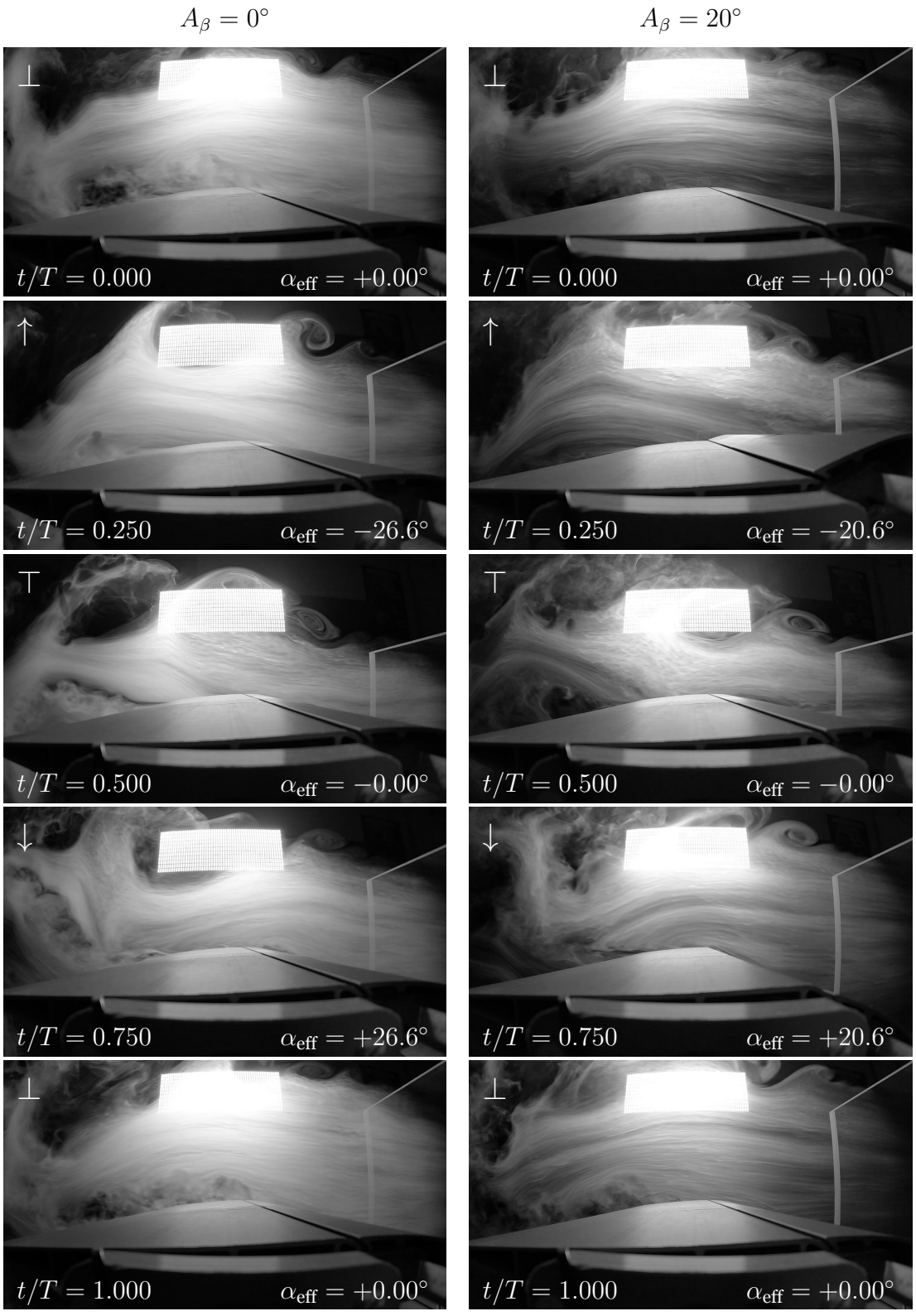

Figure 10.4: Flow visualization at $Re = 1.0 \times 10^4$, $h = 0.25$ and $k = 2.0$.

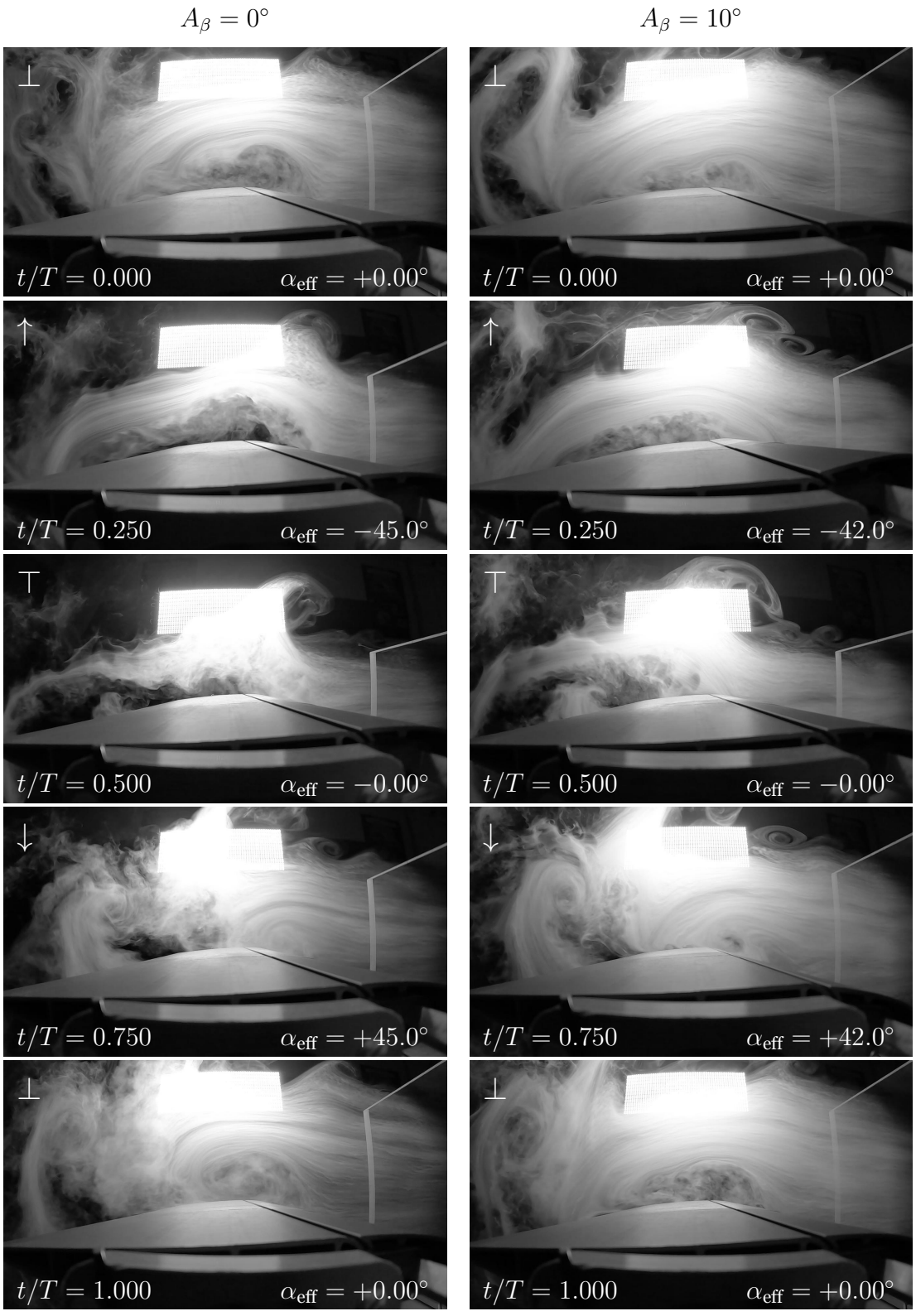

Figure 10.5: Flow visualization at $Re = 1.0 \times 10^4$, $h = 0.25$ and $k = 4.0$.

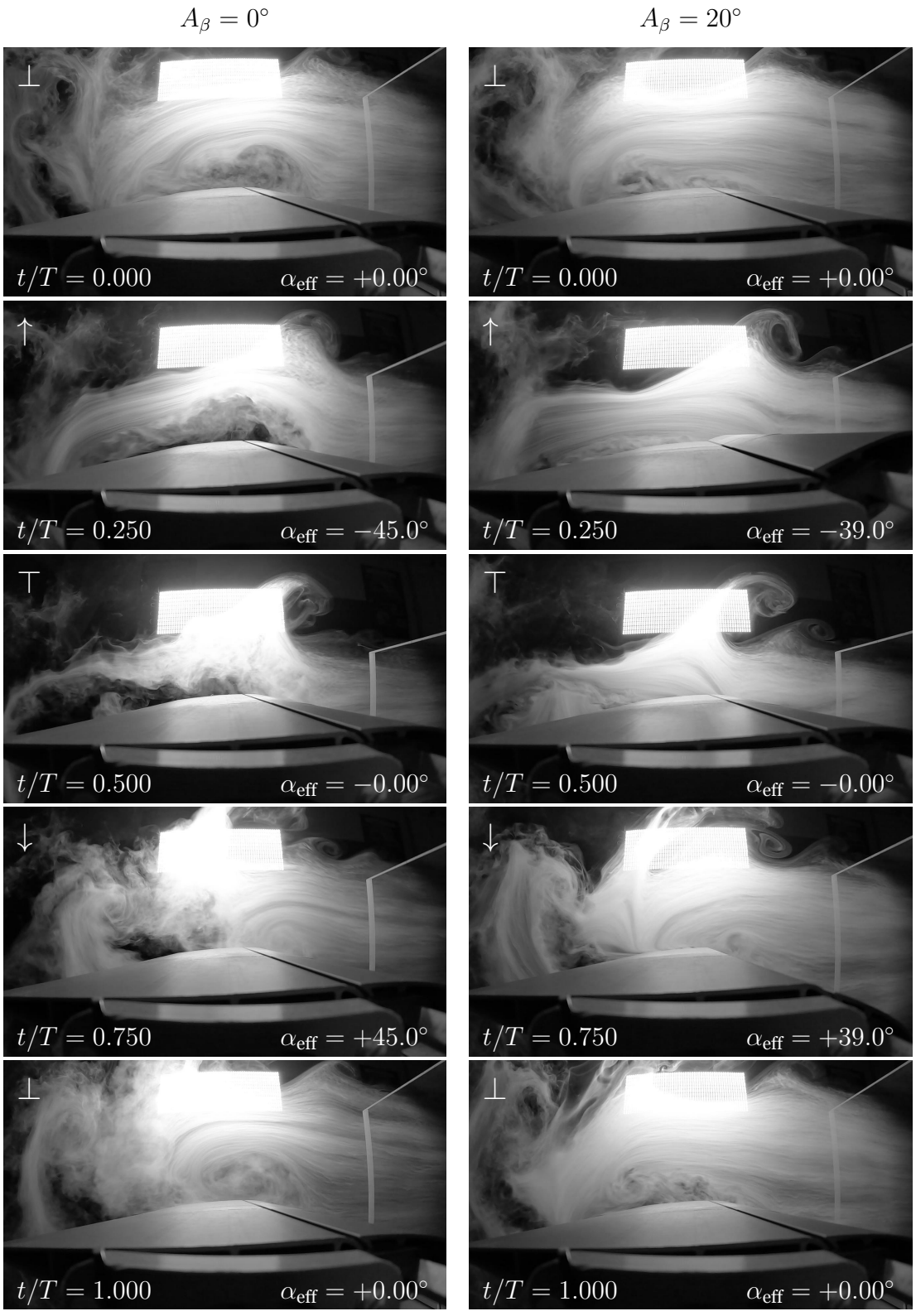

Figure 10.6: Flow visualization at $Re = 1.0 \times 10^4$, $h = 0.25$ and $k = 4.0$.

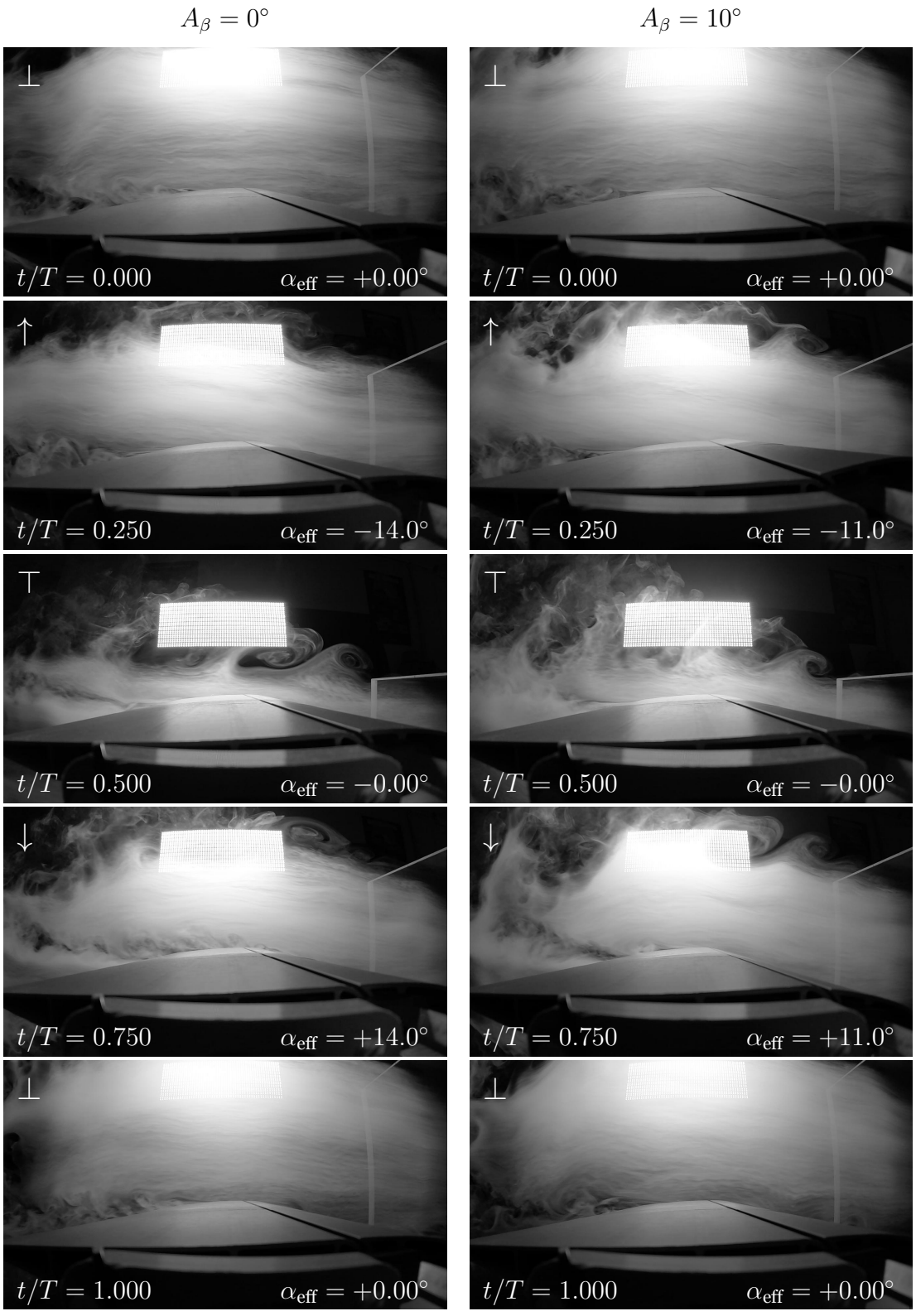

Figure 10.7: Flow visualization at $Re = 1.0 \times 10^4$, $h = 0.50$ and $k = 0.5$.

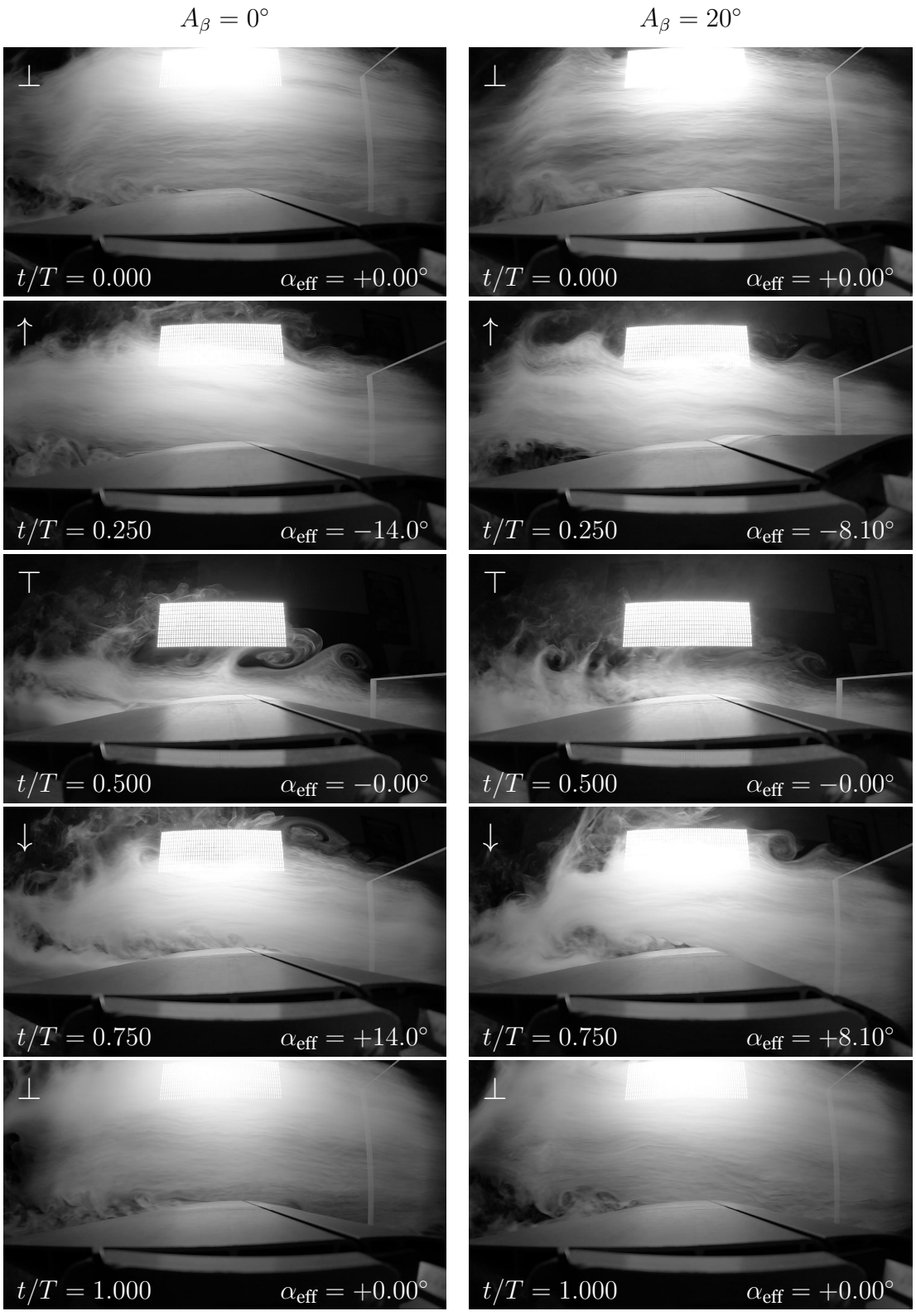

Figure 10.8: Flow visualization at $Re = 1.0 \times 10^4$, $h = 0.50$ and $k = 0.5$.

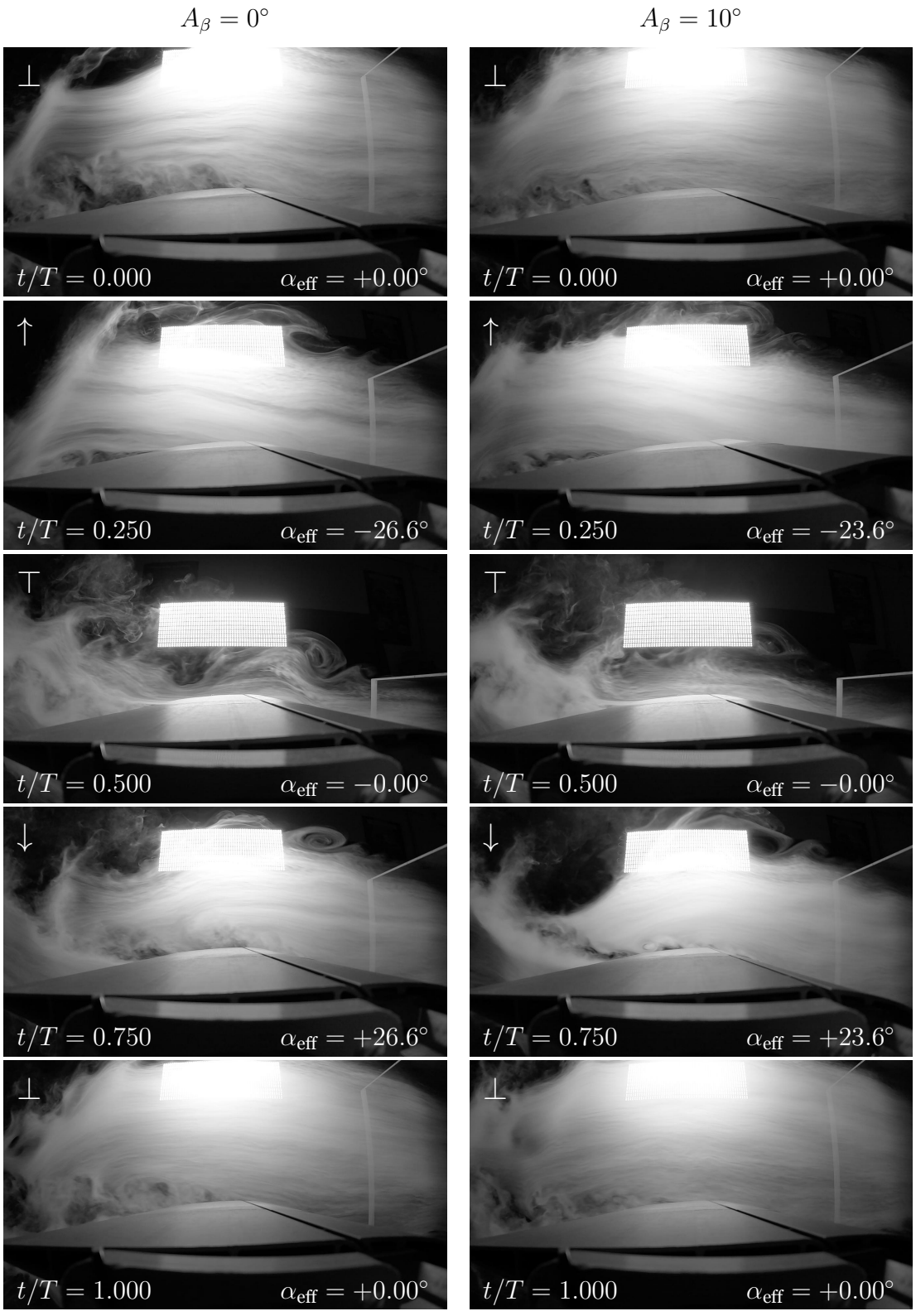

Figure 10.9: Flow visualization at $Re = 1.0 \times 10^4$, $h = 0.50$ and $k = 1.0$.

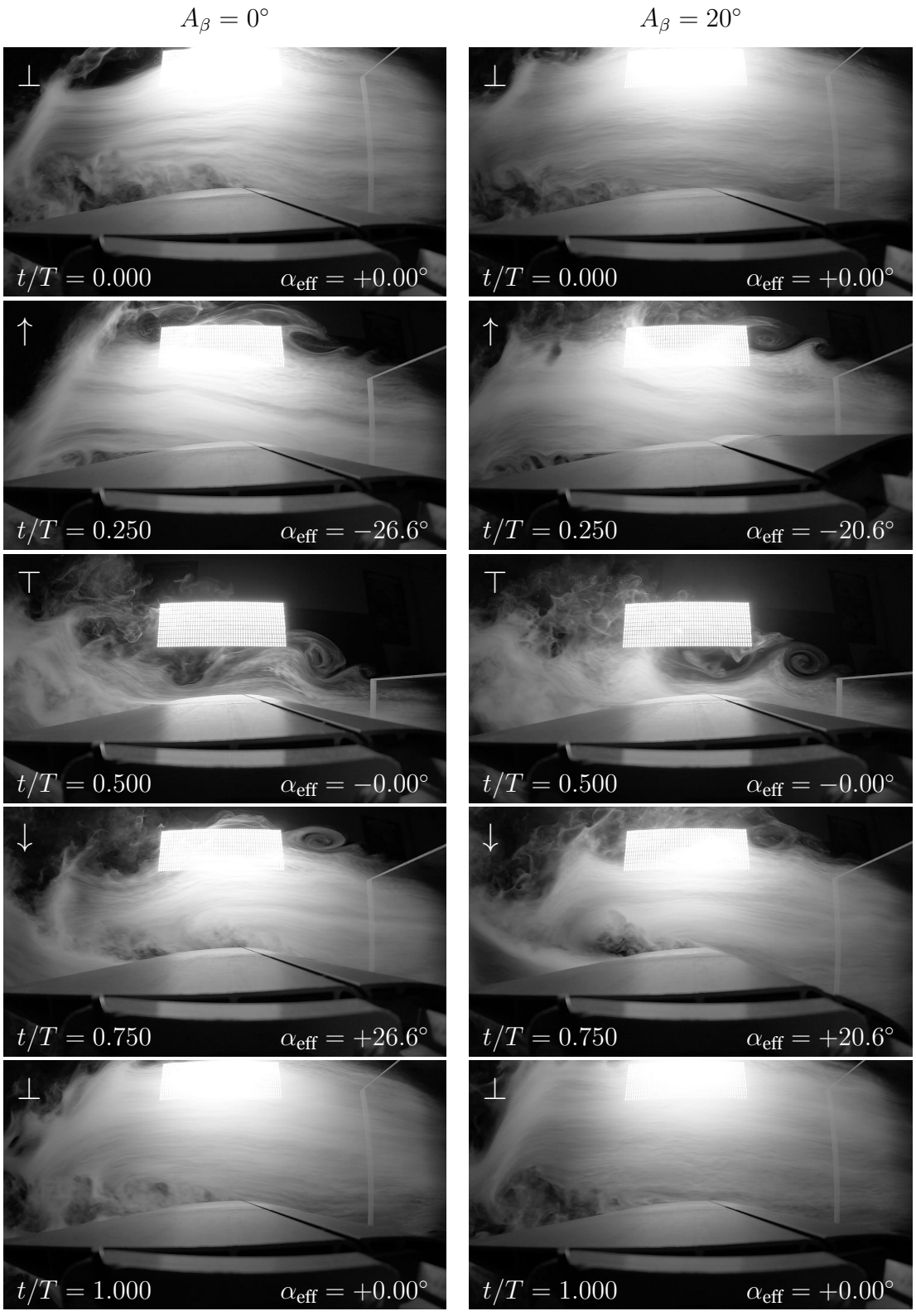

Figure 10.10: Flow visualization at $Re = 1.0 \times 10^4$, $h = 0.50$ and $k = 1.0$.

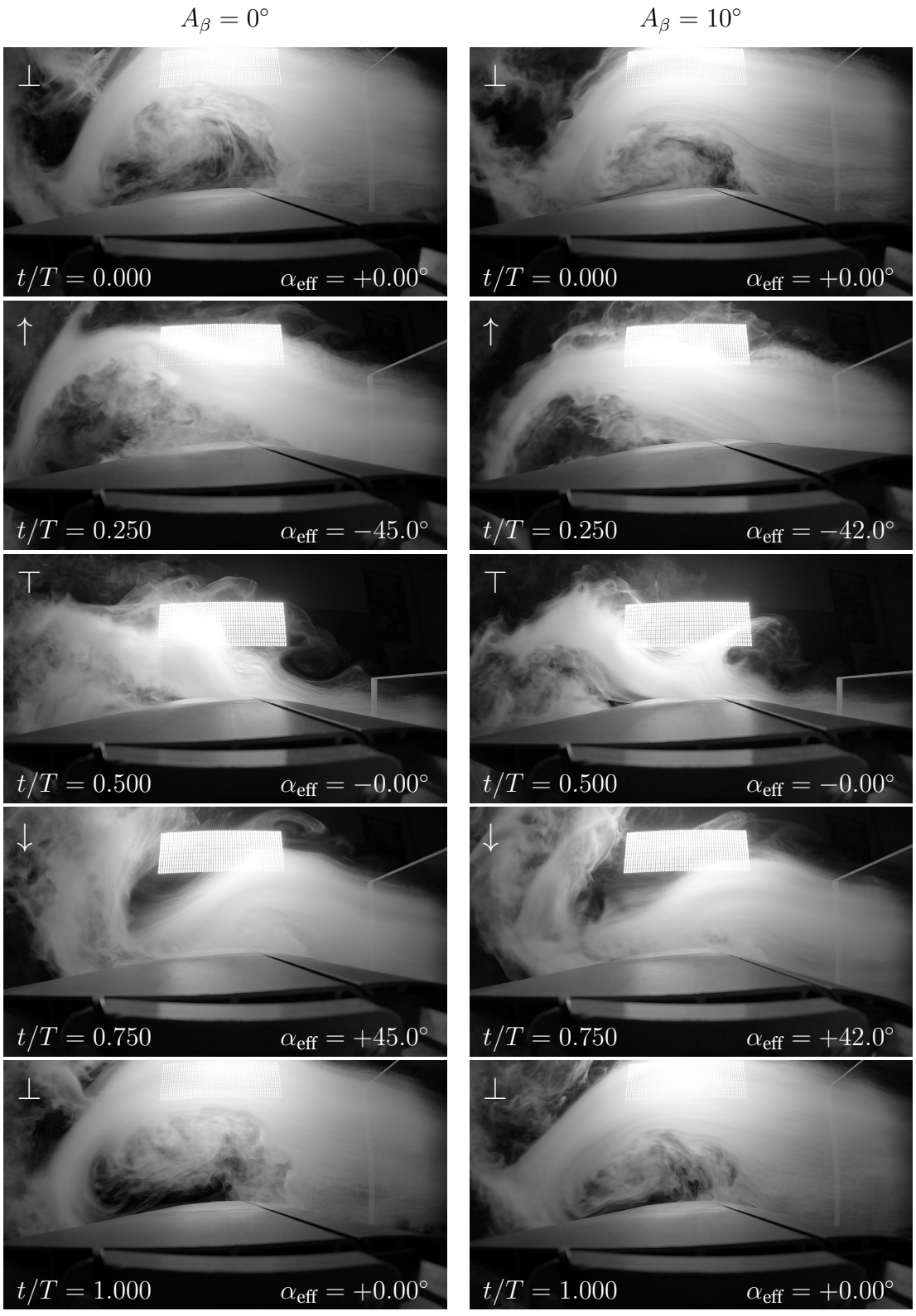

Figure 10.11: Flow visualization at $Re = 1.0 \times 10^4$, $h = 0.50$ and $k = 2.0$.

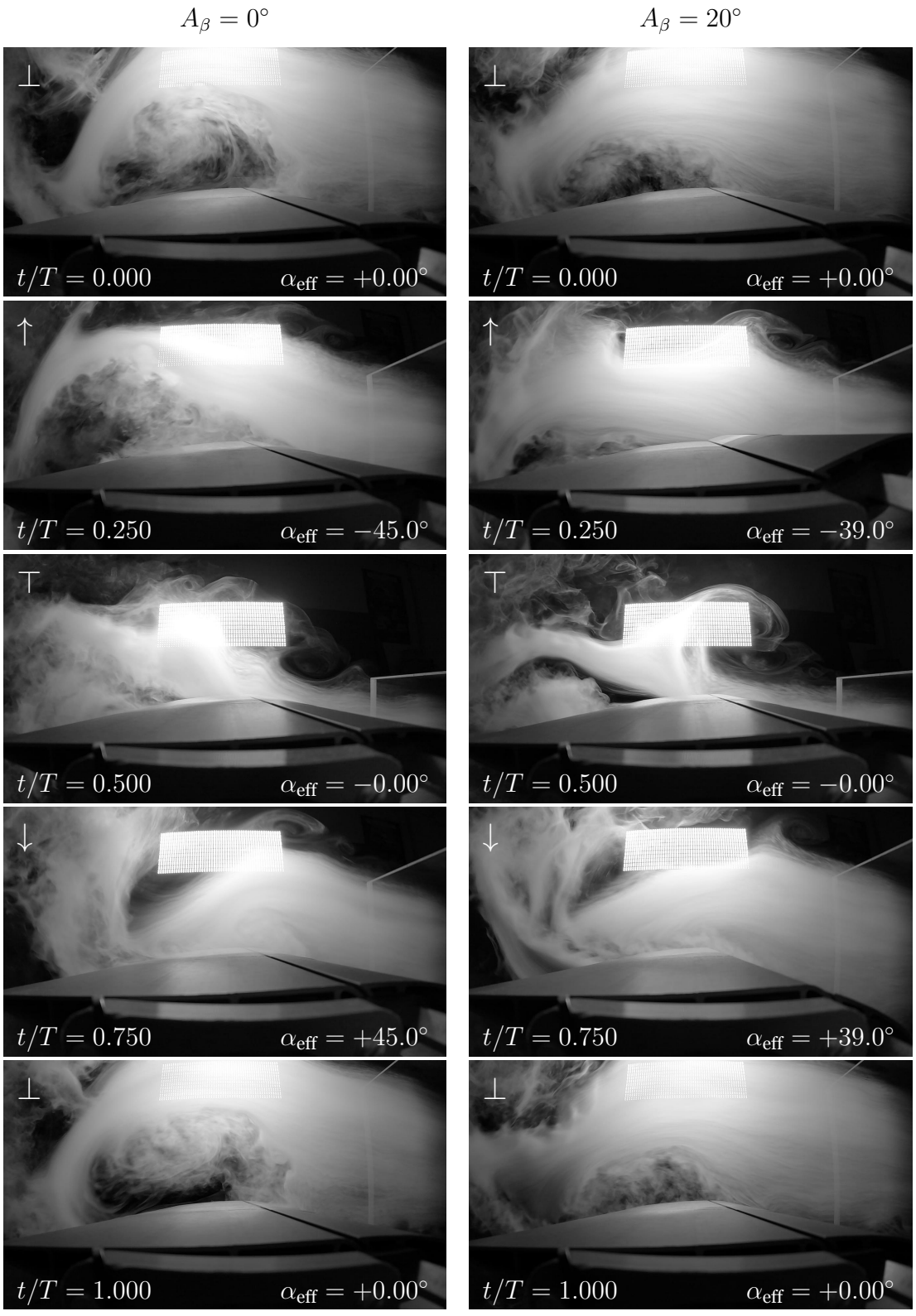

Figure 10.12: Flow visualization at $Re = 1.0 \times 10^4$, $h = 0.50$ and $k = 2.0$.

Appendix A2 - Plunging Results

Graphs start on the next page.

Appendix containing the dynamic stall mitigation tests of plunging cases considering a nondimensional amplitude of 0.25. Data may be found at **https://www.earc96.com/PhD**.

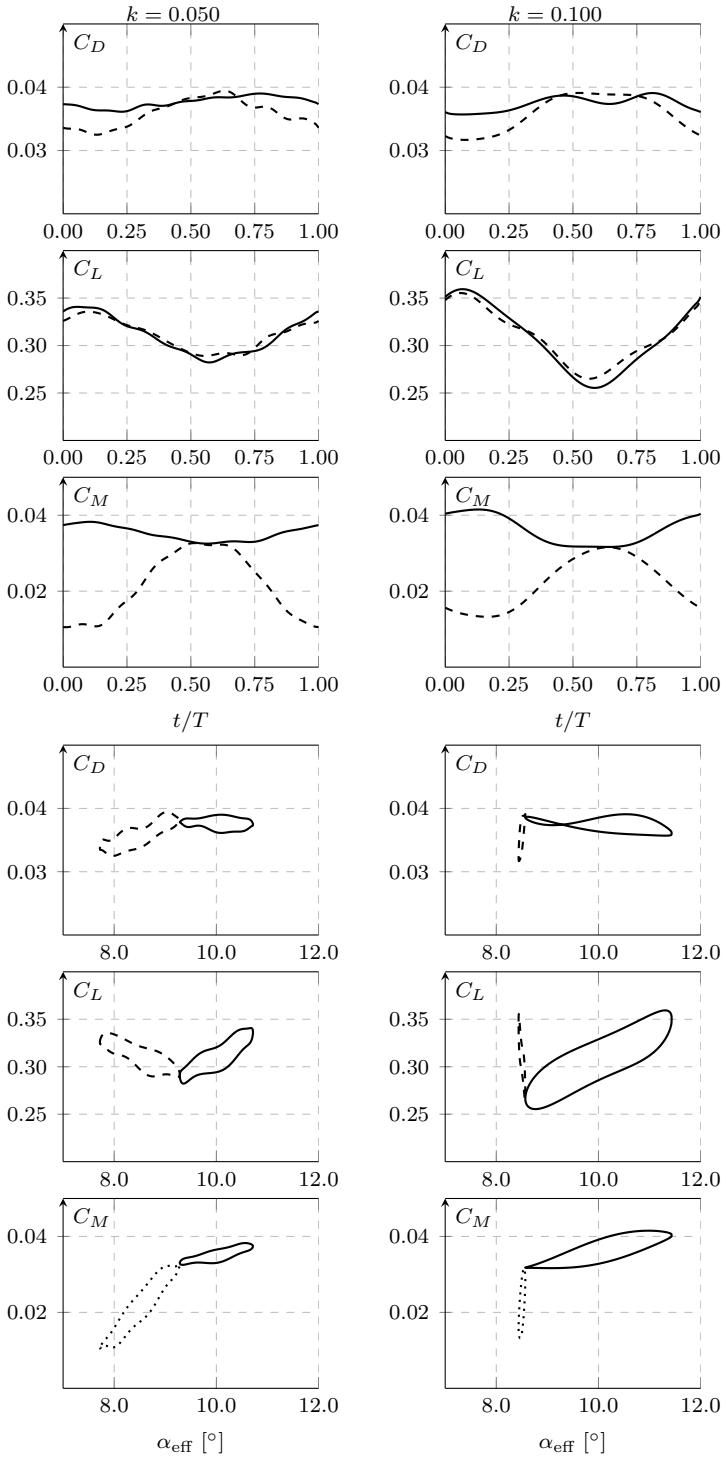

Figure 10.13: Aerodynamic coefficients with $h = 0.25$ and $\overline{\psi} = 10^\circ$ ($\dot{\psi} = 0$).

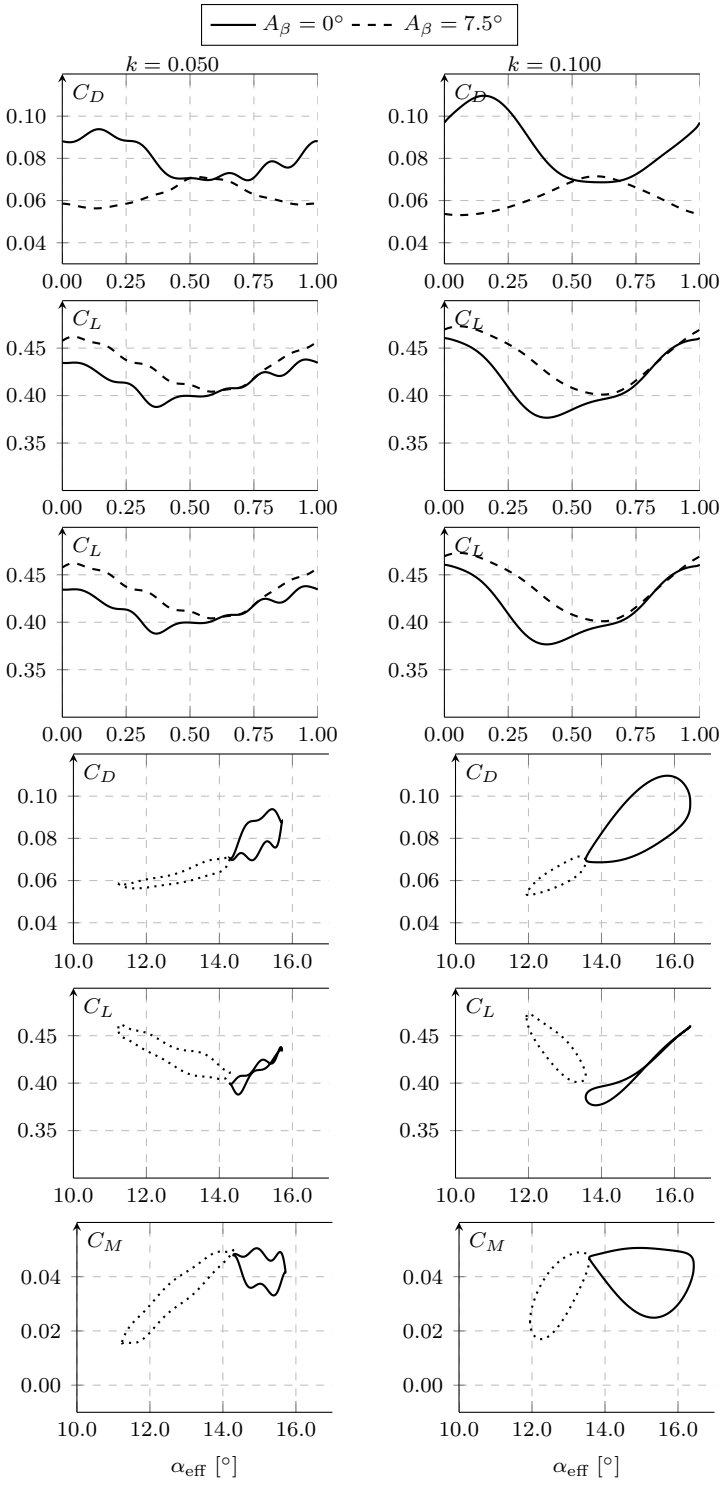

Figure 10.14: Aerodynamic coefficients with $h = 0.25$ and $\overline{\psi} = 15°$ ($\dot{\psi} = 0$).

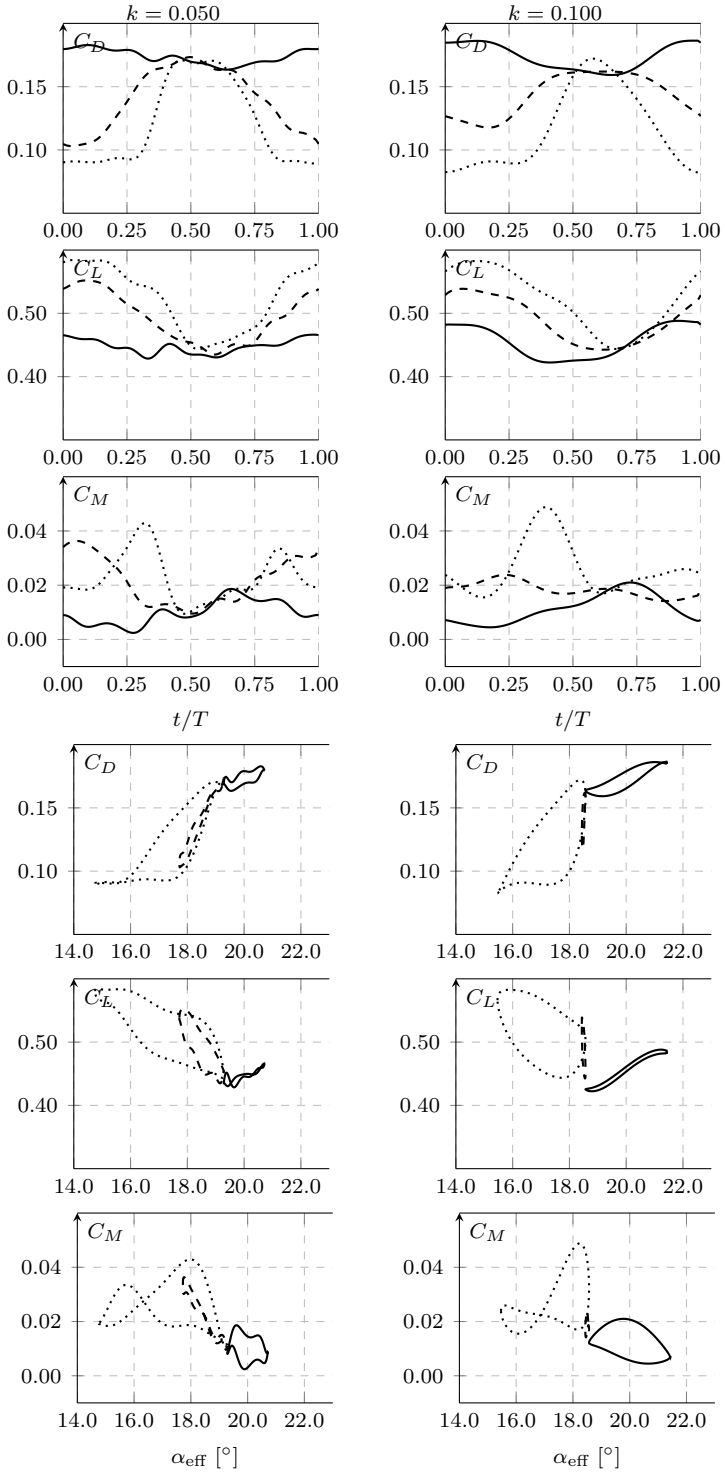

Figure 10.15: Aerodynamic coefficients with $h = 0.25$ and $\overline{\psi} = 20^\circ$ ($\dot{\psi} = 0$).